Renewable and Sustainable Energy Reviews 215 (2025) 115570

Contents lists available at ScienceDirect

Renewable and Sustainable Energy Reviews

journal homepage: www.elsevier.com/locate/rser

Graphdiyne-based metal-free catalysts: Innovations in synthesis, properties, functionalization, morphology and applications

Hamid Ali [a], Obaid Iqbal [b], Muhammad Sadiq [c], Jawad Ul Hassan [d], Basem Al Alwan [e], Atef El Jery [e], Ahmed M. Abu-Dief [f,g], R.A. El-Kasaby [h,i], Asif Hayat [j], Dewu Yue [a,*], Ma Xingyi [k,l,m,**]

[a] Information Technology Research Institute, Shenzhen Institute of Information Technology, Shenzhen, 518172, China
[b] School of Materials Science and Engineering, Institutes of Physical Science and Information Technology, Anhui University, Hefei 230601, Anhui, China
[c] School of Computer Science, Shenzhen Institute of Information Technology, Shenzhen, 518172, China
[d] Department of Electrical Engineering, Bahria University, Islamabad, Pakistan
[e] Department of Chemical Engineering, College of Engineering, King Khalid University, Abha, 61411, Saudi Arabia
[f] Department of Chemistry, Faculty of Science, Sohag University, Sohag, 82524, Egypt
[g] Department of Chemistry, College of Science, Taibah University, P.O. Box 344, Madinah, Saudi Arabia
[h] Department of Chemistry, College of Science, Taibah University, Al-Madinah Al-Munawarah, 30002, Saudi Arabia
[i] Chemistry Department, Womens College for Arts Science and Education, Ain Shams University, Cairo, Egypt
[j] Department of Chemistry, Lishui University, 323000, Lishui, China
[k] School of Science, Harbin Institute of Technology, Shenzhen, Guangdong, 518055, China
[l] Biosen International, Jinan, Shandong, 250117, China
[m] Briteley Institute of Life Sciences, Yantai, Shandong, 264003, China

ARTICLE INFO

Keywords:
Graphdiyne
Synthesis reactions/methods
Morphology
Functionalization
Dimensionality
Potential applications

ABSTRACT

Graphdiyne (GDY) is a novel two-dimensional carbon material characterized by unique properties, positioning it as a promising candidate for various applications in catalysis, energy storage, and electronics. This review offers a comprehensive analysis of GDY, covering its theoretical simulations, structural characteristics, and properties. This research examines the molecular structure, electronic characteristics, mechanical strength, optical behavior, and thermal and conductive properties. In addition, the potential of GDY as a metal-free catalyst, as well as its tunable pore size and surface area, are investigated. Similarly, several synthesis methods, including dry and wet chemistry, Cu-surface-mediated synthesis, and template-based strategies, are discussed, emphasizing progress in the synthesis of GDY derivatives with improved performance. The review examines various synthesis reactions, including Glaser coupling and alkynylsilane coupling, as well as methods to enhance GDY performance through bandgap engineering, doping, defect engineering, and surface functionalization. Additionally, the various dimensionalities of GDY were examined, ranging from zero-dimensional/quantum dots to three-dimensional structures, each presenting distinct advantages in applications. The functionalization of GDY with different organic and inorganic molecules, including anthraquinone and porphyrin, is examined to enhance its catalytic and electronic properties. Finally, the wide-ranging applications of GDY were explored, including its role in photocatalytic and electrocatalytic reactions for hydrogen production, oxygen evolution, overall water splitting, CO_2 reduction/conversion, as well as its use in supercapacitors, batteries, and solar cells. This review serves as a comprehensive guide for scientists interested in exploring the potential of GDY across various scientific and technological domains.

1. Introduction

The demand for renewable energy sources has arisen due to increasing worldwide environmental issues. A major challenge of the twenty-first century is achieving environmental sustainability through the development of a dependable and extensive renewable energy

* Corresponding author.
** Corresponding author. School of Science, Harbin Institute of Technology, Shenzhen, Guangdong, 518055, China
E-mail addresses: yuedewu@sziit.edu.cn (D. Yue), maxy@hit.edu.cn (M. Xingyi).

https://doi.org/10.1016/j.rser.2025.115570
Received 28 October 2024; Received in revised form 26 February 2025; Accepted 28 February 2025
Available online 17 March 2025

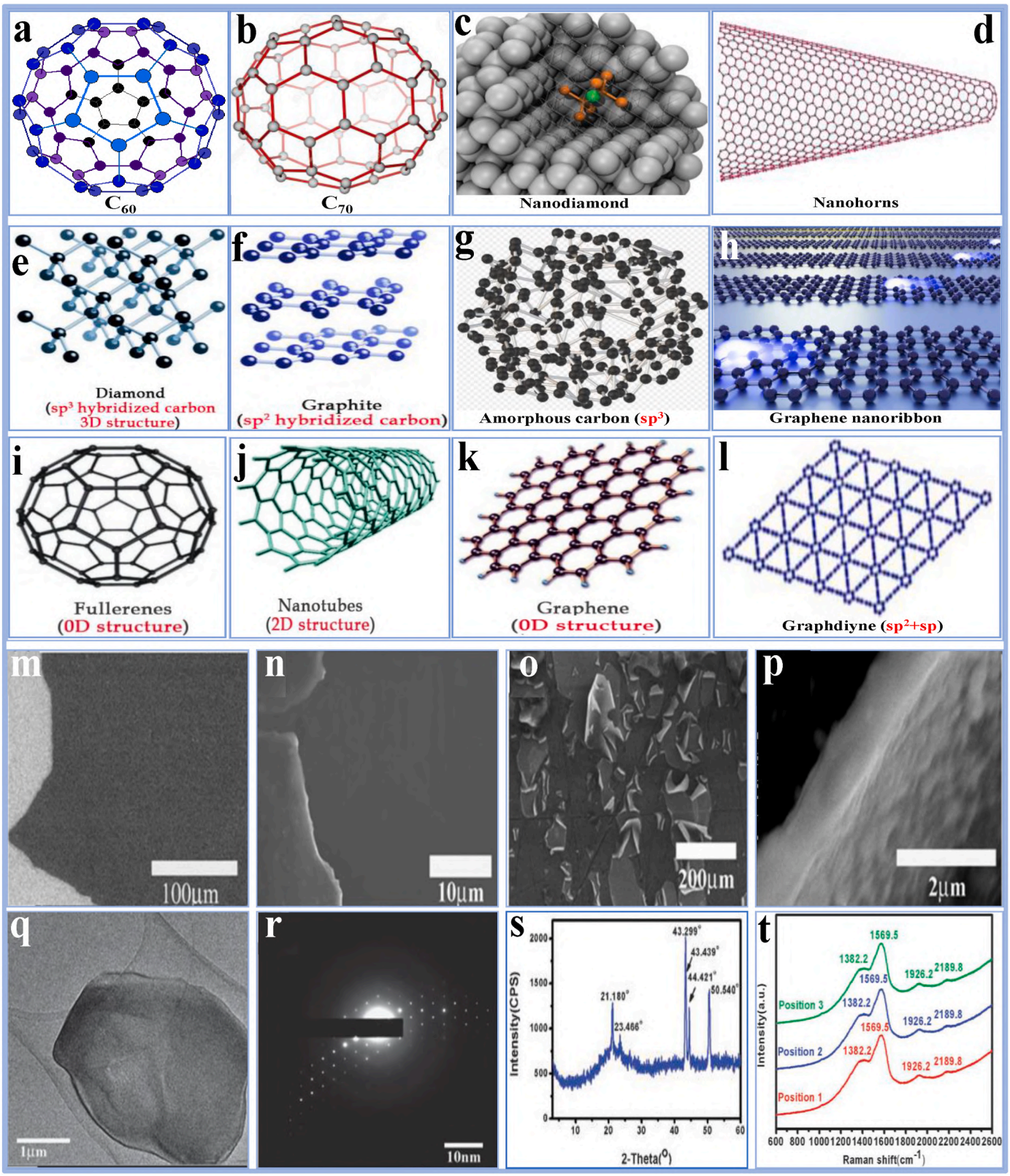

Fig. 1. (a–l) Synthetic and naturally occurring carbon allotropes [37] Copyright © 2019, Springer Nature. The SEM patterns of GDY films synthesized on the surface of copper foil (m) Larger-area GDY film; (n) High magnification pattern; (o) Cracked film on the brim of copper foil; (p) A turned-up film; (q) TEM; (r) SAED; (s) XRD; (t) Raman analysis of GDY film [26] Copyright © 2010, Royal Society of Chemistry.

system [1–3]. The protection of a sustainable and eco-friendly future for mankind may be accomplished via inventive breakthroughs and enhancements in existing energy generation and storage technologies [4]. Conventional energy generation techniques, including fossil fuel power plants, substantially contribute to the degradation of the environment and global warming [5]. The depletion of fossil fuels results in significant shortages, requiring the transition to renewable and sustainable alternatives and a reduction of chemical processes that depend primarily on fossil fuels [6]. As a result, there is a strong need to enhance conventional energy sources by reducing dependence on fossil fuels and using environmentally friendly energy for fuel cell conversion [7]. But, alternative sustainable energy sources, such as solar, wind, and hydroelectric power, have limited potential. Globally, conventional fossil fuels are undergoing significant changes owing to rapid progress in energy sources used for both commercial and residential uses [8]. The development of efficient, low-cost, secure, and sustainable energy transformation and storage systems has garnered attention for their extensive applications in portable electronics, electric cars, and resilient power-grid storage facilities, owing to their pollution-free characteristics [9]. The large specific surface area (SSA) and excellent electrical porosity of 2D materials, particularly graphene, are drawing interest in enhanced catalyst design [10]. The graphene family, which consists of 2D ultrathin nanosheets, is well-suited for preventing the aggregation of nanoparticles and enhancing the transmission of electrons due to its highly conjugated structure [11]. Carbon-based electrode materials have attracted considerable interest owing to their wide availability, versatile bonding structure, cost efficiency, and environmental sustainability, among other advantages. Graphdiyne (GDY) has received particular attention, partly due to the interest in graphene, because of its exceptional structure, physical properties, and chemical attributes, making it a promising material for renewable energy production and storage. Carbon materials (CMs) are significant for all organisms on Earth and are extremely desired owing to their three unique hybridizations (sp, sp^2, and sp^3) [12]. For the past two decades, there has been a significant increase in the research of comprehensive CMs in the field of organic synthetic chemistry. At present, scientists are developing innovative 2D CMs and evaluating their potential uses by combining CMs of various forms, including 0D fullerenes [13], 1D carbon nanotubes [14], and graphene [15]. For example, various C-allotropes, carbon nanotubes (CNTs) (sp^2), fullerene (sp^2), and diamond (sp^3) were effectively synthesized and used in various applications during the last twenty years by hybridization of carbon molecules. Several optimized functionalities were observed as a result of the outstanding electrical, mechanical, and electrochemical properties of carbon-coated substrates and materials, such as graphene, diamond, graphite [15], fullerene nano structure [16], and unstructured carbon [17,18] (Fig. 1a–l). Carbon allotropes (C-allotropes), determined by their distinctive structures of carbon atoms with sp^2 and sp hybridizations (GDY), demonstrate remarkable flexibility and accessibility, making them very promising for advanced material applications [19].

New carbon allotropes with enhanced structural and electronic properties and long-term stability will be developed through analytical and quantitative attempts. Diederich et al. [20] synthesized several highly desirable (but ineffective) structures for 2D/3D carbon systems, differing from diamond and graphite structures. The Cyclo-Cn is an n-membered monocyclic loop made of sp-hybridized carbon atoms (HCAs). It showed a distinct electronic structure derived from sp- and sp^2-hybridized π-orbitals assembly in two vertical arrangements. The graphene family is a highly novel subject in the field of low-dimensional condensed matter materials, aiming to develop new condensed matter systems by the integration of sp and sp^2 hybrid carbon allotropes using certain periodic patterns [21]. The graphene possess a distinctive structure and set of properties as a result of the presence of carbon molecules formed through sp-hybridization by comparing with different carbon allotropes composed of sp^2-hybridized CAs (e.g., CNT [14] and graphene [22]). For example, graphene have pore topologies that are evenly distributed and large π-conjugation structures, which make them very suitable for catalysis [23] and energy-related areas [24]. Baughman et al. [25] predicted the first GYs structural model in 1987. Li et al. [26] synthesized the first graphene film, known as GDY, on a copper (Cu) substrate via the in situ Glaser coupling reaction of hexaethynylbenzene (HEB) monomers, using the high energy and elasticity of sp-bonds (Fig. 1m–t). Notably, more than half of the literature on graphene focusses on GDY. The GDY system, composed of phenyl butadiyne, can be synthesized via targeted polymerization of cyclo-C18 or oxidative synthesis of HEB. The properties of 2D CMs were not well-defined over decade ago due to the coupling of carbon molecules with uneven electron dispersion [27]. GDY consisting of interconnected carbon materials at the atomic scale, was the first all-carbon material synthesized using intermediate temperatures and wet chemistry in 2010 [28]. This breakthrough attracted significant attention in its potential applications, including batteries, solar energy cells, electrochemical sensors, radioactivity protection, solar steam production, and catalysis. In recent decades, CMs have led progress in organic synthetic chemistry. Scientists are now focusing on carbon variations with unique structures, electronic, and optical properties [29]. An example is the 2D structure of planar hexagonal carbon atom cells (C6) with sp^2 hybridization, referred to as graphene, which facilitated progress in CMs [30]. Novel carbon variations including sp and sp^2 HCAs may demonstrate increased variation and accessibility comparable to naturally occurring CMs [31]. Haley et al. [32] predicted the primary synthesis of GDY, which featured alternating double and single bonds and was composed of di-acetylene-containing sp- and sp^2-CMs [33]. The graphene and GDY structures are considered to be acetylene-linked C6 hexagons in graphene with a distinct electronic structure and atomic shape [34]. A homogeneous carbon system with coordinated electronic properties, a higher degree of π-conjugation, and pores that are propagated uniformly may exhibit flexible or even enhanced performance relative to graphene. Their potential applications include battery anodes [35], which have been synthesized experimentally. This review not only highlights the increasing number of research on the nano-structure of GDY, but it also provides a strategy for synthesizing highly functional materials using GDY. As a 2D material, GDY has become an ideal candidate for applications in various conventional and emerging research areas due to its porous structure, unconventional electronic arrangement, and accessibility to diverse carbon structures. GDY-based materials are used in a wide range of applications, such as energy storage, electronic devices, catalysis, and photovoltaic cells. These materials are synthesized in various nanostructures, including nanotubes (NTs), nanosheets (NSs), nanowires (NWs), nano-wall (NWls) arrays, and stripe patterns, which allow for the modifications of their functionalities to suit specific applications. The chemical composition of optimized GDY is a monocrystalline material with an atomic-scale size, while the width of synthetic GDY is challenging to regulate and is relatively heterogeneous or amorphous. Therefore, the properties of as-synthesized GDY are inadequate to those estimated by theoretical studies [36]. The 2D structure is the result of di-acetylenic bonding between benzene groups in a generalized ring arrangement. It is a synthetic C-allotrope that is highly solid and conjugated by di-acetylene atoms. It has a strong band gap of 0.46 eV and an increased electron kinetics at room temperature that ranges from 104 to 105 $cm^2\ V^{-1}\ s^{-1}$ [26]. Consequently, it is a material that has high potential for the development of future nanotechnology. GDY-related research has experienced rapid growth since its inception in 2010. GDY materials have emerged in various designs, including micro particles, films, and NWls, and have been used in significant applications such as energy preservation and catalysis. These materials were made using both moist and dry processes. A considerable gap persists between conceptual advancement and practical synthesis of controlled GDY, impeding its use in practical applications. This work thoroughly examines the synthesis, functionalization, and applications of GDY and its analogs. The synthesis of GDY has been accomplished by many strategies, including dry chemistry, on-surface synthesis,

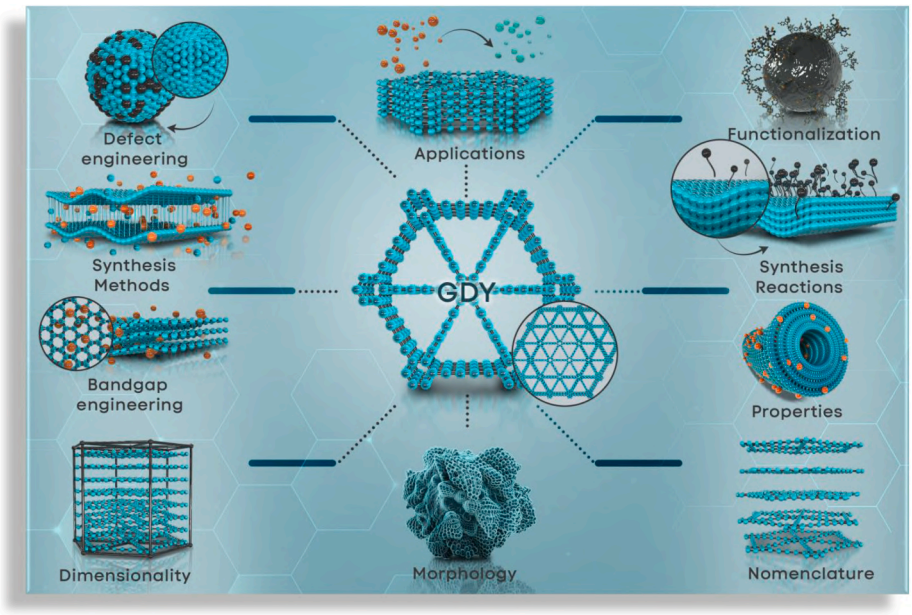

Scheme. 1. Graphical representation of the fundamental areas addressed in this review.

top-down approaches, explosive techniques, wet chemistry, and Cu-surface-mediated synthesis, facilitating the production of GDY with customized characteristics for particular purposes. Similarly, various functionalization techniques, including the adsorption of guest molecules, hydrogenation, fluorination, metal decorating, and the insertion of diverse organic moieties (e.g., anthraquinone, benzyl, cyanine, porphyrin, pyridine, triazine), increase the diversity and functionality of GDY. GDY demonstrates structural variety across dimensions (0D to 3D) and morphologies, including films, nanosheets, nanospheres, nanotubes, nanowalls, porous structures, and nanowires, hence enhancing its performance for many applications. This work also emphasizes important parameters for enhancing the performance of GDY. GDY exhibits considerable multifunctionality and transformative potential in energy and materials science, with applications in photo/electrocatalytic CO_2 reduction, hydrogen evolution reaction (HER), oxygen evolution reaction (OER), overall water splitting (OWS), supercapacitors, solar cells, batteries and electronic devices. The research continues with an assessment of existing outcomes and prospective trends in the synthesis, functionalization, and application of GDY-based nanostructures (Scheme 1).

1.1. Nomenclature

The nomenclature of GDY indicates its distinctive structural and chemical characteristics [38]. The word “graphdiyne” derives from its basis in graphitic carbon and the inclusion of diacetylene (−C ≡ C−C ≡ C−) links in its structure [39]. The diacetylene units, consisting of sp-HCAs, differentiate GDY from other carbon allotropes, including graphene, graphite, and graphyne [40]. The term “diyne” denotes the existence of two adjacent triple bonds essential to its acetylenic structure [41]. This specific name not only reflects the molecular structure but also denotes its extensive π-conjugation and hybridization complexities, which are essential to its exceptional electrical, structural, and chemical characteristics [42,43]. Consequently, the name encompasses its structural distinctiveness and its importance in the development of CMs research. In addition, graphynes may be named using either nomenclature or customized nomenclature [44]. The concentration of CAs inside their ring structure determines the nomenclature of graphynes. This system allows graphynes to be designated with the following prefixes: a, b, and g-graphyne, where a and b are the numbers of carbon molecules in the thinnest ring of the graphynes. The a and b rings are interconnected via $C(sp^2)C(sp)C(sp^2)C(sp^2)$ (Fig. 2a). The coefficient g represents the total carbon molecules in the third ring of graphynes, which is linked to the b ring by $C(sp^2)C(sp)C(sp)C(sp)C(sp^2)$. This nomenclature refers to the graphyne as 12,12,12-graphyne (Fig. 2b). Additionally, the graphyne shown in Fig. 2c might be designated as 6,6, 12-graphyne. For simplicity, certain graphynes are identified using Greek letters, which is called standard nomenclature. By employing such standard nomenclature, we may designate 12,12,12-graphyne as b-graphyne. Several graphynes are shown in Fig. 2b–e and are designated in accordance with standard nomenclatures: graphyne (Fig. 2b), α-graphyne (Fig. 2c), β-graphyne (Figs. 2d), 6 and 6,12-graphyne lattices (Fig. 2e) [45]. Most graphynes can be identified as utilizing both nomenclatures, but their naming methods are limited and require improvement. For instance, systemic nomenclature is complex and challenging, but standard nomenclature is restricted and incapable of representing all types of graphynes. In addition, the position and structure of graphyne Dirac cones using 2D contour charts of the VB and CB energies in reciprocal regions (Fig. 2f and g). For example, Serafini et al. [46] performed an extensive analysis of GDY fragments to examine the impact of topology on their electrical and vibrational characteristics. Their work specifically investigates the relationship between the highest occupied molecular orbital (HOMO) and the lowest unoccupied molecular orbital (LUMO) gap and the extent of conjugation, which is influenced by the interaction of sp-domains to aromatic six-member rings. The linkages are classified as para, ortho, or meta, based on the kind and length of the diacetylenic units involved. The nomenclature utilized during the research denotes the structural attributes of the GDY fragments. "T1” signifies the basic triangular unit, whereas “TXC” or “TX (PY)Z″ indicates the quantity of triangular units (X), their condensation (C, denoting shared diacetylenic linkages), the length of para-conjugated pathways (Y, derived from diacetylenic units), and the multiplicity of these pathways (Z) (Fig. 2h and i). Similarly, Fig. 2j illustrates the HOMO-LUMO gap as a function of fragment length for all structure. The gap values for 2D fragments composed of “triangular” units (constituted by three sp-chains and aromatic rings) are shown for comparison, extending to the infinite limit associated with the smallest GDY nanoribbon. The objective is to highlight the impact of the 2D extension of the pieces in contrast to the simplistic 1D conjugation shown by other models. Their work presents a comprehensive structure for characterizing the structural fluctuations of GDY and clarifies the correlation between these fluctuations and their electrical

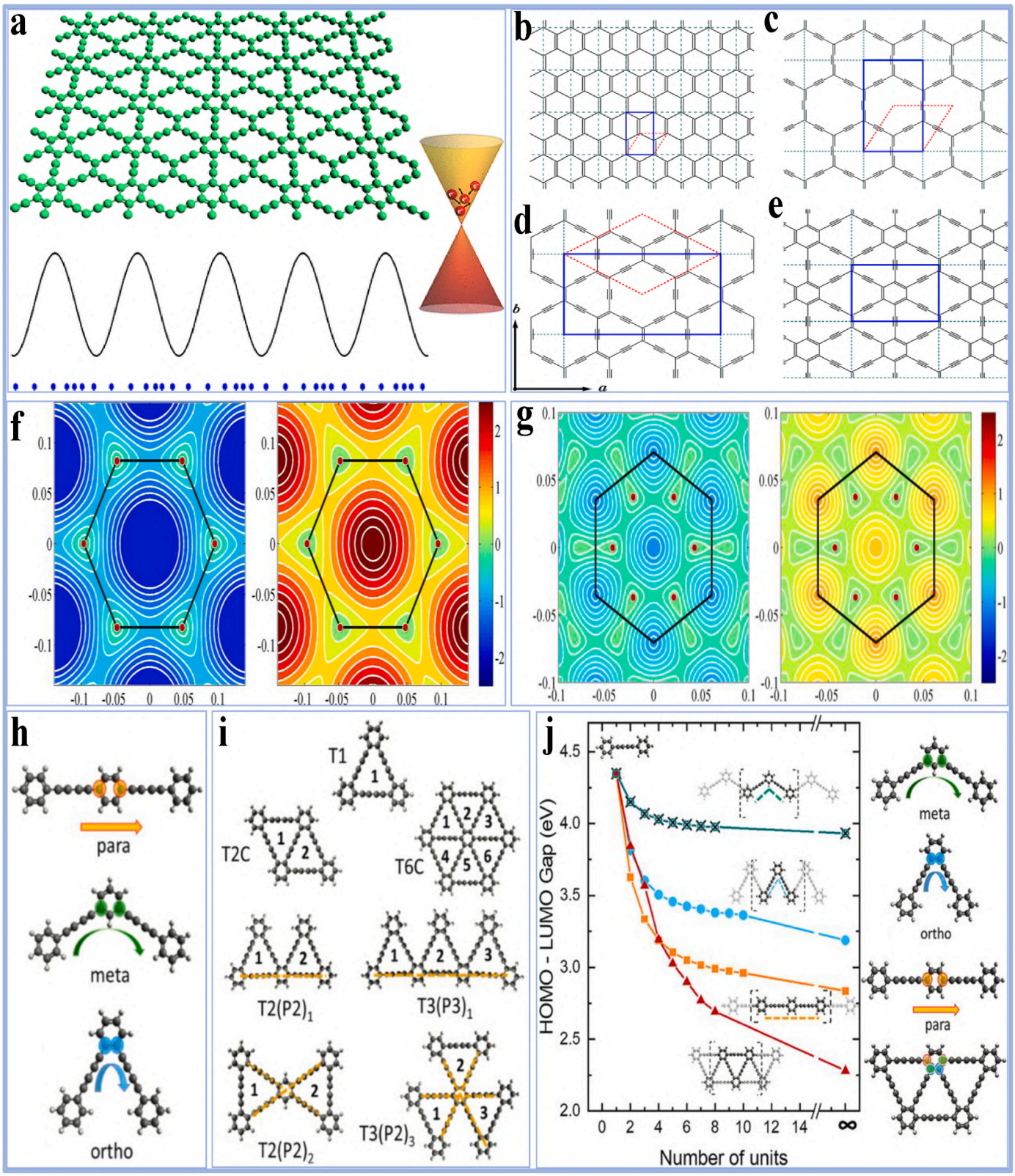

Fig. 2. (a) Schematic illustration of carrier mobility in graphyne; Graphical illustration of (b); graphyne; (c) α-graphyne; (d) β-graphyne; (e) 6,6,12-graphyne lattices. Contour plots of VB and CB energies of the (f) α-graphyne; (g) β-graphyne [45] Copyright © 2013, American Chemical Society. (h) Graphical illustrations of para, meta, and ortho conjugation pathways; (i) Graphical illustrations of various 2D-GDY segments examined and their corresponding nomenclature; (j) HOMO-LUMO gap as a function of the fragment length [46] Copyright © 2021, Elsevier..

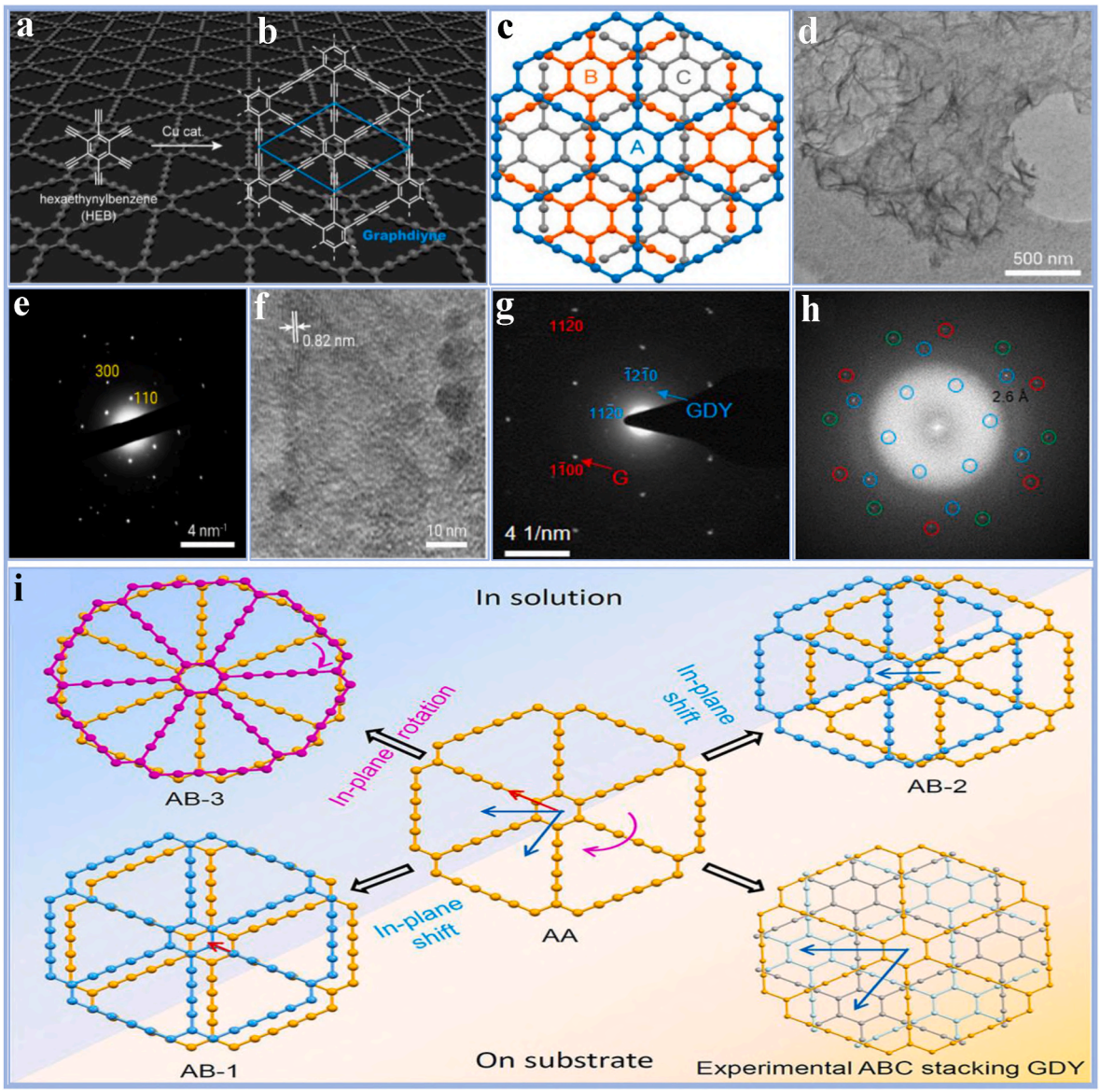

Fig. 3. (a–c) Stacking structures; Simulation patterns from the top view of (d) TEM; (e) SAED; (f) HRTEM [54] Copyright © 2017, American Chemical Society. (g) Electron diffraction pattern of as-prepared GDY; (h) FFT pattern of HRTEM image [55] Copyright © 2018, Science Advances. (i) Potential configurations of layer GDY from the superior perspective. The red, blue, and purple arrows denote the in-plane displacement or spins of the two layers, leading to unique packing configurations [56] Copyright © 2024, American Chemical Society. (For interpretation of the references to color in this figure legend, the reader is referred to the Web version of this article.)

characteristics, therefore providing insights for the production of GDY-based materials with tailored functions.

1.2. Basic structure and material properties

The subsequent research on 2D materials was promoted with the discovery of graphene and the prediction of graphyne. A GDY variation has two acetylenic bonds per unit cell, in contrast to graphyne which has a single acetylenic bond [47]. The length of the carbon bonds that connect the hexagonal bands is doubled by the additional acetylenic bonds in GDY. As a result, the mechanical durability of graphyne is not matched by GDY [48]. In terms of flexibility, GDY is comparable to graphene and graphyne, which have remarkable planar strengths of 120 N/m and Young's modulus of 375 GPa at a thickness of 0.320 nm [49]. The concept of GDY was initially introduced by Haley et al. [50] in 1997. The initial studies focused on the synthesis of materials from similar chemical compounds and employed theoretical computations of similar materials to estimate the features of GDY. Pei et al. [51] evaluated the Poisson's ratio (0.453) and predicted the planar strength of materials using the VASP technique. A bandgap of 0.47 eV and 1.12 eV was observed in the non-strain phase. The gradient estimation method, using the Perdew-Burke-Ernzerhof exchange-correlation function, resulted in an increased bandgap, providing insights into the electrical characteristics of materials. The Heyd-Scuseria-Ernzerhof exchange-correlation function exceeds the bandgap but, indicates that the bandgap could be adjusted with external strain, exhibiting values from 0.28 eV at $\varepsilon = -0.05$–0.71 eV at $\varepsilon = 0.06$, with a strain-free value of 0.47 eV. This strain-dependent fluctuation enables modification of the bandgap for certain applications. The Dirac conical shape further validates the almost passive electron behaviour, resulting in the production of a novel semiconductor material. Cui et al. [52] used the PAW method to examine the influence of biaxial strain on the bandgap, confirming previous findings. They noted that uniaxial strain reduces the bandgap by modifying electron density in di-acetylenic bonds, presenting a viable

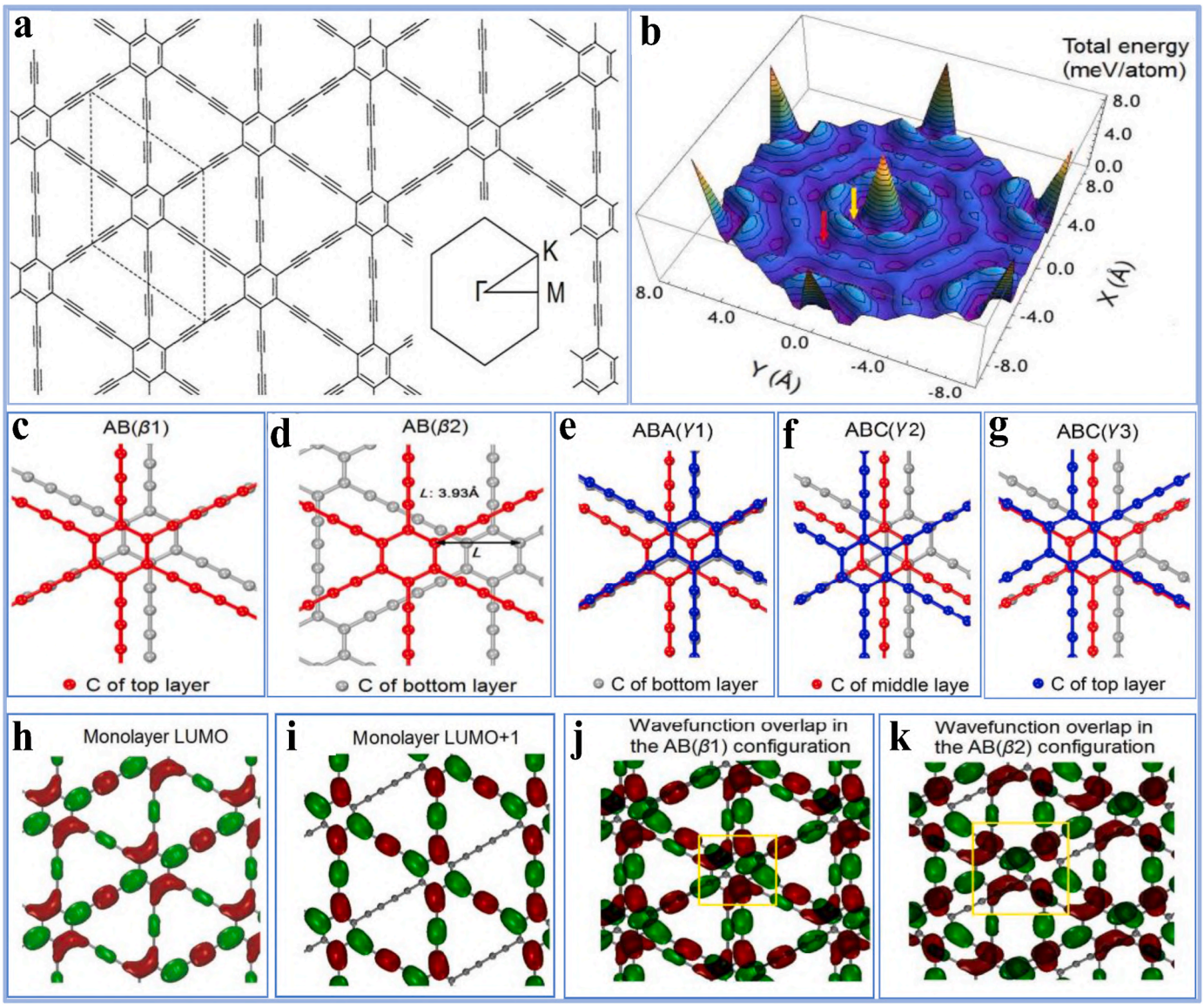

Fig. 4. (a) Geometric structure of single GDY; (b) The comparative in-plane alignment of the estimated energy surface was analyzed through rainbow-color contour mapping; (c, d) An overview of AB(β1) and AB(β2) from above; (e–g) Three alternative top-view structures for the trilayer GDY; (h–k) Wavefunctions of GDY [36] Copyright © 2012, Royal Society of Chemistry. (For interpretation of the references to color in this figure legend, the reader is referred to the Web version of this article.)

method to adjust electrical attributes via structural alterations. The stiffness of GDY is about 30 % more than that of graphyne, attributable to the presence of acetylenic linkages that reduce atomic coordination and strength. Likewise, the GDY demonstrates isotropic mechanical properties, rendering it less appropriate for nanomaterials, notwithstanding its elevated electrical conductivity. Shuai et al. [53] investigated the GDY NSs structure with VASP calculations, determining an ideal lattice constant of 9.48. The GDY monolayer has a hexagonal configuration with a *P6/mmm* space group comparable to graphene. The determined d-spacing values for the (100) and (110) planes were 0.821 nm and 0.474 nm, respectively (Eq. (1)).

$$1/d^2 = 4/3[(h^2 + hk + k^2)/a^2] + l^2/c^2 \quad (1)$$

In addition, few-layer GDY exhibits three distinct stacking modes with significant asymmetry, namely AA-, AB-, and ABC-stacking types (Fig. 3a–c) [54]. The AA-, AB-, and ABC-stacked GDY structures are classified under the *P6/mmm*, $P6_3/mmc$, and R $\bar{3}$ m space groups, respectively. Matsuoka et al. [54] conducted a theoretical analysis of the stacking types of AA, AB, and ABC in the SAED pattern for the first time that the (100) reflections of ABC-stacked GDY were missing, indicating the systematic suppression of the rhombohedral (R) core (Fig. 3d–f)). Gao et al. [55] investigated the SAED patterns and HR-TEM of six-layer GDY NSs (Fig. 3g and h). Hu et al. [56] demonstrated that the strongest bilayer and trilayer GDY both possess hexagonal carbon chains packed in the Bernal manner, having an in-plane shifting across the angle bisector of two neighboring diyne linkages (AB-2) or across one diyne linkage (AB-1) (Fig. 3i). Zhang et al. [57] recently examined the SAED pattern and HRTEM analysis of a trilayer ABC-stacked GDY layer, providing strong evidence for including few-layer GDY NSs. Theoretical research is projected to offer more dependable insights into the properties of GDY despite its recent development. The main problem is the low effective electron density, which is caused by the bandgap Dirac cone. The results indicate that the bandgap increases as the ribbon size of GDY NRs decreases, as the actual electron mass of GDY with a semi-conducting bandgap is examined [58]. The drifting behaviour of GDY NRs was consistent in both diagonal and armchair orientations despite a minor data difference. As the ribbon width increased, two

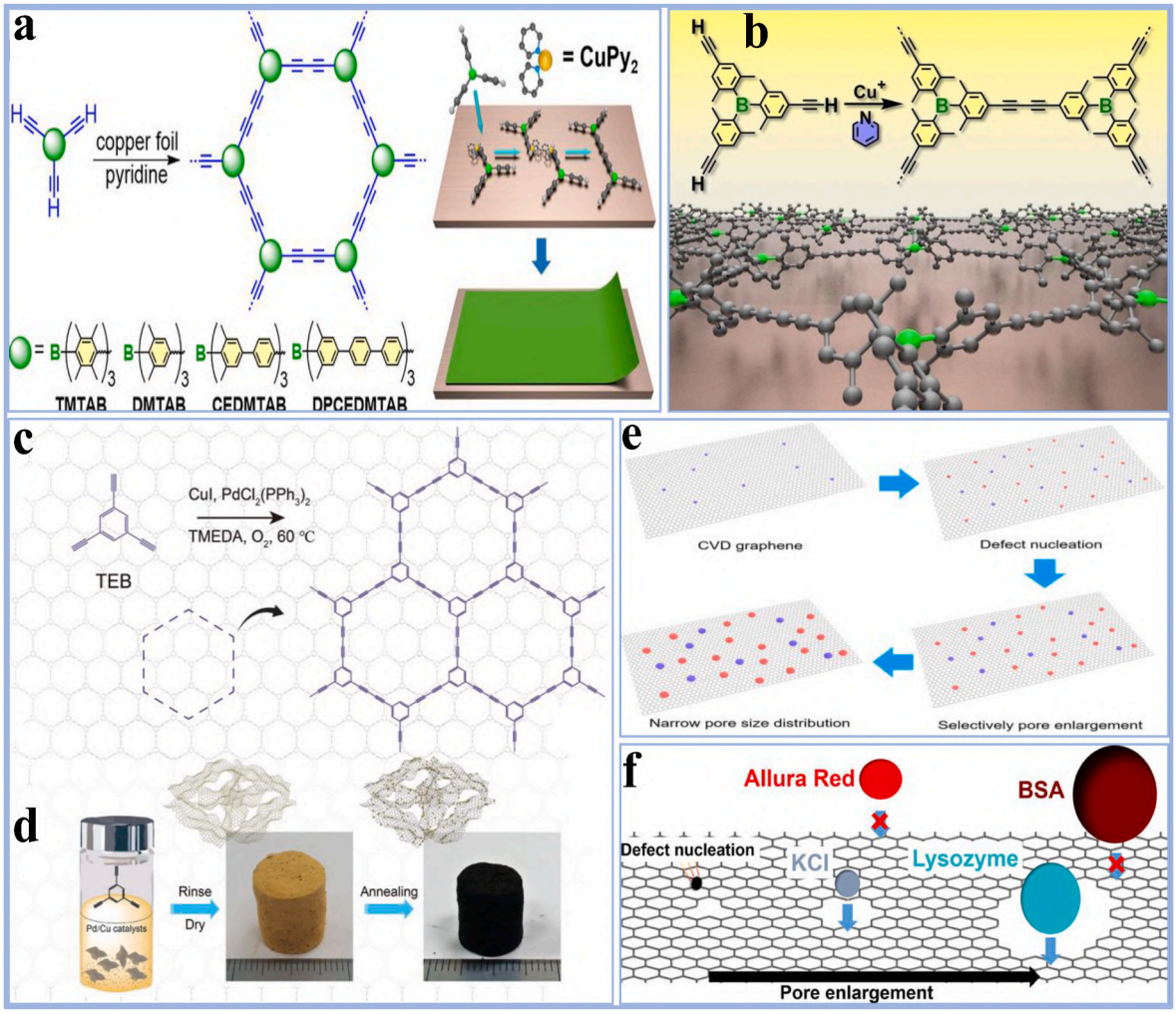

Fig. 5. (a) Synthetic process; (b) Tunable pore sizes route of TAB-GDY [76] Copyright © 2023, John Wiley and Sons. (c) Synthesis of Pd/HGDY; (d) Experimental procedure and images of 3D monolithic Pd/HGDY prior to and following annealing [77] Copyright © 2023, John Wiley and Sons. (e) Synthetic process; (f) Tunable pore sizes route of NATMs [78] Copyright © 2021, American Chemical Society.

assembly methods developed, indicating that infinite GDY NSs are not directionally dependent. The bandgap is reduced by perpendicular fields, resulting in a closure of 0.11 V/Å, as demonstrated by research on the bandgap under electric fields. Although GDY is mechanically weaker and less flexible than graphene and graphyne, it is appropriate for semiconductive applications due to its tunable bandgap. The electronic potential of GDY is improved by the application of strain; but additional experimental proof is necessary to determine its material properties and layering modes.

Furthermore, the molecular structure of GDY comprises a 2D carbon structure that includes both sp- and sp^2-HCAs. The unique structure has linear acetylenic (C ≡ C) bonds linking benzene-like rings, so yielding a highly conjugated system [59]. The structure of GDY is defined by alternating sp- and sp^2-HCAs, which enhance its electrical characteristics. Additionally, the graphynes are composed of benzene rings that are connected by acetylenic bonds (-C ≡ C-). The structural and electronic attributes of materials are influenced by the primary connections between the benzene rings, which are these acetylenic bonds (Fig. 4a–k) [36]. The development of monoatomic layered solid carbon structures with sp- and sp^2-hybridization can result in the formation of a variety of graphynes (GYs), such as graphdiyne (GDY), graphyne (GY), and graphtriyne (GTY). Planar carbon atom layers with varying acetylene bond arrangements, including 6,6,12-and -GY, are present in these materials [60,61]. GYs are distinguished from other carbon materials by the presence of four distinct forms of C-C bonds.

1. Csp^2–Csp^2 bonding in the benzene rings.
2. Csp^2–Csp bonding exists between C–double and C–triplet bonds.
3. Tri–carbon bonded carbon atoms C_{sp}–C_{sp}.
4. Csp–Csp singular carbon atoms connect adjacent carbon triplet atoms. The standard values for bonding sizes in benzene rings -C ≡ C and C-C are 1.48–1.50 Å, 1.18–1.19 Å, and 1.46–1.48 Å [62].

The combined effects of sp^2 and sp-hybridization in carbon allotropes result in the shortening of C–C single bonds and an extension of corresponding aromatic bonds, attributed to the weak interactions between alkynyl atoms and aromatic ring systems. The theoretical investigations indicate that the C–C single, aromatic, and triple bond lengths in graphyne are 1.407 Å, 1.426 Å, and 1.223 Å, respectively [63]. In comparison to benzene ring bonding and C ≡ C, the strength of a single bond is inferior and more readily broken. The bond lengths of Csp^2–Csp^2 atoms in benzene rings are 1.41 Å, 1.40 Å, 1.24 Å, and 1.33 Å [64]. GDY planes have the same hexagonal structure (p6m) as graphene planes. The structural crystallographic constants of GDY are a = 9.38 Å, b = 9.38 Å, c = 3.63 Å, and θ = 120° [65]. The GDY spacing between layers is 3.7 Å [66]. The lattice spacing was increased to 2.66 Å as a result of the addition of one ethyne atom through the use of broad atomic analysis [67]. At the quantum scale, ethyne bonds have the

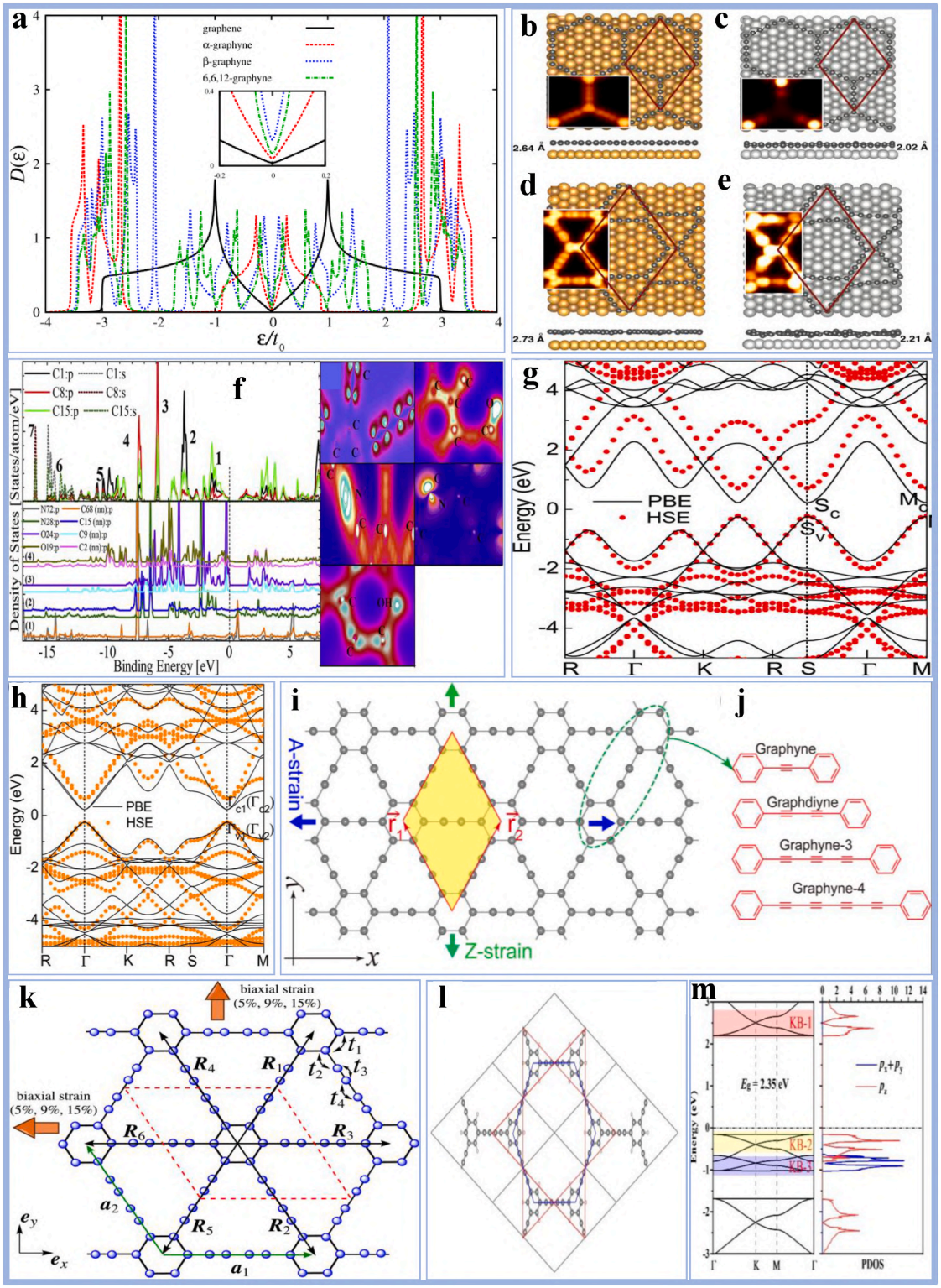

Fig. 6. (a) The corresponding DOS for semiconducting systems, including γ-graphyne and GDY [92] Copyright © 2020, IOP Publishing. Top and side views of GDY configurations on different substrates are presented in panels of (b) α-GDY on Au(111); (c) α-GDY on Pt(111); (d) β-GDY on Au(111); (e) β-GDY on Pt(111) [93] Copyright © 2021, IOP Publishing. (f) Estimated PDOS for non-equivalent C sites of oxygen and hydroxyl groups on GDY [94] Copyright © 2017, Elsevier. (g, h) The unstrained graphene band structure; (i) The geometry of a graphene sheet in which a yellow parallelogram represents the primitive cell. Green and blue arrows represent Z- and A-strain deformation orientations; (j) A schematic representation of the graphyne family units, which are formed through acetylene linkages connecting hexagonal units [95] Copyright © 2013, American Chemical Society. (k) Effect of biaxial strain on the electronic properties of GDY [96] Copyright © 2022, Elsevier. (l) A geometric structure of m-HsGDY with a 2 × 2 supercell; (m) Band structure (left) and partial density of states (PDOS) (right) of m-HsGDY calculated inside the PBE functional [97] Copyright © 2020, Elsevier. (For interpretation of the references to color in this figure legend, the reader is referred to the Web version of this article.)

potential to increase lattice spacing by approximately 2.58 Å [68]. GYs have more structural flexibility than GR because of their coupled carbon atoms. The structural flexibility of GYs enabled the formation of curved structures; but, the structural rigidity was low. Graphyne are thought to have a lower formation efficiency than graphite, but they exhibit exceptional thermal stability. Baughman et al. [69] demonstrated that graphyne maintain a high level of thermal stability; but, their strength is reduced in comparison to graphene as a result of the presence of -C ≡ C- bonding. The strength of graphyne decreases as the quantity of -C ≡ C- bonding increases. The Gibbs free energy (G) is an important factor for stability, with lower values suggesting more stable structures. In comparison, the G values of a variety of carbon materials (carbide, diamond, fullerene, graphite, carbon nanotubes, and graphene) range from 0 to 1.037 eV per atom. But, the GDY has a G value of 0.803 eV, and GDY NRs have even lower G values, ranging from 0.520 to 0.775 eV. Sheka et al. [70] revealed that the molecular radical potential is typically treated as a single electron. The interaction of triplet carbon atoms and the GDY structure indicates that GDY could demonstrate high polarization, with radicals primarily occurring in the center, thereby enhancing its reaction. The structural flexibility of graphyne is greater than that of graphene, despite the fact that their mechanical strength is reduced due to the bonding structure of the benzene rings, which is connected by acetylenic bonds (-C ≡ C-) and Csp^2–Csp^2 and Csp–Csp bonds. In comparison with graphene, GDY exhibits superior thermal durability, but its stability is diminished by the inclusion of -C ≡ C- bonds. This potential for enhanced electronic attributes is demonstrated by the Gibbs free energy analysis of GDY and its nanoribbons, which indicates that they are more dynamic.

1.2.1. Tunable pore size and surface area

The tunable pore size and surface area of GDY are essential for improving its performance in diverse applications [71]. By modifying the pore size, GDY can proficiently regulate the dimensions and diffusion of molecules, hence enhancing its selectivity in applications such as gas separation and catalysis [72]. An increased SSA offers more active sites, enhancing adsorption and interaction with reactants or target molecules [73,74]. GDY's adjustable features make it a flexible material for applications requiring high performance and selectivity, such as energy storage, gas sensing, catalysis, and environmental remediation [75]. For example, Zhao et al. [76] synthesized a series of triaryl boron-derived GDY analogs (TAB-GDYs) with tunable pore sizes using a bottom-up methodology including a coupling process on copper foil in a mixture of pyridine. They utilized m-xylene as the protective aryl group for the boron atom to improve chemical stability and employed the Suzuki reaction to elongate the phenylene bridge to adjust the dimensions of the TAB building unit. Four distinct TAB-GDYs (TMTAB-GDY, DMTAB-GDY, CEDMTAB-GDY, and DPCEDMTAB-GDY) were synthesized by coupling the respective monomers on copper foil in the presence of pyridine. The exfoliated TAB-GDY films exhibit uniformity and continuity. The refined single-layer frameworks belong to the two-dimensional hexagonal crystalline group. TMTAB-GDY and DMTAB-GDY exhibit pore sizes of 2.3 nm and 2.5 nm, respectively, but CEDMTAB-GDY and DPCEDMTAB-GDY, with extended phenylene bridges, possess much higher pore diameters of about 3.8 nm and 5.4 nm, respectively (Fig. 5a and b). Similarly, Hao et al. [77] propose a scalable method for the synthesis of ultrathin holey GDY (HGDY) nanosheets through a palladium/copper co-catalyzed homocoupling reaction involving 1,3,5-triethynylbenzene. This approach yields large-area, ultrathin HGDY that self-assembles into a 3D foam-shaped framework, efficiently anchoring palladium atom clusters on its surface. The tunable pore sizes and substantial SSA of these nanosheets greatly improve the material's catalytic characteristics by enhancing charge transference, increasing the number of active sites, and facilitating effective energy and electron flow in electrocatalytic reactions. Pd/HGDY hybrids demonstrate enhanced electrocatalytic efficiency and durability for ORR, exceeding the effectiveness of conventional Pt/C catalysts. The tunable pore size and large SSA of GDY significantly enhance the material's electrocatalytic productivity, positioning it as an attractive option for electrochemical catalysis and energy applications (Fig. 5c and d). Furthermore, Chen et al. [78] examine the interaction between permeation and selectivity in conventional polymeric membranes by investigating nanoporous atomically thin membranes (NATMs), including GDY, which present the potential for enhanced selectivity and permeance. Their research presents a method to enhance separation efficiency by adjusting pore density and size via two sequential plasma procedures: lower-energy argon plasma for the introduction of higher-density imperfections, succeeded by controlled oxygen plasma to expand these imperfections into nanopores of specified dimensions. This scalable method produces graphene membranes featuring sub-nanometer pores that efficiently separate substances such as KCl and Allura Red, demonstrating excellent selectivity and permeance. The pore size can be modified for specific applications, including gas separation and dialysis, resulting in high selectivity and permeance, which provides a versatile solution for various separation procedures (Fig. 5e and f).

1.2.2. Electronic properties

The intrinsic electronic characteristics of materials are essential for comprehending their numerous applications. In this context, GDY demonstrates distinct electronic properties that distinguish it from other carbon allotropes, including graphene [79,80]. GDY possesses a natural bandgap, while graphene has a zero bandgap. The bandgap of GDY varies from 0.46 to 1.22 eV [74,81], demonstrating excellent tunability influenced by structural and environmental influences, thereby making it a very flexible material for electrical and optoelectronic uses [82,83]. Simulations indicate that GDY displays Dirac cone behavior attributed to its unique C ≡ C triplet bonding, which enhances its distinctive electrical mobility characteristics [84]. The lattice configuration of GDY promotes flexible modulation of the Dirac cone, allowing for exact control over its bandgap [85]. The tunability of the bandgap is a significant characteristic that distinguishes GDY from all other 2D materials, including graphene. Gorling et al. [60] revealed that graphyne display Dirac cones via first-principles investigations. In α-graphyne, the CB and VB correspond with the Dirac points of graphene [25], and the density of states (DOS) at the Fermi level is zero, hence reinforcing its semiconducting characteristics [86]. Furthermore, the 6,6,12-graphyne framework has rectangular symmetry in contrast to the hexagonal framework of graphene. It exhibits two bands of indistinct Dirac peaks at locations I and II, along with four Dirac points [87]. Multiple research groups have calculated the bandgap of graphyne to range from 0.79 to 1.22 eV utilizing various theoretical approaches [88]. The bandgap of GDY is affected by many parameters, including strain, nanoribbon size, nanotube diameter, stacking configuration, and induced electric fields. In contrast to graphene nanoribbons, graphyne nanoribbons have a unique bandgap that diminishes with increasing ribbon width [89]. Graphyne NTs structures exhibit markedly different electrical characteristics in comparison to single-walled carbon nanotubes (SWCNTs) [86]. Armchair GDY NTs have elevated bandgaps, while zigzag GDY NTs, characterized by bigger diameters, display reduced bandgaps that grow with the expansion of the NT size [90]. The bandgap of GDY was computed utilizing DFT, yielding values between 0.44 and 1.29 eV, which correlated well with the experimental findings [91]. Sani et al. [92] examined the electronic characteristics of graphyne-like compounds, such as α-, β-, γ-, 6, 6, 12-graphyne, and GDY, using a tight-binding approach. α-, β-, and 6, 6, 12-graphyne are identified as semi-metallic, exhibiting a zero-bandgap similar to single-layer graphene, but γ-graphene and GDY lack Fermi levels. Furthermore, intra-bandgap states may be present in the DOS of graphene structures, along with van Hove singularities in the DOS of all systems (Fig. 6a). Achilli et al. [93] examined the electronic and vibrational characteristics of α- and β-GDY on Au(111) and Pt(111) substrates. Their research demonstrated that gold and platinum substrates elicited distinct deformations in both α- and β-GDY. They

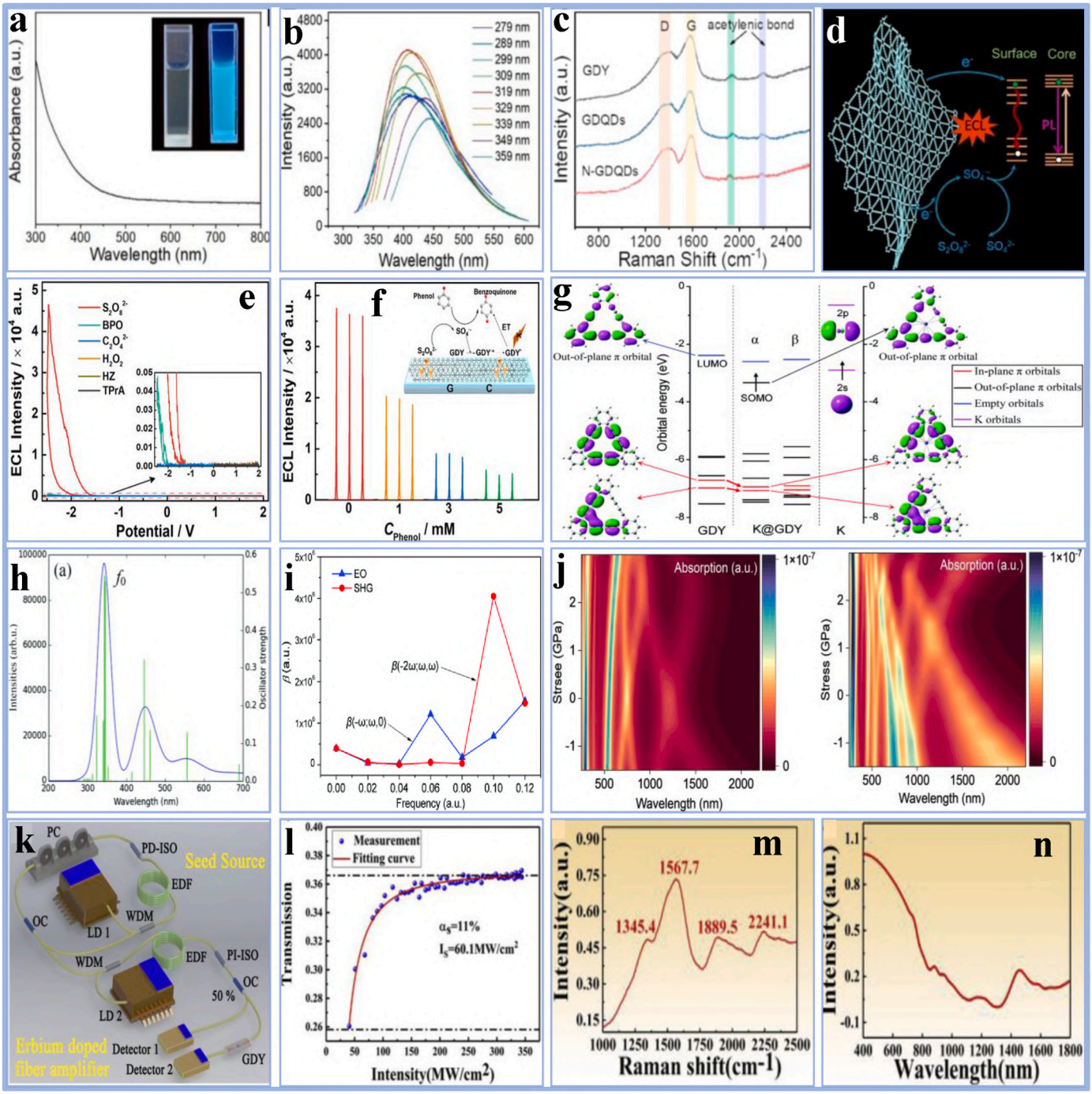

Fig. 7. Optical properties of GDY. (a) UV–vis absorption spectra (b) Fluorescence spectra; (c) Raman spectra of N-GDYQDs [100] Copyright © 2022, Elsevier. (d) Schematic depiction of the GDY ECL emission of GDY; (e) ECL-potential of GDY electrode; (f) ECL intensity of GDY [102] Copyright © 2022, John Wiley and Sons. (g) Orbital energy diagram; (h) Simulated optical absorption spectra; (i) Frequency dependency of the K@GDY [98] Copyright © 2019, Royal Society of Chemistry. (j) Absorption spectrum of the A(3)-GDYNR [103] Copyright © 2024, Nature. (k) Experimental setup; (l) Nonlinear optical spectra; (m) Raman spectra; (n) Optical absorption spectra of GDY [104] Copyright © 2019, Elsevier.

assessed the influence of surface contacts on the band arrangement and Raman spectra through comparisons of adsorbed and freestanding layouts. Significantly, charge transference interactions induced substantial alterations in the Dirac cone of semi-metallic α-GDY, while β-GDY experienced a transition from a semiconducting to a metallic state. The alterations in the Raman spectrum further corroborated these electronic transitions (Fig. 6b–e). Ketabi et al. [94] investigated the electronic characteristics of GDY employing X-ray absorption spectroscopy (XAS), X-ray emission spectroscopy (XES), and density functional theory (DFT) computations. Their research examined the impacts of oxidation, aging, and functionalization involving oxygen and hydroxyl groups. They discovered that these alterations substantially changed the electrical framework of GDY, with functionalization and variables such as dispersion, synthesis process, and film thickness affecting the material's bandgap (Fig. 6f). Furthermore, Yue et al. [95] examined the strain-induced changes in the mechanical and electronic properties of graphene and related materials using first-principles calculations and revealed that the in-planer stiffness reduces as the number of acetylenic

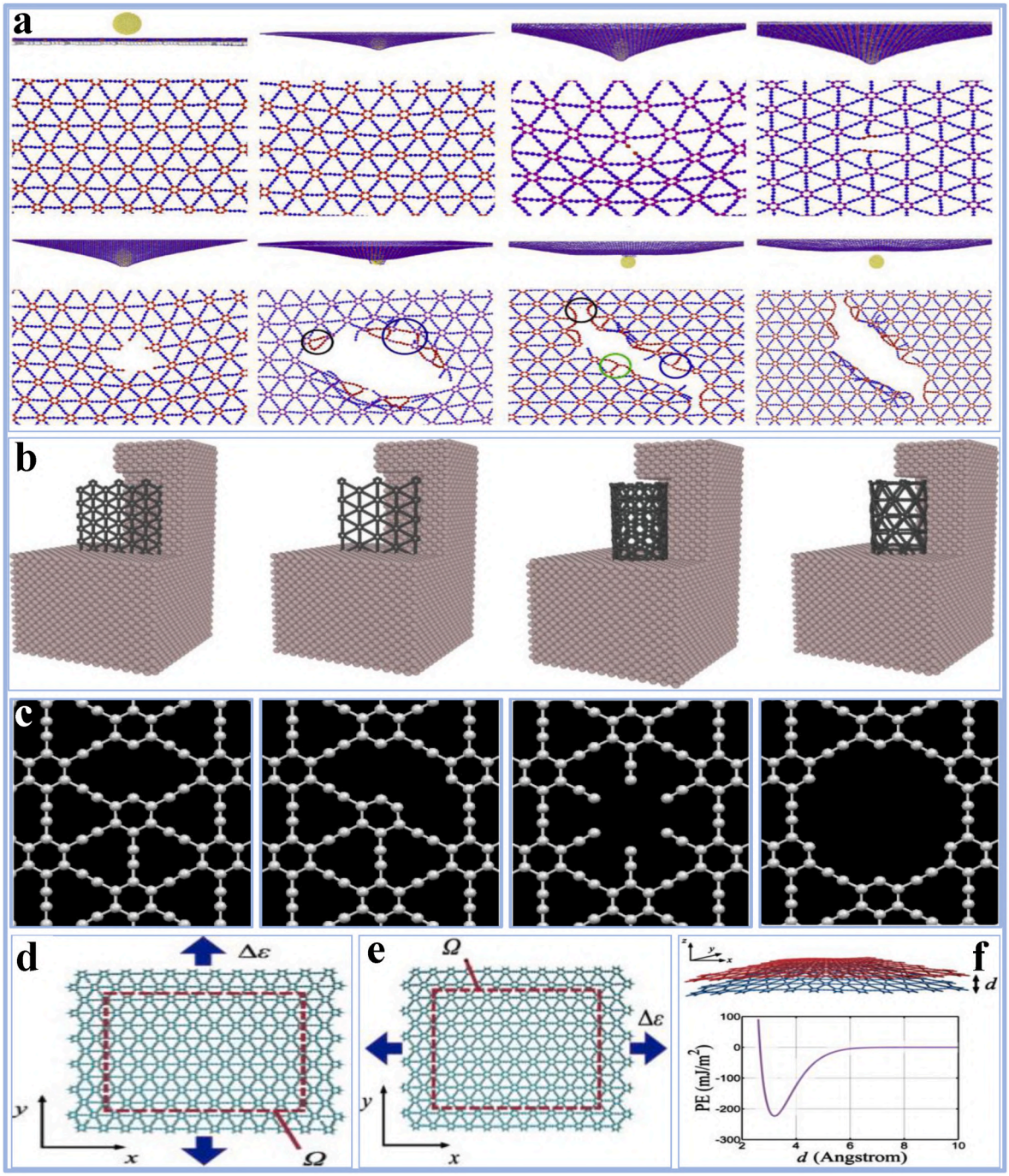

Fig. 8. (a) Lattice fracturing mechanism during GDY film growth, highlighting the sequence of bond breakage under nanoindentation [109] Copyright © 2019, Elsevier. (b) Schematic illustration of four GDY-Al nanocomposites [110] Copyright © 2020, Elsevier. (c) Trends in vacancy formation within GDY, showing the impact of different defects on its mechanical properties [111] Copyright © 2015, Elsevier. (d, e) Stress–strain diagrams and results of uniaxial tension experiments performed in the zigzag and reclined chair orientations, demonstrating the mechanical response of GDY in different structural configurations; (f) The analysis of interlayer adhesion in graphene [112] Copyright © 2011, Elsevier.

bonds increases. The bandgap of the graphene family is observed to undergo modification when strain is applied using various methodologies (Fig. 6g–j). Moreover, Mousavi et al. [96] investigated the electronic properties of GDY under biaxial strain using the tight-binding (TB) Hamiltonian modeling and Green function technique. The bandgap around the Fermi level of GDY grows gradually with strain owing to reduced orbital overlap among carbon atoms. The density of states (DOS) slopes of all processes exhibits intra-bandgaps and van Hove singularity (Fig. 6k). In another study, Pan et al. [97] investigated the electronic properties of bulk layered HsGDY (b-HsGDY) using first-principles calculations. The ABC-layered structure was determined to be the most advantageous structure. Under biaxial strain, b-HsGDY displays auxetic properties, with its bandgap growing under both tensile and compressive stresses throughout the strain range of −0.03 to 0.05 (Fig. 6l and m).

1.2.3. *Optical properties*

Optical properties represent a fundamental characteristic of nanomaterials, especially in optoelectronic composites, where their interaction with light significantly influences efficiency [98]. Comprehending

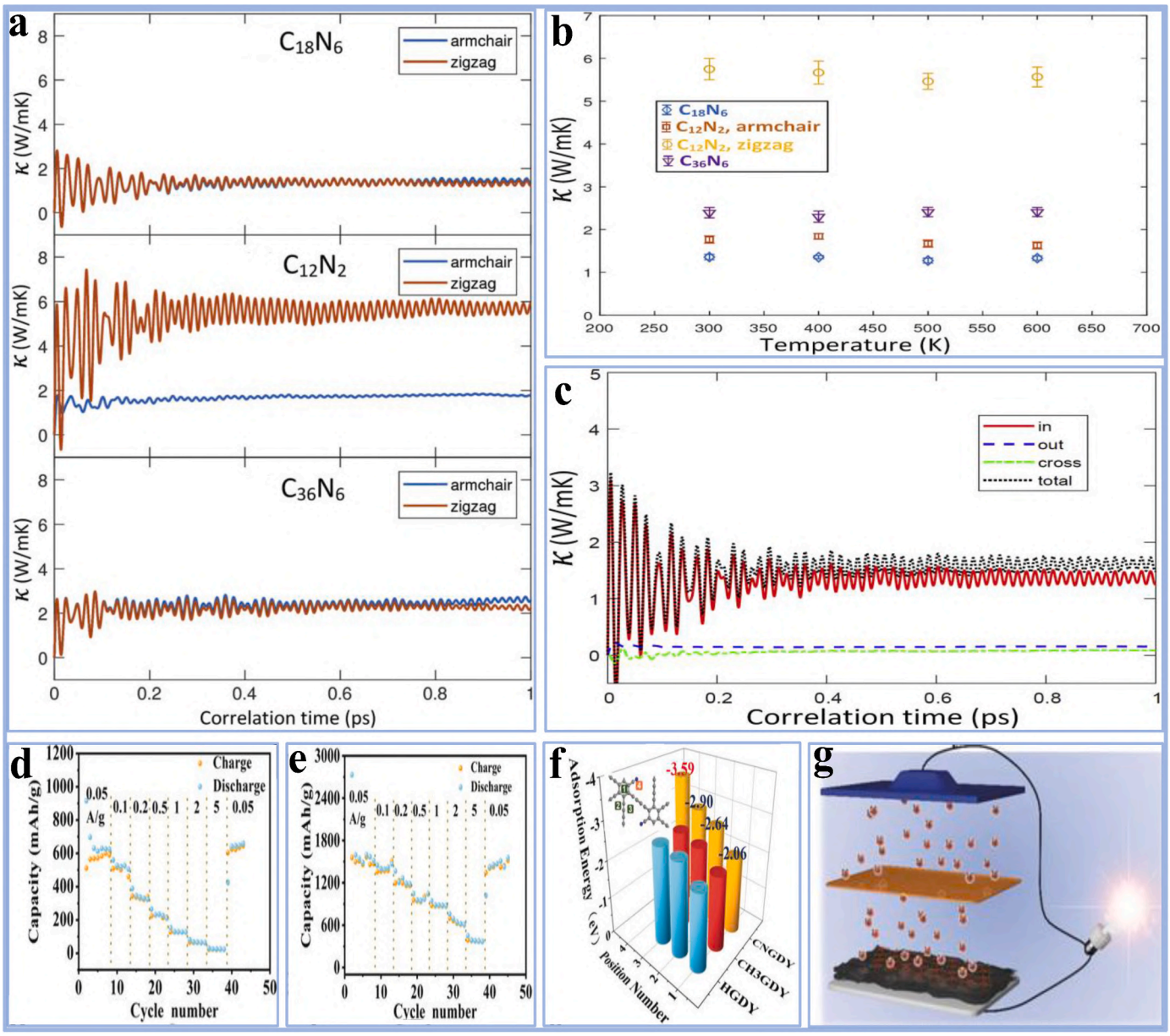

Fig. 9. (a) Calculated thermal conductivity; (b) EMD predictions of single-layer $C_{18}N_6$, $C_{12}N_2$ and $C_{36}N_6$ at room temperature; (c) EMD findings for single-layer $C_{18}N_6$ thermal conductivity elements at room temperature: out-of-plane (out), cross-plane (cross), and in-plane (in) [117] Copyright © 2018, Elsevier. (d, e) The rate performance of HGDY, MeGDY, and CNGDY; (f) The estimated adsorption energies of single lithium-occupied modes across various samples and their corresponding storage sites; (g) The various adsorption arrangements of a single lithium atom on CNGDY, along with the corresponding adsorption energy [118] Copyright © 2020, John Wiley and Sons.

these properties is important for estimating the interactions between light and matter, as well as for leveraging these interactions in diverse applications [99]. Bai et al. [100] examined the optical properties of nitrogen-doped GDY quantum dots (N-GDYQDs) through a facile, environmentally friendly one-step hydrothermal approach [101]. The N-GDYQDs exhibited optimal fluorescence at 410 nm when excited at 319 nm. Nitrogen doping enhanced surface imperfections, resulting in a significant increase in quantum yielding from 14.6 % to 48.6 %. The modification enhanced both electron mobility and conductivity. A highly effective photoelectrochemical nanosensor for dopamine (DA) detection has been invented utilizing N-GDYQDs. DA quenched the fluorescence of N-GDYQDs by developing a non-fluorescent complex, allowing for detection with a limit of 0.14 μM and a linear detection range from 0.32 to 500 μM (Fig. 7a–c) [100]. Gao et al. [102] found that GDY demonstrates notable electrochemical luminescence (ECL) emission in the presence of potassium persulfate ($K_2S_2O_8$) as a co-reactant. The ECL emission results from the movement of a weak-energy interface level, in contrast to a bandgap transition. The ECL emission exhibits a peak at approximately 705 nm in the near-infrared region, accompanied by a substantial ECL yield of 424 % (Fig. 7d–f). Li et al. [98] conducted DFT calculations to investigate the nonlinear optical characteristics of graphene, graphyne, and GDY with the adsorption of alkali metal atoms. Their results indicated that Li ions specifically adsorb onto the benzene rings of graphene, while alkali ions particularly bind to the triangular gaps in both graphene and GDY. Alkali metal (AM) deposition on GDY (AM@GDY) demonstrated significantly higher binding energies compared to graphene (AM@GE), attributed to enhanced interactions and van der Waals durability (Fig. 7g–i). Liu et al. [103] examined the influence of strain on the optical characteristics of GDY nanoribbons (GDYNRs). Their findings

indicated that strain can deform the composite network, modify the band framework, and adjust the bandgap of GDYNRs, thereby affecting their optical characteristics (Fig. 7j). Zhao et al. [104] investigated the nonlinear optical characteristics of GDY through a saturable absorber, effectively attaining a mode-locked laser frequency at a wavelength of 1564.70 nm. This represents the initial application of GDY as a saturable absorber in the generation of femtosecond mode-locked fiber lasers, highlighting its possibilities for integration in fiber lasers and facilitating future advancements in fast photonics and electronic devices (Fig. 7k–n).

1.2.4. Mechanical properties

GDY has garnered significant scientific attention owing to its remarkable mechanical characteristics. The addition of acetylenic linkages in GDY reduces the bond density and lowers the planar density, hence increasing elasticity and fragility [27]. The versatility of GDY renders it especially appropriate for applications necessitating complicated components, such as membrane separation. GDY demonstrates elastic distortion, with strain energy increasing continuously under both tensile and compressive strain [105]. Significantly, its fracture strain exhibits directional dependence, being lower in the armchair direction than in the zigzag direction [106]. These characteristics provide GDY with a potential material for existing nanomechanical composites exhibiting anisotropic behavior, facilitating customized efficiency in particular applications [107,108]. For example, Xiao et al. [109] examined the fracture behavior of GDY films by molecular dynamics (MD) modeling during nanoindentation. It was observed that when the indentation depth is beyond a certain threshold, the GDY film experiences considerable stretching, resulting in the progressive rupture of bonds: acetylenic (-C ≡ C-), double (-C=C-), and single (-C-C-). The order of bond breaking is ascribed to the greater strength of σ bonds relative to π bonds. Certain cracked bonds reassemble, facilitating further deformation and resulting in the creation of asymmetrical lathy fractures, as opposed to the symmetrical fracturing seen in graphene sheets (Fig. 8a). Similarly, Faria et al. [110] investigated the mechanical characteristics of several Al-nanocomposites, namely graphyne -Al, GDY-Al, graphyne NT-Al, and GDYNT-Al, determining three principal factors that affect the mechanical behavior of these composites: the elasticity of the nanofiller, the growth rate within the lattice, and the interfacial bonding of the nanofillers to the Al lattice (Fig. 8b). Furthermore, Ahangari et al. [111] used MD simulations to investigate the temperature-dependent mechanical characteristics of both pure and defective GDY (Fig. 8c). Buehler et al. [112] investigated the mechanical characteristics of extended GDY in various orientations (zigzag and reclined-chair) and found that the ultimate strain did not signify complete fracture of the graphyne sheet, but instead indicated a localized rupture coupled with a reduction in load size (Fig. 8d–f).

1.2.5. Thermal and conductive properties

The thermal and conductive properties of GDY significantly enhance its efficiency in diverse applications, especially in electronics and energy storage [49]. The unique framework of GDY facilitates superior charge transport capabilities, rendering it an effective electrical conductor [75]. The high conductivity of GDY enables efficient electron transference in applications such as electrocatalysts and electronic circuits [113]. Furthermore, GDY's thermal conductivity, while lower than that of certain materials such as graphene, remains adequate for effective heat dissipation [114], which is essential for ensuring durability and hindering overheating in operational devices. These characteristics position GDY as an exciting material for advanced applications in energy transformation, sensors, and flexible electronics [115,116]. For example, Mortazavi et al. [117] studied the thermal characteristics of GDY 2D nanomaterials, revealing that the thermal conductivities of single-layer $C_{18}N_6$, $C_{12}N_2$, and $C_{36}N_6$ are markedly lower nearly three orders of magnitude compared to pure graphene. Their research demonstrated that heat conduction is isotropic in $C_{18}N_6$ and $C_{36}N_6$, whereas it is anisotropic in $C_{12}N_2$ (Fig. 9a). At room temperature, $C_{18}N_6$ and $C_{36}N_6$ demonstrated thermal conductivities of 1.36 ± 0.06 W/mK and 2.39 ± 0.12 W/mK, respectively. $C_{12}N_2$ exhibited superior thermal conductivity in the zigzag direction (5.75 ± 0.25 W/mK) relative to the armchair direction (1.77 ± 0.08 W/mK). This difference is attributable to the longer carbon chains, which enhance phonon transfer in the zigzag direction. Fig. 9b demonstrates that the thermal conductivity of $C_{18}N_6$, $C_{12}N_2$, and $C_{36}N_6$ monolayers remains largely stable across varying temperatures. This behavior is in contrast to that observed in pure graphene, where thermal conductivity diminishes with rising temperature as a result of phonon-phonon scattering. The limited phonon-phonon dispersion in N-GDY monolayers leads to thermal conductivity that is independent of temperature. Furthermore, in pure graphene, out-of-plane phonons play a more significant role in thermal transport compared to in-plane phonons. In N-GDY monolayers, in-plane phonon dynamics are predominant, while out-of-plane contributions are minimal. This indicates that the in-plane thermal conductivity of N-GDY monolayers may extend to their multilayer configurations, positioning them as potential prospects for low-temperature thermoelectric applications owing to their low thermal conductivity and semiconducting characteristics (Fig. 9c). Similarly, Xie et al. [118] investigated the conductive properties of GDY derivatives, demonstrating that these characteristics can be modified through the incorporation of electron-withdrawing (cyano groups) and electron-donating (methyl groups) groups. The electron-donating and electron-withdrawing capabilities, coupled with the size variations of these groups, significantly influence the characteristics of GDY derivatives such as MeGDY, HGDY, and CNGDY. Cyano and methyl groups decrease the bandgap and improve the conductivity of the GDY network. Furthermore, these groups influence GDY aggregation, resulting in a greater quantity of micropores and an enhanced specific surface area. The lithium storage efficiency of three GDY derivatives (HGDY, MeGDY, and CNGDY) as anodes in lithium-ion batteries (LIBs) was investigated. Their findings indicate that HGDY and MeGDY demonstrate charging/discharging capacities of 510.7/915.5 mAh g^{-1} and 997.3/1785.1 mAh g^{-1}, respectively. In contrast, CNGDY exhibits notably higher capacities of 1612/2420 mAh g^{-1}, accompanied by a Coulombic efficiency of 66.6 %. The presence of the electron-withdrawing cyano group in CNGDY improves its lithium storage capacity and Coulombic efficiency. All three materials regain their reversible capacity upon reduction of the current density. CNGDY exhibits the highest specific capacity of 495 mAh g^{-1} and demonstrates stability at a high current density of 5 A g^{-1}. First-principles calculations validate the enhanced electrochemical features of CNGDY, assigned to its tailored physical and chemical characteristics, such as morphology, surface area, pore size, and interlayer spacing (Fig. 9d–g).

1.2.6. Catalytic properties

The theoretical analyses predicted the remarkable catalytic capabilities of GDY, attributed to its distinctive electrical configuration, elevated accessibility, and adjustable bandgap. DFT simulations indicate that its porous structure and sp-HCAs provide many active sites, whereas doping improves efficiency, establishing GDY as a viable material for energy transformation and catalysis [119,120]. The ORR is a fundamental process in energy systems and metal-air batteries, among other high-energy performance systems [121,122]. Various strategies were used to improve the performance of the ORR, given the limited sustainability of innovative metal catalysts in attaining cost-effective energy supplies. Moreover, these catalysts have insufficient long-term durability. Substantial advancements have been achieved in non-metal carbon catalysts for the ORR process [123]. The non-metal carbon catalysts have significant promise as potential alternatives for innovative metal catalysts owing to their inherent durability, economic efficiency, and eco-friendliness. [124]. Although several conventional sp^2-HCAs have been deployed to achieve substantial performance improvements over the past decade. Similarly, additional research is necessary to

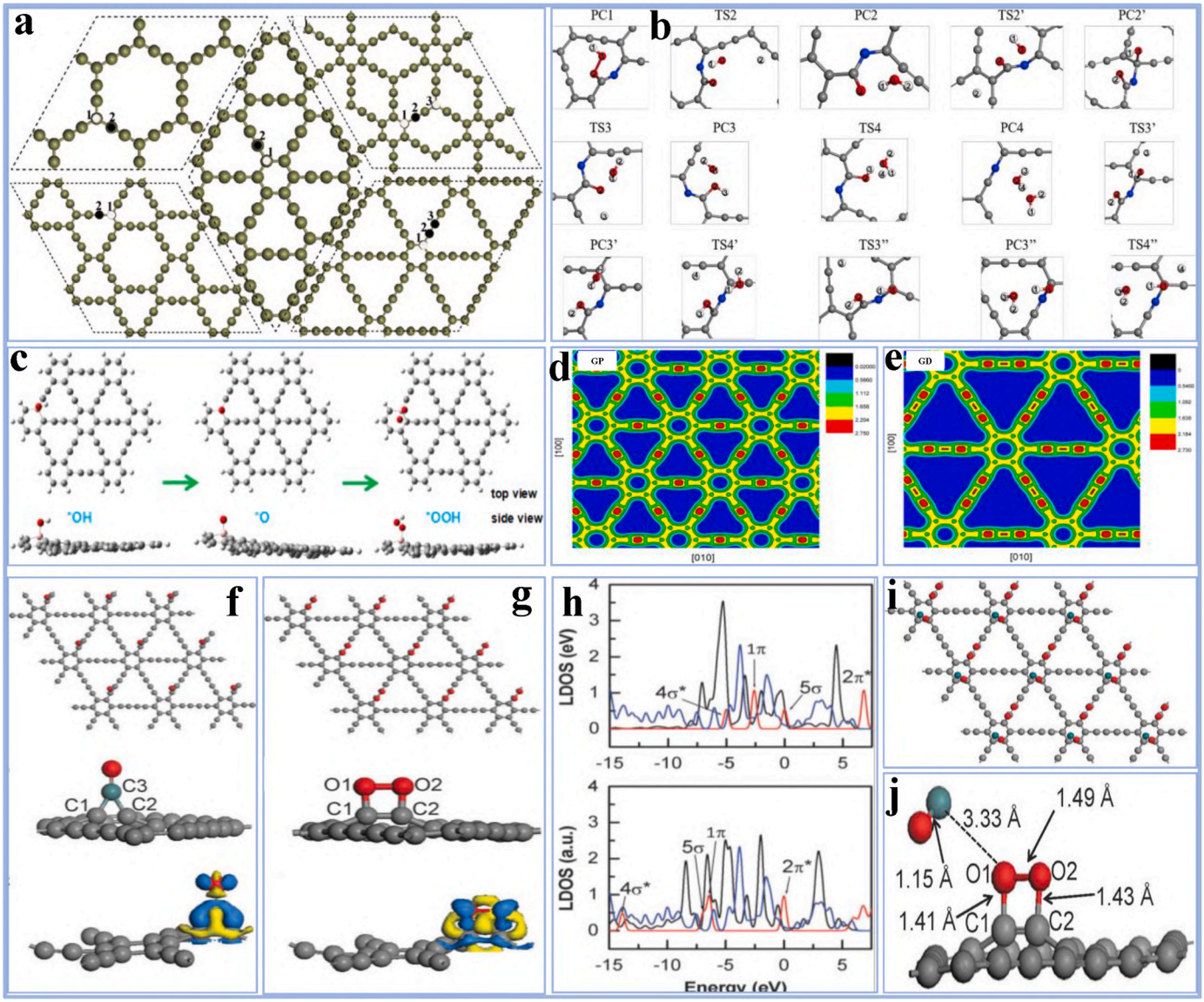

Fig. 10. (a) Potential N-doping sites in several kinds of carbon-enrich sp-hybrid composites [126] Copyright © 2016, Elsevier. (b) The proposed ORR mechanism of N1-βGy involves the substitution of one sp-HCA by N [127] Copyright © 2017, Elsevier. (c) The orderly processes that are involved in OER on B-graphyne [145] Copyright © 2017, Elsevier. The catalytic emission of hydrogen from metal-based composites is facilitated by graphyne and GDY: (d, e) Localized charge densities of graphene and GDY on the (001) plane [137] Copyright © 2013, American Chemical Society. GDY catalyzes oxidation of CO. (f, g) Different structures and positions of electron density for CO and O_2 deposited on the GDY layer, shown from above; (h) Representations of LDOS on C-O (top) and O-O (down) on GDY; Top (i) and side (j) The optimum compositions of O_2 and CO from the perspective of GDY sheet-co-adsorbed [138] Copyright © 2014, Royal Society of Chemistry.

develop innovative materials that outperform or match the efficiency of other materials [125]. In particular, GDY offers multiple possibilities for the development of highly effective catalysts for the ORR. Numerous theoretical hypotheses have been proposed regarding the characteristics of heteroatom-coupled GDY. The two most common forms of heteroatoms in the GDY structure are sp- and sp^2-HCAs [75]. Chattopadhyay and Kang et al. [126,127] investigated the effect of heteroatoms on ORR efficiency using systematic computations of graphyne and GDY composites (Fig. 10a). The sp-HCAs in GDY serve as optimal locations for nitrogen doping, and the resultant nitrogen-doped defects demonstrate a significant tendency for storing O_2 molecules, hence increasing catalytic activity (Fig. 10b) [127]. It was anticipated that a thermal four-electron reaction would catalyze ORRs in nitrogen-doped graphyne and GDY. Studies have demonstrated that the fourth O_2 variation process is required for the majority of N-doped graphyne and GDY composites, as it generates linearly scalable precursors that are similar to current catalysts. Furthermore, Chattopadhyay et al. [128] studied the feasible ORR efficiency of B-loaded GDY catalysts. The synthesis efficiencies of standard B-loaded locations on specific carbon structures were calculated. The Boron (B)-loaded materials exhibited enhanced stability owing to synthesis efficiency and preferential development at sp^2-HCA sites. In these complexes, boron atoms possess a positive charge, while neighboring carbon atoms have a negative charge, hence increasing the ionic nature of the covalent B-C bonds. The B atoms have a stronger attraction to sp^2-HCAs than to sp-HCAs, due to the substantial coupling between the B and C atoms via these complex affinities. The B doping facilitates oxygen adsorbent by anchoring the oxygen atoms. The oxygen molecules are substantially dissolved on B atoms that substitute sp-HCAs, but these oxygen species may initiate reactions that affect the ORR process. Liu et al. [129] anticipated the performance of B-loaded graphyne in stimulating the OER process. The specific electrical/chemical properties of graphene were determined to be influenced by B atoms. The presence of B atoms may enhance catalytic efficiency, particularly when B is doped at edge locations. Therefore,

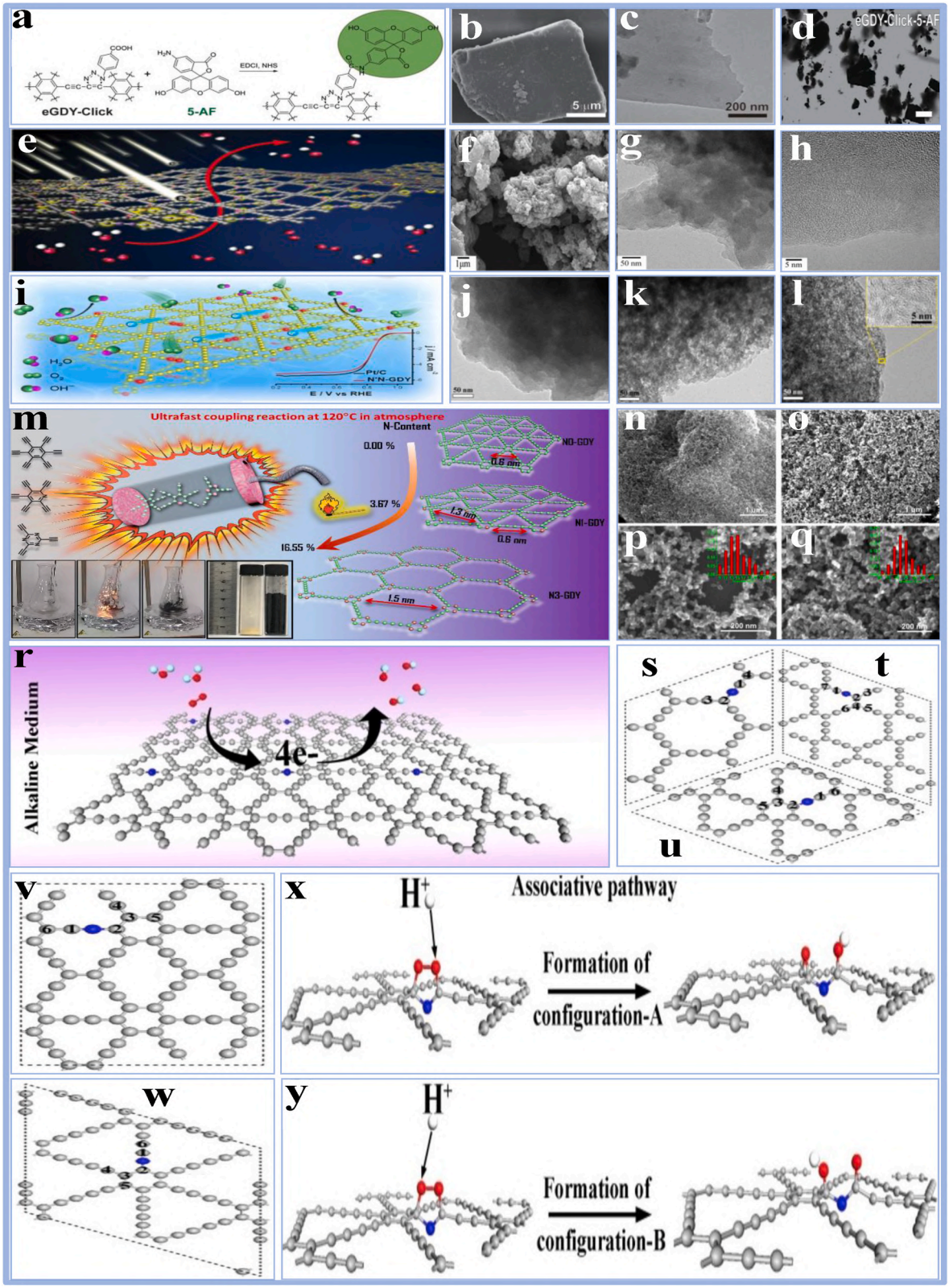

Fig. 11. (a) Synthetic process; (b) SEM; (c) TEM; (d) Confocal laser analysis of sp-N rich GDY [153] Copyright © 2022, John Wiley and Sons. (e) Schematic representation of metal-free N-rich GDY; (f) FESEM; (g) TEM; (h) HRTEM analysis of as-prepared samples [156] Copyright © 2014, Royal Society of Chemistry. (i) Schematic representation; (j) SEM; (k) TEM; (l) HRTEM analysis of metal-free (Py, N)-enriched GDY [157] Copyright © 2017, American Chemical Society. (m) The explosion method for preparation of N-doped GDY with a precise N-configuration; SEM analysis of (n, o) N0-GDY; (p, q) N1-GDY [160] Copyright © 2018, Elsevier. Optimized structures of N doped (r, s) αGy; (t) βGy; (u) γGy; (v) 6,6,12Gy; (w) GDY; Formation procedure of (x) configuration-A and (y) configuration-B during first hydrogenation via the associative route at the reaction coordinate [161] Copyright © 2022, John Wiley and Sons.

B-loaded GDY should be an effective electrocatalyst for water-splitting and metal–air devices (Fig. 10c). The potential applications of H_2 will be dependent upon the strategies used for its safe preservation [130]. In addition to their high H_2 content per mass, $NaAlH_4$, $LiBH_4$, and $LiAlH_4$ are good materials for efficiently storing H_2. [131]. However, controlling H_2 at low temperatures from these very stable molecules has been an ongoing challenge for decades [132]. The safe preservation and consumption of H_2 renewable energy sources will require the deployment of new destabilization techniques [133]. The nature of metal-atom components in these materials was examined, and it was determined that carbon nanoparticles with multiple curves could be beneficial as "real catalysts" for two reasons: (i) the patterns of these carbon structures are highly stable and resistant to repeated reactions, and (ii) the significant bonding between the carbon nanoparticles and light elements should reduce the energy required to remove H_2. In GDY composites, a novel method of binding a single metal material for a substantial catalytic reaction may be identified. These composites have a theoretically superior bonding between portable metal components and sp-HCAs than conventional sp^2-HCAs [134]. The use of these benefits may provide an innovative approach to maintaining individual metal materials, thereby improving catalytic performance [135,136]. Song et al. [137] used DFT, incorporating wide-ranging van der Waals dispersing modification, to analyze the interrelationships between sp^2-HCAs and lightweight metal complexes (Fig. 10d and e). GDY and graphyne demonstrated a superior affinity for lightweight metal particles compared to fullerene because of their intrinsic abundance of in-plane trapezoidal holes with sp-HCAs. These significant couplings may significantly influence the rate of charge transfer from the alkaline metal materials to the integrated AlH_4 or BH_4, lowering the stability of the Al-H or B-H bindings. It is worth noting that in the first two phases, the inclusion of GDY or graphyne significantly reduced the H-elimination potential for $LiBH_x$ complexes ($x = 1–4$), but in the third phase, it raised for $LiBH_4$ on the fullerene. The result implies that the existence of sp-HCAs could enhance the performance of the dehydration reactions. Therefore, the use of GDYs is required to promote the utilization of this ongoing issue with the reversible and safe storage of H_2. It is essential to develop an effective approach for the decomposition of hazardous carbon monoxide (CO) to enhance the future reliability of catalysts in petroleum systems and reduce environmental issues associated with CO pollution. Noble metal nanocatalysts are currently in use, but they are expensive, non-renewable, and are susceptible to CO toxicity. Cai et al. [138] investigated CO the oxidation mechanism of CO on a non-metal GDY structure using DFT (Fig. 10f–j). GDY possesses a non-uniform dispersed charge intensity due to the π-coupled structure of sp- and sp^2-HCAs. The Mulliken charge density analysis revealed that the sp-HCAs in the diyne interactions are conducting, whereas the sp^2-HCAs in the benzene rings have negative charges. Their research highlights electron transitions between sp- and sp^2-HCAs in GDY, with sp-HCAs serving as efficient adsorption sites for CO and O_2 owing to their electron shortage. A comprehensive investigation verified that CO and O_2 may be absorbed or co-adsorbed only at sp-HCAs, resulting in chemically stable structures. The two sp-HCAs of GDY connect with CO to generate a triangular intermediate structure, unlike metal-loaded graphene, where adsorption requires carbon-metal bonding. This distinctive electrical design highlights the potential of GDY for extensive adsorption and catalytic processes [139,140]. The GDY permits considerable transmission of charge to adsorbed CO and O_2, modifying their bond lengths and durability. Significantly, O_2 has a greater adsorption potential (−3.27 eV) compared to CO (−1.43 eV), promoting its presence on the GDY surface and decreasing CO toxicity. These characteristics emphasize the performance of GDY in adsorption and catalytic reactions [141,142]. The absorbed O_2 exhibited an expansion of around 27.9 % in its O-O bonding, suggesting the formation of a substantially productive phase for CO oxidation. GDY may also oxidize CO by the Eley–Rideal method [143], in which CO immediately mix with an active O_2 cell on the GDY. Significantly, GDY C–C bonding retains enough strength throughout the reaction phases. The results suggest that GDY may function as an economical and eco-friendly catalyst for the decomposition of CO at low temperatures in fuel cell applications and other natural uses [144].

1.2.7. GDYs as metal-free catalysts

Metal-based materials are frequently employed in catalysis for fuel and environmental sustainability because of their efficiency. Still, their costs are considerable, influenced by elevated consumption rates and constrained resource accessibility [146]. Therefore, scientists are creating metal-free, carbon-based catalysts that can function on a scale with or better than metal-based substitutes [147]. Conventional carbon composites, including graphene and carbon nanotubes, often exhibit inadequate catalytic efficiency due to the uniform distribution of their electron cloud [148]. Their catalytic characteristics may be strengthened by the incorporation of heteroatoms, which alter the charge and spin ratios [149,150]. But, the chemical homogeneity of these traditional carbon composites makes it difficult to regulate the doping positions, as heteroatoms are typically added at the edges. This complicates the comprehensive understanding of how doping sites affect catalytic activity. GDY has a highly integrated structure, vertically distributed pores, and adjustable electrical characteristics, rendering it suitable for energy preservation and transmission applications [151]. For example, Zhao et al. [152] were the first to show that the site-specific insertion of a new nitrogen doping framework, sp-N, into GDY resulted in outstanding catalytic productivity equivalent to platinum-derived catalysts. Similarly, Liu et al. [153] developed metallic-free sp-N-doped GDY catalysts by a pericyclic method for oxygen reduction reaction (ORR). The sp-N-doped GDY exhibited markedly enhanced electroreduction performance for CO_2 to CH_4 conversion relative to GDY infused with other nitrogen configurations. This improvement is ascribed to the sp-N-doped electronic structure, which more effectively stabilizes chemical intermediates (Fig. 11a–d). Likewise, Wu et al. [154] synthesized two GDY-based materials, PTEPB and PTEB, using the polymerization of 1,3,5-tris(4-ethynylphenyl)benzene and 1,3,5-triethynylbenzene. These materials were assessed as non-metallic photocatalysts for water splitting caused by visible light. PTEPB and PTEB effectively dissociate neutral water, generating H_2 and O_2 in a stoichiometric ratio under UV illumination. PTEPB attained an optical quantum efficiency of 10.3 % under 420 nm light, while PTEB obtained 7.6 %. In contrast to C_3N_4-derived catalysts, GDY-derived materials improved the OER by a $4e^-$ mechanism, as shown by first-principles calculations. The sp-HCAs in GDY exhibited more reactivity than the sp^2-HCAs. Furthermore, Fan et al. [155] investigated the catalytic active sites for HER via DFT. The principal activation sites for the photochemical synthesis of H_2 in PTEB were the CAs located inside the benzene clusters. Sites 1 and 3 facilitated single-site H_2 fabrication, while sites 1 and 2 promoted dual-site H_2 formation. Moreover, Zhang et al. [156] revealed that N-doped GDY serves as an exceptional metallic-free electrocatalyst for the ORR. N-doped GDY demonstrated exceptional electrocatalytic efficiency relative to industrial Pt/C in alkaline energy devices, including improved stability and heightened sensitivity to transition-state impacts. Experimental findings demonstrated that nitrogen loading markedly enhanced the positive energy on CAs next to nitrogen atoms, increasing their capacity to attract electrons from the anode and improving the ORR (Fig. 11e–h). In another study, Lv et al. [157] improved the doping of non-metallic GDY by including nitrogen-based donors (pyridine, NH_3) by higher-temperature calcination. Pyrimidine-saturated GDY was first soaked in pyridine for three days, then dried, and annealed at 700, 800, 900, or 1000 °C for 1 h to integrate minimal amounts of nitrogen from the deposited pyridine, yielding N-GDY-700, 800, 900, and 1000 °C. The GDY-900 °C sample was further annealed at 800 °C in the presence of NH_3 to boost the nitrogen content, resulting in N'N-GDY. N'N-GDY, characterized by a high nitrogen doping concentration, demonstrated catalytic performance on par with a conventional Pt/C catalyst (20 %) and surpassed other

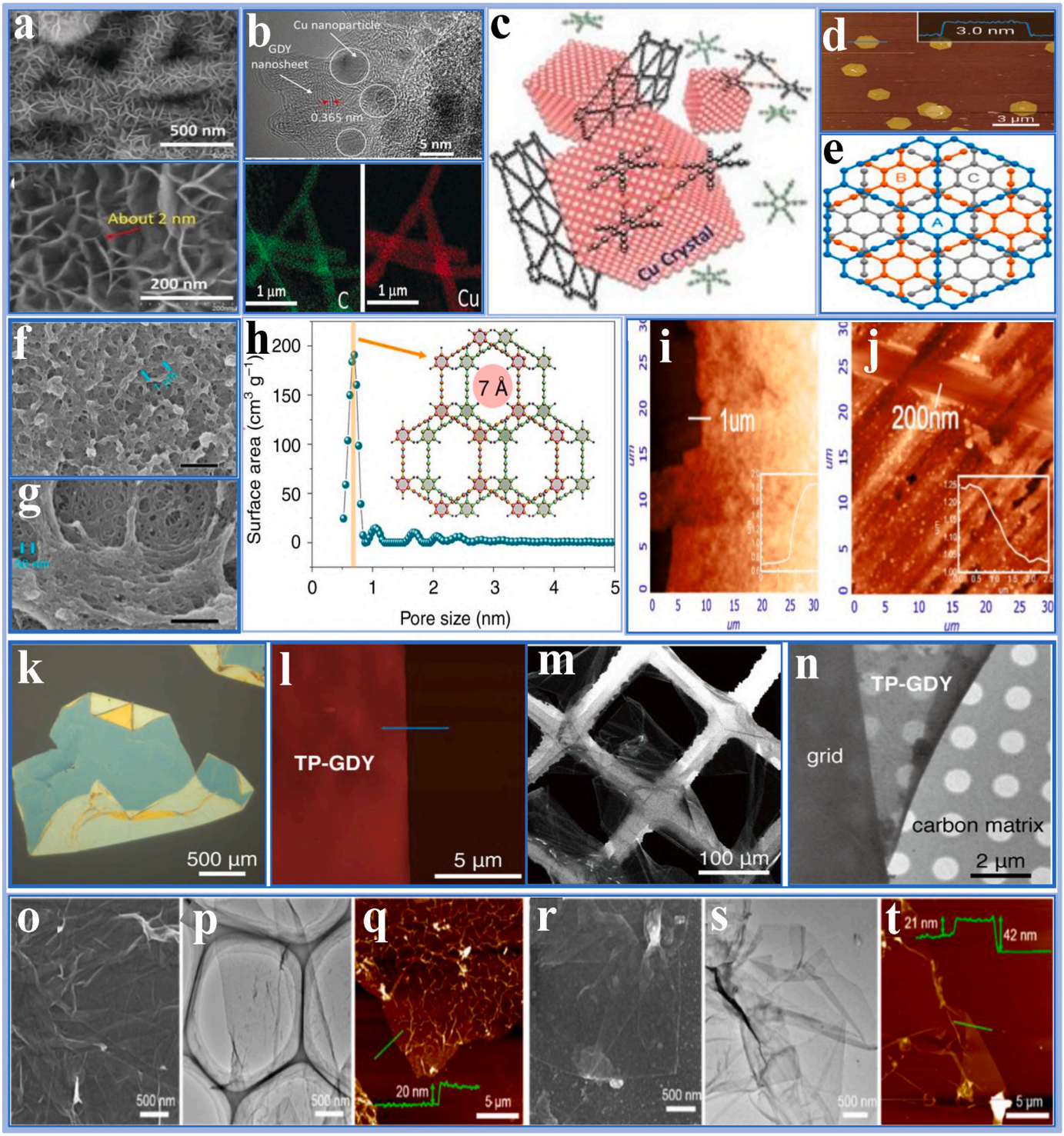

Fig. 12. (a) SEM; (b) TEM analysis of Cu@GDY; (c) GDY nanosheet growth at Cu nanoparticle crystalline interfaces [162] Copyright © 2017, John Wiley and Sons. (d, e) AFM topographic image of hexagonal GDY nanosheets prepared at a gas–liquid interface [54] Copyright © 2017, American Chemical Society. (f, g) SEM image of a hydrogen-substituted GDY; (h) The corresponding DFT incremental pore size distribution curve for GDY [165] Copyright © 2017, Nature. (i, j) AFM image of carbon ene–yne on a Cu foil [166] Copyright © 2017, Elsevier. (k–n) A fused-ring substituted GDY [167] Copyright © 2018, American Chemical Society. (o–t) Precisely N-doped GDY films [168] Copyright © 2018, American Chemical Society.

non-metallic catalyst (Fig. 11i–l). But, a significant challenge remains in controlling the chemical composition of non-metallic catalysts based on popular sp^2-HCAs [158,159]. The complex nature of these processes hinders a comprehensive understanding of non-metallic catalysts, and effective catalyst design mostly depends on trial-and-error approaches. Li et al. [160] synthesized N-doped GDY nanocomplexes with well-ordered nitrogen frameworks using air implosion. This technique efficiently generates GDY-based composites under alkaline environments. The resultant N-doped GDY nanochains demonstrated superior dispersion in solutions, enhancing electrode fabrication. Their research indicated that nitrogen loading substantially influenced initial efficiency for the ORR. Pyridyl nitrogen molecules specifically elevated the onset

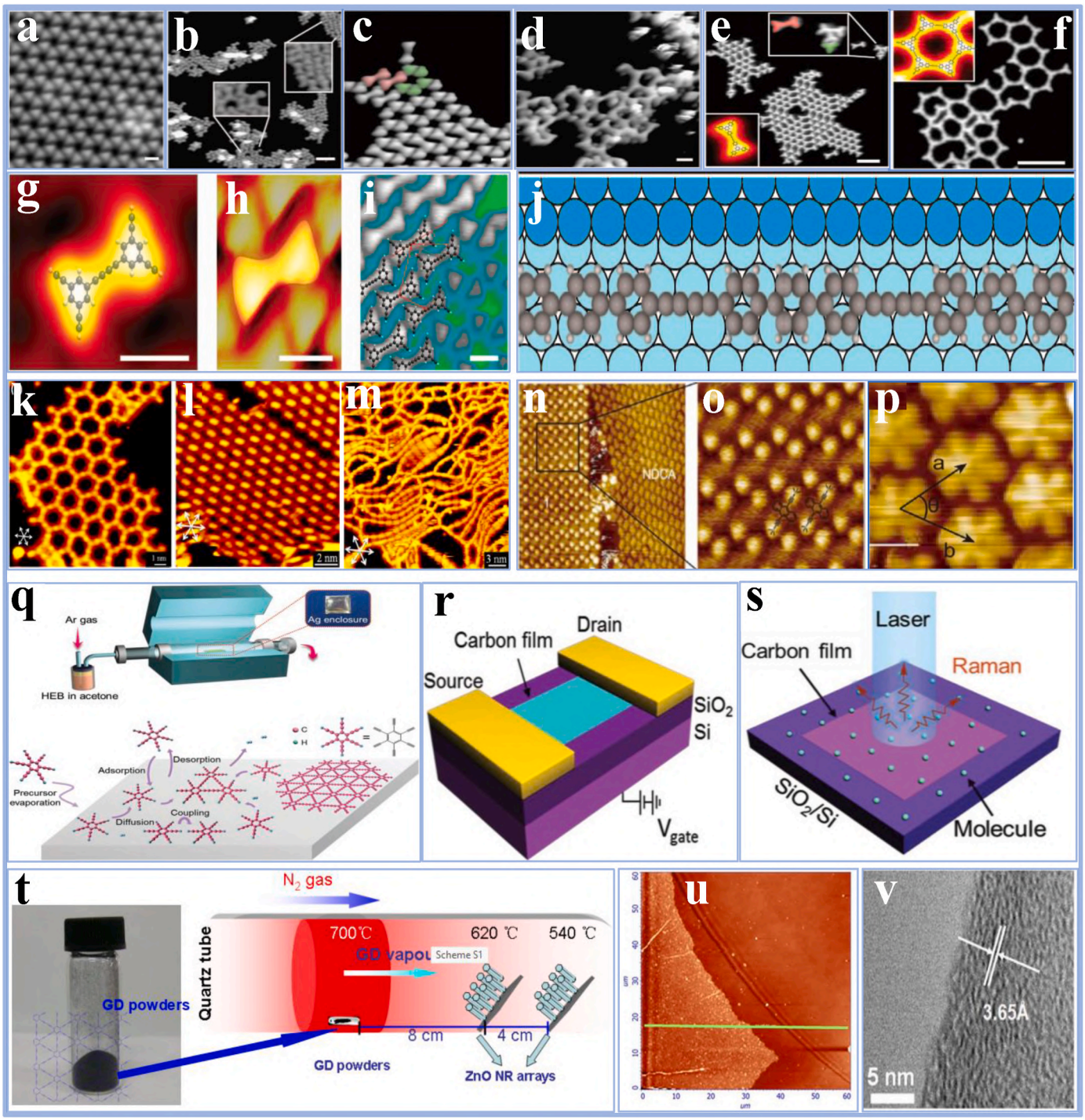

Fig. 13. (a–i) STM topographic images of Ag(111) reaction products (1–4) TEB molecules; (5, 6) Ext-TEB molecules; (7–9) DFT simulations and comparison with STM observations [170] Copyright © 2012, Springer Nature. (j) Chemo-performance higher-index phase interface of Ag(877) [171] Copyright © 2014, American Chemical Society. (k–m) High-resolution STM images of the C–C coupled network [173] Copyright © 2016, American Chemical Society. (n–p) High-resolution STM image on the Glaser polymers [174] Copyright © 2017, American Chemical Society. (q) Schematic of the growth of GDY on Ag foil via a CVD process by using HEB as the precursor; (r) Schematic illustration of a two-terminal back-gated FET device synthesized GDY film; (s) Schematic illustration of the molecules on substrates and measurement procedure [176] Copyright © 2017, John Wiley and Sons. (t) Synthesis of GDY films on ZnO nanorod arrays. (u) AFM image of the as-grown GDY film by top-down method (thickness: 22 nm); (v) HRTEM image of the as-grown GDY film. The layer-to-layer distance between the GDY films is 0.365 nm [178] Copyright © 2015, Nature.

potential to 0.87 V (vs. RHE), which is 0.05 V more than the onset potential of N0-GDY (0.82 V). Nonetheless, the N-doped material exhibited poor photochemical efficiency compared to pure GDY, which adheres to a $4e^-$ ORR route. The introduction of nitrogen atoms reduced electron transference productivity, and GDY with pyridyl nitrogen dopants adhered to a $2e^-$ ORR mechanism, presumably owing to distinctive nitrogen-activated sites inside each unit. This problem was overcome by triazine-like nitrogen units, which had three activated nitrogen atoms per unit, leading to a greater electron transference number throughout the full potential range than N1-GD (Fig. 11m–q). Das et al. [161]

performed a comprehensive first-principles analysis of the ORR processes on nitrogen (N)-loaded graphynes (αGy, βGy, γGy, and 6,6,12Gy) and GDY in alkaline environments. In contrast to graphene, which consists only of sp^2-HCAs, these materials include both sp^2 and sp-HCAs, providing many symmetric sites for nitrogen replacement. The sp-HCAs in the acetylene linkages between hexagonal rings were determined to be the most advantageous doping sites, exhibiting exothermic formation energies of −1.06 eV, −1.61 eV, −1.82 eV, and −1.93 eV for αGy, βGy, γGy, and 6,6,12Gy, respectively, and −1.56 eV for GDY adjacent to the hexagonal ring. Additionally, the doping phenomena of nitrogen contents elevates the Fermi level into the conduction band (CB), resulting in n-type loading and converting semimetallic αGy, low-bandgap semiconductor γGy, and GDY into metallic conductors, thereby enhancing electron transport in electrocatalysis. The ORR process was examined using the Eiley-Ridel model, in which reactants engage directly with adsorbed O_2 atoms or O atoms from the electrolyte. The reaction occurs by either an associative route, characterized by the stretching of the O–O bond while maintaining its integrity, or a dissociative pathway, in which the connection is completely severed, depending upon the adsorption geometry (Fig. 11r−y). Their research highlights the effectiveness and tunability of N-loaded graphynes and GDY as ORR electrocatalysts.

2. Synthesis methods of GDY

GDYs, belonging to the extensive carbon family, exhibit a conjugated framework featuring a periodic configuration of diacetylene chains on a 2D surface. Multiple synthetic methods facilitate the formation of structured GDY-derived composites via uniform coupled reactivities, rendering them flexible carbon catalysts with extensive applications [54]. Maximizing the promise of GDY-derived composites as carbon catalysts necessitates an advanced 2D structure. The effective synthesizing techniques for GDY composites commenced with the effective creation of HEB on copper foil [26]. Numerous studies have investigated synthetic strategies to determine optimal catalysts (Fig. 12a–c) [162], as well as the impacts of calcination, mixture frameworks, and composite development (Fig. 12d and e) [54]. These methods facilitate the accurate modification of GDY frameworks, resulting in the formation of nanosheets, ultrathin nanoribbons [162], nanospheres [163], nanotubes [53], and nano-complexes [164]. The distinctive frameworks confer essential characteristics to GDY, thereby improving its effectiveness as a non-metallic catalyst. A variety of intriguing composites in the GDY family has emerged, differing in their aromatic chain frameworks and acetylene molecules. Huang et al. [165] prepared GDY sheets featuring nanoporous frameworks through the substitution of hydrogen and chlorine atoms at three linking sites (Fig. 12f−h). The multifaceted nanoporous structure, characterized by planar chemical holes, enabled the efficient transfer of Li^+ and Na^+ ions, thereby establishing these sheets as suitable anode materials. The production, electrical features, planar porosity, and structural characteristics of GDY composites are influenced by the concentration of sp-HCAs [95]. The framework of β-GDY attains the highest sp-HCAs density, reaching up to 80 % (Fig. 12i and j) [166], while triphenylene-cored GDY exhibits the lowest density, at up to 40 % (Fig. 12k−n) [167]. Shang et al. [168] integrated nitrogen and boron into the substrates to produce structured GDY variants (Fig. 12o−t). These systematically arranged structures facilitate accurate determination of catalytic reactions. Moreover, conventional doping techniques, including the introduction of heteroatoms at high temperatures, are applicable to GDY-based composites [156].

2.1. Dry chemistry

There are three primary ways to produce GDY utilizing the dry chemical methodology: the top-down methodology, the explosion methodology, and on-surface synthesis in scanning tunneling microscopy (STM)/chemical vapor deposition (CVD) mechanisms.

2.1.1. On-surface synthesis

The on-surface synthetic process involves the formation of covalently bonded molecular structures on metallic surfaces through the use of selected intermediates [150,169]. This technique may take place in CVD devices working in regulated atmospheric settings as well as STM devices running in ultra-high vacuum (UHV) conditions. CVD is highly efficient for the production of GDY-derived structures, facilitating rapid analysis of bonding processes, precursors, and residues. For example, Zhang et al. [170] revealed a surface-induced alkyne-coupled reaction on Ag(111) utilizing intermediates 1,3,5-triacetylenylbenzene and 1,3,5-tri-(4-ethynylphenyl)benzene. This method enabled an alkyne-coupling response, yielding a structured macrocycle fragment with H_2 as the exclusive byproduct (Fig. 13a−i). Similarly, Cirera et al. [171] improved coupling response by utilizing the higher-index phase interface of Ag(877), resulting in the formation of 30 nm wide GDY wires along the interface (Fig. 13j). Additionally, the incorporation of carbonitrile (CN) features in alkaline intermediates facilitated selective alkyne homo-coupling procedures, resulting in the formation of polymeric wires as opposed to linear intermediates [172]. Furthermore, Sun et al. [173] employed intermediates containing target alkynyl chloride for dehalogenative homo-coupling on Au(111). This approach leverages the comparatively weaker C–Br bond relative to the C–H bond, leading to a structured 2D permeable matrix with acetylenic linkages, which enhances flexibility and reduces impurities (Fig. 13k−m). Likewise, Gao al [174]. presented a metallic interface s-bonding metathesis method, employing TMS-HEB-1 as an intermediate. Long-term annealing at ambient temperature resulted in the removal of trimethylsilyl protective groups, leading to the formation of an orderly HEB structure on the Ag (111) interface. The synthetic process of Glaser polymers was accomplished through s-bonding metathesis and Glaser-coupled response of 3 at 170 °C on the Au(111) interface (Fig. 13n−p). However, insufficient information concerning the Glaser-coupled response of HEB in the synthesis of GDY may result from side reactions occurring at the metallic interface and inadequate stability of HEB during the linkage process. In another study, Liu et al. [175] synthesized polymeric wires featuring –CRC– linkages on Cu(111), Ag, and Au interfaces through the coupling of two $–CCl_3$ groups from 1,4-bis(trichloromethyl)benzene (BTCMB) in ultra-high vacuum (UHV) conditions. Furthermore, Liu et al. [176] utilized an on-surface synthesis method via CVD to produce a GDY-derived monolayer on an Ag sheet, with HEB intermediates facilitated by Ar fluid for Glaser recombination (Fig. 13q–s). The AFM analysis indicated a uniform 0.6 nm carbon sheet, whereas XPS identified C–C (sp^2), C–C (sp), and CQO orbitals. Despite advancements in on-surface synthetic methods utilizing terminal alkynes, existing techniques primarily produce GDY-like monomers. This limitation arises from the fragility of alkynyl subunits and the presence of side reactions, including cis/trans hydrogenations and cyclotrimerization, on metal surfaces [169].

2.1.2. Top-down methodology

Top-down methodologies, such as micromechanical removal and exfoliation of multilayered bulk substances in a chemical solution, have been widely utilized in the fabrication of 2D materials, transition-metallic disulfides (TMDs), and graphene with one or a few layers [177]. Another method for synthesizing GDY thin films was top-down methodology. Li et al. [178] synthesized GDY thin films on ZnO nanotubes utilizing a pre-prepared bulk GDY mixture and self-catalyzed VLS growth (Fig. 13t). The as-synthesized GDY films displayed a stratified morphology with a width of 22 nm (Fig. 13u and v).

2.1.3. Explosion methodology

Explosion methodology is essential in GDY production, facilitating the fabrication of higher-quality, versatile materials with regulated attributes. This method enables the synthesis of higher-purity GDY, characterized by minimal impurities and imperfections, which is essential for accurate applications [179]. The synthetic procedure is fast

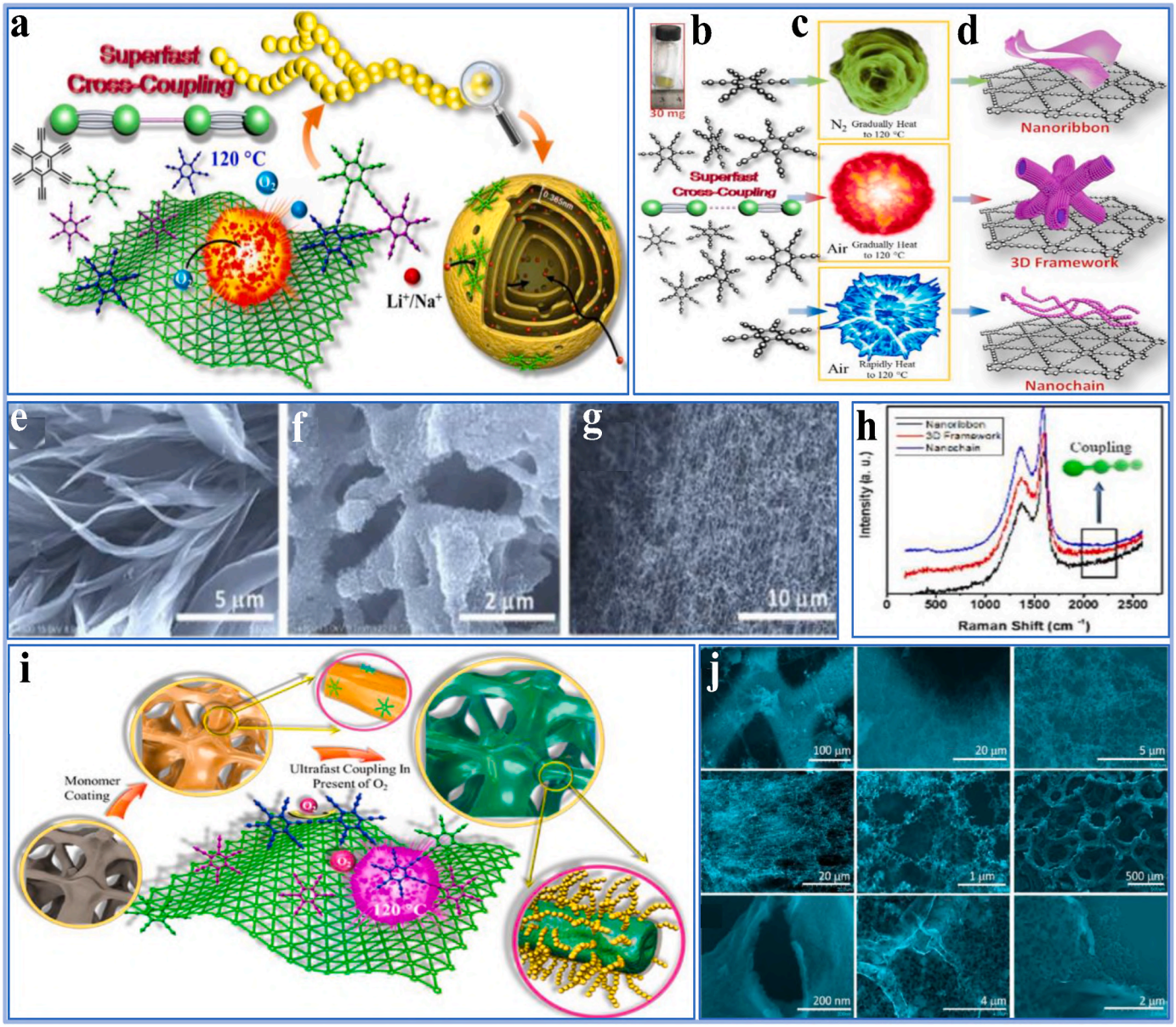

Fig. 14. (a) Graphical depiction of explosion strategy; (b) The HEB image before reaction; (c) The reactivity during three treatments; (d) The GDY morphologies; (e) GDY nanoribbons; (f) 3D GDY framework; (g) GDY nanochain; (h) Raman spectra of the as-prepared GDY: blue line denotes nanochain; red line, 3D framework; and black line, nanoribbon [164] Copyright © 2017, Royal Society of Chemistry. (i) Schematic fabrication and assembly of a GDY nanostructure using various substrates; (j) Corresponding SEM images of the GDY nano-chains [181] Copyright © 2019, American Chemical Society. (For interpretation of the references to color in this figure legend, the reader is referred to the Web version of this article.)

and effective, making it appropriate for industrial-scale fabrication. The explosive conditions facilitate accurate regulation of the structural and electronic characteristics of GDY, allowing for modification for specific applications [180]. Overall, explosion methodology serves as a successful approach for the productive production of advanced GDY materials. Li et al. [164] proposed a scalable explosive method for the production of GDY, employing gaseous-state homocoupling of HEB without the need for metallic catalysis, achieved through the annealing of HEB polymers in N_2 or air (Fig. 14a–d). The microstructure of GDY granules can be modified by altering the heating process, which involves the environmental conditions and heating temperature. Heating HEB molecules at a controlled rate of 10 °C/min to a temperature of 120 °C in nitrogen led to the formation of GDY nanobelts (Fig. 14e). Upon heating in air, the identical HEB molecules produced 3D GDY frameworks, resulting in a volume substantially greater than that of the reactants (Fig. 14f). A more intense explosion transpired upon the introduction of the monomer mixture to a heated air beaker at 120 °C, resulting in the formation of a nanochain framework (Fig. 14g). The Raman spectrum of the synthesized material validated HEB linkage and identified GDY-specific peaks (Fig. 14h). This novel method facilitates the production of all-carbon composites without metallic catalysts, enhancing the scalability of GDY fabrication and enhancing crystallization. Wang et al. [181] utilized the same approach to produce GDY at 120 °C in the air (Fig. 14i and j). Their research demonstrated that the as-synthesized GDY on substrates produces ultrafine nano-chains with a substantial SSA and 3D interconnectivity, which strongly adhere to all-carbon films. These substrates exhibit superhydrophobic properties, with a static contact angle reaching up to 148°, rendering them effective absorbents for organic contaminants. The continuous GDY coating on 3D foams enhances its suitability as a supercapacitor electrode, offering superior area capacitance, high productivity, and extended retention.

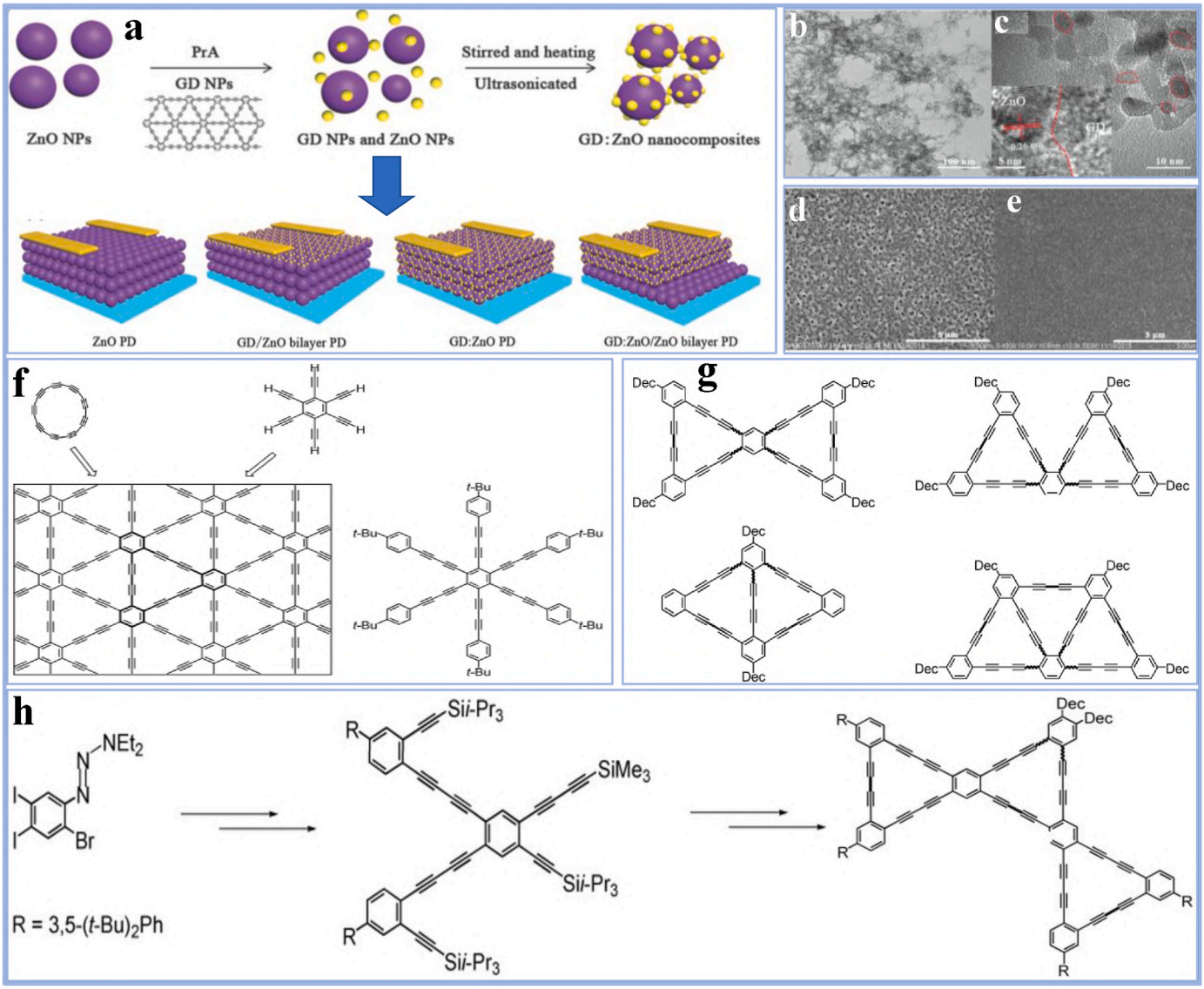

Fig. 15. (a) Synthesis scheme; (b, c) TEM; (d, e) SEM of the GDY:ZnO nanocomposites [184] Copyright © 2016, John Wiley and Sons. Potential precursors and synthetic approaches to graphynes; (f) GDY; (g) In-situ cross-coupling process; (h) Assembly of the "supersized" subunits [185] Copyright © 2009, De Gruyter.

2.2. Wet chemistry

The wet chemical technique offers a more effective and flexible process for developing GDY films appropriate for commercial uses compared to the previously mentioned dry chemistry approaches [182]. Three primary wet chemical methods for the fabrication of GDY are Cu-surface-facilitated, interface-assisted, and solution-phase van der Waals epitaxy [183]. Jin et al. [184] employed the wet chemistry method to synthesize GDY:ZnO nanocomposites utilizing PrA-enriched ZnO nanoparticles. The interface between the GDY and ZnO nanoparticles improves the carrier-exchange process, leading to an essential improvement in photo-response (Fig. 15a–e). Fig. 15f–h illustrates different synthetic methods and developed examples for the production of GDY [29,185,186].

2.3. Cu-surface-mediated synthesis

Cu-surface-mediated synthesis is important for GDY fabrication, offering an optimized and effective approach for the growth of higher-quality GDY films [187]. This approach improves the structural and electronic characteristics of GDY by providing a catalytic surface that promotes the accurate bonding and alignment of carbon atoms. This method facilitates the production of homogeneous, large-area GDY films, rendering them suitable for applications in electronics, energy storage, and catalysis [188]. Additionally, the Cu-surface approach facilitates scalable fabrication, enhancing the overall productivity of the synthesis procedure [189]. Li et al. [26] were the first to successfully synthesize GDY utilizing a Cu-surface-facilitated method in 2010. They employed tailored HEB compounds in an in-situ Glaser-coupling method on a Cu sheet [190]. The Cu sheet served as both a catalytic source and a substrate, promoting the symmetrical formation of GDY (Fig. 16a). Pyridine functioned as a solvent and mediator, facilitating the removal of Cu particles from the interface. Cu particles play a catalytic role in the Glaser coupling procedure, facilitating the growth of GDY layers reaching sizes of up to 1 mm, exhibiting a conductivity of 2.516×10^4 S m^{-1} (Fig. 16b). But the catalyst was not completely preserved on the material because of its strength gradient, causing a distribution of Cu particles in the mixture, which led to bulk polymerization of monomers and suboptimal 2D materials. To improve reactivity, Liu et al. [163] suggested an improved Glaser-Hay coupling approach that enhances reactivity for the formation of GDY nanowalls on Cu sheets, utilizing acetone as the synthesis agent in place of pyridine. They regulated the

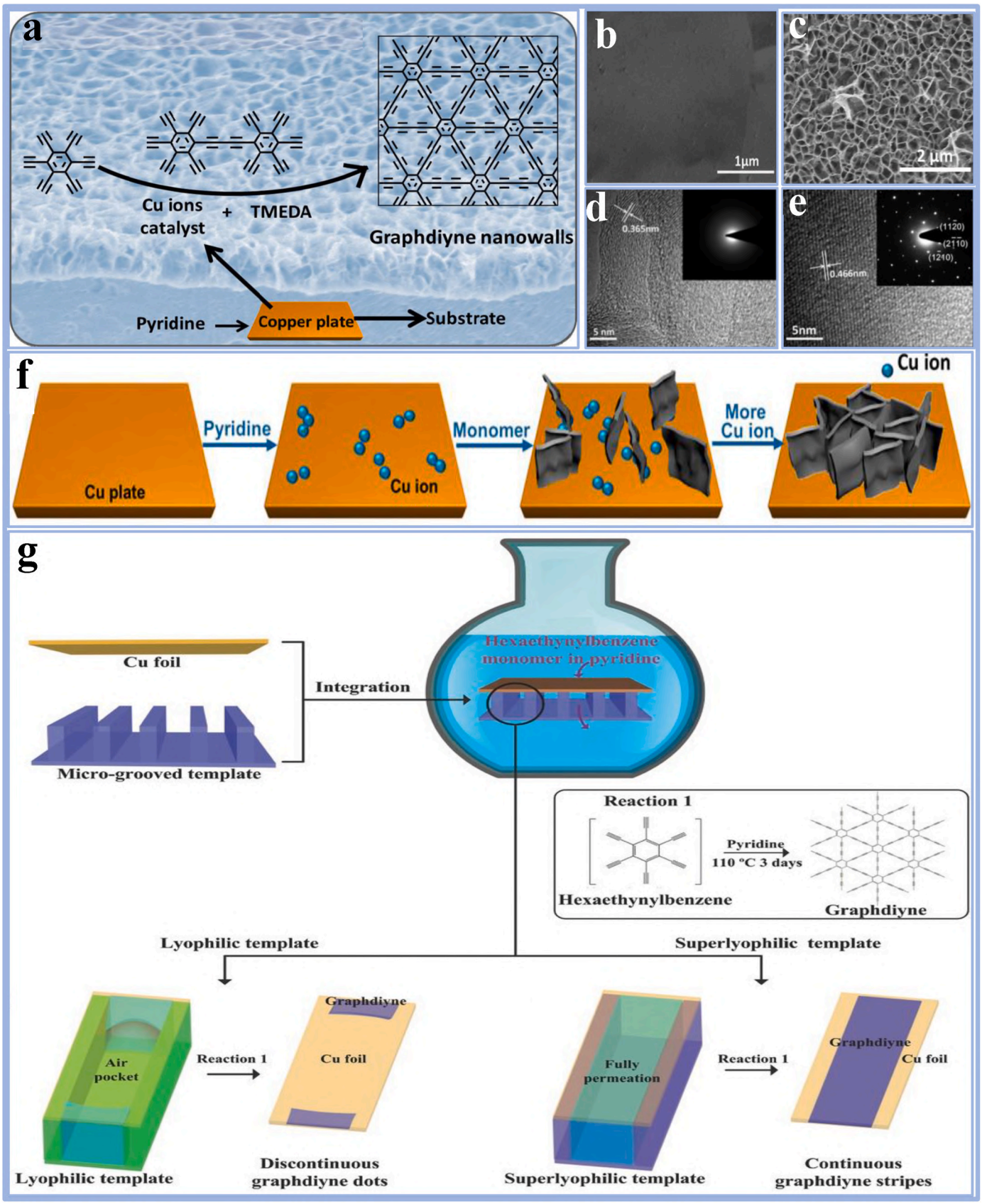

Fig. 16. Synthesis of GDY on Cu substrates. (a) Synthesis of GDY films using in situ Glaser coupling reaction on Cu foils; (b, c) SEM; (c, d) HRTEM; (e) SEM; (f) Proposed reaction process of GDY nanowalls [163] Copyright © 2015, American Chemical Society. (g) The synthesis of organized GDY striping patterns on Cu via a wettability-assisted approach [191] Copyright © 2016, John Wiley and Sons.

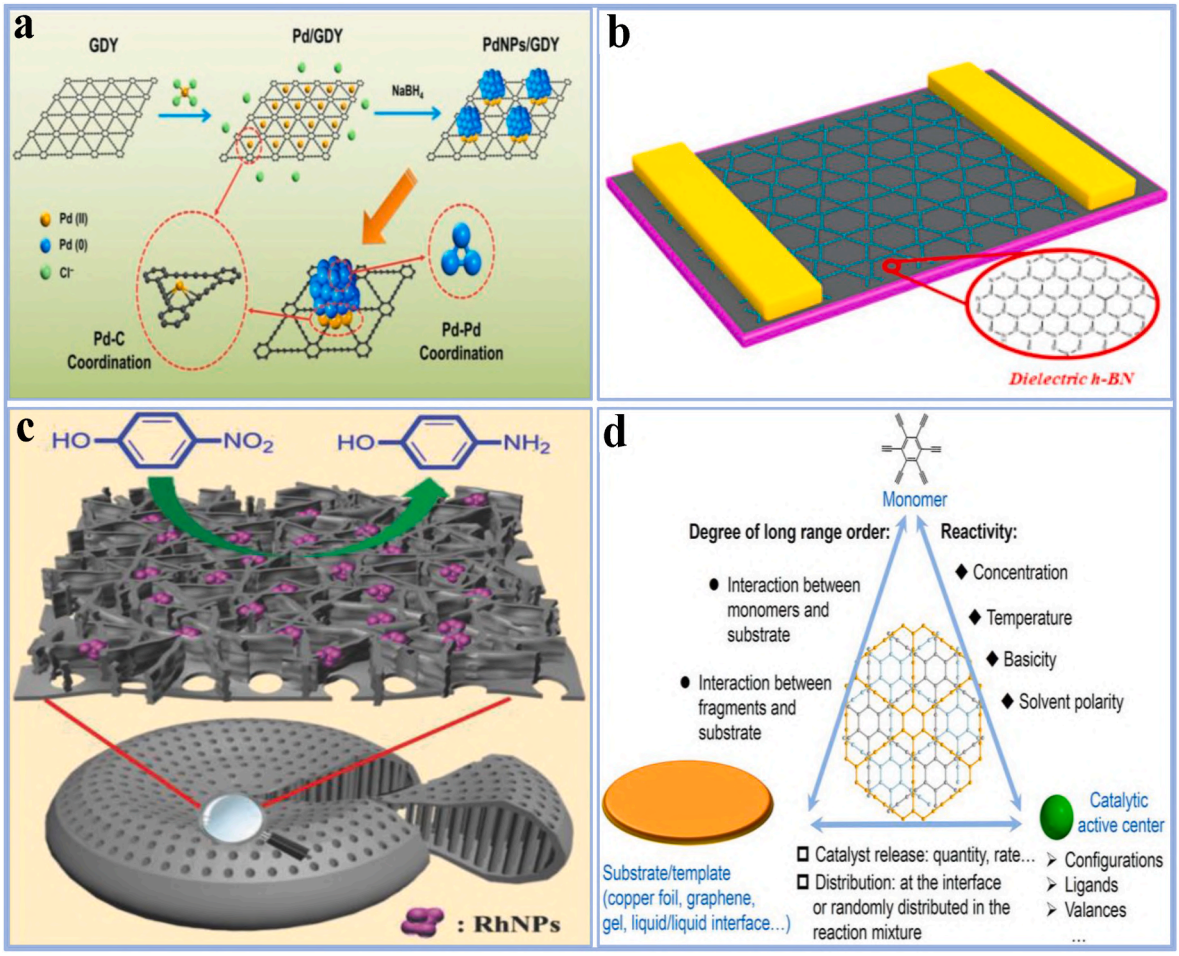

Fig. 17. (a) Synthetic process of PdNPs/GDY [197] Copyright © 2020, Elsevier. (b) Synthetic process of β-GDY-like film grown on graphene [198] Copyright © 2019, American Chemical Society. (c) Synthetic process of 3DGDY [66] Copyright © 2018, John Wiley and Sons. (d) Synthetic process of nanoGDY [199] Copyright © 2024, American Chemical Society.

amount of catalyst particles by modifying the quantity of organic-derived additives, including pyridine and TMEDA. Initially, a reduced number of Cu particles disintegrated on the Cu sheet, resulting in the development of localized GDY nanosheets. As the process advanced, increased dissolution of Cu particles occurred, and the reacting regions expanded, ultimately resulting in the creation of 3D honeycomb-like GDY nanowalls (Fig. 16d–f), thereby confirming the fabrication of GDY. The as-prepared nanowalls have an approximate length of 1 mm (Fig. 16c), and nanosheets are 10 nm thick. Their research demonstrated that the fabrication of GDY nanowalls necessitated a minimal quantity of monomer. GDY films generated with elevated monomer concentrations exhibit chaotic frameworks. The previously mentioned approaches are applicable to GDY creation on Cu-based materials. Additionally, the Cu-surface-facilitated method has been utilized for various Cu-based materials, such as 2D Cu sheets, 1D Cu lines, 3D Cu lattices, and Cu foams, demonstrating similar in-situ binding of HEB [35]. Additionally, GDY striping structures have been created on Cu substrates through a wettability-assisted approach (Fig. 16g) [191].

2.4. Template-based synthesis

Template-based synthesis is a technique used to direct the formation of specific frameworks in materials by employing a pre-existing template [192]. For GDY, this method utilizes templates, often porous or nanostructured materials, to guide the formation of GDY nanosheets or structures with tailored morphology and properties [193]. The template controls the dimensions, morphology, and porosity of the resulting GDY, thereby enhancing its characteristics such as surface area, catalytic efficiency, and ion transport [194]. This approach is essential for optimizing GDY for targeted applications, including energy storage, electrocatalysis, and sensing, where controlled surface area, regulated porosity, and structural integrity are essential for performance [195]. Template-assisted synthesis allows for the production of highly organized, nanostructured GDY materials with customized properties, which are challenging to achieve through conventional methods [196]. For example, Liu et al. [197] used 2D GDY as a template to immobilize palladium nanoparticles (PdNPs) for the synthesis of a stable nanocatalyst. The PdNPs/GDY composite effectively decomposes H_2O_2 to generate oxygen, mitigating tumor hypoxia and inhibiting tumor growth. The GDY template ensures stable PdNP distribution, preventing oxidation and aggregation, which enhances the catalytic efficiency and stability compared to commercial Pd/C and PdNPs/graphene oxide (GO). In tumor models, PdNPs/GDY increases oxygen generation, reduces HIF-1α expression, and, when combined with chemotherapy (doxorubicin), significantly enhances antitumor activity (Fig. 17a). Similarly, Li et al. [198] devised a graphene-templated approach for the synthesis of ultrathin β-GDY-like films, leveraging the robust π−π interactions between β-GDY and graphene. The GDY film exhibited a uniform framework, high crystallinity, and a conductivity of 1.30×10^{-2} S m^{-1}. This method demonstrates the potential for generating single-crystalline β-GDY films in a monolayer, dependent upon further refinement of synthesis parameters (Fig. 17b). In another study, Li et al. [66] devised a method for the preparation of freestanding 3D GDY

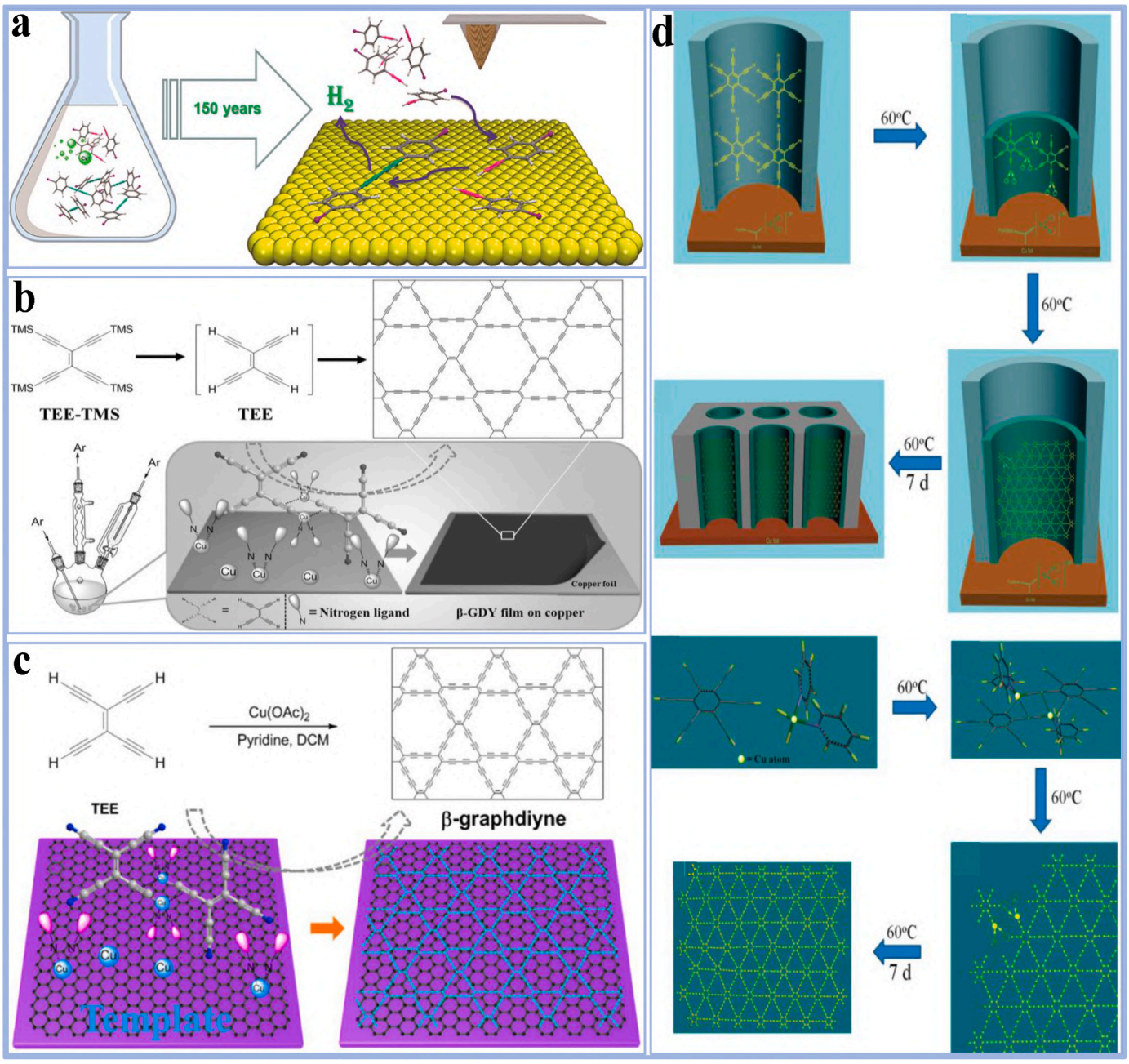

Fig. 18. (a) Synthetic process of GDY via Glaser coupling reaction [169] Copyright © 2015, American Chemical Society. (b) Synthetic process of β-GDY-containing film growth on copper substrate via Glaser coupling reaction [61] Copyright © 2017, John Wiley and Sons. (c) Synthetic process of β-GDY via Eglinton coupling reaction [198] Copyright © 2018, American Chemical Society. (d) Synthetic process of GDNT arrays via Alkynylsilane coupling reaction [225] Copyright © 2011, American Chemical Society.

utilizing cost-effective diatomite as a template, thereby overcoming the constraints associated with expensive copper substrates. The 3D GDY possesses a porous framework and a higher SSA, rendering it appropriate for use as Lib's anodes and as a scaffold for the development of Rh@3DGDY composites, which may have applications in energy storage and catalysis (Fig. 17c). Moreover, Hu et al. [199] explored the assembly of nanographdiyne (nanoGDY) by modifying peripheral substituents to regulate stacking configurations. Substrates and substituents were found to influence π-stacking, allowing nanoGDY to act as a template for GDY formation. Using a rigid template, they successfully produced high-quality, micrometer-scale crystalline GDY flakes, verified through various characterization methods. This scalable approach enables the production of wrinkled 2D structures, applicable to a wide range of GDY-based applications (Fig. 17d).

2.5. *Synthesis reactions of GDY*

The synthetic reactions of GDY are essential for modifying its framework and characteristics. Glaser and Glaser-Hay coupling reactions facilitate the effective construction of sp and sp^2 hybridized frameworks, resulting in consistent films that exhibit improved electronic and photochemical properties. Eglinton coupling enhances GDY synthesis, enabling the production of ultrathin, higher-conductivity films on substrates such as graphene. Alkynylsilane coupling enables precise control over distinct morphologies, including nanotubes, which have applications in nanoelectronics and energy devices. Collectively,

these methods offer adaptable and scalable approaches for enhancing GDY's applicability across diverse technological domains. The details of different important synthesis reactions of GDY are given in this section.

2.5.1. Glaser coupling reaction

The Glaser coupling reaction is a chemical mechanism that involves the oxidative coupling of terminal alkynes to produce diacetylenes by the creation of a C ≡ C bond [200]. This reaction, usually catalyzed by copper salts and aided by an oxidant, is particularly efficient at synthesizing conjugated carbon-rich frameworks [201,202]. The Glaser coupling process is essential for the production of GDY. GDY's distinctive 2D design is realized by the coupling of monomers with terminal alkynes through the Glaser reaction [203]. This technique allows exact regulation of the alignment and interconnection of carbon atoms, which is essential for attaining the favorable characteristics of GDY, including its adjustable bandgap, elevated conductivity, and improved charge carrier mobility [204]. The Glaser coupling reaction is fundamental for the scalable and repeatable synthesis of GDY, enabling its investigation in electrical, catalytic, and energy-related applications [205]. For example, Klappenberger et al. [169] highlighted the importance of Glaser coupling and its advanced techniques for the fabrication of carbon-based structures that include sp^2-and sp-HCAs, such as carbyne chains and 2D graphyne or GDY networks. Their research emphasizes the prospect of interfacial production using terminal alkynes to produce atomically accurate, low-dimensional carbon-enrich nanomaterials. The Glaser coupling process differs from traditional on-surface synthesizing, which typically relies on thermally triggered aryl dehalogenation that produces halogen byproducts. Instead, the Glaser reaction produces excess hydrogen, rendering it particularly advantageous for chemically sensitive GY/GDY-related frameworks. Their research examines the coupling process in solution and surface-confined environments, proposing strategies to reduce undesirable side reactions and improve control and precision in the production of GDY (Fig. 18a).

2.5.2. Glaser-Hay coupling reaction

The Glaser-Hay coupling reaction extends the traditional Glaser coupling by facilitating the oxidative homocoupling of terminal alkynes, resulting in the formation of diacetylene bonds [206]. The reaction is catalyzed by copper(I) salts and utilizes a chelating ligand, such as N,N,N′,N′-tetramethylethylenediamine (TMEDA), to improve reaction productivity and selectivity [207,208]. The Glaser-Hay coupling reaction plays an essential part in the fabrication of GDY, enabling the growth of diacetylene linkages that characterize GDY's distinctive 2D framework, which consists of sp- and sp^2-HCAs [38]. This reaction facilitates accurate molecular assembly and scalability, which is essential for the consistent and reproducible production of GDY [209]. The coupling mechanism reduces side reactions and is especially effective for forming the highly conjugated carbon network of GDY, which is fundamental to its remarkable characteristics, including a tunable bandgap, outstanding electrical conductivity, and superior charge carrier mobility [210]. The Glaser-Hay coupling reaction is a fundamental technique in the fabrication of GDY, facilitating progress in its applications within electronics, catalysis, and energy storage systems [211]. For example, Li et al. [61] presented a viable synthetic approach for the fabrication of a β-GDY--containing thin film, approximately 25 nm in thickness, on copper foil utilizing tetraethynylethene (TEE) as the precursor. The method utilized a tailored Glaser-Hay coupling reaction, which is an established technique for the synthesis of symmetric diyne compounds. TEE, originating from tetra[(trimethylsilyl)ethynyl]ethene (TEE-TMS), was coupled onto pretreated copper foils using acetone, pyridine, and TMEDA as reagents. The copper foil served dual functions as a substrate and a catalytic source, facilitating the development of a uniform β-GDY carbon network. The film demonstrated an electrical conductivity of 3.47×10^{-6} S m^{-1}. The β-GDY film served as a metallic-free electron transference layer in TiO_2@β-GDY composites, markedly improving the photocatalytic efficiency of TiO_2 (Fig. 18b).

2.5.3. Eglinton coupling reaction

The Eglinton coupling reaction is a well-established organic reaction characterized by the oxidative homocoupling of terminal alkynes, resulting in the formation of symmetrical diynes [212]. The reaction is catalyzed by copper(II) salts, commonly copper(II) acetate, and necessitates an oxidant, such as molecular oxygen, to promote the coupling process [213]. To synthesize GDY, the Eglinton coupling reaction plays an important role in generating the diacetylene links that create GDY's distinctive sp- and sp^2-hybridized carbon structure [214,215]. The reaction facilitates an effective coupling of terminal alkynes, offering a direct method for the construction of the highly conjugated and ordered 2D framework of GDY. The structural accuracy is essential for GDY's notable properties, including its adjustable electronic bandgap, high conductivity, and exceptional charge transport capabilities [216]. The Eglinton coupling reaction serves as an essential technique in the scalable production of GDY, enabling its advancement for applications in energy storage, catalysis, and electronic devices [217]. For example, Li et al. [198] investigated the production of β-Graphdiyne (β-GDY) through the Eglinton coupling reaction, utilizing an innovative template-induced approach. The procedure started with the synthesis of tetrakis[(trimethylsilyl)ethynyl]ethene (TEE), which was then introduced into a reactor comprising dichloromethane (DCM), pyridine, toluene, copper acetate [$Cu(OAc)_2$], and a SiO_2/Si-supported single-layer graphene (SLG). DCM and toluene promoted deprotection and improved the solubility of $Cu(OAc)_2$ in pyridine. The terminal alkynes of TEE, which are highly reactive, chemically combined to create a consistent β-GDY system on the graphene interface, leading to the formation of a carbon film approximately 1.5 nm thick. The electrical metrics of the film, developed on a dielectric hexagonal boron nitride (h-BN) template, indicated a conductivity of 1.30×10^{-1} S m^{-1}, which is markedly greater than that of β-GDY generated on copper foil, measured at 3.47×10^{-6} S m^{-1}. Their research indicates that the additional efficiency of this template approach may enhance the production of single-crystalline, single-layer β-GDY (Fig. 18c).

2.5.4. Alkynylsilane coupling reaction

The alkynylsilane coupling reaction is a synthetic method that involves the coupling of alkynylsilanes, usually facilitated by transition metal catalysts, to generate carbon-carbon bonds [218]. This reaction has been utilized in the synthesis of GDY [219]. In GDY production, alkynylsilane coupling enables the formation of acetylene linkages that characterize GDY's distinct framework [220]. The reaction utilizes the excessive reactivity of terminal alkynes alongside the stability of alkynylsilane precursors, facilitating accurate regulation in the construction of extended carbon structures [221]. This technique facilitates the creation of consistent GDY films that exhibit improved structural integrity and electronic characteristics [222,223], thus serving as an effective approach for the development of GDY-derived materials for use in catalysis, energy storage, and electronic devices [224]. For example, Li et al. [225] described the formation of GDY NTs arrays utilizing an anodic aluminum oxide (AAO) template and copper foil as a catalyst via an alkynylsilane coupling reaction. The synthesized GDY NTs displayed smooth surfaces with an initial wall thickness of approximately 40 nm, which decreased to around 15 nm following annealing. The annealed GDY NTs exhibited superior field emission characteristics, featuring a turn-on field of 4.20 V/μm and a threshold field of 8.83 V/μm. The synthesis utilized a Cu-pyridine complex to initiate the linkage of alkynyl units. The hydrogen bonds formed between Al-O bonds in the AAO template and the acetylenic hydrogen of hexaethynylbenzene enabled the deposition of a precursor film on the template walls. The reaction was performed at 60 °C for seven days in a nitrogen atmosphere and exhibited self-limiting behavior due to the product's coverage of the Cu catalyst. The process produced high-quality GDY NTs suitable for advanced field emission device applications (Fig. 18d).

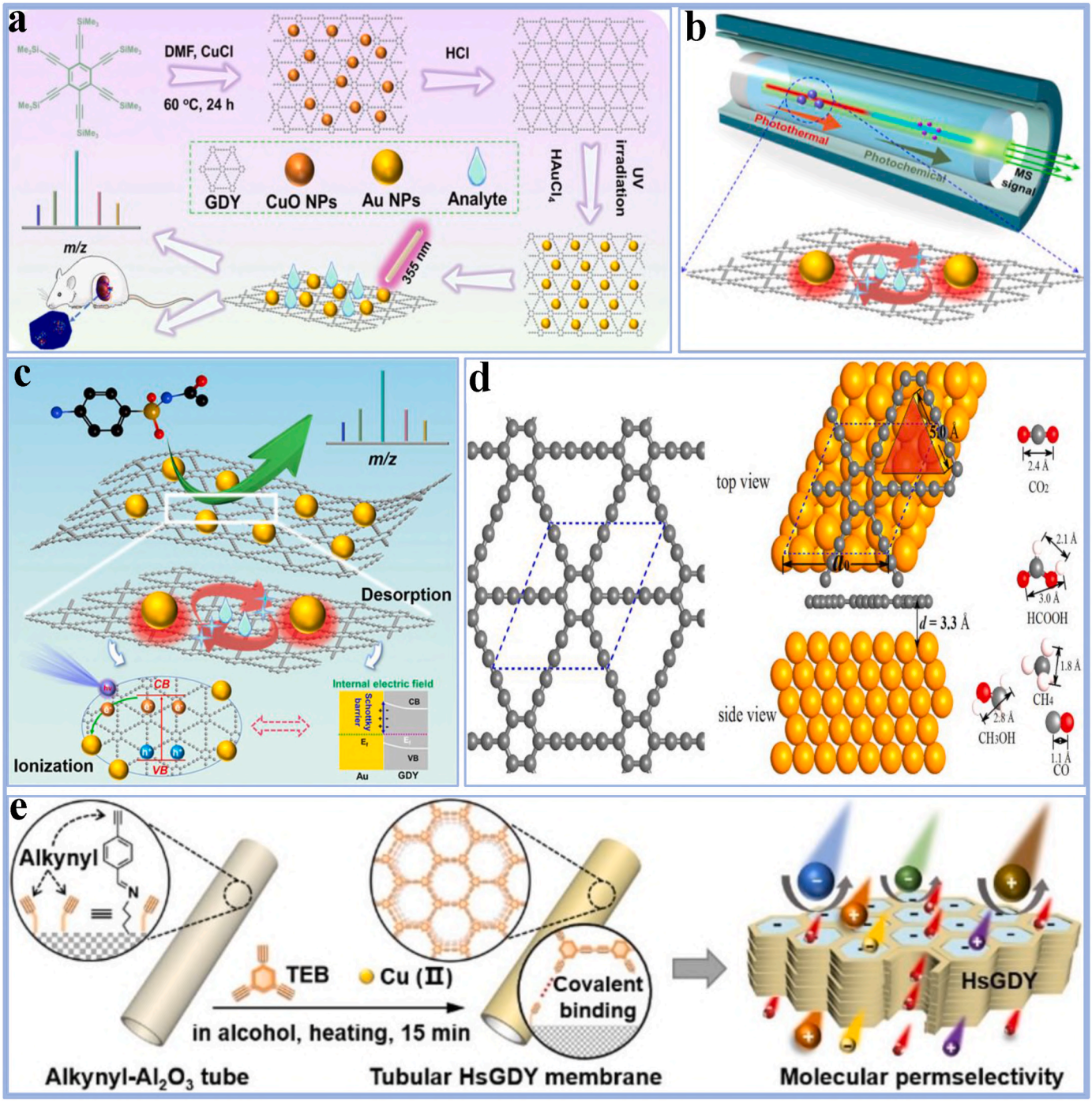

Fig. 19. (a) Synthetic process of Au/GDY matrix; (b) Schematic diagram of the LDI process; (c) Potential mechanisms for the improved charge separation performance of Au/GDY hybrids [231] Copyright © 2023, American Chemical Society. (d) Synthetic process of free-standing GDY sheet [187] Copyright © 2019, Elsevier. (e) Synthetic process of tubular HsGDY membranes [232] Copyright © 2023, John Wiley and Sons.

3. Strategies to improve GDY performance

3.1. Surface functionalization

Surface functionalization is essential for improving the efficiency of GDY by adding new functionalities and optimizing its inherent characteristics [226]. Adding functional groups to the surface of GDY can alter its electronic framework, adjust its bandgap, and enhance charge transference productivity, thereby increasing its applicability across various domains [227]. Furthermore, functionalization may enhance the chemical reactivity of the material, improve adsorption capacity, and offer additional active sites for catalytic reactions [228]. This method enhances GDY's compatibility with various materials in composite systems and facilitates its specific application in energy storage, photocatalysis, and gas separation technologies [229,230]. Surface functionalization is an effective strategy to enhance the potential of GDY in various domains. For example, Pei et al. [231] fabricated a hybrid material consisting of Au nanoparticle-decorated graphdiyne (Au/GDY) intended for application as a surface-induced laser desorption/ionization mass spectrometry (SALDI-MS) matrix. The enhanced desorption and ionization performance of the material is attributed to the interaction between the thermal field and the internal electric field, as

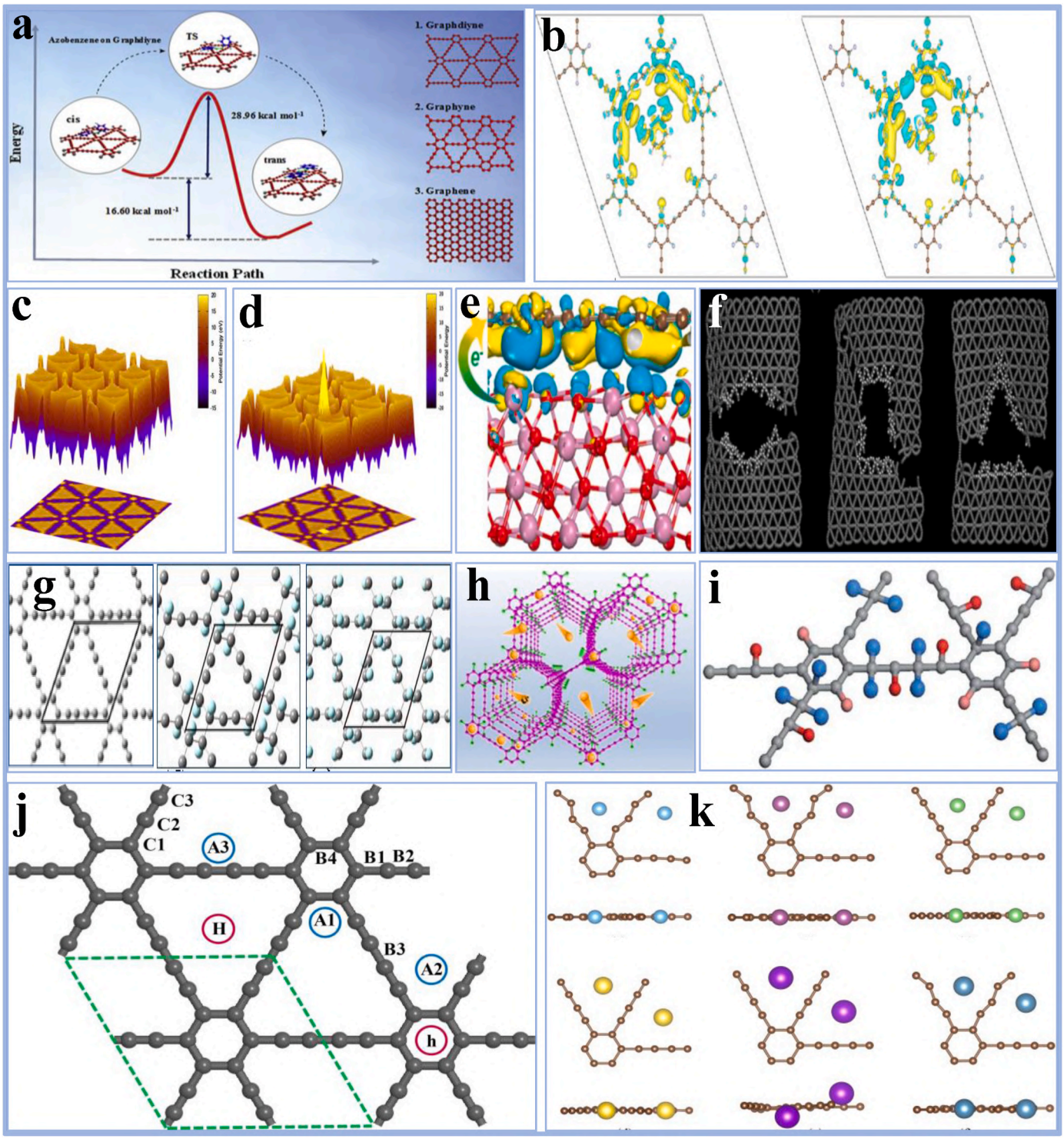

Fig. 20. (a) Schematic mechanism of guest molecular switching of GDY [239] Copyright © 2018, Elsevier. (b) The charging difference between guest molecules of GDY-3F-3NH_2-Ben and GDY-3F-Melamine [240] Copyright © 2024, Royal Society of Chemistry. Site-dependent hydrogenation on (c) GDY; (d) Its hydrogenated form [247] Copyright © 2014, Elsevier. (e) Effect of hydrogenation on charged dispersion on GDY/In_2O_3 nanocomposites [248] Copyright © 2024, Elsevier. (f) Hydrogenated GDY loaded along a zigzag direction [249] Copyright © 2020, Springer Nature. (g) Optimized configurations of fluoro-GDY [255] Copyright © 2014, IOP Publishing. (h) The diffusion of Li^+ in F-GDY [256] Copyright © 2019, John Wiley and Sons. (i) Schematic illustration of FGDY-2 [257] Copyright © 2019, Royal Society of Chemistry. (j) Structural illustration of TM decoration PGDY [260] Copyright © 2023, Elsevier. (k) Optimized structure of metal decorated GDY sheets [261] Copyright © 2018, IOP Publishing.

demonstrated by theoretical simulations and microstructural evaluation. Laser-excited ablation resulted in the introduction of strain and defects, which diminished charge carrier recombination and improved analyte ionization. The tailored Au/GDY matrix facilitated accurate trace detection of sulfacetamide and the visualization of biological tissue elements. Their research emphasizes the prospect of collaborative photothermal transformation and internal electric fields in the creation of advanced semiconductor-derived SALDI-MS matrices (Fig. 19a–c).

Similarly, Chen et al. [187] investigated 2D confined catalysis employing GDY as an overlayer on a copper surface for the electrochemical reduction of CO_2. DFT calculations indicate that GDY improves catalytic efficiency by lowering the free energy of critical intermediates and onset voltage. The restricted area beneath the GDY layer strengthens reaction intermediates through charge transference, while GDY's porous framework provides enhanced molecular transport relative to graphene. Their research emphasizes the perspective of porous 2D materials in enhancing catalyst efficiency via confined catalytic environments (Fig. 19d). Furthermore, Yang et al. [232] devised a facile alkynylated surface-mediated technique for the fabrication of ultra-thin hydrogen-substituted graphdiyne (HsGDY) membranes on commercial alumina tubes. The copper-catalyzed interaction facilitated the nanoscale lateral expansion of HsGDY, resulting in continuous membranes approximately 100 nm thick within a 15-min timeframe. The membranes exhibited remarkable molecular sieving capabilities, high water permeance (~1100 L/m^2 h MPa), and sustained durability in nanofiltration, which can be ascribed to their superhydrophilic surfaces and hydrophobic pore walls. Their research presents a pragmatic method for enhancing the scalability of advanced GDY-derived membranes (Fig. 19e).

3.1.1. Absorption of guest molecules

Guest molecular switches exhibit considerable promise for use in data storage, sensors, and optical devices, serving an important purpose in molecular nanomaterials. The adsorption of guest molecules onto different metallic surfaces (Cu, Au, Ag, Bi, Si) has been extensively studied to support the creation of functional systems [233]. A recent trend involves the utilization of guest molecules for functioning carbon nanomaterials, such as fullerenes, CNTs, and GDY. The purpose of this functionalization is to improve the performance of these materials in solar energy applications, sensors, and storage devices [234]. Theoretical studies indicate that azo-derivatives covalently bonded to multi-walled carbon nanotubes can function as efficient solar-powered energy materials [108,235]. Additionally, graphene oxide/azo composites exhibit enhanced photo-switching and optically regulated conductivity characteristics [236]. The physisorption of azo molecules on graphene can result in n-type or p-type doping, thereby improving its electronic characteristics [237]. Additionally, guest molecules have been integrated into self-assembled polyelectrolyte multilayer screens for the intent of energy retention [238]. Shekar et al. [239] investigated the absorption of guest molecular switching in GDY, revealing that the adsorption energy levels on these frameworks encompass both physisorption and chemisorption regimes, thereby enabling exact regulation over the cis-trans isomerization mechanism (Fig. 20a). Xiong et al. [240] presented a supramolecular method for the synthesis of binary-enriched, non-metallic GDY. This method involves the functionalization of trifluoro-loaded GDY with guest molecules, including melamine or 1,3,5-triaminobenzene, via hydrogen bonding. The integration of these guest molecules into the porous structure of trifluoro-GDY facilitates non-metal binary doping with nitrogen and fluorine atoms. The electron flow and charging distribution in the supramolecular system can be regulated by altering the guest molecules, dependent upon the characteristics of the trifluoro-GDY framework (Fig. 20b).

3.1.2. Hydrogenation

The recent discovery of graphene generated considerable interest in additional 2D materials, especially those within the graphyne group [60]. Graphene, a type of carbon allotrope, is composed of acetylenic groups that connect benzenoid rings [25]. These networks consist of sp and sp^2-HCAs, displaying characteristics comparable to graphene, including the Dirac cone, while also allowing for the possibility of nonzero electronic bandgaps [60]. Graphyne, similar to graphene, has the potential to yield nanotubes [52] and porous fullerenes [241]. GDY is a unique variation of graphyne characterized by the presence of diacetylene groups. Graphene and GDY demonstrate remarkable characteristics, including significant dynamic optoelectronic sensitivity, thermal resistance, and enhanced ion mobility [242,243]. Functionalization of GDY allows for the adjustment of its electronic bandgap and its contact with the external atmosphere, rendering it extremely intriguing for various applications [244]. Several investigations have examined the mechanical, electrical, and structural characteristics of pristine and functionalized graphynes and GDY [245]. But, some theoretical investigations on GDY hydrogenation use simplistic designs, which may fail to represent the complexities of the chemical events involved. Enhancing comprehension requires the development of more realistic models that incorporate structural disorders [246]. In this regard, Autreto et al. [247] performed an atomistic molecular dynamics analysis of GDY's hydrogenation activity, demonstrating complex temporal changes in hydrogen binding kinetics. Hydrogenation primarily occurs on the carbon atoms with triple bonds, as anticipated. Over time, single-bonded CAs emerge as the preferred locations for hydrogenation. In contrast to hydrogenated graphene, GDY does not exhibit the formation of extensive hydrogenated domains (Fig. 20c and d). Similarly, Li et al. [248] investigated the impact of hydrogenation on GDY/In_2O_3 nanocomposites and assessed their photocatalytic performance for CO_2 reduction to C^{2+} hydrocarbons. Their research indicates that the incorporation of hydrogenated GDY increases light absorption and enhances the photocatalytic efficiency of the composite (Fig. 20e). Furthermore, Rouhi et al. [249] examined the mechanical characteristics of hydrogenated GDY through MD simulations, emphasizing on different nanosheet configurations, such as circular, rhombic, square, and triangular shapes. Their findings indicate that an increase in the hydrogenated surface area leads to a reduction in the elastic modulus. Additionally, armchair-structured GDY demonstrated a greater elastic modulus compared to zigzag-structured GDY; but this disparity decreased with the expansion of the hydrogenated region (Fig. 20f).

3.1.3. Fluorination

The creation of robust and effective fluorescent materials is important for use in biological sensing and optoelectronics [250]. Carbon-based nanomaterials, such as graphene analogs and quantum dots (QDs), are preferred for their low toxicity and durable emission characteristics [202,251]. The luminescence of these materials is thought to originate from surface imperfections or isolated sp^2 CAs [252]. Two main strategies to improve quantum productivity are surface modification using organic materials and the integration of light-emitting composites [253]. Photoluminescence (PL) can be optimized through bandgap adjustments or the implementation of functional frameworks to enhance charge transference [251]. GDY and associated materials demonstrate significant potential as efficient photocatalysts and fluorescence sensors, owing to their superior optical responsiveness and swift reaction rates, which result from improved conductivity [254]. But, studies on the intrinsic fluorescence spectra and strategies of GDY are currently limited, presenting a significant opportunity for further investigation. Bhattacharya et al. [255] examined the structural alterations in GDY following fluorination and its impact on electronic characteristics through DFT analysis. Simulations of band structure indicate that fluoro-GDY variants function as wide-bandgap semiconductors, with the tunability of the bandwidth dependent on the extent of fluorination. This tunability offers adaptability for applications in nanoelectronics. The PDOS analysis provides insights into the bonding features of these materials, whereas the crystal orbital hamilton population (COHP) analysis emphasizes the orbitals present in bonding and antibonding interactions (Fig. 20g). Shen et al. [256] synthesized F-GDY through an innovative solvothermal method, resulting in significant interlayer separation and consistent fluorine distribution. The properties of F-GDY render it extremely appropriate for energy preservation applications. F-GDY exhibited superior efficiency as an anode material in lithium-ion batteries (LIBs). A lithium-ion capacitor (LIC) with a 7:1 AC/F-GDY mass ratio demonstrated an energy density of 200.2 Wh/kg at a power density of 131.17 W/kg, and 122.4 Wh/kg at a

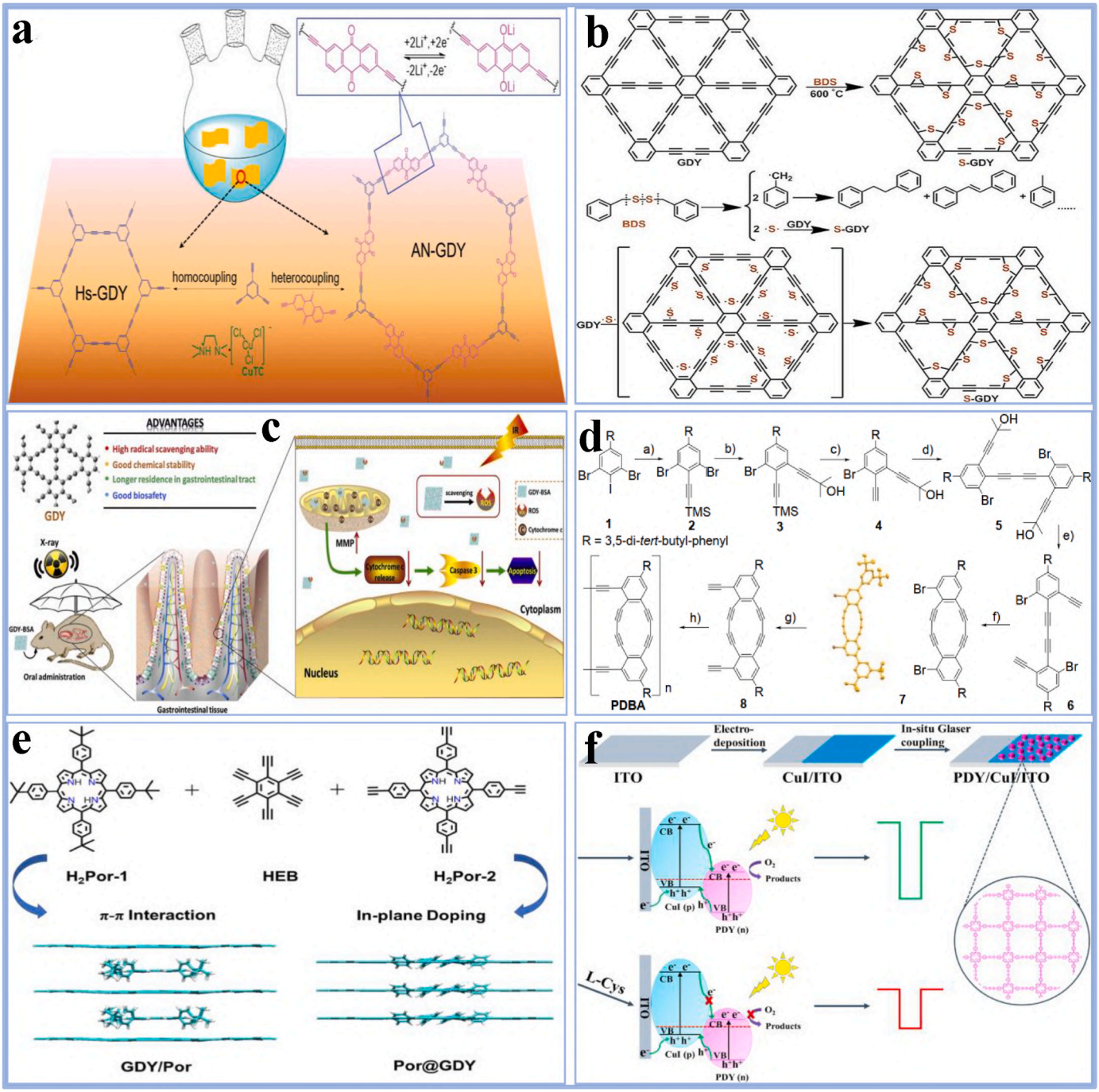

Fig. 21. (a) The synthesis process of AN-GDY and Hs-GDY [268] Copyright © 2024, John Wiley and Sons. (b) Synthetic process of benzyl-based S-GDY [272] Copyright © 2019, John Wiley and Sons. (c) Schemes of the cyanine-based GDY-BSA NPs for GI [278] Copyright © 2020, Elsevier. (d) Schematic mechanism of PDBA-GDY [283] Copyright © 2020, Royal Society of Chemistry. (e) Synthetic process of GDY/Por and Por@GDY [288] Copyright © 2023, Elsevier. (f) Schematic preparation of PDY/CuI/ITO [289] Copyright © 2023, Elsevier.

power density of 13,117 W/kg. The LIC demonstrated significant cycle stability at elevated current densities of 2 and 5 A/g (Fig. 20h). Xiao et al. [257] presented an approach for fluorinating GDY through the thermal treatment of a mixture of XeF_2 and GDY. XPS analysis indicated that pure GDY possesses a considerable amount of oxygen, and the levels of fluorination can be regulated by modifying the XeF_2-to-GDY mass ratio. Fluorine ions exhibit a preference for bonding at the nodes of triple carbon chains. PL spectra demonstrate that fluorine doping improves the fluorescence of GDY, with F-GDY-2 (which contains 15.2 % fluorine) displaying the most intense blue emission at 482 nm. The enhancement is due to a decreased probability of non-radiative transitions in the fluorinated material. The fluorescence intensity of F-GDY-2 decreased with increasing pH from 3 to 11, indicating its sensitivity to environmental changes (Fig. 20i).

3.1.4. *Metal decoration*

The metal decoration of GDY includes the incorporation of metallic atoms into the GDY framework to improve its characteristics for various applications. Doping with transition metals such as Fe, Sc, and Ti markedly enhances the gas-sensing performance of GDY [258]. For instance, Fe-doped GDY demonstrates significant selectivity and efficiency in the detection of hazardous gases, including AsH_3 and PH_3,

positioning it as a viable material for environmental surveillance. The incorporation of metal decoration influences the electrical characteristics of GDY, which may broaden its applications in nanoelectronics [259]. Tabandeh et al. [260] examined the structural and electrical characteristics of 3D transition metal (TM)-decorated GDY films for CO_2 capture through DFT-D2 analysis. Metals like Ti and Cu exhibit a preference for the A_2 site on graphene-derived materials, whereas Sc and Zn tend to favor the A_3 and H sites. Among these, Sc-doped GDY demonstrated the greatest binding energy. Metal decoration alters pure GDY (PGDY) from a semiconductor to a semimetal or introduces magnetic characteristics. The incorporation of metals such as Sc and Cr increases CO_2 adsorption, especially on Sc-doped GDY, thereby enhancing its productivity in trapping and releasing (Fig. 20j). Panigrahi et al. [261] conducted DFT calculations (GGA, vdW-DF, and DFT-D3) to investigate H_2 adsorption on both pristine and metal-doped GDY nanosheets. Light metals, including Li, Na, K, Ca, Sc, and Ti, were employed to dope GDY, facilitating its transition from a semiconductor to a metallic state, which is essential for effective H_2 adsorption. Each doped GDY framework can host a maximum of eight H_2 molecules, exhibiting favorable adsorption energies. The metal-doped GDY nanosheets demonstrate significant potential for hydrogen storage, attaining a capacity of 6.50 wt% (Fig. 20k).

3.2. Functionalization of GDY by derivatives

Recently, GDY has shown great promise in fundamental and applied research, particularly in renewable energy, catalytic processes, photoelectric transformation, life sciences, and microelectronics. Its unique composition and controlled structure offer numerous opportunities for future customization, broadening its application potential. The significant stability of the acetylene linkages in GDY provides an exceptional framework for functionalization, enhancing its applicability across a wide range of scientific domains [262]. The details of different functionality units of GDY are given in this section.

3.2.1. Anthraquinone-based GDY

Anthraquinone-based functionality units, derived from anthraquinone are used to functionalize GDY to enhance its stability, charge storage, and conductivity [263]. In energy storage applications like LIBs, AQ prevents GDY degradation, improves electrochemical performance, and supports faster charge/discharge cycles [113]. Its electron-withdrawing properties enhance lithium-ion interactions, boosting GDY's capacity, durability, and efficiency in battery electrodes [264]. Anthraquinone (AQ), with its reliable redox-activated groups, facilitates electron transport and has elevated theoretical efficiency in energy-storing devices [265,266]. When coupled with GDY, which has good conductivity and compositional strength, the resultant AQ-GDY composites increase Li^+ storage capacity while improving overall electrochemical efficiency, making them suited for future battery usage [267]. For example, He et al. [268] designed a novel framework that couples AQ with GDY to improve the performance of LIBs. This composite inhibits AQ deterioration in the electrolyte while preserving robust electrochemical reactions and strength. The AN-GDY structure facilitates the secure coating and etching of lithium in symmetrical batteries for over 800 h, demonstrating notable capacity retention after 5000 cycles. This method enhances the power productivity and lifespan of organic-based LIBs, presenting a viable method for advancing secure, higher-energy-density lithium-metallic batteries (Fig. 21a).

3.2.2. Benzyl-based GDY

Benzyl-based functionality units, derived from benzyl groups [269], are used to functionalize GDY to improve its structural stability and electronic properties [270]. These units enhance the conductivity and ion transport of GDY, making it more suitable for applications like energy storage and catalysis [217]. In particular, benzyl groups help to increase the material's surface area and facilitate better interaction with other components, thereby improving the performance of GDY in devices such as supercapacitors and batteries [271]. For example, Yang et al. [272] utilized diethyl sulfide (DS) as a sulfur source for modifying the sp-HCAs of benzyl-derived GDY, a carbon material characterized by a high density of butadiyne linkages (-C ≡ C-C ≡ C-). Sulfur radicals from DS react with the acetylenic linkages in GDY, resulting in sulfur-modified GDY (S-GDY) encapsulating the sulfur within the triangular pores of GDY. The technique promises the integration of sulfur atoms as stable C-S-C bonds, free from impurities. The S-GDY demonstrates superior electrochemical efficiency, featuring increased reversible functions and boosted cycling reliability in LIBs relative to unmodified GDY. These changes create heteroatom imperfections and reactive sites, which are essential for the material's electrical characteristics (Fig. 21b).

3.2.3. Cyanine-based GDY

Cyanine-based functional units are organic molecules characterized by a conjugated framework of carbon-carbon double bonds, often including nitrogen atoms [273], which facilitate robust absorption in the visible to near-infrared light range [274]. Cyanine units, when included in GDY, increase the material's optical characteristics, notably enhancing light absorption and photostability [275]. The integration of cyanine groups into GDY enhances charge transference efficiency and improves the material's photocatalytic and electrochemical properties [276]. This alteration is especially beneficial in applications like energy storage, sensors, and solar energy transformation, where improved light absorption and charge transfer are essential for enhancing performance [277]. For example, Xie et al. [278] designed bovine serum albumin (BSA)-modified cyanine-derived GDY nanoparticles (GDY-BSA NPs) for protecting the gastrointestinal (GI) tract against radiation. GDY NPs demonstrated significant free radical scavenging activities, durability in acidic digestive conditions, and an extended residence time in the gastrointestinal system. In vitro tests demonstrated that GDY-BSA NPs decreased DNA degradation and improved cell viability in irradiated gastrointestinal tissues. In vivo studies in mice demonstrated that GDY-BSA NPs mitigated radiation-induced diarrhea, weight loss, and tissue damage. Further analysis demonstrated that GDY-BSA NPs reduced reactive oxygen species, consequently decreasing cell death in the gastrointestinal tract. Their research presents a viable approach to reduce radiation-induced gastrointestinal damage and contributes important findings regarding the application of nano-drugs in the treatment of gastrointestinal disorders (Fig. 21c).

3.2.4. Dehydrobenzoannulene-based GDY

Dehydrobenzoannulene-derived functional units are aromatic chemicals integrated into GDY to improve its structural and electrical characteristics [279]. These units facilitate the development of helical nanofiber structures, enhancing optical characteristics for photocatalytic applications such as OWS [280]. The twisted morphology and butadiyne connections in PDBA-GDY promote electron-hole separation and rapid charge absorption while acting as active sites for the HER [281]. This improves GDY's catalytic effectiveness, making it appropriate for energy conversion and storage applications [282]. For example, Shen et al. [283] developed crystallized 3D alkyne structures utilizing dehydrobenzoannulene-based GDY (PDBA-GDY), resulting in the formation of helical nanofiber structures through polymerization. PDBA-GDY demonstrates superior optical characteristics for OWS, with its spiral framework facilitating enhanced photocatalytic hydrogen generation. The butadiyne groups enhance electron-hole separation efficiency, and the substantial SSA promotes rapid charge absorption. The twisted butadiyne molecules serve as active sites for the HER. Their findings underscore the possibility of PDBA-GDY as a functional polymeric material, with its alkyne triple bonds providing accurate regulation over electronic characteristics and microporosity. The tunable assembly facilitates the development of sophisticated non-metallic photocatalysts for solar water oxidation (Fig. 21d).

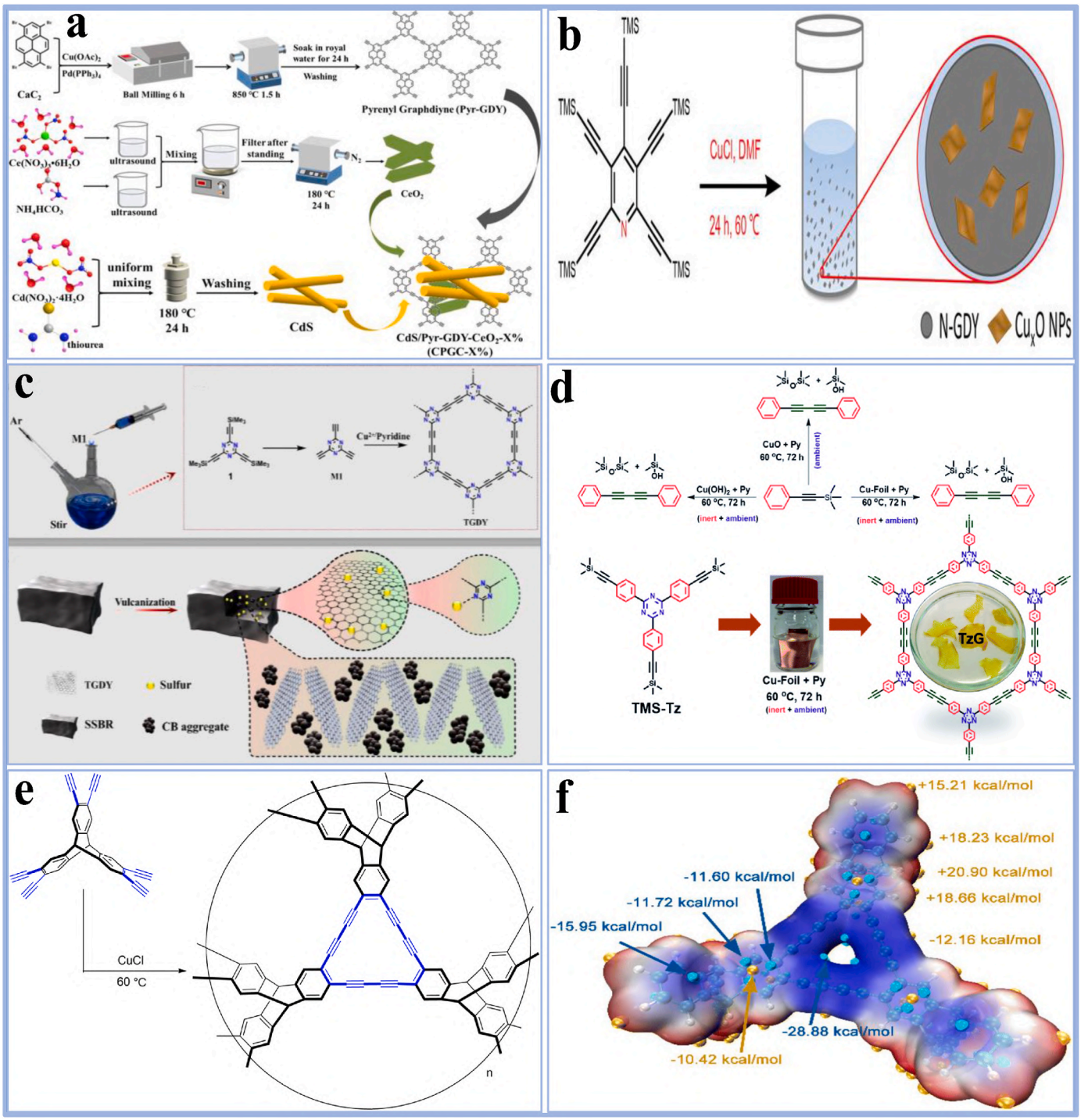

Fig. 22. (a) The synthesis process of Pyr-GDY, CPGC-X%, and CeO_2 [292] Copyright © 2023, American Chemical Society. (b) Schematic illustration of the synthesis of pyridine-based Cu_xO/N-GDY [299] Copyright © 2024, John Wiley and Sons. (c) The preparation process of monomer M1 and TGDY [306] Copyright © 2022, Elsevier. (d) Schematic illustration of TGDY [307] Copyright © 2021, Royal Society of Chemistry. (e, f) The synthesis of G-PTN [313] Copyright © 2022, Royal Society of Chemistry.

3.2.5. *Porphyrin-based GDY*

Porphyrin-based functional units are cyclic organic molecules that may be included in GDY to improve their electrical and photocatalytic characteristics [284]. These units are recognized for their capacity to coordinate metal ions, allowing GDY to demonstrate enhanced catalytic activity and stability [285]. In GDY, porphyrin derivatives enhance the material's capacity to absorb light and promote electron transference operations, rendering it suitable for photocatalytic applications such as WS and CO_2 reduction [286]. Moreover, porphyrins in GDY may provide active sites for reactions, enhancing the material's effectiveness in energy transformation and storage devices [287]. For example, Hao et al. [288] developed two GDY-porphyrin materials, GDY/Por and Por@GDY, through π-π interactions and an in-plane coupling procedure. GDY/Por exhibited enhanced electrochemical efficiency regarding capacity, deficiency, and cycling durability as anodes in LIBs, surpassing Por@GDY. Theoretical studies indicate that this enhancement results from the increased effective interface area in GDY/Por and the incorporation of the porphyrin layer, which promotes interlayer growth and

improves lithium storage capacity. Their results indicate that porphyrins serve as a potential nitrogen-doped material for carbon-derived products (Fig. 21e). Similarly, Niu et al. [289] produced a CuI/Porphyrin-based GDY (PGDY) p-n heterostructure photocathode through the electrodeposition of CuI and the in-situ fabrication of PGDY. The PGDY improves light absorption, whereas the CuI/PGDY heterostructure improves electron-hole pair dissociation and transference. The photocathode demonstrates significant resistance to photodegradation and strong photoelectrochemical (PEC) efficiency. The system has been optimized to develop a sensitive, reproducible, and stable PEC sensor for L-Cys detection, employing the selective Cu-S bonding interaction between L-Cys and Cu^{+} (Fig. 21f).

3.2.6. Pyrenyl-based GDY

The pyrenyl-based functional unit in GDY denotes the inclusion of pyrene, a polycyclic aromatic hydrocarbon, as a functional group inside the GDY framework [287]. The substantial π-conjugation and aromaticity of pyrene boost the electronic characteristics of GDY, establishing a robust basis for charge transference, electron delocalization, and enhanced conductivity [290]. When included in GDY, pyrenyl-groups enhance charge separation and transfer efficiency, rendering the material very appropriate for photocatalysis, energy preservation, and sensor applications [243,291]. The pyrene units enhance the stability and usefulness of GDY, facilitating its interaction with other materials and allowing for the fabrication of composites with customized characteristics for particular purposes [291]. For example, Liu et al. [292] developed the first 2D Pyr-GDY utilizing 1,3,6,8-tetrabromopyrene and CaC_2 via mechanical ball-milling. CdS nanowires were selected as the primary photocatalyst, and Pyr-GDY was combined with CdS to create an S-scheme heterostructure. CeO_2 was incorporated as a cocatalyst in the CdS/Pyr-GDY hybrid to reduce the photocorrosion of CdS. The CdS/Pyr-GDY-10 % hybrid demonstrated a HER rate 4.4 times greater than that of pure CdS and 574.5 times greater than that of pure Pyr-GDY. The HER rate of CdS/Pyr-GDY-10 % reduced after 3 h due to CdS photocorrosion, but the incorporation of CeO_2 markedly mitigated this effect. In-situ XPS verified the establishment of the S-scheme heterostructure between Pyr-GDY and CdS, while fluorescence and electrochemical analyses elucidated the photocatalytic HER process (Fig. 22a).

3.2.7. Pyridine-based GDY

Pyridine-based functional units in GDY denote nitrogen-containing aromatic groups characterized by a nitrogen atom integrated into a six-membered ring framework, exemplified by pyridine [293]. The units significantly enhance the electrical characteristics and sensitivity of GDY [294]. Pyridine groups serve as electron-rich sites that interact with metallic centers or other functional groups [295], enhancing the catalytic properties of GDY in diverse reactions, including electrocatalysis and gas adsorption [296,297]. Pyridinic nitrogen sites strengthen the efficiency of GDY-derived catalysts in nitrogen reduction, oxygen reduction, and ammonia production by supporting charge transference and preserving reaction intermediates [285]. Pyridine units can affect the framework and porosity of GDY, enhancing its suitability for energy conversion and storage applications [298]. For example, Li et al. [299] designed an effective one-pot technique for synthesizing Cu_xO/N-GDY catalysts, characterized by a predominant pyridine-N framework with an 80 % amount of pyridinic N. The integration of pyridinic nitrogen in GDY with Cu_xO resulted in faradaic yields of NH_3 surpassing 85 % in both commercial H-cells and anionic exchange membrane electrolyzers. Their investigation investigated the influence of temperature (25–40 °C), flow field geometry, and nitrate concentration (0.001–1 M) on NH_3 activity and selectivity. At ambient temperature, the catalyst exhibited a faradaic efficiency of 93 % and a yield of 1950 μmol μmol h^{-1} $mgcat^{-1}$ at 3.3 V in 1 M KNO_3, underscoring its promise for industrial-scale applications (Fig. 22b).

3.2.8. Triazine-based GDY

Triazine-based functional units in GDY comprise nitrogen-based heterocycles [300], generally characterized by a three-membered ring framework (C_3N_3), in which nitrogen atoms are integrated into the aromatic system [301]. The units exert a substantial impact on the electronic framework and chemical sensitivity of GDY, particularly in catalytic applications [302]. Triazine groups improve the material's capacity to function as an electron-rich center, thereby promoting electron transference in electrocatalytic reactions such as ORR, HER, and nitrogen fixation [303]. Triazine groups enhance the durability and conductivity of GDY, thereby improving the efficiency of energy preservation and conversion appliances [304]. The triazine moiety enhances the durability of GDY in harsh chemical environments, including photocatalytic reactions, by offering a durable framework that resists degradation [48]. Triazine-derived units improve the catalytic productivity, structural integrity, and electronic characteristics of GDY, rendering it a promising material for various applications in energy and environmental technologies [305]. For example, Sun et al. [306] developed triazine-based GDY (TGDY) through a stirring approach and analyzed its effects on the curing procedure, carbon black (CB) dispersion, and mechanical characteristics in CB/TGDY hybrid-filled solution-polymerized styrene-butadiene rubber (SSBR) composites. These were analyzed in comparison to CB/GO hybrid-filled SSBR composites. The curing procedure was examined using DSC and FTIR, while SEM and TEM were employed to study the distribution of CB. Their findings indicated that TGDY enhanced the curing procedure by decreasing sulfur fission frequency and enhancing cross-linking densities through sulfur interactions. Furthermore, the 2D sheet framework of TGDY improved the distribution of the CB within the SSBR lattice (Fig. 22c). In a similar approach, Kulkarni et al. [307] employed a single-pot approach to synthesize crystallized triazine-based GDY films, achieving thicknesses of up to 3 mm and lateral dimensions of 2–3 cm, utilizing trimethylsilylated alkynes on economical copper foil. This approach integrates on-surface Glaser and Hiyama coupling, facilitating the synthesis of freestanding, organized diyne-bridged polymer films (Fig. 22d).

3.2.9. Triptycene-based GDY

The triptycene-based functional unit in GDY denotes the integration of triptycene [308], a polycyclic aromatic compound characterized by a rigid 3D framework, within the GDY structure [309]. Triptycene's unique design, marked by its rigid and bulky framework, enhances stability and promotes the growth of porous networks [310]. Integrating triptycene units into GDY enhances the material's surface area and porosity, facilitating effective gas adsorption and separation [311]. The triptycene-based functionality improves the selective adsorption of molecules such as CO_2, C_2H_2, and C_2H_4 by GDY, rendering it a promising material for gas storage, separation, and sensing applications [263]. The firm framework of triptycene contributes to the integrity of the GDY network, enhancing its mechanical characteristics and improving the material's efficiency across various applications [312]. For example, Ma et al. [313] developed a 3D GDY-based triptycene network (G-PTN) exhibiting an increased BET surface area of 1046 m^2/g. At 298 K, the gas sorption capacities for CO_2, C_2H_2, and C_2H_4 were measured at 51.5 cm^3/g, 59.6 cm^3/g, and 44.7 cm^3/g, respectively, indicating a significant preference for C_2H_2 compared to C_2H_4. The integration of GDY molecules into selective adsorbents for C_2H_2/C_2H_4 separation presents new opportunities for enhancing the efficiency of gas separation materials. Their research seeks to enhance separation productivity through modifications of pore dimensions and the 3D framework (Fig. 22e and f).

3.3. Bandgap engineering

Bandgap engineering is essential for improving the efficiency of GDY in multiple applications [314]. Bandgap engineering allows for the modulation of intrinsic electronic characteristics, facilitating accurate regulation over the conductivity, optical absorption, and charge carrier

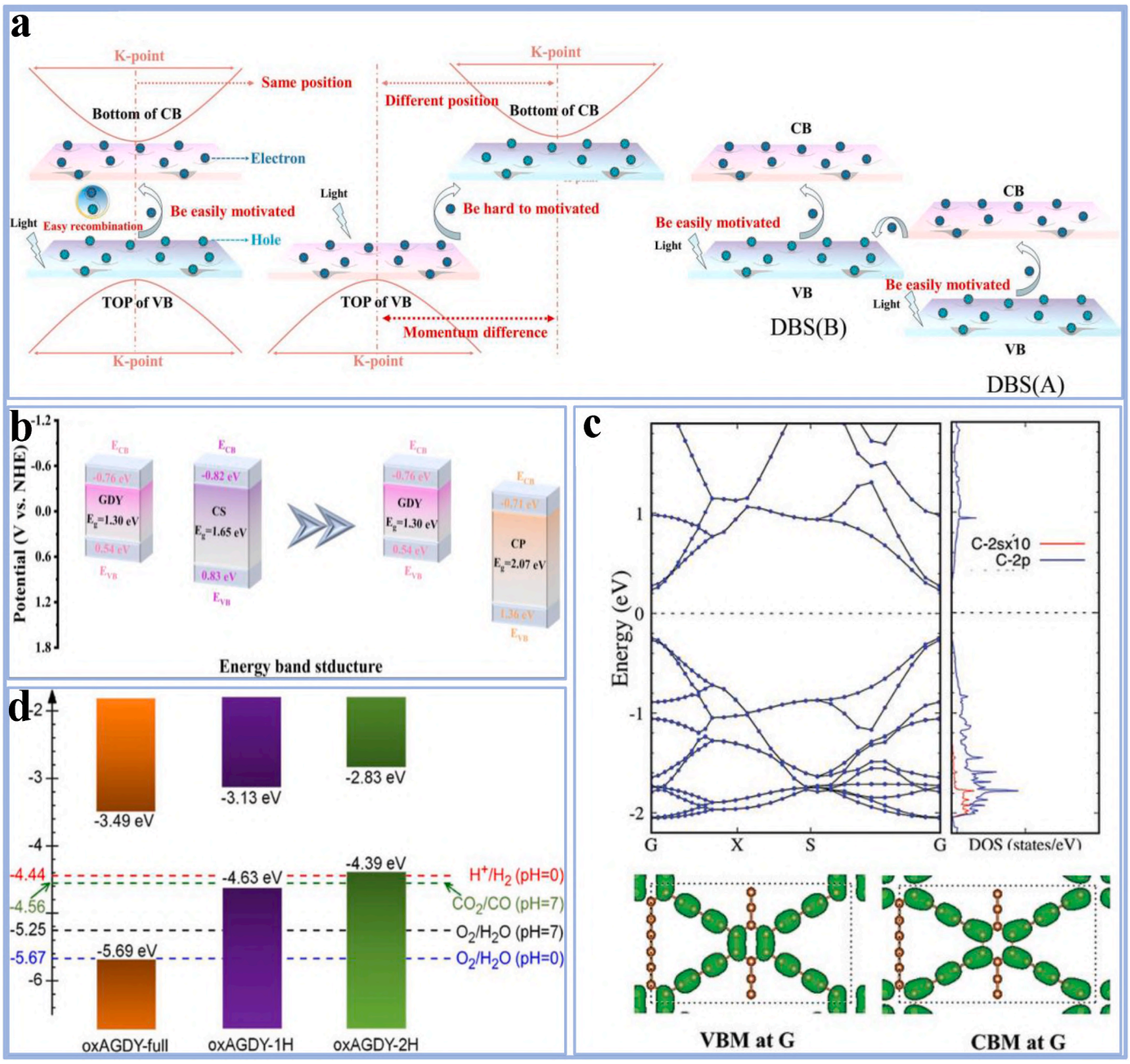

Fig. 23. (a) Schematic illustration of bandgap engineering of GDY/Co_2VO_4 S-scheme heterojunction [320] Copyright © 2024, Elsevier. (b) Energy band structure diagram of CS, GDY, and CP [321] Copyright © 2024, Elsevier. (c) Band structure and projected density of states on the carbon orbitals of GDY [322] Copyright © 2021, John Wiley and Sons. (d) Band edge arrangements of the oxAGDY systems related to their vacuum levels [323] Copyright © 2023, American Chemical Society.

dynamics of GDY [315]. This method can effectively adjust the bandgap of GDY, converting it into a semiconductor or enhancing its metallic properties [316]. This optimization holds significant importance in applications such as photocatalysis, where a suitable bandgap is necessary for effective light absorption and charge transfer [317,318]. In electronic devices, optimizing the bandgap enhances charge carrier mobility and overall device productivity. Bandgap engineering enhances the versatility of GDY, rendering it appropriate for advanced applications in energy conversion, storage, and nanoelectronics [319]. For example, Zhou et al. [320] designed a double direct band gap GDY/Co_2VO_4 S-scheme heterojunction through an immersion approach to improve photochemical hydrogen evolution. Utilizing DFT calculations, the creation of the heterojunction was confirmed, with cobalt (Co) recognized as the most effective active site. The S-scheme heterojunction engineering significantly decreased electron-hole recombination, extended carrier lifetimes, and preserved productive electronic transitions. PDOS analysis indicated that GDY influences the d-band center of cobalt atoms, leading to a decrease in antibonding electron occupancy, an improvement in bonding stability, and an increase in electron state density near the Fermi level, thereby promoting charge migration. Their research offers perspectives on the dynamics of the d-band center and the creation of effective heterojunctions (Fig. 23a). Likewise, Liu et al. [321] investigated bandgap engineering to improve GDY efficiency, concentrating on challenges such as elevated recombination rates of photoelectron-hole pairs and restricted REDOX capacity in individual photocatalysts for water splitting. Phosphate-loaded cadmium sulfide (CP) was developed with an increased bandgap to minimize recombination rates, and it was combined with GDY synthesized through ball

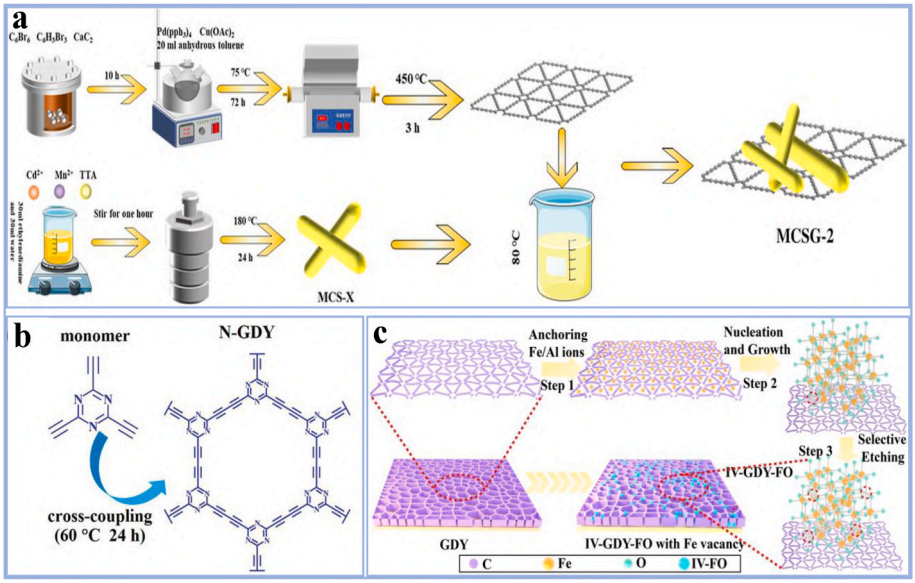

Fig. 24. (a) Synthetic process of $Mn_{0.3}Cd_{0.7}S$/GDY-X (MCSG-X) MCSG-2 [327] Copyright © 2023, John Wiley and Sons. (b) Synthetic process of N-GDY [328] Copyright © 2021, John Wiley and Sons. (c) Synthetic process of IV-GDY-FO [329] Copyright © 2023, John Wiley and Sons.

milling. GDY's elevated conductivity and extensive surface area diminished CP aggregation and revealed additional active sites. The CP-GDY combination established an S-scheme heterojunction, enhancing interfacial charge migration, carrier separation, and reduction capacity. Their research presents a method for the development of effective GDY-derived heterojunction photocatalysts (Fig. 23b). In addition, Li et al. [322] showed that adjusting the bandgap of GDY through hydrogen substitution (H-GDY) markedly improves its photochemical efficiency. GDY possesses a narrow bandgap of 1.1 eV, which is inadequate for optimal band alignment with semiconductors. In contrast, H-GDY demonstrates an enhanced bandgap of approximately 2.5 eV, along with advantageous conduction and valence band edges. The hybridization of TiO_2 with H-GDY creates a heterojunction that improves photochemical H_2 generation by a factor of 1.35 under UV–visible light and by a factor of four under visible light, relative to GDY/TiO_2. This enhancement is ascribed to improved band alignment and effective charge carrier separation (Fig. 23c). Moerover, Zhang et al. [323] used DFT computations to study 2D GDY derivatives containing imino groups. The structural strength, geometric arrangements, and mechanical characteristics of these derivatives were confirmed. The bandgaps of imino-GDY structures at the G0W0 level range from 1.50 to 2.20 eV, making them suitable for visible light absorption. The derivatives demonstrate increased dispersive band edges relative to other GDY variants (e.g., F-, H-, and CN-GDYs), leading to enhanced charge carrier motion. Their band edge arrangements facilitate photochemical water splitting and CO_2 reduction, indicating that imino group substitution significantly improves GDY's solar energy harvesting capabilities (Fig. 23d).

3.4. Defect engineering

Defect engineering is essential for improving the efficiency of GDY through the introduction of specific defects in its framework [324]. Defects, including vacancies, dopants, and edge alterations, can substantially influence the electronic, optical, and chemical characteristics of GDY [325]. Defect manipulation allows for bandgap tuning, enhancing light absorption and charge carrier mobility in photochemical processes [326]. Defects generate active sites that improve catalytic activity, thereby allowing procedures such as hydrogen evolution and CO_2 reduction [6]. Defect engineering enhances interfacial charge separation and transference in heterojunction systems, thereby increasing the overall productivity of GDY-derived devices in energy transformation and storage applications [72]. For example, He et al. [327] revealed that the engineering of surface defects markedly improves photochemical efficiency through the introduction of sulfur vacancies in $Mn_{0.3}Cd_{0.7}S$ nanorods. The regulated inclusion of thioacetamide resulted in the formation of vacancies, which induced dislocation phenomena and enhanced hydrogen evolution behavior by a factor of 17 relative to standard $Mn_{0.3}Cd_{0.7}S$. The sulfur-vacancy-enriched substance, when combined with GDY to create an S-scheme heterojunction, demonstrated improved light absorption, enhanced electron affinity, decreased electron-transference resistance, and accelerated photoexcited electron migration. The dual catalyst enabled effective spatial separation of electrons and holes, thereby optimizing electron accessibility for hydrogen evolution reactions. DFT calculations verified the presence of vacancies, the composition of the bandgap, charge distribution, and photocatalytic mechanisms, offering significant insights into defect-engineered catalysts (Fig. 24a). Similarly, Fan et al. [328] examined defects at grain boundaries in hybrid perovskite films, which adversely affect optoelectronic characteristics and contribute to hysteresis and instability. The incorporation of pyridinic nitrogen-loaded graphdiyne (N-GDY) has been proposed to address these defects. The pyridinic nitrogen atoms and acetylenic linkages in N-GDY efficiently inhibit deep-level trap states, including Pb–I antisite imperfections and under-coordinated Pb atoms, thereby reducing non-radiative recombination. The 2D framework of N-GDY facilitates spatial confinement and electrostatic repulsion, thereby reducing halide ion migration. Theoretical analyses validated the delocalization of charge density and the elevation of ion migration energy barriers. Their research emphasizes the capability of chemically modified N-GDY to improve the efficiency of polycrystalline perovskite energy conversion appliances (Fig. 24b). Furthermore, Gao et al. [329] created a GDY/ferroferric oxide heterojunction (IV-GDY-FO) to improve the efficiency of LIBs anodes through the modulation of iron cationic vacancies (IV) and the electronic framework of the materials. GDY inhibits the agglomeration of Fe_3O_4, enhances high valence Fe states, and decreases system energy. Iron vacancies influence charge dispersion, boost electronic transfer, expand lithium-ion diffusion pathways, and reduce Li^+ diffusion barriers, leading to notable pseudocapacitive behavior and improved lithium-ion storage capacity. The tailored IV-GDY-FO electrode exhibited a capacity of 2084.1 $mAhg^{-1}$ at 0.1C, notable cyclic stability, and a capacity of 1057.4 $mAhg^{-1}$ at 10C, indicating its potential for efficient LIBs

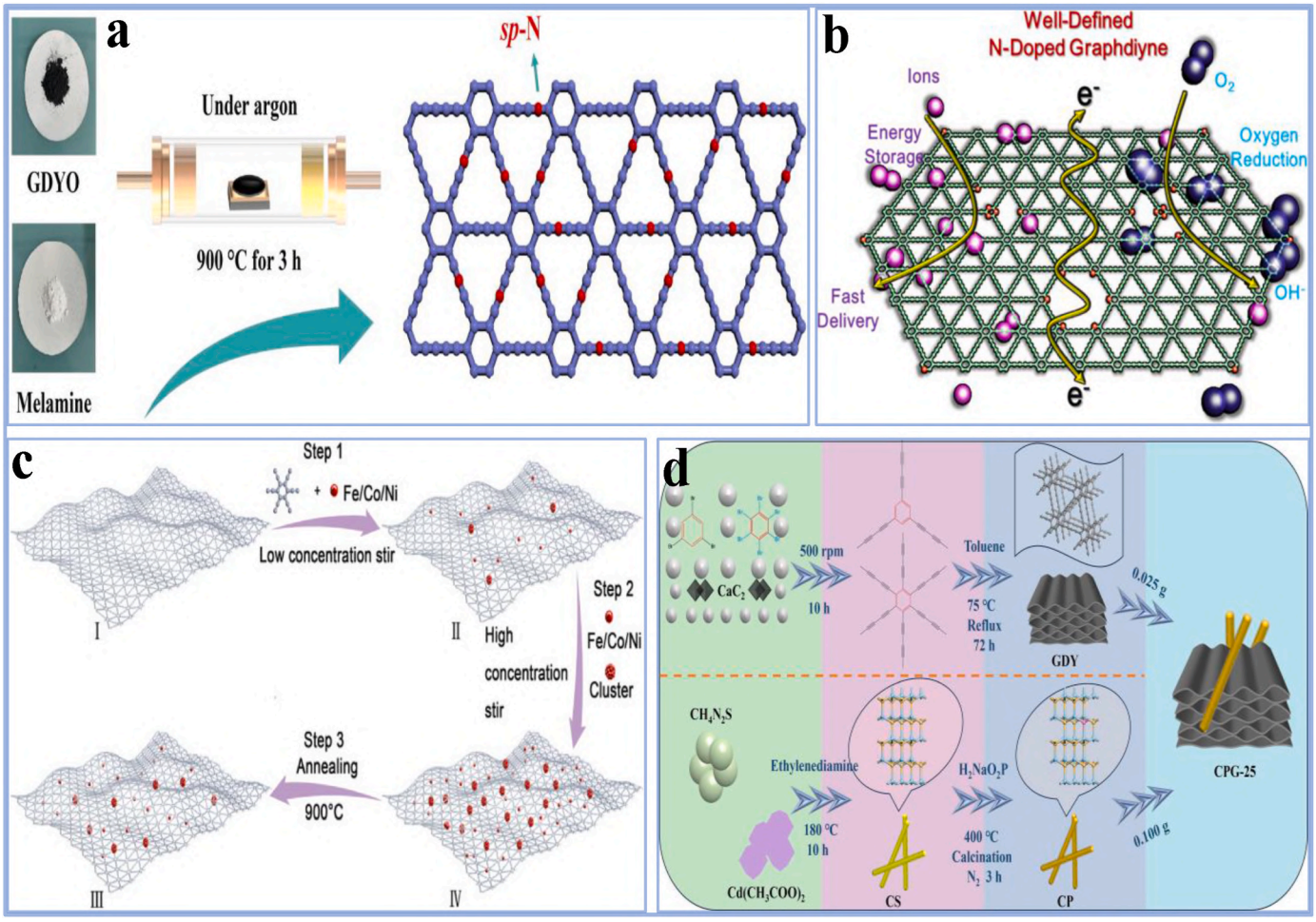

Fig. 25. (a) Synthesis process of NUGDY [333] Copyright © 2022, Elsevier. (b) Schematic illustration of well-defined N-doped GDY route [160] Copyright © 2018, Elsevier. (c) Synthesis process of Co-GDY [334]. (d) Synthetic process of phosphorus-doped CdS/GDY S-scheme heterojunction [321] Copyright © 2022, Elsevier.

(Fig. 24c).

3.5. Doping

Doping significantly enhances the efficiency of GDY by modifying its electronic, structural, and chemical characteristics [210]. Doping with heteroatoms or functional units modifies the bandgap, charge carrier flexibility, and surface reactivity of GDY, enhancing its suitability for particular applications [228]. Nitrogen or phosphorus doping enhances conductivity and catalytic activity, whereas dopants such as boron or sulfur optimize visible light absorption and charge separation in photocatalysis [330,331]. Doping can create active sites for reactions, decrease recombination rates of photoexcited electron-hole pairs, and enhance overall durability [332]. The alterations enhance the applicability of GDY in energy preservation, transformation, and photochemical processes. For example, Yan et al. [333] synthesized sp-hybridized nitrogen-doped ultrathin graphdiyne (NUGDY) via the carbonization of GDY oxide and melamine. NUGDY maintains the folded, wrinkled 2D shape of GDY while incorporating a 3D porous system, thereby increasing its surface area and ability for analyte loading. Nitrogen doping enhances GDY imperfections, resulting in a boost in active sites, conductance, and electrochemical efficiency. NUGDY, when modified onto a carbon ionic liquid electrode, exhibited remarkable sensitivity, achieving a lower detection limit of 2.3 nM for 6,7-dihydroxycoumarin (6,7-DHC), in addition to demonstrating excellent anti-interference and durability. Their research emphasizes NUGDY's capability for the detection of sensitive drug molecules in real samples (Fig. 25a). Similarly, Shang et al. [160] introduced a method for the fabrication of N-GDY nanojunctions, allowing for precise control over nitrogen patterns (pyridinic N and triazine-like N clusters), nitrogen content, and porosity. The characteristics were characterized by nitrogen absorption and neutron pair dispersion function evaluation. The N-GDY exhibited significant efficiency in two-electrode supercapacitors, attaining a specific capacitance of 250 F g^{-1}, an energy density of 8.66 Wh kg^{-1}, and a power density of 19.3 kW kg^{-1}. N-configurations elucidate nitrogen's function in facilitating the oxygen reduction process in sp^2 carbons. Their method presents new opportunities for GDY uses in energy sectors (Fig. 25b). Likewise, Li et al. [334] investigated the synthesis of GDY-derived magnetic semiconductors via doping with transition metals such as Fe, Co, and Ni. Co-doped GDY (Co-GDY) exhibited the strongest ferromagnetic characteristics, featuring a Curie temperature exceeding room temperature and an easy magnetization characteristic with a coercive field of 78 Oe at 300 K. Spin-polarized DFT computations indicate that the pronounced ferromagnetism arises from substantial local magnetic moments due to Co doping. The minimal doping levels maintained the integrity of the material's bandgap. Their research presents an approach for enhancing doping elements to enhance carbon-derived semiconductors for applications in spintronics and information technology (Fig. 25c). Furthermore, Liu et al. [321] incorporated phosphorus (P) into carbon spheres (CS) through higher-temperature calcination, resulting in CP with improved photocatalytic characteristics. P-doping decreased the recombination rate of photoexcited electron-hole pairs and altered the band framework. GDY was integrated into CP through a solvothermal approach, enhancing the

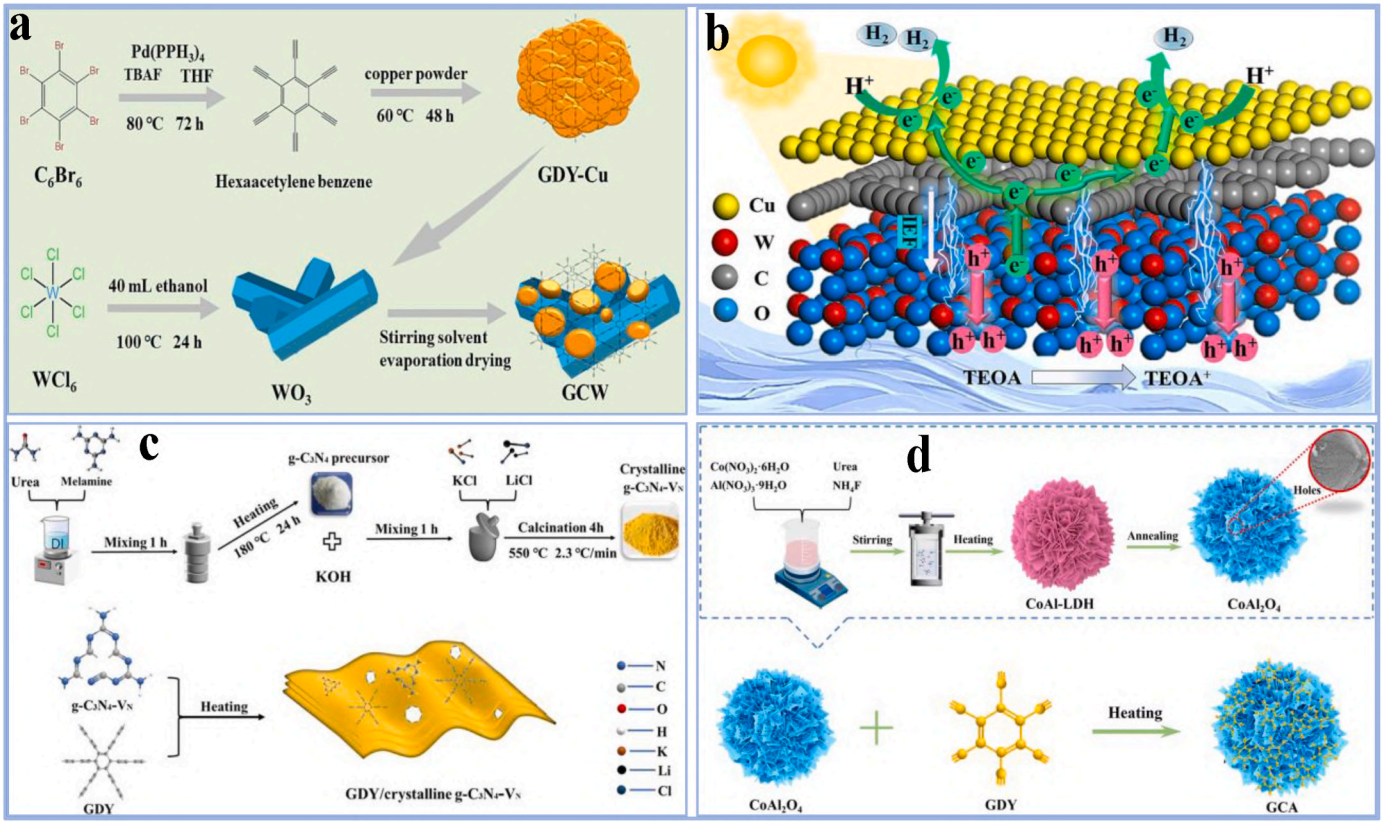

Fig. 26. (a) Synthetic process of GCW heterojunction; (b) Proposed photocatalytic HER mechanism of GDY-Cu/WO_3 heterojunction [339] Copyright © 2023, Elsevier. (c) Synthetic process of crystalline g-C_3N_4-V_N and GDY/crystalline g-C_3N_4-V_N [340] Copyright © 2023, Elsevier. (d) Synthetic process of 2D/3D GDY/-$CoAl_2O_4$ heterojunction [341] Copyright © 2024, Royal Society of Chemistry.

specific surface area and boosting the availability of active sites for hydrogen evolution while maintaining the higher-activity (100) crystal surface. The formation of an S-scheme heterojunction between CP and GDY, facilitated by P doping, enhanced carrier separation and preserved robust redox capabilities, thereby improving hydrogen evolution efficiency (Fig. 25d).

3.6. Formation of heterojunctions

The emergence of heterojunctions is essential for improving the efficiency of GDY through the optimization of charge separation and transference procedures [335]. The incorporation of GDY with other semiconductors or materials to create heterojunctions facilitates effective spatial separation of photoexcited electron-hole pairs, thereby decreasing recombination rates and enhancing overall photochemical or photoelectrochemical efficiency [122,227]. This is accomplished via customized band alignment, enabling directional electron transport while maintaining robust redox potential [336]. Heterojunctions, including S-scheme and type-II structures, offer alternative pathways for electron transfer, thereby improving conductivity, light absorption, and catalytic efficiency [337]. The enhancements render GDY-derived heterojunctions particularly operational for hydrogen evolution, pollutant degradation, and energy transformation applications [338]. For example, Jin et al. [339] developed the idea that the creation of heterojunctions serves as an effective approach to improve solar-based photochemical water decomposition. A GDY-driven composite catalyst (GDY-Cu) was developed, incorporating an ohmic contact surface, and combined with WO_3 nanorods exhibiting surface imperfections to create an S-scheme heterostructure. The dual-junction creation markedly enhanced electron transference productivity due to the built-in electric field at the junction, resulting in a hydrogen evolution rate 12.2 times greater than that of pure GDY. Comprehensive investigations utilizing in-situ XPS and DFT validated the mechanisms of charge transference and the dynamics of photo charge migration. Their research emphasizes the integration of ohmic and S-scheme heterostructures to improve GDY-driven photochemical systems, presenting a new creation approach for advanced photocatalysts (Fig. 26a and b). Similarly, Ding et al. [340] fabricated a 2D-2D S-scheme heterojunction by integrating GDY with nitrogen-defective-enrich g-C_3N_4 nanosheets (g-C_3N_4-V_N) to improve photochemical OWS. The synthesis of GDY involved the cross-coupling of hexaethynylbenzene, whereas g-C_3N_4-V_N was prepared through an alkali-molten salt technique. The design of the heterojunction has been verified via DFT calculations, indicating enhanced charge density and photoexcited carrier separation. The tailored catalyst (CNG-25) demonstrated a hydrogen HER of 17.87 μmol h^{-1}, representing a 25.23-fold enhancement relative to GDY alone. The system, when loaded with Co_3O_4 and Pt cocatalysts, accomplished OWS, yielding H_2 and O_2 at rates of 0.48 μmol h^{-1} and 0.24 μmol h^{-1}, respectively. Their research presents a clear approach for the fabrication of GDY-derived S-scheme heterojunctions aimed at improving photochemical efficiency (Fig. 26c). Furthermore, Hao et al. [341] fabricated a hierarchical S-scheme heterojunction in 2D/3D form by integrating GDY nanosheets with porous $CoAl_2O_4$ nanoflowers (GCA). GDY was produced through cross-coupling, whereas $CoAl_2O_4$ was obtained from CoAl-LDH. The distinctive 3D porous design improved active sites, increased light absorption, and diminished GDY aggregation. The tailored GCA-15 demonstrated a photochemical HER rate of 5009.28 mmol g^{-1} h^{-1} under visible light, which is 4.78 times greater than that of pristine $CoAl_2O_4$. This efficiency arises from the synergistic impacts of the S-scheme heterojunction and hierarchical framework. DFT analyses verified electron transference from GDY to $CoAl_2O_4$, underscoring an effective approach for the creation of GDY-derived photocatalysts

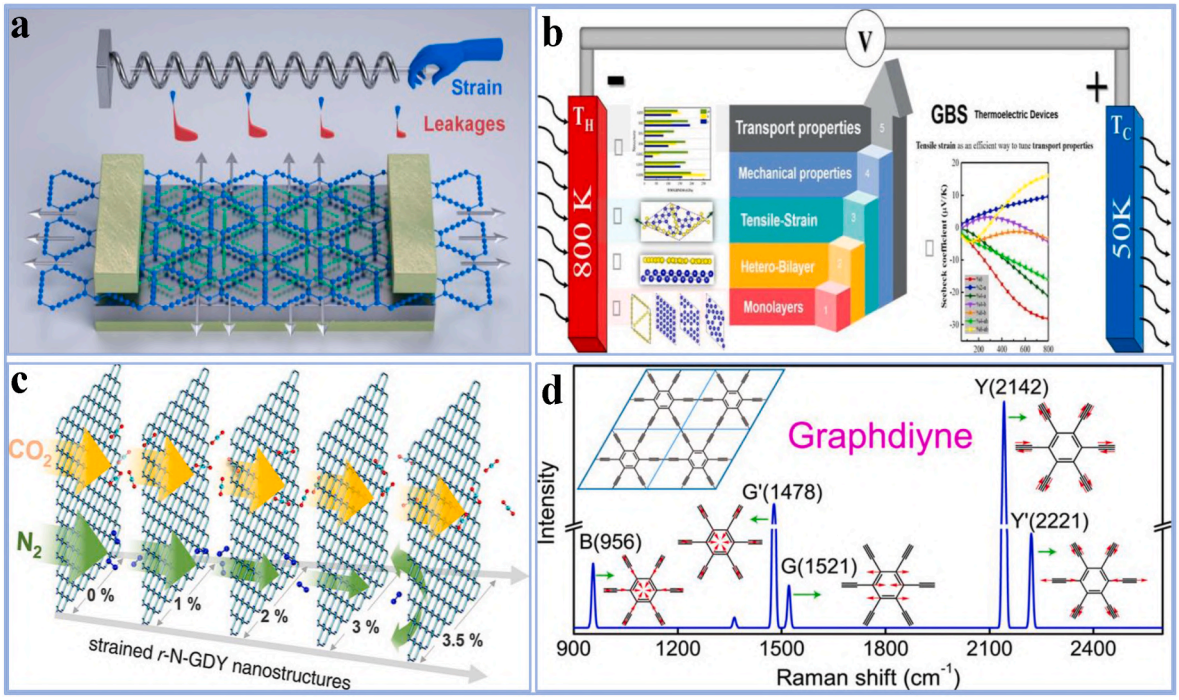

Fig. 27. (a) Schematic illustration of strain engineering impact of GDY-FET [346] Copyright © 2021, Elsevier. (b) Schematic illustration of strain engineering impact of GDY/Borophene hetero-bilayers [347] Copyright © 2023, Elsevier. (c) Schematic illustration of strain engineering impact of r-N-GDY monolayers [348] Copyright © 2024, American Chemical Society. (d) Schematic illustration of strain engineering impact of GDY [65] Copyright © 2016, American Chemical Society.

(Fig. 26d).

3.7. Strain engineering

Strain engineering is essential for improving the efficiency of GDY through the alteration of its fundamental characteristics and electronic composition [342]. Strain application can modify bond angles, bond lengths, and the overall lattice structure of GDY, thereby adjusting its bandgap and charge carrier mobility [343]. This optimization results in optimized electron transfer, boosted light absorption, and superior interaction with reactants in catalytic applications [97]. Strain-based alterations can enhance catalytic site activation, stability under operational conditions, and charge separation and transference, thereby increasing the efficiency of GDY for applications such as photocatalysis, energy storage, and electrocatalysis [344,345]. For example, Sang et al. [346] conducted first-principles calculations indicating that GDY is a promising candidate for sub-10 nm field-effect transistors (FETs) owing to its superior 2D semiconductor characteristics. Strain engineering markedly improves GDY-FET efficiency by decreasing leakage currents by 2–4 orders of magnitude and enhancing scalability. Pure GDY-FETs demonstrate ON currents of 1904/1264 μA/μm at 7.3/8.8 nm nodes, whereas strain-engineered GDY-FETs can be scaled down to 6.1 nm, achieving ON currents ranging from 1335 to 1424 μA/μm, in accordance with the International Technology Roadmap for Semiconductors standards. Moreover, a strain of 8–10 % leads to a reduction in subthreshold swing by 15–37 %, facilitating enhanced efficiency and reduced power consumption (Fig. 27a). Similarly, Jalili et al. [347] examined the influence of strain on the thermoelectric characteristics of GDY/Borophene hetero-bilayers through DFT and transport models. Bilayer construction improves mechanical strength, specifically ultimate stress, and Young's modulus, particularly in GBS_0 under equibiaxial strain. Temperature-based analyses demonstrate that strain serves as an effective mechanism for modulating thermoelectric properties, influencing power factor, electrical and thermal conductivity. The strain affects the Seebeck impact, resulting in either positive or negative parameters depending on the mode of strain. Their research underscores the effectiveness of strain engineering in enhancing thermoelectric device performance (Fig. 27b). Furthermore, Wang et al. [348] investigated the efficiency of rhombic N-GDY (r-N-GDY) monolayers for the separation of CO_2 and N_2 through first-principles computations and molecular dynamics modeling. The usage of uniaxial tensile strain in the zigzag direction improved separation productivity. At strains of 3–3.5 %, the membrane demonstrated ultrahigh CO_2/N_2 selectivity (1.4×10^3 to 2.9×10^4) and elevated CO_2 permeance (1.3×10^{-4} to 1.3×10^{-3} mol m^{-2} s^{-1} Pa^{-1}), attributed to enhanced nanopore confinement of N_2 molecules. Calculations of energy barriers indicated that CO_2 exhibits lower barriers (19.3 kJ/mol) than N_2 (47.3 kJ/mol) at a strain of 3.5 %. The results indicate that r-N-GDY serves as a strain-tunable, advanced material suitable for renewable gas separation technologies (Fig. 27c). Moreover, Zhang et al. [65] examined the Raman spectra of graphyne and GDY under mechanical strain through group theory and first-principles computations. The G bands in graphyne and GDY exhibited greater softness compared to those in graphyne, acting as production fingerprints. A unified model was developed to elucidate Raman spectral changes under uniaxial and shear strains. Doubly deteriorate modes separate into two branches when subjected to strain, exhibiting red-shifting under uniaxial strain, whereas one mode red-shifts and the other blue-shifts under shear strain. The splitting impact was observed to be double higher under shear strain than under uniaxial strain (Fig. 27d). A comprehensive evaluation of the several synthesis strategies used for the synthesis of GDY is shown in Table 1. It emphasizes the distinct attributes and challenges of each approach, notably addressing the challenges related to the scalability of these strategies for extensive production. The obstacles might include poor yield, difficulties in regulating the shape and consistency of the synthetic material, and the complex nature of regularly growing the synthesis technique at a commercial level.

4. Dimensionality of GDY

The dimensionality of GDY greatly impacts its properties and applications. Quantum dots/zero-dimensional graphdiyne (QD/0D-GDY)

Table 1
The synthesis methods for GDY, including their challenges in large-scale production.

Synthesis method	Description	Challenges in large-scale production
On-surface synthesis [172,349,350]	GDY synthesis on metallic or semiconductor surfaces using CVD.	Large-area film transfer issues. Increase uniformity on large substrates. Control of airflow and temperature is expensive.
Top-down methodology [351–353]	GDY is etched or cleaved from graphene.	Reduced yield and efficiency from incomplete cleavage. Minimal size and structural control. Insufficiently scalable.
Explosion methodology [211, 305,354]	Fast thermal breakdown or explosions of carbon precursors yield GDY.	Uncontrollable technique causes consistency and quality issues. Substantial safety risks. Hard to manage size and shape.
Wet chemistry [49, 355,356]	Chemical processes in the liquid state polymerize monomers into GDY.	Trouble controlling monomer dissolution. Poor scalability outputs. Problems with uniformity.
Cu-surface-mediated synthesis [38,357, 358]	Polymerizing carbon precursors on copper yields GDY.	Consistent GDY layers on large copper surfaces are complicated. Ensuring interface stability via synthesis is hard.
Absorption of guest molecules [226, 359,360]	Polymerizing organic molecules on a surface yields GDY.	Poor substrate contacts limit scaling and yields. Inadequate large-scale repeatability. Problems with homogeneous absorption and polymerization.
Hydrogenation [361–363]	Hydrogenating GDY improves durability and electrical qualities.	Large energy needs. Massive sample regulation issues. Excessive hydrogenation may damage characteristics.
Fluorination [351, 364,365]	Fluorination adds durability to GDY.	Structural degradation concern. Problems regulating fluorine replacement. Qualities change with scalability.
Metal decoration [260,366,367]	GDY is obtained and coated with metallic atoms for catalysis.	Regulating metallic atom dispersion on GDY is difficult. Trouble sustaining consistency and homogeneity in enormous-scale designing.
Template-based Synthesis [120, 368,369]	Synthesis of GDY uses templates to regulate size and form.	Hard to remove the template. Uncertain template processing. Intricate elimination hinders scalability.

hybrids combine QDs' tunable properties with 0D-GDY's charge separation and energy transfer capabilities, enhancing performance in photocatalysis, energy storage, and bioimaging. One-dimensional (1D) GDY nanowires are promising for advanced electrical and optoelectronic systems with their semiconductor nature and high conductivity. Two-dimensional (2D) GDY excels in optoelectronics and biomedical applications due to its high charge transfer capabilities and large surface area, making it effective in photodetectors and drug delivery systems. Three-dimensional (3D) GDY stands out for its extensive applications, including water filtration, catalysis, and energy storage, due to its large surface area, mechanical strength, and unique electronic properties. Overall, while 1D and 2D GDY have specialized uses, 3D GDY offers the most diverse and impactful potential across multiple fields. The details of different dimensionalities of GDY are given in this section.

4.1. QDs/0d GDY

QD/0D-GDY hybrids constitute a sophisticated category of nanomaterials that integrate the unique characteristics of QDs with the specific properties of 0D GDY [6]. QDs are distinguished by their adjustable optical and electronic characteristics resulting from quantum confinement impacts, demonstrating significant photoluminescence productivity and emission that varies with size [370,371]. The integration of 0D-GDY, a 0D allotrope of GDY with sp-HCAs and discrete nanoscale frameworks, results in a hybrid that exhibits improved charge separation, effective energy transference, and synergistic interactions between the components [71]. This combination results in enhanced characteristics, such as increased catalytic activity, enhanced light absorption, and exceptional charge mobility [49]. QD/0D-GDY materials exhibit significant potential for use in photocatalysis, energy preservation, optoelectronics, and bioimaging, as the combination of quantum confinement and molecular-level interactions improves efficiency beyond that of the separate components [117]. For example, Deng et al. [372] presented the creation of an effective and environmentally friendly $ZnCo_2O_4$ QDs/GDY (ZCOG) S-scheme heterojunction aimed at improving photochemical efficiency. The ZCOG heterojunction was developed using a hydrothermal process, with $ZnCo_2O_4$ QDs produced by calcination and GDY nanosheets obtained through a reduction-elimination process (Fig. 28a). The photocatalyst produced a maximum HER rate of 2472.80 μmol g^{-1} h^{-1}, exceeding the individual efficiency of $ZnCo_2O_4$ QDs and GDY by factors of 30.75 and 10.84, respectively. The increased activity is due to the firmly coupled S-scheme heterojunction, which promotes effective charge separation and transference while reducing carrier recombination. The quantum size impact of $ZnCo_2O_4$ QDs boosts the electronic bandgap, enhancing the energy levels of electrons and holes. SEM and TEM analyses demonstrated the morphology of GDY, $ZnCo_2O_4$ QDs, and the ZCOG-5 composite. GDY demonstrated a 2D lamellar stacking framework that facilitates the distribution of QDs, enabling the development of 0D heterojunctions and improving charge separation and migration. The ZCOG-5 composite maintained the lamellar framework of GDY, with $ZnCo_2O_4$ QDs uniformly distributed on its surface. TEM analysis verified the nanometer-scale dimensions of $ZnCo_2O_4$ QDs, measuring 3.25–4.25 nm in diameter, and their strong attachment to GDY, resulting in a stable interface. HRTEM revealed lattice spacings associated with the (311) and (400) crystal planes of $ZnCo_2O_4$ QDs, as well as amorphous GDY regions (Fig. 28b−e). Their work presents a promising method for the development of advanced GDY-derived photocatalysts. Similarly, Ahmed et al. [373] showed the hydrothermal production of fluorescent GDY QDs from GDY sheets, exhibiting their distinct fluorescence and nanozymatic characteristics. GDY QDs demonstrate peroxidase-shaped activity, facilitating the oxidation of H_2O_2 and allowing for the sensitive detection of H_2O_2 (LOD: 0.13 μM) and dopamine (LOD: 8.65 μM). The UV–vis and fluorescence peaks are observed at 395 nm and 450 nm, respectively (Fig. 28f). The TEM analysis indicates that GDY possesses a multilayer sheet framework, exhibiting a diffraction pattern at 0.365 nm. Upon conversion to QDs, the size reduces substantially to an average of 2–5 nm, while maintaining a similar lattice framework to the original GDY. This indicates that most GDY QDs are directly developed from GDY and maintain their internal lattice features (Fig. 28g and h). Their findings indicate that GDY QDs serve as exciting enzyme-mimicking nanocrystals for the development of advanced fluorescence and colorimetric biosensors. Furthermore, Bahari et al. [374] fabricated a ratiometric fluorescence resonance energy transference (FRET) assay utilizing GDQDs for the sensitive and specific detection of microRNA-21 (miRNA-21). GDYQDs produced through a solvothermal method demonstrate uniform size, adjustable emission peaks, and satisfactory crystallization (Fig. 28i). GDYQDs, modified

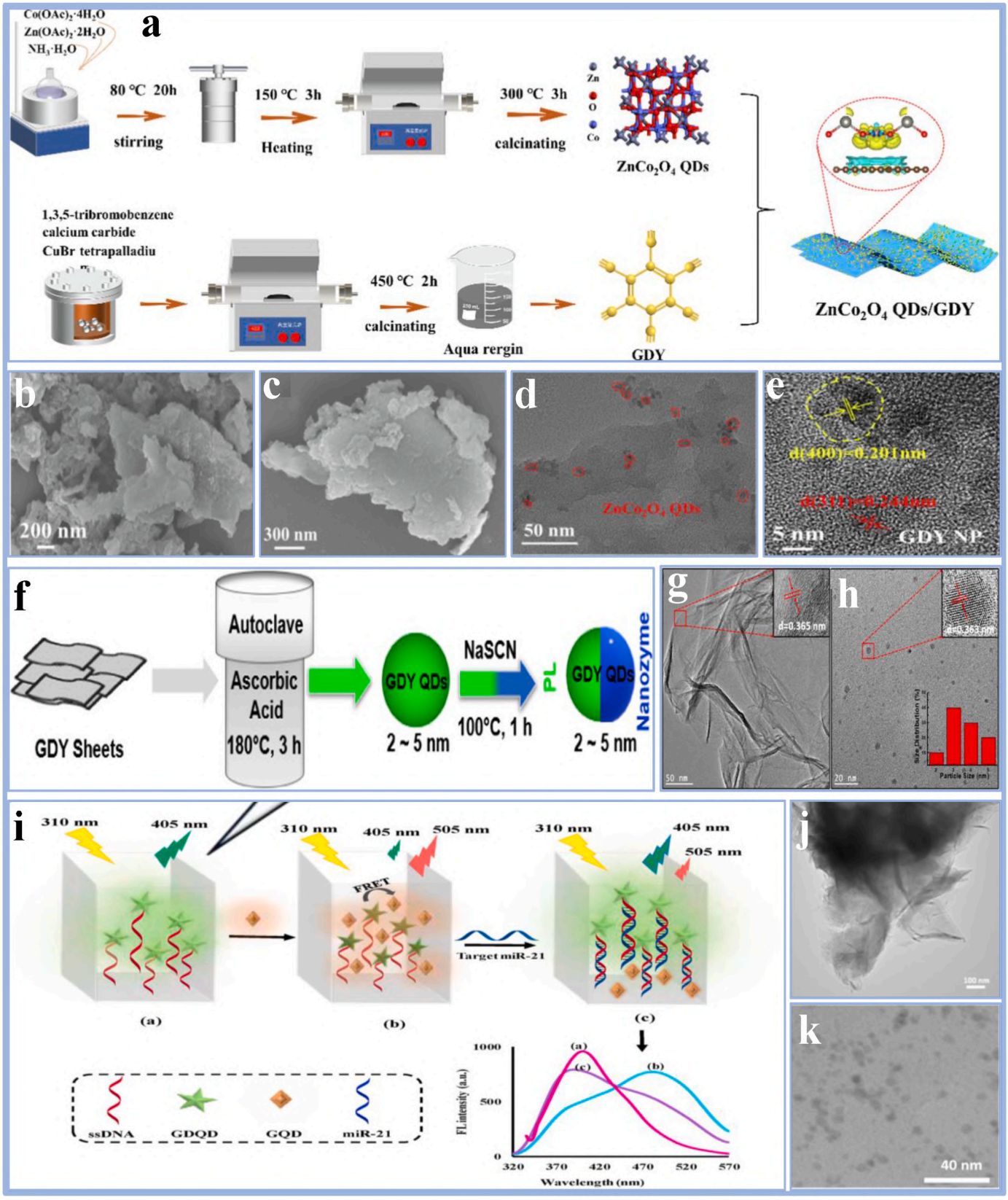

Fig. 28. (a) Synthetic process; (b, c) SEM; (d) TEM; (e) HRTEM of ZCOG [372] Copyright © 2024, Elsevier. (f) Synthetic process; (g, h) TEM of GDY QDs and surface modification [373] Copyright © 2023, American Chemical Society. (i) Synthetic process; (j, k) TEM of GQDs and GDYQDs [374] Copyright © 2021, Elsevier.

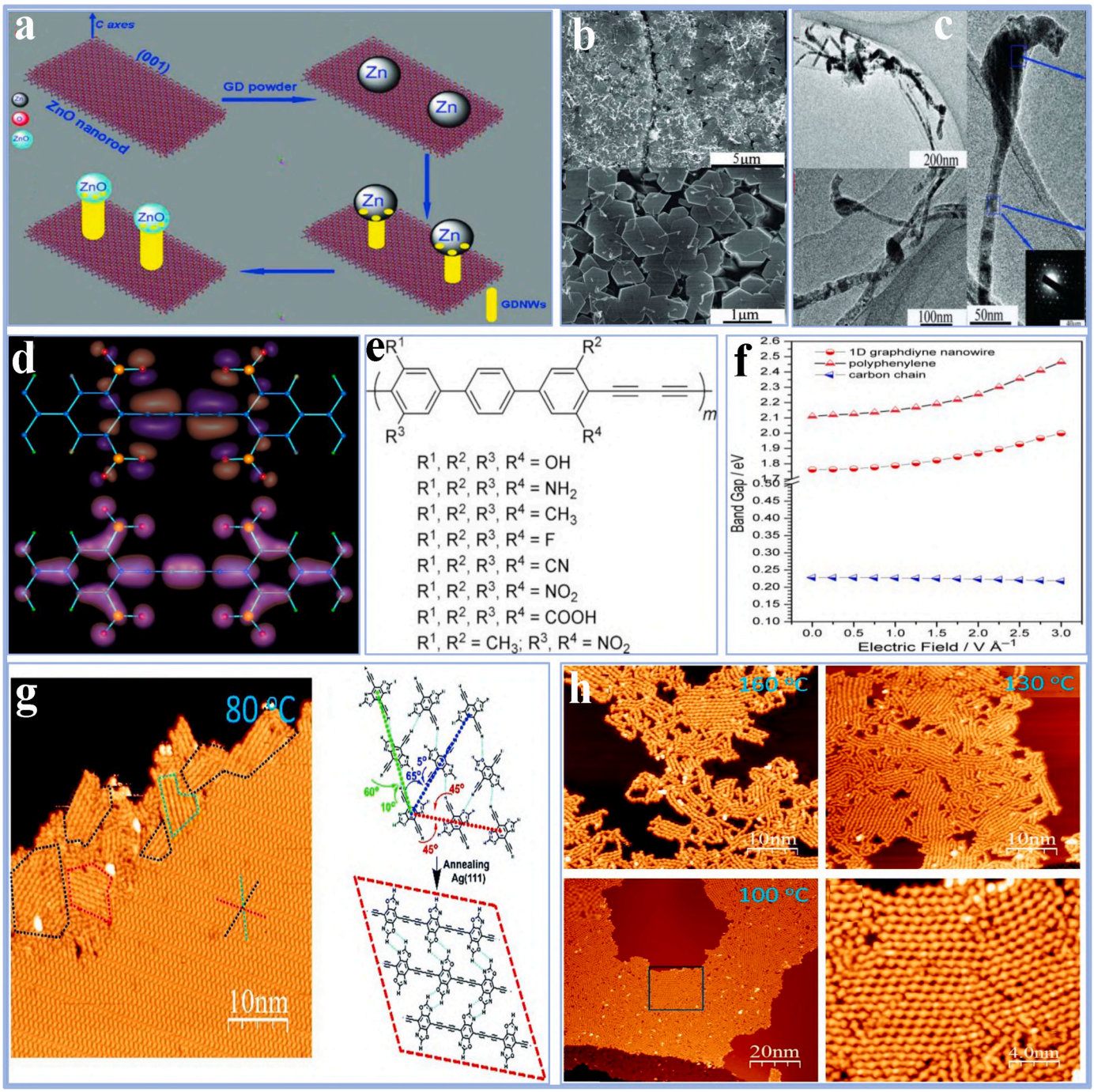

Fig. 29. (a) Schematic illustration of the synthesis; (b) SEM; (c) TEM of 1d GDY nanowires [383] Copyright © 2012, Royal Society of Chemistry. (d) The synthesized 1D extended GDY nanowire; (e) 1D extended GDY nanowire with chemical formulas; (f) Bandgap engineering of 1D extended GDY nanowires [384] Copyright © 2015, John Wiley and Sons. (g) Schematic illustration of the synthesis; (h) SEM analysis of 1D GDY DEBBA [385] Copyright © 2019, Royal Society of Chemistry.

with a DNA probe, exhibited strong fluorescence at 405 nm, which was suppressed by graphene DQs (GQDs) through FRET, resulting in a new fluorescence signal at 505 nm. The existence of miRNA-21 resulted in a higher donor-acceptor distance during hybridization with the GDYQDs-DNA probe, leading to the recovery of GDYQD fluorescence. The assay exhibited a detection range from 5 pM to 200 nM, with a detection limit of 0.5 pM, effectively identifying miRNA-21 in human serum and MCF-7 cell lines. Furthermore, the low cytotoxicity of GDYQDs enabled multicolor imaging of MDA-MB231 cancer cells. TEM characterization indicated that the as-synthesized GDY demonstrated a uniform, continuous microstructure characterized by layered accumulation. In contrast, GDYQDs, produced by fragmenting GDY nanosheets, exhibited a hexagonal carbon network with a near-spherical morphology and an average size of 4–6 nm. The analysis of optical characteristics was conducted using UV–vis and photoluminescence (PL) spectra. GDY displayed an absorption band at 305 nm, while GDQDs demonstrated increased absorption intensity at this wavelength, which is ascribed to the n−π* transition of C–O bonds. GDQDs exhibited excitation-dependent fluorescence emission across a wavelength range of 200–370 nm (Fig. 28j and k). Their research indicated that the low cytotoxicity and superior efficiency of GDYQDs as fluorescence probes render them extremely intriguing for the development of sensitive and

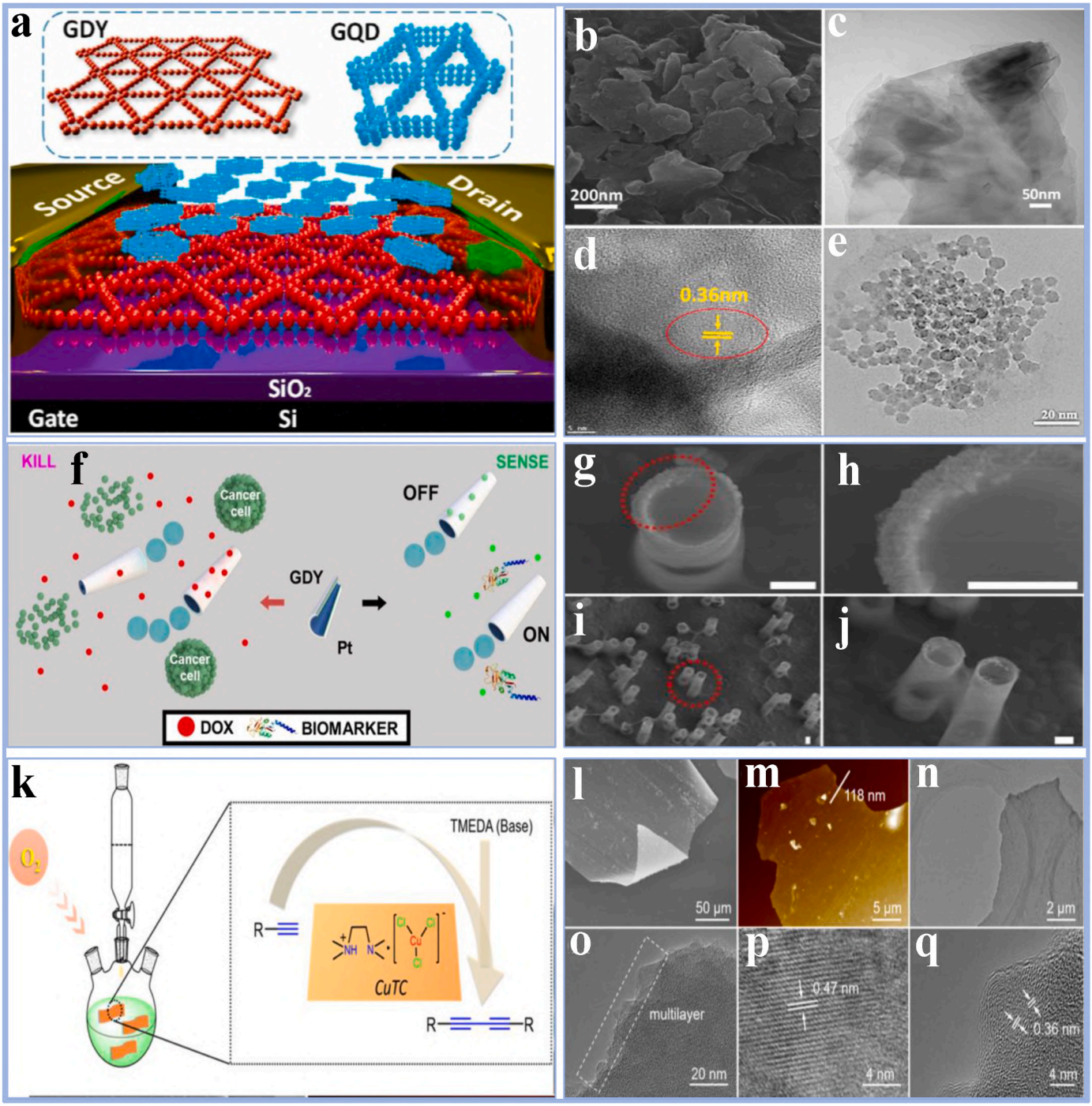

Fig. 30. (a) Schematic illustration; (b) SEM; (c) TEM; (d, e) HRTEM of the 2D GDY/GQD heterostructure [370] Copyright © 2023, Elsevier. (f) Schematic illustration; (g–j) SEM analysis of the 2D GDY-Ni/Pt micromotors [391] Copyright © 2020, John Wiley and Sons. (k) Graphical representation of the synthesis for 2D GDY expansion on a copper substrate; (l) SEM; (m) AFM; (n, o) TEM; (p, q) HRTEM analysis of 2D GDY sheets [217] Copyright © 2022, American Chemical Society.

robust biosensors for microRNA detection, with potential applications in COVID-19 diagnosis.

4.2. 1D GDY

Carbon nanomaterials, such as fullerenes, carbon nanotubes (CNTs), and graphene, have seen extensive utilization in real-world applications over the last two decades, greatly enhancing materials studies and nanoelectronics [208,375]. The diverse hybridization states of carbon (sp, sp^2, sp^3) facilitate the formation of intricate networks essential to organic production and creativity [376]. Graphene and its analogs, characterized by distinct frameworks and characteristics, have attracted significant interest. Carbon chains containing –C ≡ C– units exhibit significant potential, improving mechanical, electrical, and optical properties [377]. Recent advancements in organic production have resulted in the development of new molecules, including benzene [378] and cubane [379]. Among these materials, GDY demonstrates significant promise for potential uses in electrical and optoelectronic structures. Experimental attempts have effectively generated GDY nanowalls, nanoribbons, and nanotubes [380]. Notably, Cirera et al. [171] revealed the production of 1D extended GDY nanowires, which exhibit distinctive characteristics and potential applications. First-principles computations

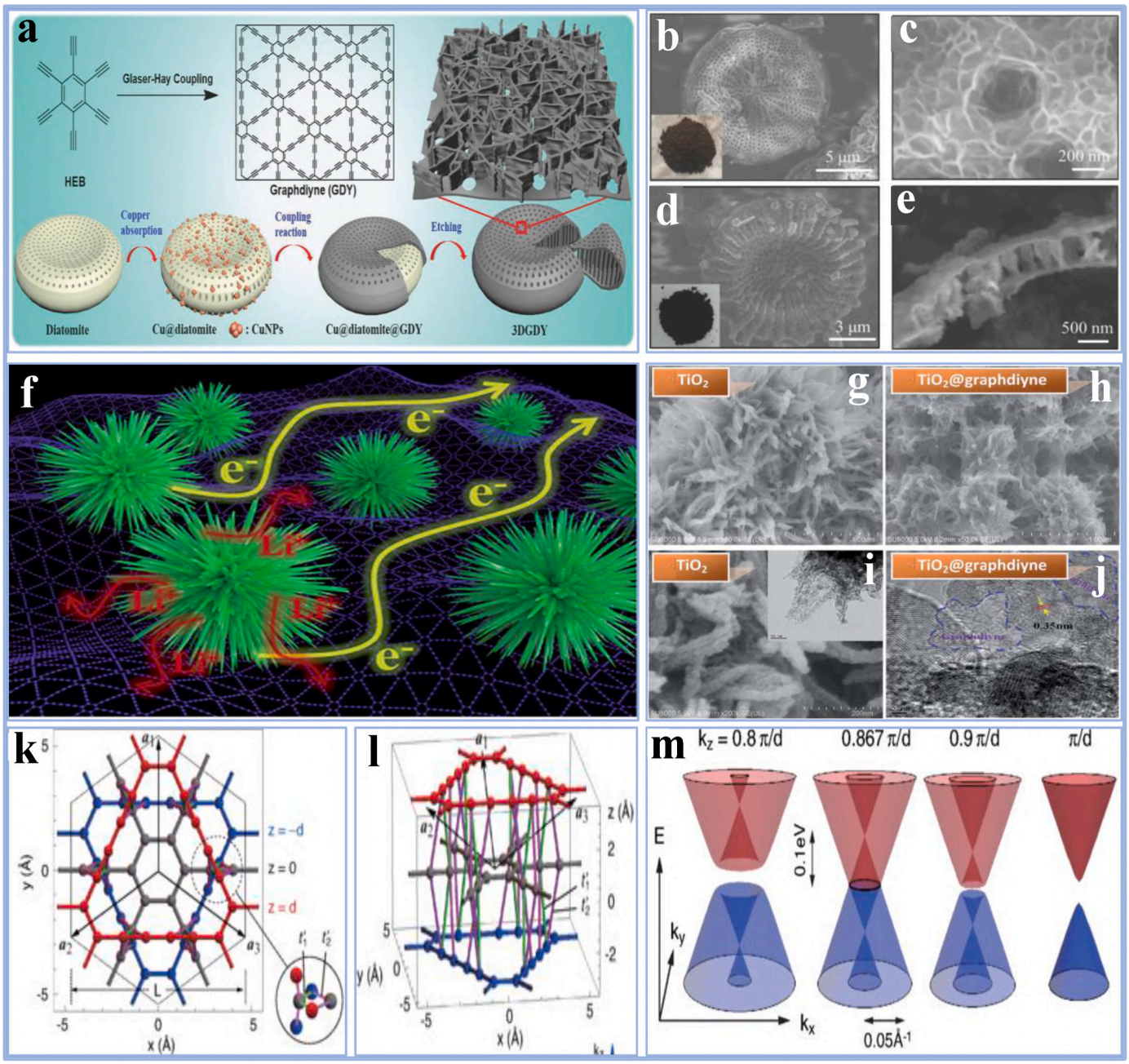

Fig. 31. (a) Schematic illustration of the synthesis process of 3DGDY; SEM analysis of (b, c) GDY@Cu@diatomite; (d, e) 3DGDY [66] Copyright © 2018, John Wiley and Sons. (f) Graphical depiction of the increased electrochemical efficiency; (g, h) SEM; (i, j) TEM analysis of 3D TiO_2@GDY [399] Copyright © 2018, Royal Society of Chemistry. (k, l) 3D stacking configuration of ABC-stacked GDY; (m) Energy band structure of a 4 × 4 effective model for ABC-stacked GDY [400] Copyright © 2018, American Physical Society.

indicate that these nanowires function as 1D semiconductors with a narrow bandgap, which is essential for prospective semiconductor applications [381]. Changing the bandgap of lower-dimensional nanomaterials is essential for improving their functionality [382]. For example, Qian et al. [383] developed 1D GDY nanowires through a facile and effective method, facilitating their accessibility for the examination of their anticipated properties. Their findings suggest that 1D GDY nanowires represent a novel form of carbon, offering significant potential for scientific investigation and practical applications due to their capacity for large-scale synthesis. The 1D GDY nanowires exhibit a conductivity of 1.9×10^3 S m^{-1} and mobility of 7.1×10^2 cm^2 V^{-1} s^{-1}. Their investigation area positions GDY nanowires at the forefront of the materials industry (Fig. 29a–c). Similarly, Zhu et al. [384] employed first-principle calculations to investigate 1D extended GDY nanowires. A thorough investigation into modifying their electrical characteristics using a range of physical and chemical techniques, including electric fields, carbonization, and chemical functionalization, was carried out. The application of an electric field perpendicular to the surface resulted in an enhanced bandgap, while chemical functionalization and carbomerization led to a reduction in the bandgap without affecting the semiconducting properties. Their research emphasized on the configuration of bandgap in relation to field intensity and the number of –C ≡ C– units. The charge transfer characteristics of modified nanowires have been compared to those of pure nanowires, utilizing crystalline orbital modeling to improve the electronic and charge transfer properties of the modified nanowires (Fig. 29d–f). Furthermore, Chen et al. [385]

synthesized 4,8-diethynylbenzo[1,2-d-4,5-d′] bisoxazole (DEBBA), incorporating both alkyne and oxazole functional groups. The intermediaries facilitate the self-assembly of molecules on the Ag (111) interface, leading to the formation of a hydrogen-loaded matrix that can subsequently be annealed to yield closely packed 1D GDY wires. Their findings demonstrated a new method for fabricating covalently linked 1D organic frameworks structured into a supramolecular lattice through hydrogen bonding (Fig. 29g and h).

4.3. 2D GDY

2D GDY is a novel material recognized for its unique structural and electronic properties, making it applicable in various fields [49]. The 2D design provides a significant SSA, exceptional mechanical strength, and enhanced conductivity, which are essential for applications in electronics, energy preservation, and catalysis [386]. The incorporation of triple-bonded carbon units (C ≡ C) within the GDY framework enhances its ability to host charge carriers, facilitating efficient electron transference [387]. The adjustable electronic properties enable the development of materials with specific functions, such as photocatalysis, HER, and CO_2 reduction [215,388]. The significant SSA and pore structure enhances its utility in gas adsorption and separation devices [389]. GDY's relevance in flexible, advanced devices such as photodetectors, sensors, and batteries positions it as an important material for essential studies and industrial uses [390]. For example, Ghafary et al. [370] designed a responsive FET photodetector utilizing 2D GDY as a p-type channel, leveraging its superior charge transference characteristics. Graphene quantum dots (GQDs) served as photosensitizers in the fabrication of the FET device, achieved by sintering a GDY mixture at 70 °C for 2 h. The GDY/GQD heterostructure demonstrated a photoresponsivity that was 4.45 times greater than that of pristine GDY. The device showed a notable enhancement in its on/off ratio ($1.5 \pm 0.03 \times 10^4$) and accessibility ($3.3 \pm 0.06 \times 10^{-2}$ cm^2/Vs) when compared to pristine GDY. The response and decay times for GDY/GQD were 90 ms and 20 ms, respectively, significantly faster than the 200 ms and 250 ms recorded for pure GDY. Their results demonstrate the potential of GDY/GQD heterojunctions in the development of low-cost, highly responsive phototransistors exhibiting significant sensitivity (Fig. 30a–e). Similarly, Yuan et al. [391] showed the practicality of 2D GDY-based micromotors for biomedical applications. GDY's distinctive framework offers a high SSA for drug delivery and enhanced quenching efficiency relative to conventional 2D material-derived micromotors. The durability and defect density of GDY facilitates efficient micromotor operation at lower peroxide concentrations (0.5 %). Cytotoxicity investigations demonstrated approximately 100 % cell viability in HeLa cells, indicating high biocompatibility. These micromotors demonstrate proficiency in targeted drug loading and release, as shown by pH-induced doxorubicin (DOX) release in acidic cancer environments, effectively inactivating HeLa cells at reduced DOX dosages, thereby minimizing side impacts. The micromotors exhibited significant quenching features for "OFF-ON" fluorescence detection of toxins using affinity peptides (Fig. 30f–j). Furthermore, Hu et al. [217] introduced an innovative copper(II) trichloro catalyst (CuTC) for the synthesis of 2D GDY and its analogs on copper foil, employing an improved Glaser-Hay coupling procedure. A facile method was developed to synthesize higher-quality 2D GDY nanosheets in solution, enhancing reaction parameters at moderate temperatures, achieving a yield of 42 % on a gram scale. Their approach is applicable to the production of GDY analogs, including H-GDY, $COOCH_3$-GDY, and Py-GDY, which integrate heteroatoms and display smooth, homogeneous surfaces. The GDY produced exhibited enhanced photocatalytic performance for HER, indicating considerable potential for applications in photoelectrochemistry (Fig. 30k–q).

4.4. 3D GDY

3D porous carbon materials, including graphene foams, aerogels, and sponges, have garnered considerable interest owing to their significant SSA, superior mechanical characteristics, excellent electrical conductivity, and reduced density [371,392]. These characteristics render them suitable for applications in water purification [393], catalyst assistance [394], sensing [395], and energy preservation [396]. GDY possesses distinctive electrical, mechanical, and optical characteristics, leading to its investigation for various applications such as sensors, photocatalysis, electrochemical catalysis, and energy storage [397]. But challenges persist in the development of portable 3D GDY and in the mass production of high-quality, cost-effective GDY. Existing techniques depend on costly copper substrates with restricted surface area, thereby limiting GDY yield and elevating production expenses. To address these difficulties, it is essential to develop portable 3D GDY, improve substrate SSA, and minimize copper consumption [398]. For example, Li et al. [66] proposed an approach to yield portable 3D GDY powder utilizing diatomite as a substrate and copper ions as a catalyst. This approach reduces the reliance on metallic copper and provides a cost-efficient solution for the large-scale production of GDY. As a LIB anode, 3D graphene-derived carbon exhibits superior specific capacity, charging productivity, and prolonged cycle life. A hydrothermally produced Rh@3D GDY catalyst demonstrates significant productivity and recyclability in the reduction of 4-nitrophenol (Fig. 31a–e). Similarly, Lin et al. [399] developed 3D hierarchical mesoporous flower-shaped TiO_2 coated with GDY through a facile solvothermal approach. The TiO_2@GDY composite demonstrates significant reversible capacities, superior rate capability, and remarkable cycle stability. These attributes are ascribed to the elevated lithium preservation sites, improved electrical conductivity, and the interface electric field generated by the material's diverse functionalities (Fig. 31f–j). Furthermore, Nomura et al. [400] investigated the electrical band framework of the 3D ABC-stacked (rhombohedral) GDY using first-principles calculations. This material is identified as a nodal-line semimetal, characterized by the intersection of the CB and VB in a loop within momentum space. The model recognized a topological surface phase characterized by a distinct, self-intersecting hourglass shape of the Fermi surface, distinguishing 3D GDY from other carbon allotropes regarding its electrical characteristics (Fig. 31k–m).

5. Morphology aspects of GDY

The morphology of GDY plays a critical role in its performance across various applications. GDY films offer stability and high sensitivity for sensors and bioelectronics. Nanosheets enhance energy transfer, catalytic efficiency, and drug delivery. Nanospheres improve photocatalysis, hydrogenation, and molecular sensing. Nanotubes enhance catalytic and electronic properties, aiding hydrogen production and gas sensing. Nanowalls boost photothermal effects, catalytic performance, and energy storage, while nanowires offer excellent electron transport and are ideal for lithium-ion batteries and molecular sensing. Each morphology optimizes GDY's functionality for diverse technological innovations. The details of different morphologies of GDY are given in this section.

5.1. GDY films

The regulation of GDY formation has been a significant focus of studies since its practical synthesis [26]. Multiple wet chemical synthesis approaches employ alkyne conjugation procedures utilizing hexaethynylbenzene (HEB) as a precursor and copper as a catalyst [223,401]. However, problems such as low bonding productivity, out-of-plane creation resulting from C-C bond twisting, and challenges with regulating film thickness due to robust van der Waals interactions impede the procedure [402]. Li et al. [26] synthesized approximately 1 μm thicker GDY films at 60 °C for 3 days, employing copper foils as both

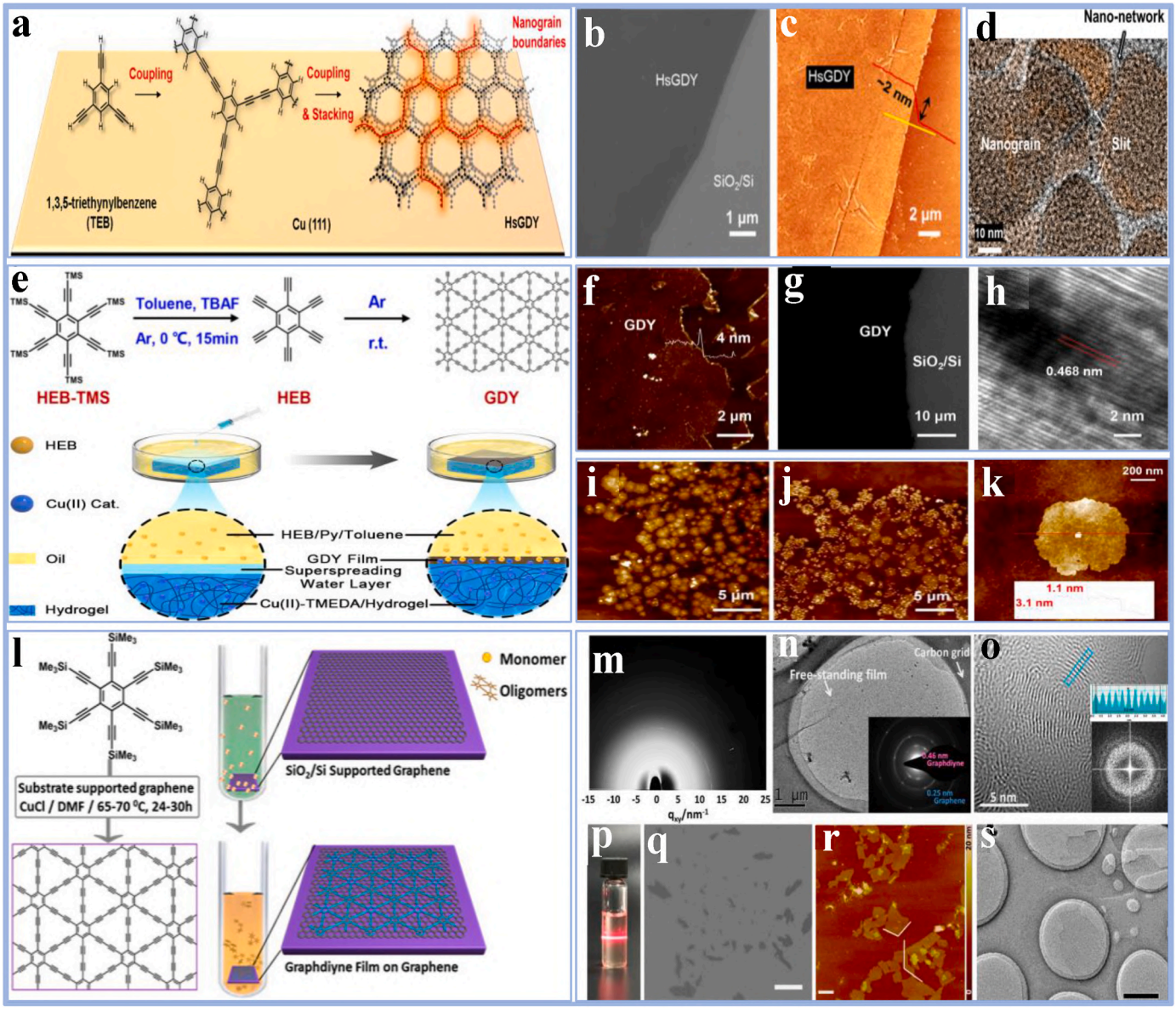

Fig. 32. (a) Synthetic process; (b) SEM; (c) AFM; (d) TEM of HsGDY nanofilms [404] Copyright © 2022, American Chemical Society. (e) Synthetic process; (f) AFM; (g) SEM; (h) HRTEM; (i–k) atomic AFM of Cu(II)-TMEDA GDY films [356] Copyright © 2022, American Chemical Society. (l) Synthetic process; (m) GIXA image; (n) TEM; (o) HRTEM; (p) Images of GDY films dispersion in EMP/EtOH; (q) SEM; (r) AFM; (s) enhanced TEM of GDY films [403] Copyright © 2019, American Chemical Society.

catalyst and precursor. Zhou et al. [403] synthesized GDY films on graphene within 24 h at ambient temperature using $Cu(OAc)_2$ as a catalyst. Nishihara et al. [54] employed a liquid/liquid interface-confined approach for producing GDY films with a thickness of 24 nm. However, the method necessitated 24 h, and the coupling productivity at room temperature could be enhanced further. In this regard, Cai et al. [404] developed conducting hydrogen-substituted GDY (HsGDY) nanofilms for on-skin sensing to mitigate anxiety and discomfort. The HsGDY sensors, characterized by their porous framework and intrinsic softness, facilitate continuous and accurate monitoring through the detection of deformation-induced alterations in interdomain tunneling conductivity. Their characteristics include excellent sensitivity (GF ~22.6 at 2 % strain), fast response time (~60 ms), and long-term durability (~5000 cycles). The sensors quantitatively evaluate human motion and health by differentiating differences in temperature and frequency of exhaled air. This strategy shows potential for the advancement of multifunctional organic bioelectronic clothing (Fig. 32a–d). Similarly, Kong et al. [356] successfully produced GDY films utilizing a Cu(II)-N,N,N′,N′-tetramethylethylenediamine (Cu(II)-TMEDA) catalyst and a superspreading liquid/liquid interfacial process. This approach yielded GDY films with diameters between 4 and 50 nm on polyacrylamide hydrogel within a duration of 2 h at ambient temperature. The films demonstrated effective photothermal transformation and improved metallic-ion release, indicating their suitability for antibacterial applications (Fig. 32e–k). Furthermore, Zhou et al. [403] presented a method for creating ultrathin GDY films on graphene substrates, employing Hiyama coupling with HEB-TMS to mitigate oxidation and self-polymerization challenges. The technique, which was applicable to hexagonal boron nitride (hBN) surfaces, produced smooth, constant GDY films exhibiting high conductivity and p-type features, indicating their potential for advanced electrical devices (Fig. 32l–s).

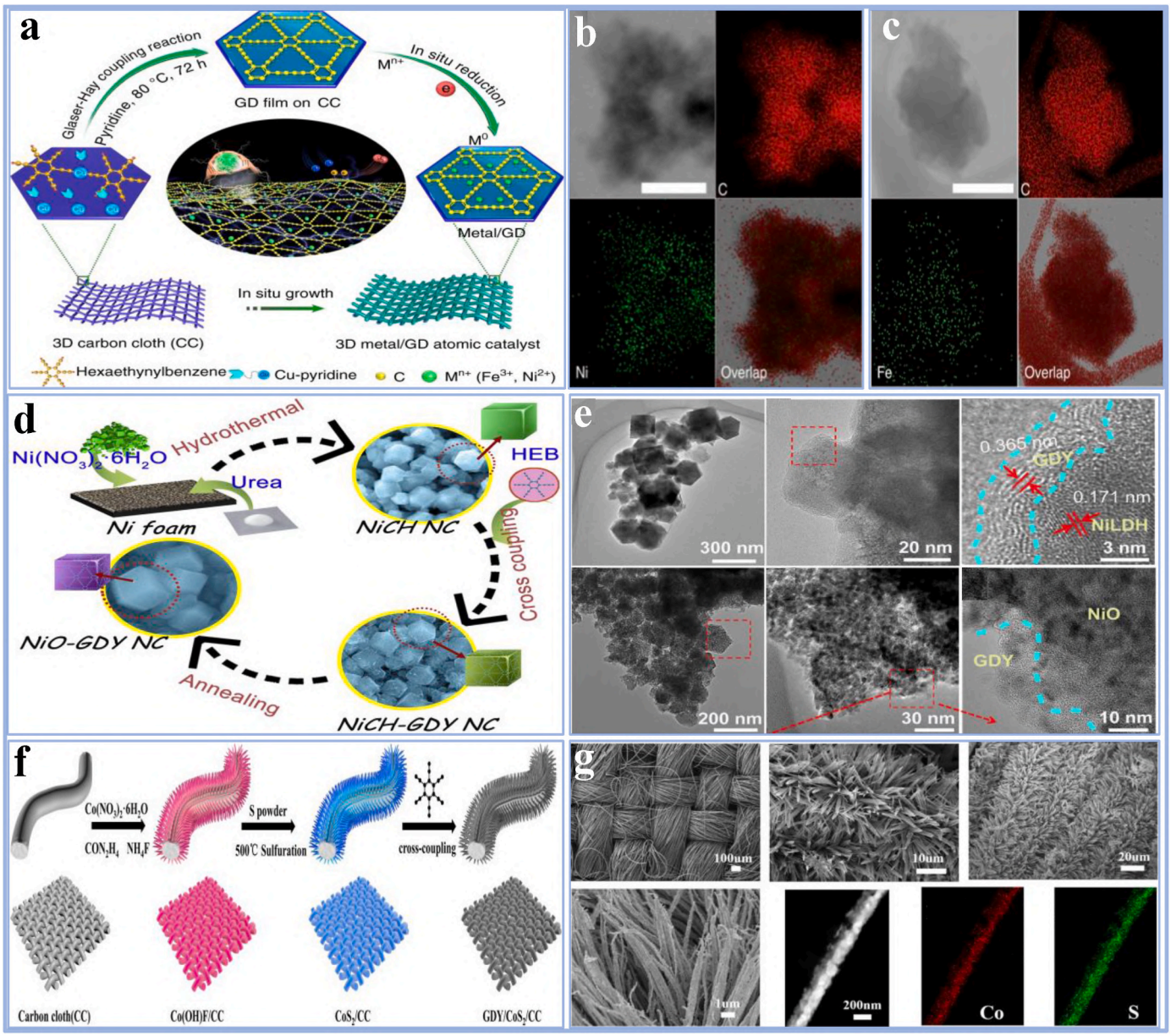

Fig. 33. (a) Synthetic process of Ni/GDY and Fe/GDY nanostructures; STEM analysis of (b) Ni/GDY; (Fe/GDY [408] Copyright © 2018, Nature. (d) The schematic process for nanostructures of NiO-GDY NC; (e) TEM analysis of NiO-GDY NC [409] Copyright © 2019, Elsevier. (f) Catalyst phased synthesis illustration; (g) SEM analysis of GDY/CoS_2/CC nanostructures [410] Copyright © 2021, Elsevier.

5.2. GDY nanostructures

The GDY structure has consistently dispersed triangular gaps that facilitate the movement of ions and molecules, rendering it an optimal material for nanomaterials. Four prospective anchoring locations on GDY include the peak of a carbon atom, the highest point of a C–C bond, the vertex of a triangular acetylene ring, and the nucleus of a benzene ring [405]. These locations facilitate the formation of durable nanostructures between GDY and nanomaterials owing to heterogeneous charge distribution and diverse C–C bonding in GDY [107]. The π/π^* orbitals of GDY readily interact with metallic ions, while the acetylene groups, characterized by elevated π-electron density, facilitate ion entrapment [406]. The pores created by 18 carbon atoms in GDY facilitate the regulation of atomic weights and electrical configurations. Moreover, sp-hybridized carbon sites provide exact placements for chemical reactions, allowing for the alteration of heteroatoms at designated regions and promoting chemical interaction with nanoparticles [407]. The interconnected structure of GDY facilitates π-π interactions with aromatic molecules [42]. For example, Li et al. [408] effectively synthesized the GDY nanostructure via atomic catalysis (ACs), composed exclusively of Ni and Fe atoms. STEM findings demonstrated that Ni and Fe atoms were associated with GDY, signifying potential adsorption sites and ultimate anchoring positions, with Ni and Fe atoms mostly localized on the surface of the acetylene ring (Fig. 33a–c). Similarly, Yu et al. [409] constructed self-supported cubic nanostructures (NiO-GDY NC) by encasing a nickel oxide (NiO) nanocube inside a thin GDY layer on a 3D nickel fiber. XRD examination demonstrated the whole transformation of nickel carbonate hydroxide (NiCH) into NiO, exhibiting peaks at 37.2°, 43.3°, and 62.9° that correspond to the (111), (200), and (222) planes of NiO. HRTEM demonstrated the effective bundling of GDY onto the NiCH nanocubes while preserving the cubic shape (Fig. 33d and e). Furthermore, Xie et al. [410] created GDY/CoS_2/CC (carbon cloth) by constructing a GDY nanowall on a CoS_2 nanowire framework. The CoS_2/CC composite was

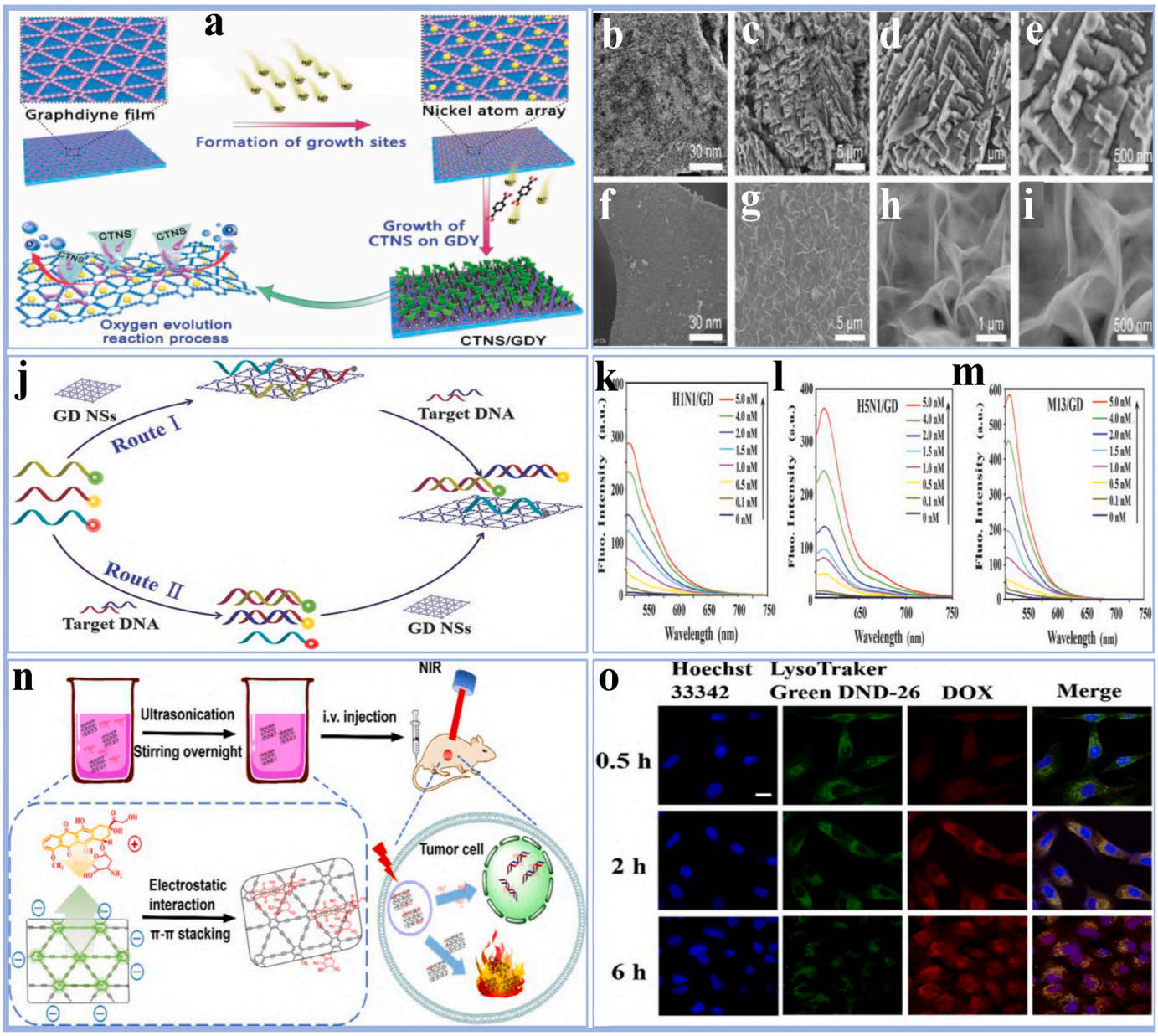

Fig. 34. (a) Schematic illustration of the synthesis of CTNS/GDY nanosheets; (b–e) SEM analysis of bulk CT; (f–i) SEM analysis of CTNS/GDY nanosheets [415] Copyright © 2021, John Wiley and Sons. (j) Scheme for the GDY NSs multiplexed DNA detection; (k–M) Fluorescence spectra of the dye-labeled ssDNA [416] Copyright © 2017, John Wiley and Sons. (n) Illustration of GDY/DOX and the Combination Treatment of Cancer; (o) fluorescence images GDY/DOX [417] Copyright © 2018, American Chemical Society.

produced by a hydrothermal process, thereafter subjected to vulcanization to produce CoS_2/CC, which was then coated with GDY. SEM demonstrated that the GDY nanowall maintained the structured 3D nanowire network, while the CoS_2/CC interface was consistently enveloped by a substantial GDY nanowall. This synergistic configuration, integrating sp-HCAs and saturated planar sulfur, markedly decreased electron transference mobility (Fig. 33f and g).

5.3. GDY nanosheets

The nanosheet morphology of GDY significantly influences its structural, electronic, and catalytic characteristics [228]. Nanosheets possess a large surface area and higher aspect ratio, offering numerous active sites for chemical reactions [75]. This characteristic renders them suitable for applications in catalysis, energy storage, and sensing [318, 411]. The planar, 2D framework of GDY nanosheets facilitates effective substrate interaction, thereby improving charge transfer and strengthening catalytic efficiency [412]. The higher surface-to-volume ratio of the nanosheets enhances the adsorption of ions and molecules, thus enhancing the material's efficiency in electrochemical applications, including supercapacitors and batteries [413]. The porosity and imperfections in the nanosheets can enhance the material's ion storage capacity and improve charging/discharging cycles [120]. The nanosheet morphology enhances the dispersion of catalytic centers, thereby improving reaction productivity in applications such as photocatalysis and HER. The nanosheet morphology of GDY improves its versatility and efficiency across various technological applications [414]. For example, Liu et al. [415] developed a facile method for regulating the formation of delicate charge-transference networks (CTs) of nickel using terephthalic acid nanosheets on GDY. This catalyst has remarkable OER performance, achieving an overpotential of just 155 mV while providing a current density of 10 mA cm^{-2} in alkaline electrolytes. DFT revealed

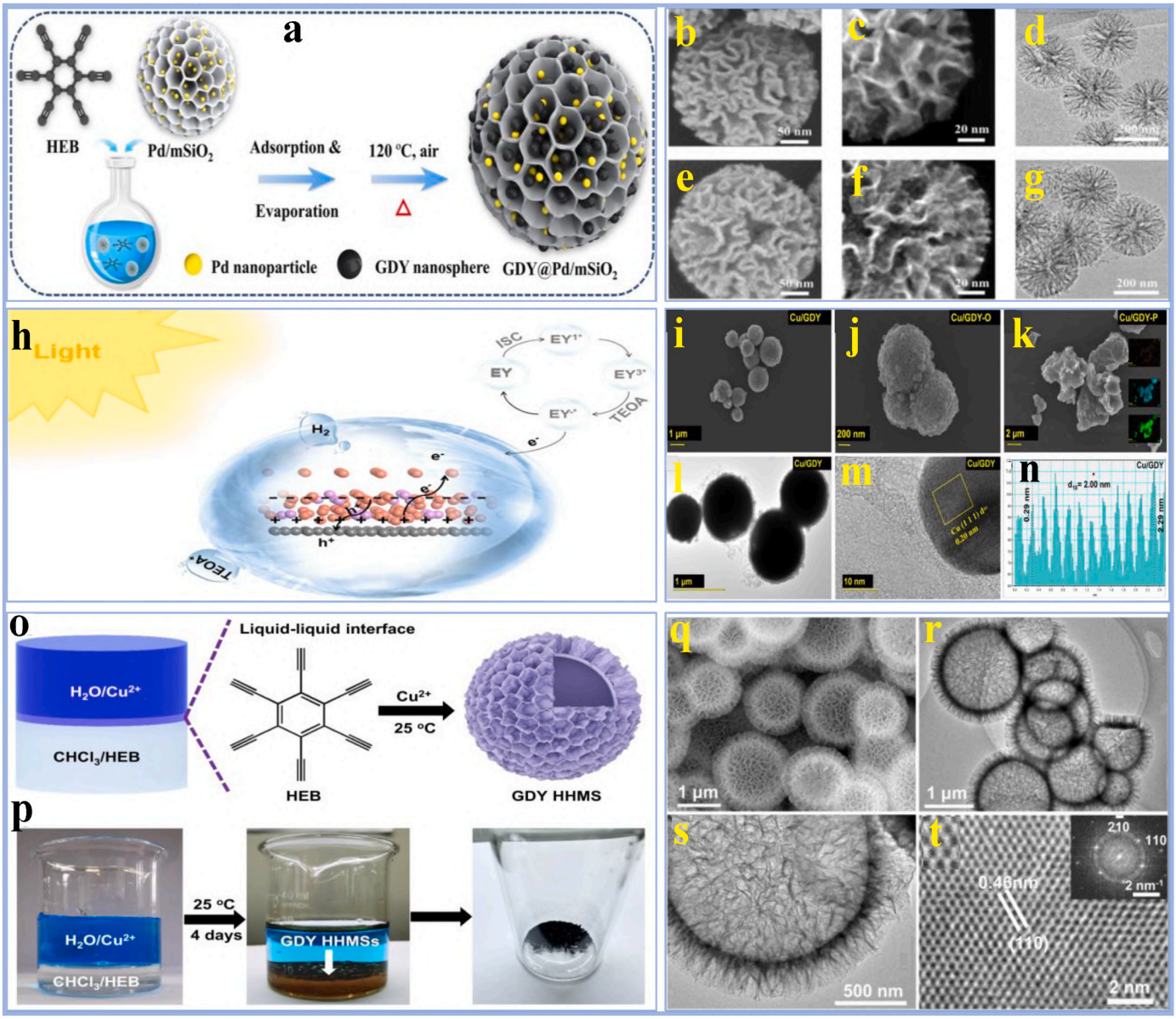

Fig. 35. (a) Schematic illustration of synthesis process; (b, e) SEM; (c, f) SEI-STEM; (d, g) TEM of GDY@Pd/mSiO$_2$ [423] Copyright © 2022, John Wiley and Sons. (h) Synthetic process; (i–k) SEM; (l, m) TEM; (n) HRTEM of Cu$_3$P/GDY nanospheres [424] Copyright © 2024, American Chemical Society. (o) Synthetic process; (p) Structural characterization; (q) SEM; (r, s) TEM; (t) HRTEM of GDY HHNSs [425] Copyright © 2023, Nature.

that a significant p-d coupling effect at the GDY-CT interface enhances electronic activity, facilitating quick reversible oxidative transitions with reduced electron-transference barriers. Experimental characterization demonstrates GDY's essential role in strengthening morphological and electrical structures, hence augmenting OER efficiency. Their findings will likely assist engineers in developing enhanced catalysts for hydrogen-powered devices (Fig. 34a–i). Similarly, Parvin et al. [416] demonstrated that few-layer GDY nanosheets (GDY NSs) possess exceptional fluorescence heating capabilities and notable selectivity for ssDNA compared to dsDNA, facilitating the development of highly sensitive biosensors for simultaneous DNA detection with a limit of 25 pM. Sensors using GDY NSs demonstrate superior productivity compared to those employing GO and MoS_2 nanoparticles. This simple and rapid mix-and-detect analysis operates in a homogeneous liquid condition, making it ideal for in-situ detection applications. GDY nano quenchers may be produced in significant quantities and incorporated with diverse dye-labeled ssDNA, making them advantageous for multiplex DNA analysis (Fig. 34j–m). Furthermore, Jin et al. [417] developed a robust multifunctional treatment approach using GDY NSs. The 2D CMs exhibit exceptional photothermal characteristics and pH and light-responsive release capabilities when included into a medication delivery system using DOX as the model agent. NIR laser irradiation significantly amplifies DOX release. Cellular and animal investigations confirmed the biosafety and enhanced antitumor activity of the photothermal and chemotherapeutic combination. The GDY-based device exhibits photostability, biocompatibility, and has promise in cancer theragnostics (Fig. 34n and o).

5.4. GDY nanospheres

GDY's nanosphere morphology is critical for improving its functioning across a wide range of applications. The spherical framework enhances SSA and facilitates effective interactions with surrounding environments, which is essential for catalysis, energy storage, and sensing [418]. GDY nanospheres serve as a stable platform for the incorporation of functional materials, such as Pd or Cu, in catalytic

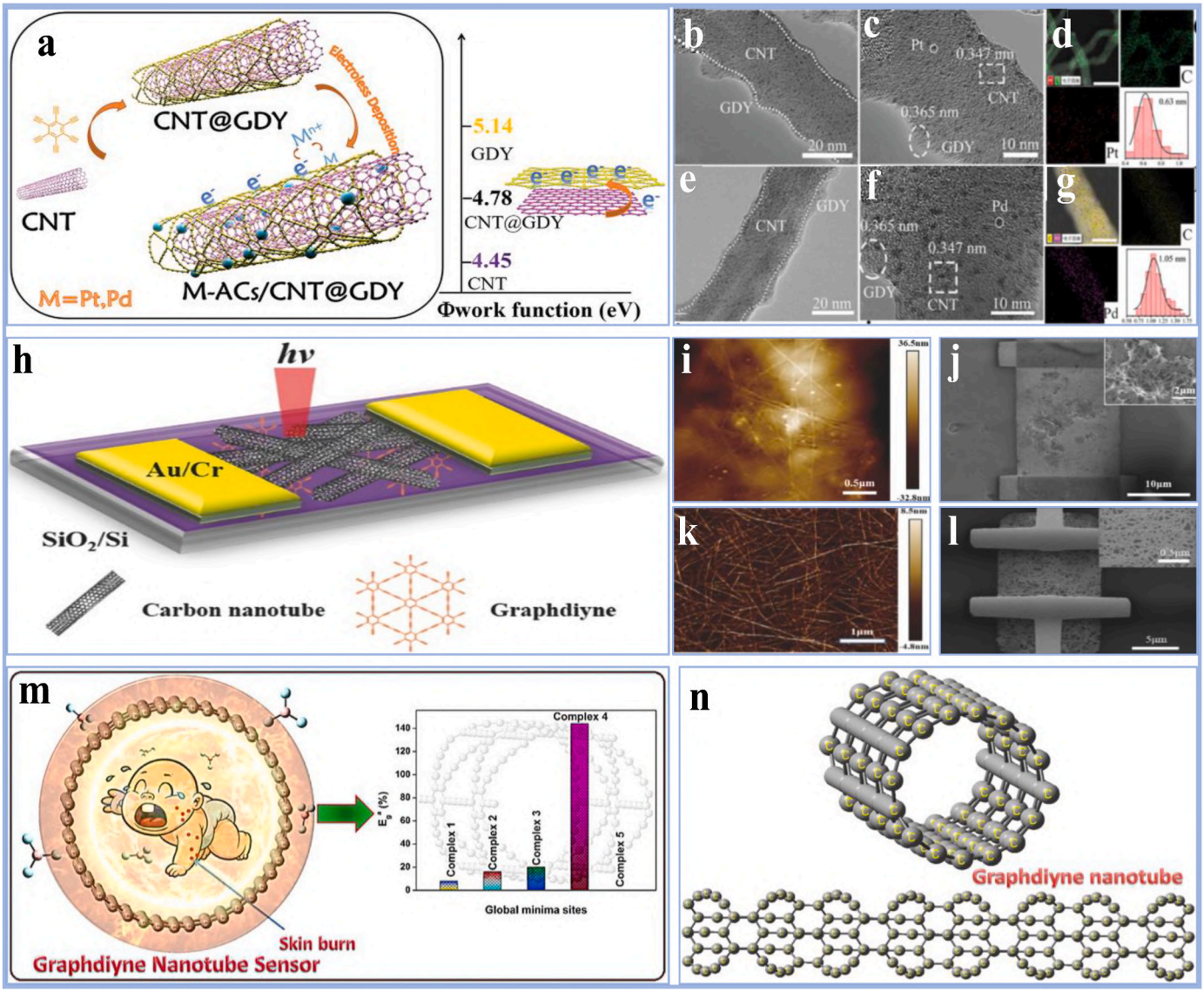

Fig. 36. (a) Schematic illustration of the synthesis process and work function; (b–d) TEM; (e–g) STEM of Pt(Pd)-ACs/CNT@GDY [433] Copyright © 2021, John Wiley and Sons. (h) Synthetic process; (i, k) AFM; (j, l) SEM of s-SWNTs and γ-GDY [434] Copyright © 2017, John Wiley and Sons. (m) Synthetic process of GDYNTs sensor for BF_3 molecules [435] Copyright © 20203, Elsevier. (n) Synthetic process of isolated GDYNTs [436] Copyright © 2018, Elsevier.

procedures, thereby enhancing reaction productivity and hydrogen storage ability [419]. Their uniform morphology facilitates improved charge distribution, which improves electrical conductivity and charge transference, making them advantageous for electrochemical applications such as hydrogenation and photocatalysis [420]. The elevated SSA of GDY nanospheres enhances their effectiveness as surface-enhancing Raman scattering (SERS) substrates, facilitating the sensitive detection of molecules at minimal concentrations [331,421]. The nanospherical shape enhances GDY's efficiency by increasing its structural stability, reactivity, and versatility across different technological domains [422]. For example, Yu et al. [423] presented an efficient method for synthesizing GDY nanospheres inside Pd/mSiO_2 mesoporous channels, therefore improving hydrogenation activities. GDY functions as a wettability and electrical modulator, rendering the channels highly aerophilic and enhancing H_2 storage. This elevates the concentration of H_2 around Pd nanoparticles, thereby enhancing hydrogenation efficiency. This method facilitates the creation of wettability-derived catalysts for gas-liquid-solid tri-phase processes at ambient temperature (Fig. 35a–g). Similarly, Wu et al. [424] produced Cu_3P/GDY composites by first oxidizing nanospherical copper powder and then phosphating cuprous oxide. The Cu/GDY-P ratio was improved by adjusting phosphating levels, and computational investigations were performed to elucidate the charge transference between Cu and GDY-P. A photoexcited charge transference mechanism in Cu/GDY-P was postulated (Fig. 35h–n). Furthermore, Zhang et al. [425] developed GDY hierarchical hollowed nanospheres (HHNSs) with self-sustaining structures and very high SSA by a non-surfactant liquid-liquid surface-excitation method. The GDY HHNSs demonstrate remarkable sensitivity as surface-increasing Raman scattering substrates, including a Raman enhancement factor (EF) of 3.7 $\times 10^7$ and a detection limit of 1.0 $\times 10^{-12}$ M for rhodamine 6G (R6G). The elevated surface interactions in the GDY-molecule mechanism enhance its exceptional sensing capabilities (Fig. 35o–t).

5.5. GDY nanotubes

The morphology of nanotubes in GDY significantly influences the efficiency of GDY-based materials [426]. Integration of GDY with nanotubes, particularly CNTs, results in enhanced structural support and conductivity from the nanotubes [427]. Meanwhile, the distinctive characteristics of GDY, such as its large surface area and π-conjugated

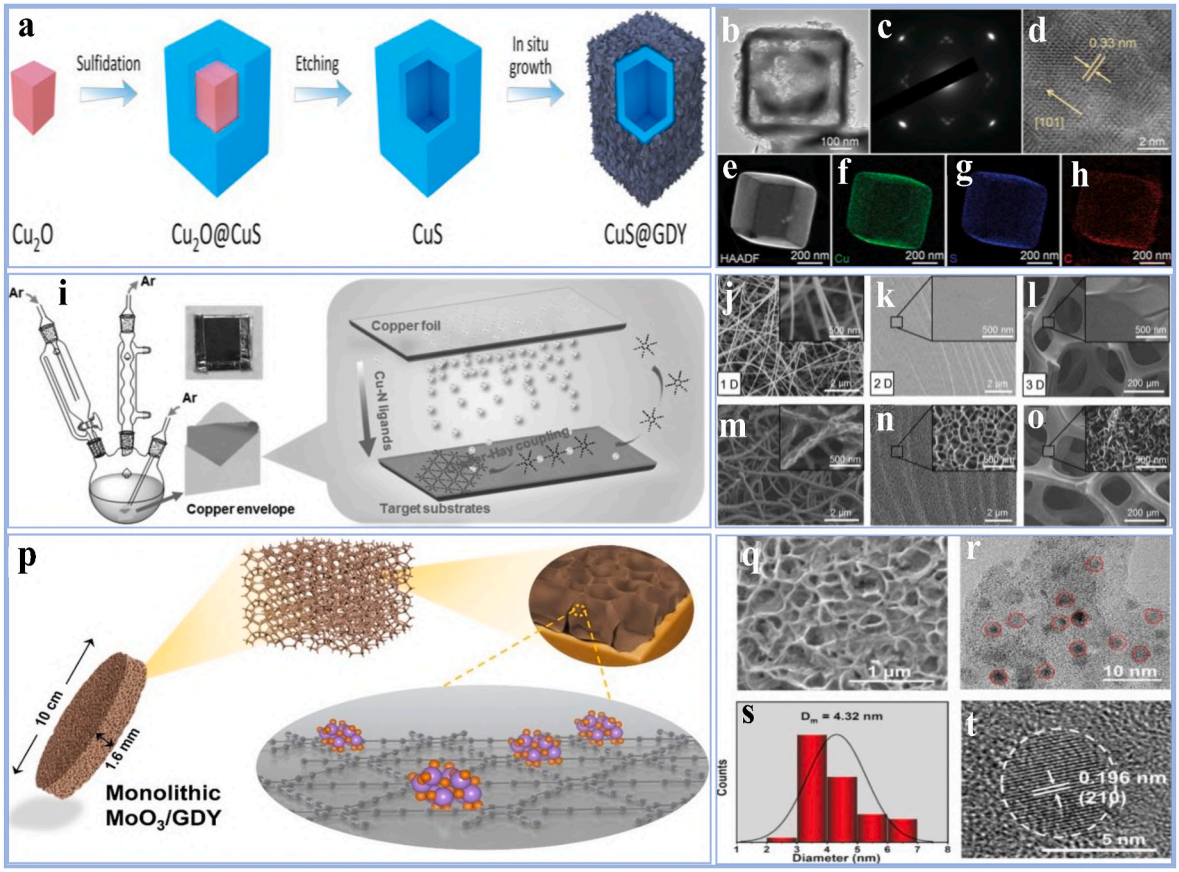

Fig. 37. (a) Synthetic route; (b) TEM; (c) SAED; (d) HRTEM; (e–h) EDS mapping of hollow cubic CuS@GDY nanowalls [443] Copyright © 2022, John Wiley and Sons. (i) Schematic illustration of synthesis process GDY nanowalls via copper envelope catalysis; SEM analysis of the growth of GDY nanowalls on (j, m) 1D silicon nanowires; (k, n) 2D Au foil; (l, o) 3D Ni foam [444] Copyright © 2016, John Wiley and Sons. (p) Schematic illustration of synthesis process; (q) SEM; (r) TEM; (s) Particle distribution; (t) HRTEM of 3D monolithic MoO_3/GDY nanowalls [445] Copyright © 2023, John Wiley and Sons. (For interpretation of the references to color in this figure legend, the reader is referred to the Web version of this article.)

system, facilitate improved interaction between the nanotubes and other components [428]. The tubular framework of CNTs enhances the distribution of active sites and promotes the homogeneous attachment of metallic components, which is evident in catalyst applications [345, 429]. This synergy leads to improved charge transference, optimized catalytic productivity, and higher stability [430]. The morphology of nanotubes enhances the mechanical robustness and flexibility of the composite material, rendering it suitable for various applications, including energy storage, sensing, and drug delivery [431]. The integration of the high surface area and conductivity of nanotubes with the practical characteristics of GDY facilitates the formation of advanced materials exhibiting enhanced performance across diverse technological domains [432]. For example, Lv et al. [433] synthesized novel catalysts, Pt(Pd)-ACs/CNT@GDY, for hydrogen generation and the reduction of aromatic nitro compounds. CNTs were enveloped with a modifiable GDY layer to create hybrid structures, whereby the CNTs offer morphological integrity and electrical conductivity, while the GDY coating promotes homogeneous adhesion of metallic constituents, hence augmenting the catalyst's effectiveness. This hybrid design diminishes the work function, enhances interface charging, and amplifies the SSA. Platinum and palladium atomic clusters were effectively deposited on carbon NT@GDY, resulting in superior dispersion and uniformity. The resultant catalysts exhibited enhanced efficiency in hydrogen generation and the reduction of 4-nitrophenol, with a facile deposition process and economical materials indicating feasibility for large-scale production (Fig. 36a–g). Similarly, Zheng et al. [434] developed an infrared (IR) photodetector employing semiconductive single-walled carbon nanotubes (s-SWNTs) and γ-GDY. The device demonstrated an on/off ratio above 105, mobility nearing 25 $cm^2\ V^{-1}\ s^{-1}$, and outstanding electrical transfer characteristics. The integration of γ-GDY improved exciton dissociation, leading to a consistent response throughout the channel. The photodetector exhibited a responsivity of 0.38 mA/W and a detectivity of 106 $cmHz^{1/2}\ W^{-1}$. Estimated enhancements are predicted with bigger γ-GDY single crystals and superior-quality s-SWNTs (Fig. 36h–l). Furthermore, Maria et al. [435] used first-principles computations to examine the adsorption of boron trifluoride (BF_3) gas molecules on GDYNTs. Studies on cohesive energy validated the stiffness of GDYNTs, whereas the adsorption of BF_3 resulted in substantial alterations in the band configuration and electron density. Their findings indicate that GDYNTs are viable candidates for the detection of dangerous BF_3 hydrocarbons (Fig. 36m). Moreover, Srimathi et al. [436] investigated the electrical characteristics of isolated GDYNTs and determined a bandwidth of 133 meV. The electrical characteristics were influenced by medications like Imuran, Pentasa, and Hyoscyamine, with Pentasa exhibiting the most significant adsorption. Their research suggests that GDYNTs has promise as drug carriers for chronic disorders, enabling the tailored administration of pharmaceuticals via covalent and hydrogen bonding interactions (Fig. 36n).

5.6. GDY nanowalls

The nanowall morphology of GDY contributes significantly to its catalytic, energy conversion, and sensing characteristics [437]. The structured, vertically aligned nanowalls offer a substantial SSA, enhancing the exposure of active sites and stimulating effective interactions with adjacent molecules [438]. GDY nanowalls efficiently

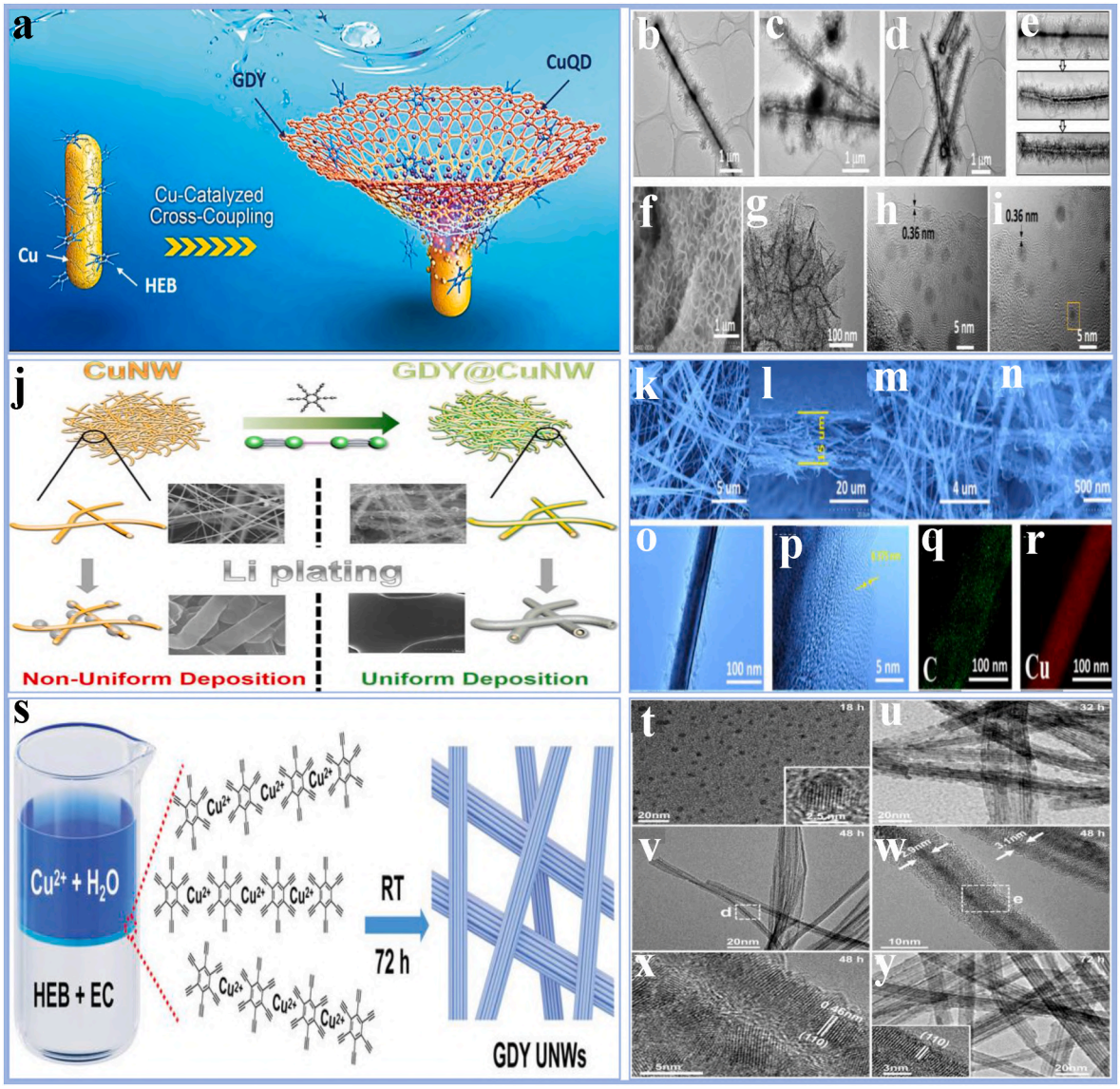

Fig. 38. (a) Synthetic growth process; (b–e) TEM; (f, g) SEM; (h, i) HRTEM of CuQD@GDY nanowires [452] Copyright © 2020, John Wiley and Sons. (j) Schematic illustration of synthesis process; (k–n) SEM; (h, i) TEM; (q, r) elemental mapping of GDY@CuNW [453] Copyright © 2019, American Chemical Society. (s) Synthesis and structural characterization; (t–y) HRTEM of GDY UNWs [454] Copyright © 2023, John Wiley and Sons.

capture and convert near-infrared (NIR) light, which increases the material's absorption capabilities and enhances photocatalytic efficiency [439]. The distinct design of the nanowalls promotes the formation of heterojunctions with various materials, thereby improving charge carrier separation and increasing catalytic efficiency [225,440]. This morphology facilitates the facile integration of diverse nanoparticles or metal clusters, enhancing the overall effectiveness of reactions, including hydrogen production, pollutant degradation, and biosensing [441]. The incorporation of nanowalls in GDY enhances the surface wettability of the material, facilitating interactions with reactants and improving its efficacy in energy storage, conversion processes, and environmental applications [442]. For example, Bai et al. [443] produced a plasmonic-enhanced enzyme by encasing GDY nanowalls around hollow copper sulfide (CuS) nanocubes. The CuS cubic shell enhances the catalyst's localized surface plasmonic resonance (LSPR), increasing the interfacial area and enabling energy transmission. Longitudinal GDY nanowalls collect near-infrared (NIR) light, increasing absorption and forming a p-p-type heterojunction with CuS to facilitate hot carrier dissociation and insertion. Carbon gaps at surfaces facilitate the adsorption and decomposition of H_2O_2. CuS absorbs localized surface plasmon resonance (LSPR), hence boosting photothermal effects and antibacterial properties. Their research examines how LSPR activates the peroxidase-like activities of CuS@GDY and demonstrates its enhanced antibacterial efficacy under NIR light both in vitro and in viv (Fig. 37a–h). Similarly, Gao et al. [444] employed copper envelope catalysis and Glaser-Hay coupling to synthesize GDY nanowalls on diverse substrates. The copper-pyridine intermediate acts as a catalyst, promoting the synthesis of GDY on 1D, 2D, and 3D materials. A GDY/-$BiVO_4$ photoanode enhanced the photoelectrochemical performance of $BiVO_4$ in water splitting. The combination achieved a photocurrent density of 1.32 mA cm^{-2} at 1.23 V vs. RHE, about double that of unmodified $BiVO_4$. This approach illustrates the potential for merging GDY's features with various materials to enhance productivity in energy conservation and photoelectric technologies (Fig. 37i–o). Furthermore, Zhu et al. [445] identified the essential significance of water reactivation in enhancing O_3 decomposition and elucidated the mechanism for the first time. Their 3D monolithic MoO_3/GDY composite exhibited enhanced O_3 removal effectiveness relative to previous carbon-derived MoO_3 composites, particularly in extreme humidity conditions. The transference of electrons from GDY to MoO_3 strengthened the Mo–O

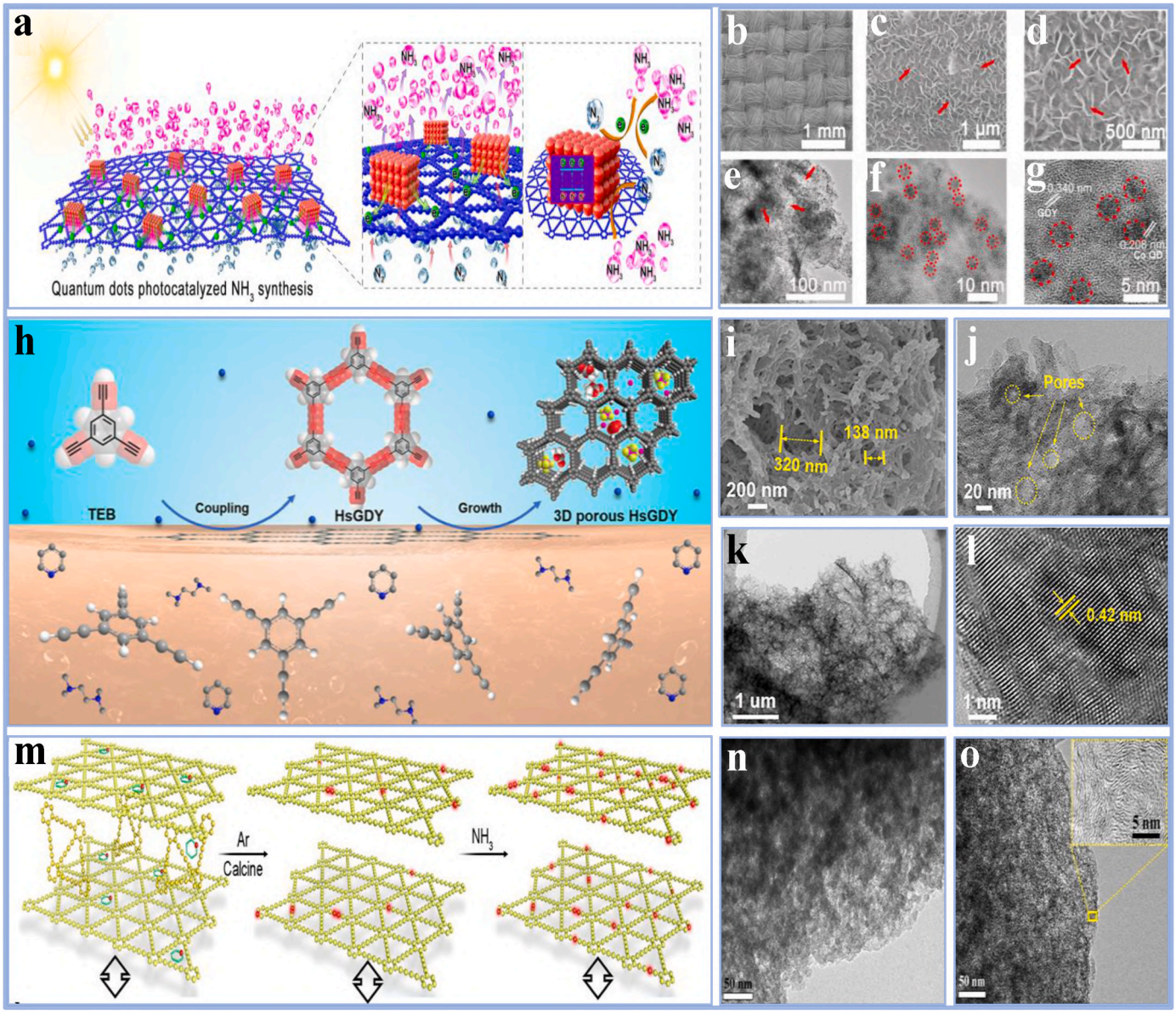

Fig. 39. (a) Synthetic process; (b–d) SEM; (e, f) TEM; (g) HRTEM of GDY@CoO_xQD [457] Copyright © 2021, Elsevier. (h) Synthetic process; (i) SEM; (j, k) TEM; (l) HRTEM of HsGDY framework [458] Copyright © 2023, American Chemical Society. (m) Synthetic process; (nTEM; (o) HRTEM of N-loaded GDY [157] Copyright © 2017, American Chemical Society.

bonds, hence aiding the activation of H_2O. The produced hydroxyl radicals served as supplementary active sites, enhancing O_3 adsorption and creating new radicals. Elevated humidity lowered the energy barrier for O_3 breakdown, enhancing overall efficiency. Their research emphasizes the advancement of efficient O_3 decomposition catalysts, especially in high-humidity settings (Fig. 37p–t).

5.7. GDY nanowires

The morphology of nanowires in GDY markedly improves its structural stability, conductivity, and catalytic efficiency [446]. The 1D structure of nanowires facilitates directional charge transfer, enhancing electron mobility and decreasing resistance in electrochemical procedures [447]. The morphology enables the development of interconnected networks that enhance electron transference and ion diffusion, rendering nanowire-based GDY materials highly efficient for energy preservation and conversion uses [448]. The elongated framework of nanowires enhances the overall surface area, facilitating the exposure of more active sites, which is essential for applications including catalysis, sensor technologies, and environmental remediation [449]. The distinctive characteristics of GDY nanowires facilitate the growth of additional nanoparticles or functional groups, thereby potentially improving the material's catalytic activity and durability [450]. Their high aspect ratio and flexibility render them suitable for integration into flexible electronic devices, providing a promising foundation for various advanced technologies, including flexible sensors, energy harvesters, and next-generation batteries [451]. For example, Zuo et al. [452] examined the influence of the crystallized configuration of the Cu substrate on the development of GDY nanowires. Crystalline boundaries were found to enhance reaction efficiency, resulting in the fragmentation of polycrystalline Cu into uniformly distributed CuQDs. This fragmentation interferes with the sequential development of GDY. Single-crystalline Cu substrates facilitate the production of ordered GDY nanosheets. CuQDs on GDY demonstrate significant lithiophilicity, positioning CuQD@GDY as an effective substrate for uniform lithium plating and the mitigation of lithium dendrite formation. The

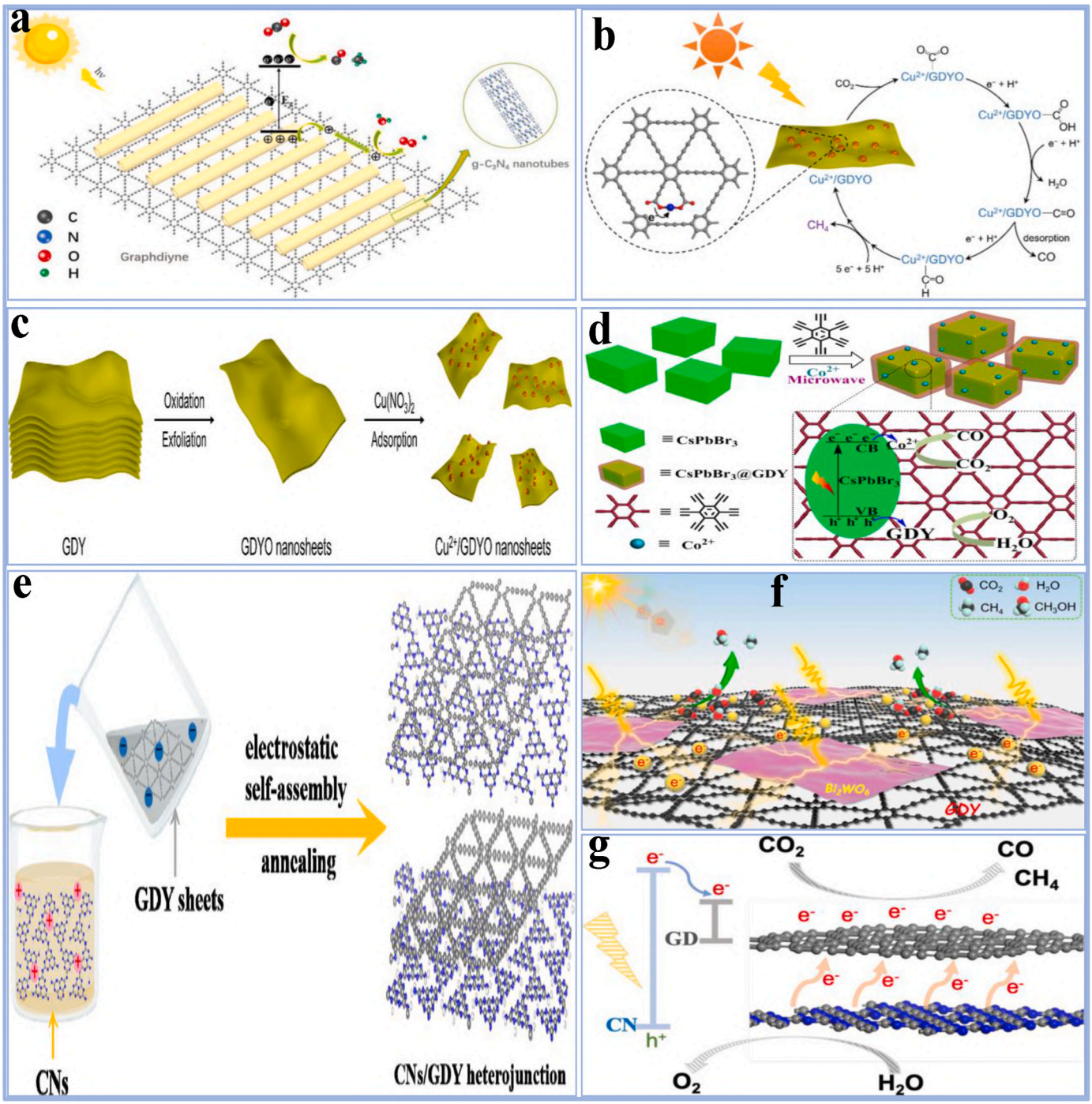

Fig. 40. (a) Graphical illustration of photocatalytic CO_2 reduction using GDY@CNtb [465] Copyright © 2021, Elsevier. (b) The suggested methodology for photocatalytic CO_2 reductivity on Cu^{2+}/GDYO nanosheets using visual illumination; (c) Graphical representation of the synthesis procedure of Cu^{2+}/GDYO nanosheets [466] Copyright © 2021, John Wiley and Sons. (d) Visualization of the photo redox processes and formation of Co-dopant $CsPbBr_3$@GDY [467] Copyright © 2020, American Chemical Society. (e) Graphic representation of the van der Waals heterostructure photocatalytic CO_2 reduction mechanism between 2D/2D CNs and GDY [468] Copyright © 2021, American Chemical Society. (f) Proposed photocatalytic CO_2 mechanism of the ultrathin 2D/2D GDY/Bi_2WO_6 heterostructure [469] Copyright © 2021, American Chemical Society. (g) Graphical depiction of GD/CN photocatalytic CO_2 reduction mechanism [470] Copyright © 2021, American Chemical Society.

spontaneous formation of CuQDs on GDY nanosheets has potential applications in water splitting, CO_2 and N_2 elimination, and batteries (Fig. 38a–i). Similarly, Shang et al. [453] demonstrated that 2D GDY exhibits greater lithiophilic epicenters compared to conventional carbon materials. The 3D self-supporting CuNW electrode, featuring ultrathin GDY nanowires, improves metallic Li deposition and mitigates dendritic growth. This significantly enhances the cycling and coulombic performance of the electrode, achieving an ultrahigh volumetric rating of 1333 mAh cm^{-3}, which is ideal for high-energy-density lithium metallic systems (Fig. 38j–r). Furthermore, Yang et al. [454] introduced a novel method for synthesizing GDY ultrathin nanowires (UNWs) at ambient temperature. These UNWs form along [110] and exhibit superior crystallization with dimensions under 3 nm. The creation process involves an oriented attachment mechanism. The UNWs exhibit

significant disparities in energy (~1.82 eV), enhanced photoelectric effects, and notable surface-enhanced Raman scattering (SERS) characteristics. Rhodamine 6G (R6G) exhibits a significant Raman enhancement factor of 3.92×10^8 and detection limits of 1×10^{-13} m (Fig. 38s–y).

5.8. GDY nanoporous

Nanoporous morphology in GDY denotes the existence of nanoscale gaps or pores within its framework, which markedly improve its characteristics [120]. The adjustable nanopores in GDY enhance SSA, boost adsorption capacity, and facilitate effective charge transfer, rendering it effective for various applications, including catalysis, energy storage, and separation techniques [39]. The nanoporous framework facilitates selective molecular sieving, improving the material's capacity to separate molecules according to size or other properties, particularly in applications such as membrane filtration, gas separation, and water desalination [455,456]. The extensive SSA and accessible pore channels enhance the number of active sites for reactions, thereby improving the catalytic efficiency of the material. The capability to regulate pore size and distribution enhances the functionality of GDY for targeted industrial applications [412]. For example, Liu et al. [457] present a new catalyst for ammonia (NH_3) production utilizing porous GDY QDs, providing a possible alternative to the energy-intensive Haber-Bosch procedure. The catalyst exhibits ultra-high efficiency due to the swift transformation of metallic valence states and improved surface plasmon resonance (SPR), which together enhance photochemical productivity. In 46 independent experiments, the catalyst produced an optimal NH_3 yielding rate of 26,502 $\mu molNH_3\ gcat^{-1}\ h^{-1}$, with an average rate of 19,583 $\mu molNH_3\ gcat^{-1}\ h^{-1}$, indicating excellent efficiency and sustained stability (Fig. 39a). The catalysts were fabricated using an in-situ growth approach, in which GDY nanosheets were initially produced on carbon cloth, followed by the deposition of CoO_xQD to create self-supported GDY@CoO_xQD nanosheet arrays. SEM images validated the 3D porous design of the electrodes, with CoO_xQDs uniformly distributed on the GDY surface, as evidenced by TEM and HRTEM images (Fig. 39b–g). Similarly, Man et al. [458] fabricated a 3D porous hydrogen-substituted graphdiyne (HsGDY) for enhanced lithium-ion storage efficiency. HsGDY, produced through an interface-induced approach, exhibits a substantial SSA of 667.9 m^2/g, hierarchical porosity, and increased interlayer spacing, which improve Li-ion availability and transfer (Fig. 39h). The material exhibits notable electrochemical efficiency, characterized by a reversible capacity of 930 mAh/g after 100 cycles, enhanced cycle stability of 720 mAh/g after 300 cycles, and rapid rate capability of 490 mAh/g at 5 A/g. DFT calculations provide additional confirmation of rapid Li-ion diffusion. A $LiCoO_2$-HsGDY full cell demonstrates significant practical charging/discharging capacity and stable cycling, thereby contributing to the advancement of next-generation lithium-ion batteries. The TEM analysis of HsGDY demonstrates its porous framework, characterized by numerous micropores measuring from tens to hundreds of micrometers, which enhance ion diffusion and offer several routes for ion transfer. The HRTEM image reveals a distinct lattice with a d-spacing of 0.42 nm, suggesting minimal ion diffusion barriers. SEM analysis illustrates a 3D porous framework characterized by rod-shaped skeletons. The distinctive porous structure increases the SSA and decreases the lithium diffusion barrier, thereby enhancing the charging/discharging capacity of HsGDY (Fig. 39i–l). Furthermore, Lv et al. [157] illustrate that GDY can be efficiently loaded with nitrogen to improve its efficiency in the ORR. N-loaded GDY, developed with pyridine and NH_3 as nitrogen sources, demonstrates electrochemical efficiency on par with commercial Pt/C in alkaline solutions while exhibiting enhanced stability and methanol tolerance (Fig. 39m). They utilized pyridine as a nitrogen source to synthesize N-loaded GDY, which was subsequently calcined at temperatures of 700 °C, 800 °C, 900 °C, and 1000 °C to modify its characteristics. The calcination procedure enhances the catalyst's electrical conductivity and ORR activity by eliminating small GDY fragments and oxygen-containing groups. TEM analysis indicates that the interface morphology exhibits increased smoothness at elevated calcination temperatures. TEM analysis indicates that Py-GDY retains a multilayered framework following calcination at 700 °C; but it becomes porous at temperatures exceeding 800 °C due to the elimination of small GDY fragments (Fig. 39n). The pore diameter diminishes with an increase in calcination temperature, as illustrated in the HRTEM image of N′N-GDY (Fig. 39o). Their research demonstrated that the method is applicable for synthesizing additional heteroatom-loaded GDY and GDY-like catalysts. Novel carbon-derived, metallic-free catalysts and nitrogen-doping techniques for fuel cells and other energy storage devices have been introduced.

6. Applications of GDY

6.1. Photocatalysts

6.1.1. Photocatalytic CO_2 reduction

The utilization of fossil fuels and the resultant CO_2 emissions are significant factors in the escalating energy crisis and environmental degradation [459,460]. Scientists are exploring the production of sustainable fuels through photochemical CO_2 reduction to address this challenge [461,462]. Photoreduction of CO_2 represents an environmentally advantageous and economically viable approach for converting CO_2 into hydrocarbon fuels utilizing solar radiation [463,464]. In this regard, Sun et al. [465] improved the photocatalytic CO_2 reductively by synthesizing the g-C_3N_4 nanotubes (CNtb) with sheet-like GDY composite through a simplified self-assembled technique. The introduction of GDY significantly increases the visual sunlight absorbance of GDY@CNtb. The SSA of CNtb and GDY@CNtb-0.07 was calculated utilizing N_2 removal and hydrolysis isotherms. The BET SSA of GDY@CNtb-0.07 is around 40.2 m^2g^{-1}, slightly higher than pure CNtb (32.9 m^2g^{-1}). The successful integration of GDY with CNtb was confirmed by uniform coverage of GDY on the CNtb surface. Photocatalytic tests showed that GDY@CNtb significantly boosted CO_2 reduction efficiency, producing CO and CH_4 as primary products at rates 18–20 times higher than pure CNtb. The optimal mass ratio of GDY to CNtb was determined to be 0.07, demonstrating consistent efficiency across multiple cycles (Fig. 40a). Similarly, Wu et al. [466] synthesized Cu^{2+}/GDYO nanosheets to enhance photocatalytic CO_2 reduction. GDYO synthesized through a simplified Glaser–Hay coupling reaction, displayed vertically aligned nanosheets resulting from robust interlayer bonding. The incorporation of Cu^{2+} into GDYO improved CO_2 reduction, yielding CH_4 as the primary product at 87 % while markedly decreasing hydrogen generation. ICP-MS analysis validated the positive influence of Cu^{2+} on CO_2 activation, while isotopic labeling demonstrated that CH_4 and CO were products of CO_2 reduction (Fig. 40b and c). Likewise, Su et al. [467] employed a microwave approach to doped $CsPbBr_3$ nanocrystals with GDY, enhancing the photocatalyst's efficiency for CO_2 reduction. The energy alignment and proximity between $CsPbBr_3$ and GDY improved electron transference, resulting in a CO production rate of 27.7 $\mu mol\ g^{-1}\ h^{-1}$, which is eight times greater than that of pure $CsPbBr_3$. The $CsPbBr_3$@GDY composite exhibited notable stability, retaining 89 % of its activity after four cycles (Fig. 40d). Furthermore, Wang et al. [468] synthesized a 2D/2D van der Waals heterostructure of GDY and carbon nitrides (CNs), which exhibited significantly enhanced CO_2 reduction efficiency. The presence of GDY increased the CO production rate to 95.8 $\mu mol\ g^{-1}$, a 19.2-fold improvement compared to pure CNs (Fig. 40e). Moreover, Yang et al. [469] prepared a novel ultrathin 2D/2D heterostructure by growing Bi_2WO_6 nanosheets on GDY nanosheets. This GDY/Bi_2WO_6 heterostructure demonstrated increased photoreduction CO_2 efficiency during synthetic sunshine. The most effective sample (BiGDY-3) converted 4.9 times more CO_2 than Bi_2WO_6. These improvements were due to better light consumption, conductivity, and an increased interaction region, resulting in the more effective division of photoexcited charges. The hybrids also showed enhanced

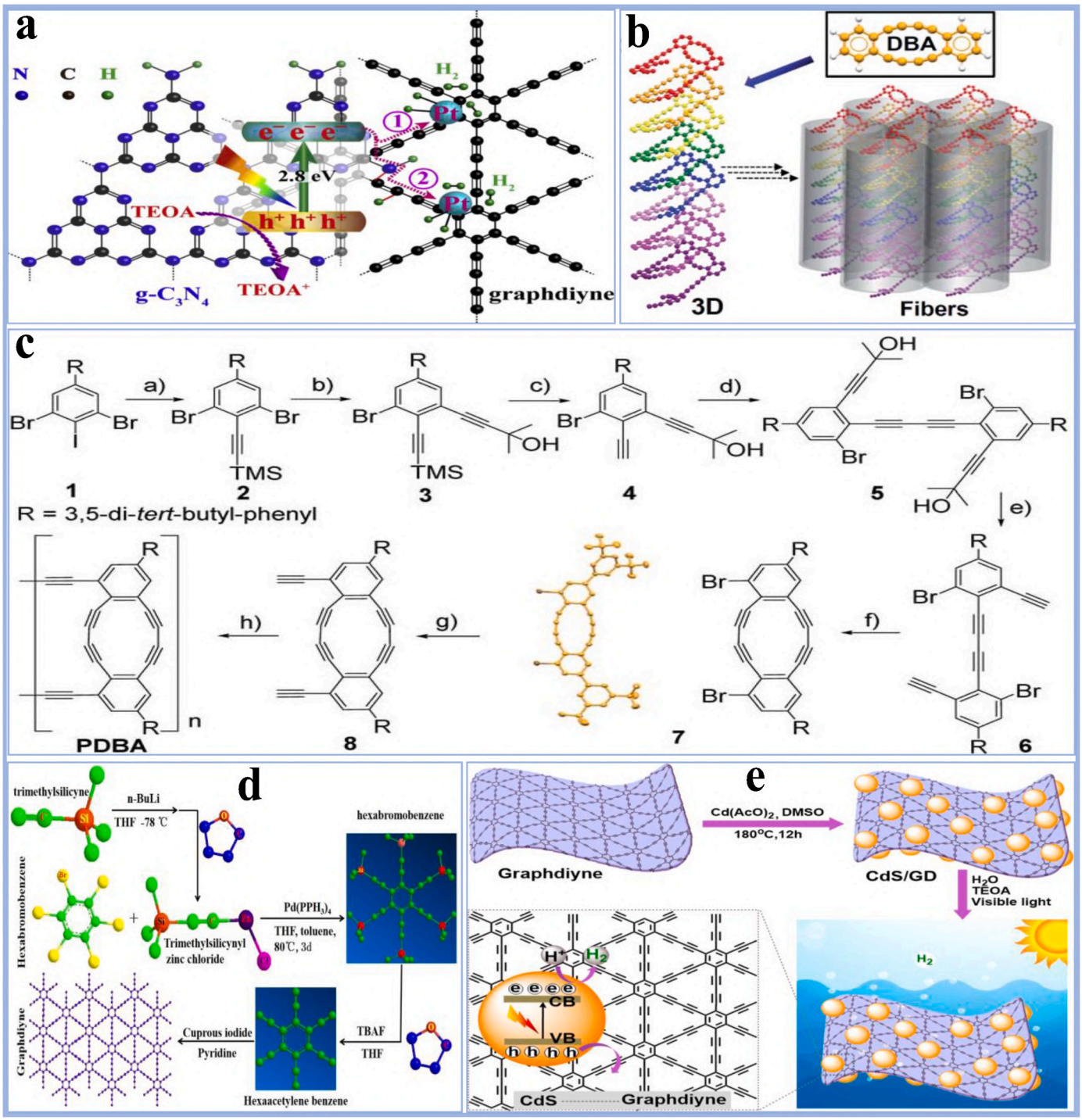

Fig. 41. (a) The photocatalysis process in GD/g-C_3N_4 shortly after Pt nanoparticle addition [476] Copyright © 2019, Elsevier. (b) Developed a 3D alkyne material based on DBA and its potential collective configuration; (c) Synthesis scheme of PDBA [283] Copyright © 2020, Royal Society of Chemistry. (d) Graphical illustration of the photocatalytic HER mechanism of GDY [477] Copyright © 2020, John Wiley and Sons. (e) Synthesis of CdS/GDY composite and photocatalytic method [478] Copyright © 2019, American Chemical Society.

small pores and relative SSA, which improved CO_2 adsorption capacities. The initial photocatalytic efficiency of Bi_2WO_6 for CO_2 reduction is inferior, with a production rate of only 0.42 μmol h^{-1} g^{-1} of CH_3OH and 0.06 μmol h^{-1} g^{-1} of CH_4. Nevertheless, the inclusion of GDY greatly enhances the performance of the activity. The BiGDY-3 hybrid shows yields of 2.13 μmol h^{-1} g^{-1} for CH_3OH and 0.23 μmol h^{-1} g^{-1} for CH_4, resulting in a 4.9-fold rise in CO_2 transformation compared to pure Bi_2WO_6. The improved efficiency may be ascribed to the ultrathin 2D heterojunction's capacity to increase light absorption, decrease charge recombination, and promote CO_2 adsorption. (Fig. 40f). In another study, Zhao et al. [470] also utilized an electrostatic self-assembled approach to prepare a 2D/2D GDY/carbon nitride (GDY/CN) heterostructure. The GDY/CN framework displayed remarkable reliability and robust relationships between CN and GDY. In GDY/CN, photoinduced holes and electrons were split efficiently due to the interface's size and tightness. In situ, XPS and energy band structural characterisation validated photoinduced electrons from CN to GDY during irradiation. Using in-situ FTIR revealed the impressive CO_2 chemisorption ability

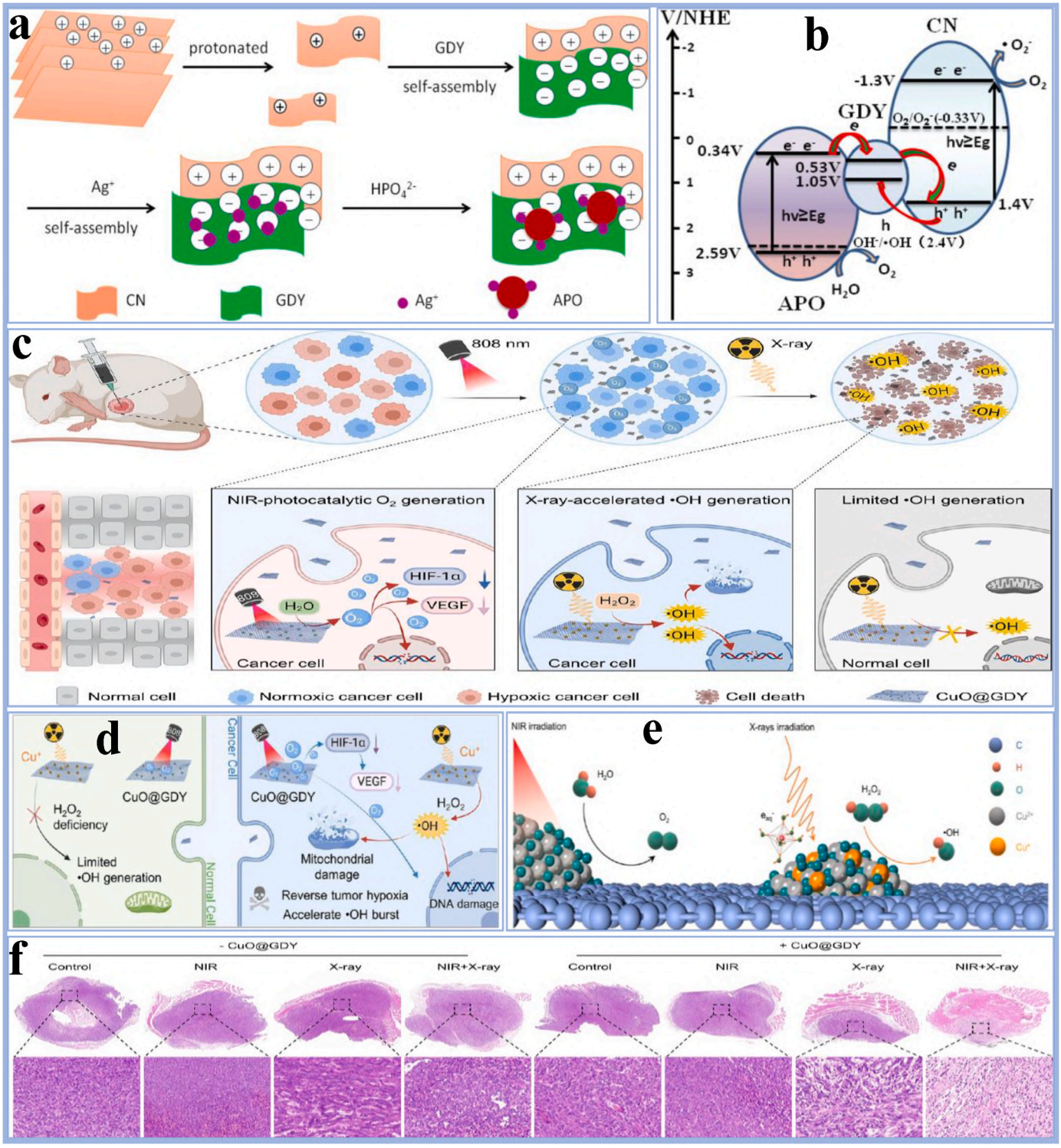

Fig. 42. (a) The synthesis process of APO/GDY/CN nanocomposite; (b) Possible electrons transference process of APO/GDY/CN Z-scheme system [484] Copyright © 2018, Elsevier. (c) CuO@GDY-Mediated Stimuli-Responsively Synergistic Oncotherapy; (d) Graphical illustration of dual-catalytic reaction based on CuO@GDY heterojunction; (e) The proposed scheme of CuO@GDY-mediated stimuli-responsively synergistic therapy; (f) Expression of H&E stained tumor sections [485] Copyright © 2022, American Chemical Society.

and converting procedure of GDY/CN. As a result, under UV light, 2 % GDY/CN produced substantially more CO and CH_4 than pure CN, with strong cycle durability (Fig. 40g). These studies highlight the significant role of GDY in enhancing photocatalytic CO_2 reduction, improving the efficiency of charge separation, and stabilizing catalytic performance across multiple cycles.

6.1.2. *Photocatalytic hydrogen evolution reaction (HER)*

Photocatalytic HER is an efficient method for water splitting (WS), as it transforms solar energy into chemical energy, yielding clean and higher-density hydrogen fuel. The technique necessitates semiconductive photocatalysts that fulfill stringent criteria: they must be adequate, strong, and economical while also having a suitable band

arrangement for adequate WS [83,471]. Layered 2D materials are becoming more popular for this application because of their distinct electronic and optical characteristics [472]. While several 2D materials, including graphene [473], carbon nitride [474], and molybdenum sulfide [475], have been extensively researched, but the novel 2D carbon material GDY has recently attracted considerable interest [38]. For example, Xu et al. [476] developed unique GDY/g-C_3N_4 nano-compounds via an intuitive calcination process, exhibiting remarkable H_2 generation during visible light. The incorporation of a GDY weight ratio of 0.5 % resulted in a 6.7 % enhancement in the HER rate relative to pure g-C_3N_4. The characterization results indicated the formation of a novel CeN interaction between GDY and g-C_3N_4 following thermal treatment, which promotes the transfer of photo-excited electrons from g-C_3N_4 to GDY. This interaction enhanced charge carrier accessibility, extended carrier lifetime, boosted electron volume, and reduced the excess potential necessary for HER. The photoelectrochemical efficiency of g-C_3N_4 and the 0.5 % GDY/g-C_3N_4 composite was analyzed, revealing that the GDY-doped sample demonstrated increased electron density and charge carrier mobility. Mott-Schottky analysis indicated that both materials function as n-type semiconductors and satisfy the thermodynamic criteria for water reduction. The photocatalytic effectiveness of 0.5 % GDY/g-C_3N_4 improved, necessitating a lower overpotential for proton reduction compared to pure g-C_3N_4. The photocurrent of 1%Pt/0.5%GD/g-C_3N_4 was 4.5 times greater, accompanied by a reduced charge-transference resistance, which suggests modified electron-hole separation and boosted charge transference (Fig. 41a). Similarly, Shen et al. [283] fabricated a crystalline 3D alkyne system, PDBA, made from dehydrobenzoannulene, which produces spiral nanofibers. PDBA demonstrated advantageous optical characteristics for WS and photocatalytic HER. PDBA exhibited stable photoresponse and p-type semiconductor properties on an ITO substrate during visible light. The material attained a saturated cathodic photocurrent density of 8.4 mA cm^2 at 0.3 V vs. RHE, surpassing the performance of g-C_3N_4 and red phosphorus. Electrochemical impedance spectroscopy (EIS) demonstrated effective electron-hole separation, while PDBA displayed remarkable stability during 3 h of continuous irradiation. Hydrogen production utilizing PDBA nanofibers, incorporating Pt nanoparticles as co-catalysts and triethanolamine (TEOA) as a sacrificial electron donor, yielded 68.0 mmol of H_2 for 32 h. The system demonstrated a HER rate of 340 mmol h^{-1} g^{-1} and a quantum efficiency of 4.68 % at 420 nm, underscoring the significance of light absorption as a limiting factor (Fig. 41b and c). Likewise, Li et al. [477] designed a CuI-GDY composite for in situ photocatalytic HER, employing Cu^+ particles as a catalytic medium. This catalyst generated 465.95 μmol of H_2 over 5 h, exceeding the performance of pure GDY and CuI by factors of 15.8 and 3.0, respectively. The GDY developed at the interface of CuI, improving photocatalytic productivity owing to its distinctive structure. The addition of platinum to Eosin Y dye sensitization resulted in enhanced hydrogen production and improved electron mobility. The GDY-CuI composite exhibits enhanced light absorption and an extended light-response wavelength, which significantly improves photocatalytic HER productivity (Fig. 41d). Furthermore, Lv et al. [478] fabricated a CdS/GDY heterostructure through in situ growth to enhance photocatalytic HER under visible light. The CdS/GDY composite demonstrated a 2.6-fold enhancement in hydrogen production relative to pure CdS, with optimal performance observed at 2.5 wt% GDY (GDY2.5), yielding 4.1 mmol g^{-1}. This enhancement results from improved electron-hole separation and the inhibition of CdS aggregation. Increased GDY content diminished activity as a result of light scattering. The CdS/GDY composite exhibited significant stability across four cycles, underscoring its promise for renewable photocatalysis (Fig. 41e).

6.1.3. Photocatalytic oxygen evolution reaction (OER)

Considerable research has focused on identifying renewable and affordable electrocatalysts for the photocatalytic OER [479,480]. Scientists have systematically proposed and categorized a range of electrocatalysts to improve efficiency and support environmentally sustainable development [481–483]. For example, Si et al. [484] fabricated a novel Z-scheme Ag_3PO_4/GDY/g-C_3N_4 nanocomposite utilizing electrochemical and π–π stacking interactions (Fig. 42a). This arrangement markedly improved the O_2 evolution rate, reaching 753.1 μmol g^{-1} h^{-1}, which is 12.2 times greater than that of Ag_3PO_4 nanoparticles. The GDY structure functioned as an electron mediator, facilitating electron accumulation and enhancing O_2 evolution while preserving Ag_3PO_4 within the composite. Photocatalytic O_2 production under visible light demonstrated that the absence of light or photocatalysts resulted in no O_2 production. Among the tested materials, APO and APO/CN demonstrated O_2 evolution rates of 61.4 and 375 μmol g^{-1} h^{-1}, respectively. The ternary APO/GDY/CN nanocomposites reached a maximum O_2 production rate of 753.1 μmol g^{-1} h^{-1} at a GDY concentration of 0.05 %, which is double that of APO and APO/CN. Higher GDY concentrations resulted in a reduction in O_2 evolution (Fig. 42b). Similarly, Wang et al. [485] fabricated a spatiotemporally controlled synergistic treatment structure employing the heterojunction CuO@Graphdiyne (CuO@GDY) nanocatalyst. The in-situ produced Z-scheme CuO@GDY heterostructure effectively alleviates tumor hypoxia by demonstrating regulated and optimal photocatalytic O_2 production when exposed to near-infrared (NIR) excitation. Subsequently, in reaction to Indigenous H_2O_2, the CuO@GDY nanocatalyst, which contains Cu^+ activated sites stimulated by X-rays, can enhance the Fenton-like catalysis of •OH production, thus promoting the targeted elimination of tumor cells while sparing healthy cells (Fig. 42c). The CuO@GDY heterostructure demonstrated high productivity in O_2 production via NIR photocatalysis. The Z-scheme CuO@GDY heterojunction exhibited enhanced charge transference and conductivity, evidenced by its peak photocurrent density and minimal resistance under 808 nm laser irradiation. This configuration facilitated the effective transference of electrons and holes generated by light, leading to enhanced O_2 production. The amount of dissolved oxygen generated was more than twice that observed with a combination of CuO and GDY. The Z-scheme process enabled efficient charge separation, optimizing the generation of both O_2 and H_2. The CuO@GDY system demonstrated controlled and replicable O_2 production, providing a means to enhance oxygen levels in real-time during tumor hypoxia therapy (Fig. 42d). This approach improved radiosensitization in hypoxic tumors by creating Cu^+ sites, which generated highly reactive •OH from H_2O_2 in the tumor, sparing healthy tissues. The process was validated by identifying Cu^+ locations and enhanced •OH signals, demonstrating a viable strategy for targeted radiosensitization (Fig. 42e). In vivo experiments on 4T1 tumor-bearing mice confirmed the efficacy of the CuO@GDY nanocatalysts. Tumor oxygenation increased significantly, reducing hypoxia and HIF-1α signals, and leading to reduced VEGF and CD31 production. Treatment with CuO@GDY + X-ray showed superior tumor suppression compared to X-ray alone, likely due to the combined effects of oxygen generation and •OH production. The CuO@GDY + NIR + X-ray treatment resulted in the most significant tumor growth inhibition and enhanced radiation sensitivity, supported by tumor weight measurement, size reduction, and histological analysis (Fig. 42f).

6.1.4. Photocatalytic overall water splitting (OWS)

GDY has emerged as a promising photocatalyst for OWS due to its exceptional stability and strong reactivity, making it both effective and cost-efficient [486]. Unlike many existing methods that rely on expensive metals or sacrificial agents, GDY offers a potential solution for more efficient OWS, drawing significant interest from scientists across various fields [116]. For example, Fan et al. [487] introduced a novel S-scheme heterostructure hybrid photocatalyst for generating H_2 and H_2O_2 from photocatalytic OWS. This composite, made from GDY and phosphorylated NiFe multilayered hydroxide (NiFe-P), was characterized using XRD, which confirmed the phase integrity and composition. NiFe-LDH exhibited peaks at 2θ = 11.5, 23.3, 34.6, 39.0, 46.4, 60.1, and 61.3°,

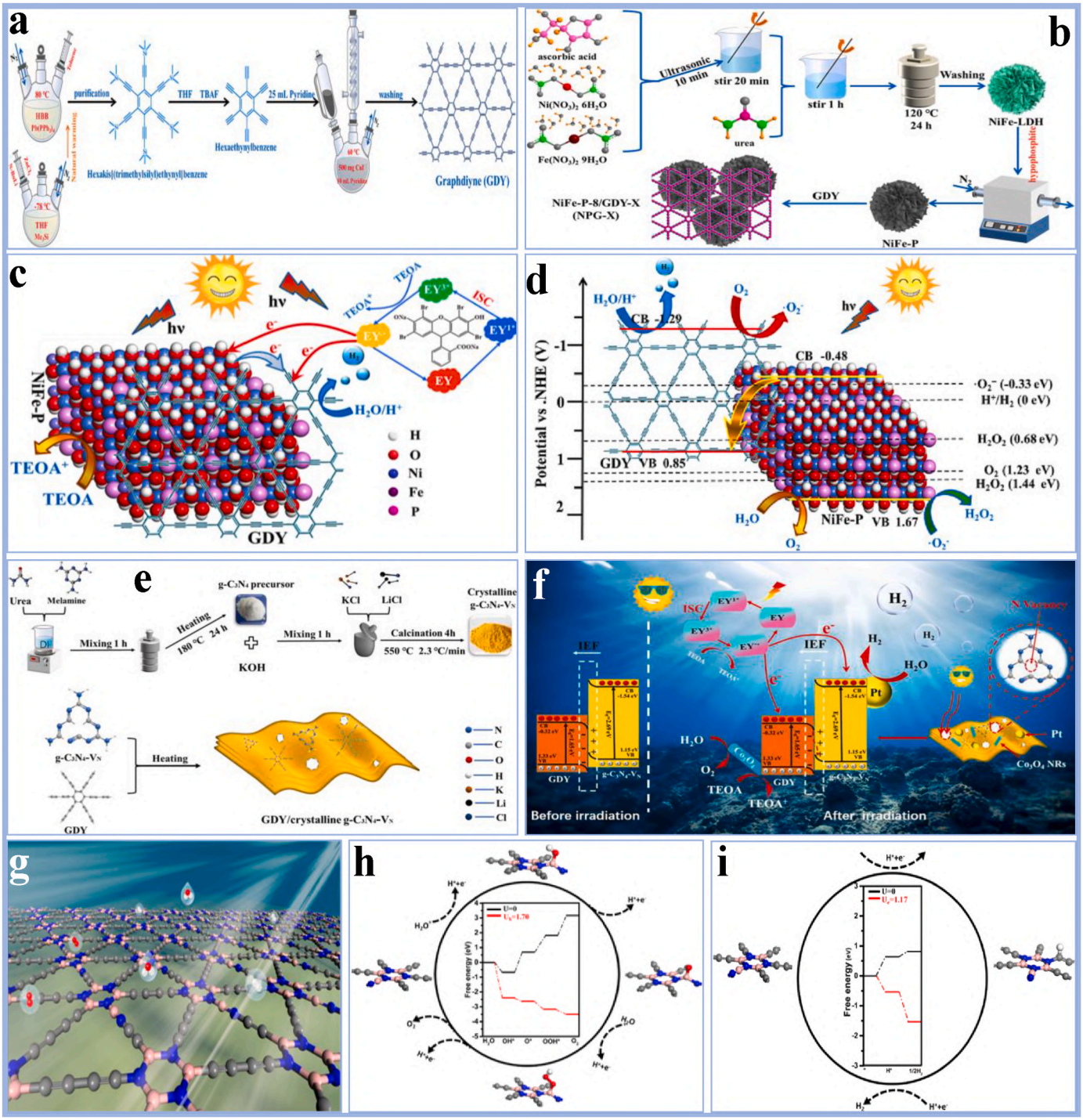

Fig. 43. The synthetic route of (a) GDY; (b) NiFe-LDH, NiFe-P, and NPG-X; (c) Graphical illustration for the charge transference and dissociation in the NPG-7 network; (d) Proposed mechanism of S-scheme NiFe-P/GDY for photocatalytic production of H_2 and H_2O_2 [487] Copyright © 2023, Elsevier. (e) The synthetic route of crystallized g-C_3N_4-V_N and GDY/crystallized g-C_3N_4-V_N; (f) The charge transference process over EY-sensitized CNG-X S-scheme heterojunction and POWS of Pt/CNG-25/Co_3O_4 composite [340] Copyright © 2023, Elsevier; (g) Graphical illustration of GDY monolayer via B, N-Codoping; Proposed POWS mechanism of (l) H_2O oxidation; (m) H_2 productivity [488] Copyright © 2020, American Chemical Society.

corresponding to specific crystalline planes, while the Ni_2P peaks were observed at $2\theta = 40.7$, 44.7, 47.4, and 54.2°, confirming full phosphorylation. GDY showed a prominent peak at 23° related to the (002) crystalline plane. Raman analysis revealed characteristic D- and G-bands at 1368 cm^{-1} and 1563 cm^{-1}, indicating efficient GDY processing. FTIR spectra further confirmed the C ≡ C stretching vibration at 2179 cm^{-1}, supporting GDY's effectiveness. Hydroxy reactive capturing tests and in-situ XPS measurements validated the electron transfer process in the S-scheme heterostructure. The composite achieved peak H_2 and H_2O_2 yields of 674 μmol $h^{-1}g^{-1}$ in purified water under photocatalytic OWS. The NPG-7 composite exhibited strong catalytic activity under visible light ($\lambda > 420$ nm), producing 4.64 mmol g^{-1} of H_2 and 0.58 μmol g^{-1} of O_2 without deactivation over four cycles. The results showed NPG-7's superior oxidation capability and potential for photocatalytic OWS. Additionally, NPG-7 produced 3.37 mmol g^{-1} of H_2O_2, highlighting its potential for OWS (Fig. 43a–d). Similarly, Deng et al. [340] developed a

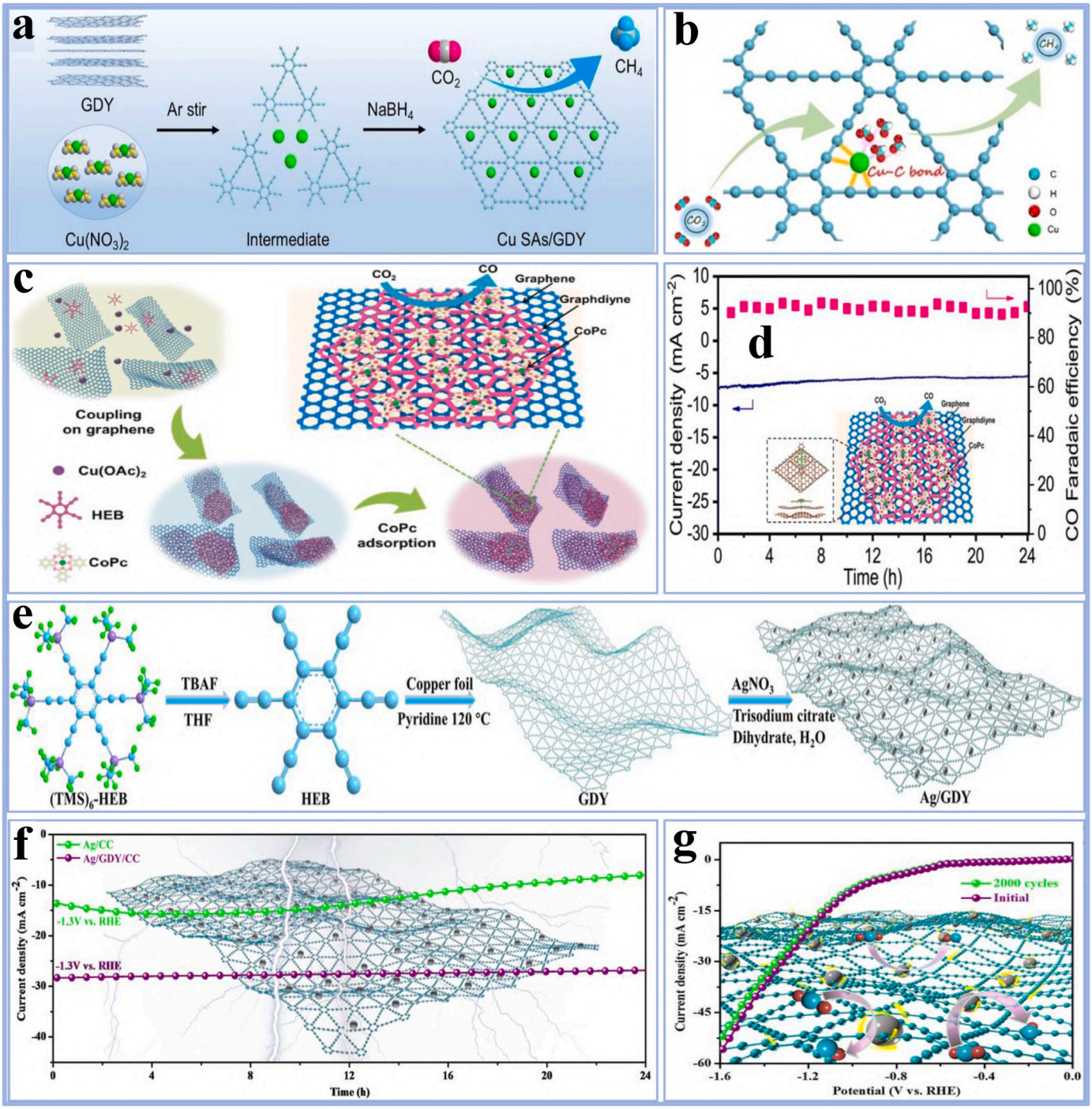

Fig. 44. (a) Synthetic process; (b) Proposed electrocatalytic CO_2RR mechanism of Cu SAs/GDY [493] Copyright © 2022, John Wiley and Sons. (c) Synthetic process; (d) Proposed electrocatalytic CO_2RR mechanism of GDY/G heterostructures [494] Copyright © 2021, American Chemical Society. (e) Synthetic process of Ag/GDY nano-electrocatalyst; (f, g) Stability test of Ag/GDY/CC LSV curves [495] Copyright © 2021, John Wiley and Sons.

2D-2D S-scheme heterostructure by combining 2D GDY with N_2-defected g-C_3N_4 nanosheets (GDY/g-C_3N_4-VN) for effective photocatalytic OWS. GDY was synthesized through cross-coupling reaction between hexaethynylbenzene and CuI. The GDY/g-C_3N_4-VN heterostructure was created using an alkali-molten salt method and its N defects. In situ XPS and ESR spectra demonstrated the successful formation of the S-scheme heterojunction, which enhanced charge separation and increased photoexcited carrier efficiency. The photocatalytic HER for CNG-25 increased 25.23-fold to 17.87 μmol h^{-1}, significantly outperforming GDY alone. For OWS, a composite of 3 % Co_3O_4 and 1 % Pt on CNG-25 produced H_2 at 0.48 μmol h^{-1} and O_2 at 0.24 μmol h^{-1}. Their research highlights the promising application of the CNG-25 photocatalyst. The efficiency of photocatalytic OWS was further enhanced by adding oxidation/reduction cocatalysts (Co_3O_4/Pt), with the highest hydrogen and oxygen production (0.47 μmol h^{-1} H_2, 0.24 μmol h^{-1} O_2) at a Co_3O_4 concentration of 3 %. But, higher Co_3O_4 content reduced performance. The catalyst exhibited excellent stability, confirming the potential of CNG-25 for photocatalytic applications (Fig. 43e and f). Furthermore, Xu et al. [488] conducted a comprehensive study using DFT analyses to explore the optical, thermal, and dynamic properties of 2D GDY

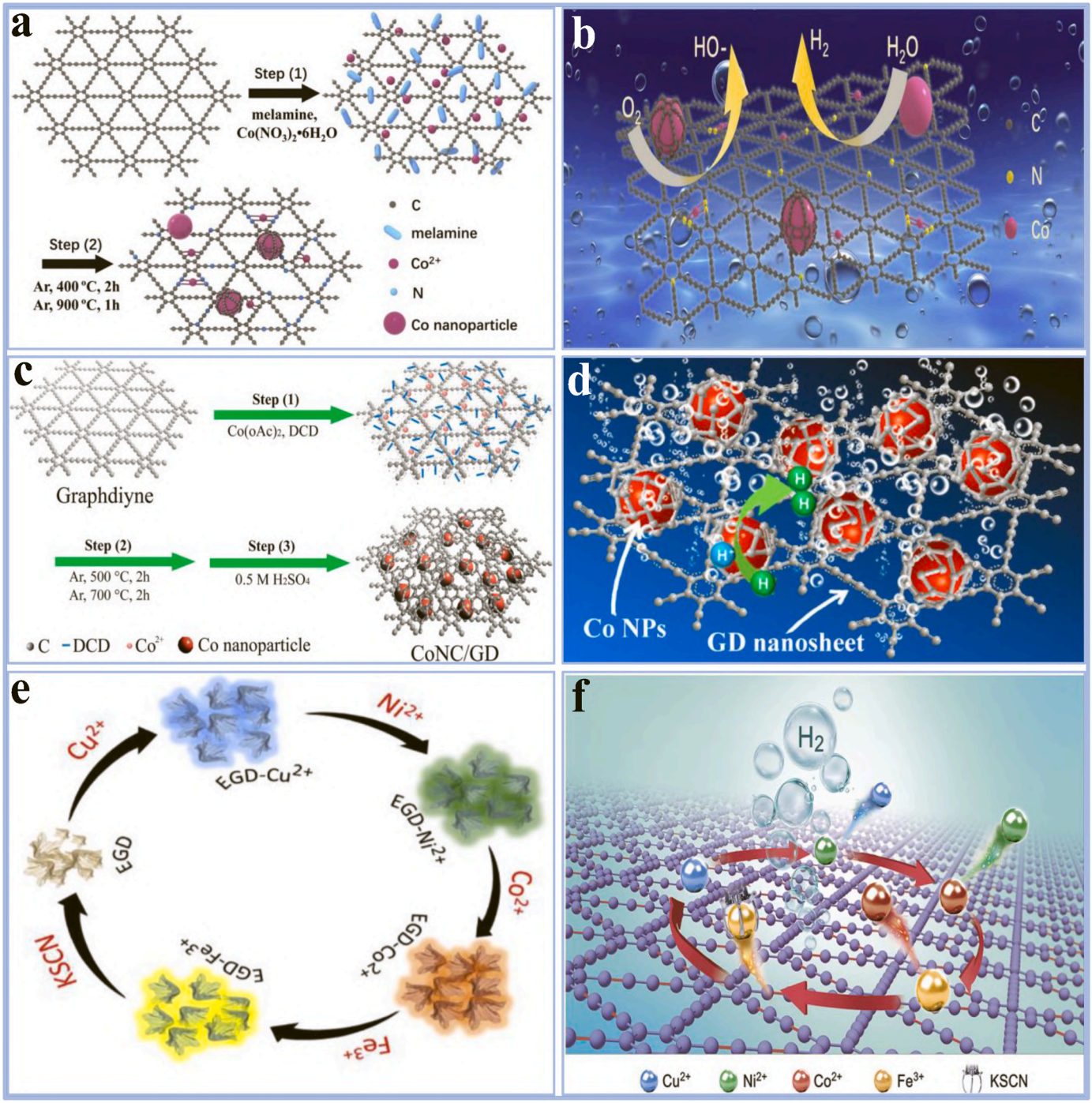

Fig. 45. (a) Synthetic process; (b) Proposed electrocatalytic HER mechanism of Co-N-GDY [501] Copyright © 2019, Elsevier. (c) Synthetic process; (d) Proposed electrocatalytic HER mechanism of CoNC/GDY [502] Copyright © 2016, American Chemical Society. (e) The HER polarization curves for EGDY, EGDYCu^{2+}, EGDY-Ni^{2+}, EGDY-Co^{2+}, and EGDY-Fe^{3+}; (f) Proposed electrocatalytic HER mechanism of GDY (EGDY-Mn^{+}) nanocomposites [503] Copyright © 2019, Elsevier.

monolayers doped with boron and nitrogen. Their results revealed that BCN ternary semiconductive monolayers, with specific N and B configurations, possess suitable band gaps for absorbing visible light. The valence band maximum (VBM) and conduction band minimum (CBM) of these monolayers align with the redox potentials for WS. Reactive sites on the BCN monolayers were found to be capable of undergoing water oxidation and hydrogen reduction processes when exposed to photoinduced electrons and holes. These monolayers exhibited strong light absorption properties, stability, and dynamic rigidity even at elevated temperatures. Without the need for sacrificial reagents or co-catalysts, BCN monolayers derived from GDY demonstrated exceptional photocatalytic performance OWS, efficiently producing H_2 and O_2. Their research contributes significantly to the field of non-metallic 2D photocatalysts for OWS applications. But, while the BCN monolayers exhibit favorable band structures for hydrogen and oxygen production, further research is needed to fully assess their efficiency in neutral pH environments, where WS is most effective. Their research also evaluated the changes in free energy (ΔG) for key water oxidation and hydrogen reduction steps on BCN monolayers. The B1 site showed the highest activity for water oxidation, while the C1 site was optimal for hydrogen reduction. At pH 7, the photoexcited electron (*Ue*) and hole (*Uh*) values were 1.17 V and 1.70 V, respectively, supporting the spontaneity of the

WS process. Their research also investigated intermediates (OH*, O*, OOH*) and reaction-free energies under both dark and light conditions, underscoring the monolayers' potential for efficient photocatalytic WS (Fig. 43g–i).

6.2. Electrocatalysts

6.2.1. Electrocatalytic CO_2 reduction

Electrocatalytic CO_2 reduction (CO_2RR) is an approach that employs electricity to transform CO_2 into valuable chemicals or fuels, such as carbon monoxide (CO), methane (CH_4), or formic acid (HCOOH) [489]. This approach provides a sustainable method for recycling CO_2, reducing greenhouse gas emissions, and facilitating sustainable energy conservation. GDY significantly contributes to the improvement of performance and selectivity in CO_2RR [490]. The sp- and sp^2-HCAs in GDY facilitate effective electron transference and activation of CO_2 molecules, which is essential for lowering the energy barrier in CO_2 transformation [366,491]. Integrating heteroatoms or introducing structural imperfections in GDY may enhance its catalytic activity, hence enhancing CO_2RR efficiency [455]. GDY's capacity to serve as a stable, effective electrocatalyst in CO_2RR positions it as a viable material for sustainable carbon capture and conversion technologies, aiding the growth of a carbon-neutral economy [492]. For example, Shi et al. [493] devised a method to improve the selectivity of electrocatalytic CO_2RR to CH_4 by immobilizing single copper atoms (Cu SAs) on GDY. The in-situ synthesis of Cu-C bonds on the GDY platform enhances charge transference and redirects the reaction route towards the generation of *OCHO intermediates rather than *COOH, hence facilitating CH_4 production. DFT simulations validated that the Cu-C bond plays an essential role in regulating reaction intermediates, thus markedly enhancing the catalytic effectiveness for CO_2-to-CH_4 conversion (Fig. 44a). The remarkable electrocatalytic effectiveness of Cu SAs/GDY arises from multiple factors: the distinctive GDY design secures Cu single atoms, guaranteeing effective catalytic sites and obstructing multicarbon product formation; robust CO_2 adsorption hinders HER; the Cu-C(GDY) bond modulates Cu's electronic configuration, promoting *OCHO intermediate generation; and proficient proton-electron coupling fosters selective CH_4 synthesis, enhancing CO_2 reduction efficiency and selectivity (Fig. 44b). Their research provides novel insights into atomic-scale catalyst design for selective CO_2 reduction processes. Similarly, Gu et al. [494] engineered a graphdiyne/graphene (GDY/G) heterostructure as a proficient electrocatalyst for electrochemical CO_2RR. The heterostructure supports monodispersed cobalt phthalocyanine (CoPc), ensuring elevated activity, selectivity, and longevity. The robust electronic interaction between GDY and CoPc, together with the elevated SSA and conductivity of graphene, improves electrochemical productivity. The catalyst attained a CO_2R effectiveness (FECO) of 96 % at 12 mA cm^{-2} and 97 % at 100 mA cm^{-2}, demonstrating remarkable endurance. The CoPc turnover frequency of 37 s^{-1} surpasses several other electrocatalysts (Fig. 44c and d). Their research emphasizes the promise of the GDY/G heterostructure in the development of effective, single-molecule distributed CO_2R catalysts for renewable energy transformation. Furthermore, Xie et al. [495] engineered a robust and effective electrocatalyst for electrochemical CO_2RR by the in situ synthesis of homogeneous silver nanoparticles (AgNPs) on 2D GDY. GDY functions as a template to inhibit AgNP aggregation while simultaneously boosting active sites and facilitating electron transport due to its distinctive electronic characteristics, hence enhancing catalytic efficiency. The Ag/GDY/CC composite attained a Faraday efficiency of 92.1 % and a current density of 25.74 mA/cm^2 at −1.3 V vs. RHE, demonstrating remarkable stability over 24 h (Fig. 44e). The stability of the Ag/GDY/CC composite for electrochemical CO_2RR was assessed using electrolysis in a CO_2-saturated 0.1 M $KHCO_3$ mixture. The Ag/GDY/CC electrode sustained a current density of 25.74 mA/cm^2 for 24 h at −1.3 V, while Ag/CC exhibited a significant decrease in current. Furthermore, after 2000 cycles, the Ag/GDY/CC electrode showed little degradation, verifying its exceptional stability for CO_2 reduction to CO (Fig. 44f and g). Their research is the first experimental evidence of GDY-derived catalysts for the CO_2RR.

6.2.2. Electrocatalytic HER

The electrocatalytic HER is a fundamental mechanism for hydrogen generation, especially in WS technologies [496]. The process involves the electrochemical reduction of protons (H^+) to generate hydrogen gas. In this regard, GDY is essential owing to its distinctive composition and features [497]. GDY, characterized by its extensive conjugated acetylenic linkages and 2D structure, provides a very conductive medium for electrocatalysis [498]. When combined with additional substances, such as metallic nanoparticles or dopants, GDY improves the effectiveness of the HER by increasing active sites, enhancing electron transport, and accelerating proton coupling [120]. GDY's distinctive electrical configuration, coupled with its capacity to immobilize metal catalysts and stable reactive intermediates, renders it an optimal choice for electrocatalytic HER applications, promising increased catalytic efficiency and durability in sustainable hydrogen generation systems [499,500]. For example, Wang et al. [501] proposed a novel electrocatalyst, Co and N enriched GDY (Co-N-GDY), aimed at substituting precious metals in ORR and HER. The Co-N-GDY, produced with 1 % cobalt, exhibited superior catalytic activity for both reactions. The catalyst demonstrated ORR behavior on par with commercial Pt/C, attributed to the synergistic impacts among Co, N, and GDY, and showed a superior half-wave potential relative to other Co-loaded carbon materials. In HER, the Co-N-GDY exhibited a low onset overpotential of 97 mV and a small Tafel slope of 132 mV per decade, surpassing numerous documented non-precious metal catalysts (Fig. 45a). The 1 % Co-N-GDY catalyst exhibited superior effectiveness in the HER within a 0.5 M H_2SO_4 solution, characterized by an onset overpotential of 53 mV and a swift increase in current, signifying its higher productivity for hydrogen production. Co-N-GDY catalysts with elevated Co concentrations (1.5 % and 2 %) demonstrated comparable HER behavior to the 1 % Co-N-GDY. The Tafel slope for 1 % Co-N-GDY was the lowest at 117 mV per decade, indicating its superior efficiency. The catalyst demonstrated remarkable stability, exhibiting minimal degradation following 20 h of testing and 5000 cycles. The relationship between Co and GDY, combined with the inclusion of pyridinic, graphitic, and sp N active sites, enhanced its bifunctional catalytic activity for OER and HER (Fig. 45b). Similarly, Xue et al. [502] fabricated a durable and effective electrocatalyst, CoNC/GDY, which comprises GDY nanosheets supported by cobalt nanoparticles and encased in nitrogen-doped carbon. This catalyst showed exceptional efficiency in the HER across all pH levels, with durability shown over 36,000, 38,000, and 9000 cycles in basic, acidic, and neutral conditions, respectively, surpassing commercial Pt/C. The catalyst exhibits higher durability and catalytic activity, positioning it as an offering perspective for practical applications in water splitting (Fig. 45c). The electrochemical efficiency of the CoNC/GDY catalyst in 1 M KOH was assessed through electrochemical impedance spectroscopy (EIS). The lowest recorded values of series resistance (Rs, 10.03 Ω) and charge transference resistance (Rct, 27.49 Ω) were found for CoNC/GDY, demonstrating its enhanced activity for the HER relative to other catalysts (Fig. 45d). Furthermore, Hu et al. [503] synthesized non-precious metallic ion-functionalized exfoliated GDY (EGDY-Mn^+) nanocomposites, demonstrating significant and adjustable catalytic efficiency for the HER. The relation in strength between metal ions and EGDY was observed in the following order: $Cu^{2+} < Ni^{2+} < Co^{2+} \ll Fe^{3+}$, where stronger interactions correlated with increased catalytic activity. The HER efficiency of EGDY-Mn^+ catalysts can be reversibly modified by altering coordination with anions of different strengths. Their research demonstrated effective OWS utilizing EGDY-Co^{2+} and RuO_2 as catalysts for HER and OER, respectively, underscoring the potential of EGDY-Co^{2+} for water electrolysis. DFT calculations elucidated the adjustable activity of these catalysts, indicating their potential applications in energy conversion and other areas (Fig. 45e). The HER function

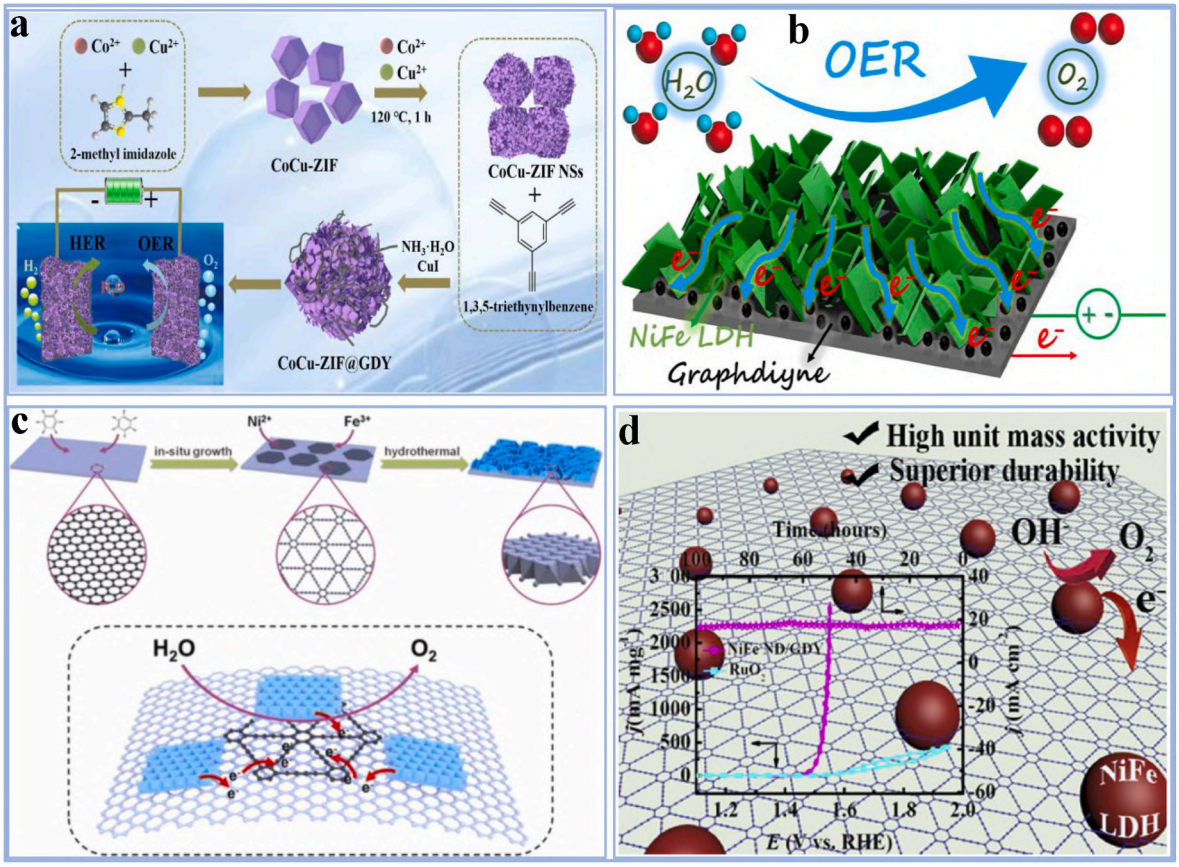

Fig. 46. (a) Proposed electrocatalytic OER mechanism of CoCu-ZIF@GDY catalyst [414] Copyright © 2020, Elsevier. (b) Proposed electrocatalytic OER mechanism of GDY-based NiFe-layered double hydroxide [510] Copyright © 2019, American Chemical Society. (c) Proposed electrocatalytic OER mechanism of NiFe-LDH [413] Copyright © 2022, Elsevier. (d) Proposed electrocatalytic OER mechanism of 3D GDY nanowalls [511] Copyright © 2020, Elsevier.

of EGDY-Mn^{+} catalysts can be reversibly adjusted through coordination with anions of varying strengths. DFT calculations indicated that enhanced anion interactions result in improved hydrogen ion adsorption and increased HER activities, with EGDY-Co^{2+} demonstrating the highest efficiency, similar to commercial Pt/C. Their research indicated that EGDY can be readily regenerated from EGDY-Mn^{+} through anionic ion exchange, providing an efficient approach for the development of cost-effective GDY-derived HER catalysts with adjustable characteristics (Fig. 45f).

6.2.3. *Electrocatalytic OER*

The electrocatalytic OER is a fundamental procedure in the energy transformation, particularly in WS, where water molecules undergo oxidation to produce oxygen gas [504]. The effectiveness of OER is significantly influenced by the efficiency of electrocatalysts, which must enable this reaction at a lower overpotential while maintaining higher durability [505]. GDY, characterized by its distinctive acetylenic bonds and elevated SSA, demonstrates significant potential as an electrocatalyst for the OER [506]. The intrinsic electronic framework of GDY can be modified through loading or functionalization, thereby improving its capacity to adsorb and activate water molecules, which increases the efficiency of the OER procedure [229]. Materials founded on GDY, particularly when integrated with transition metals such as cobalt or iron, can markedly decrease the energy barriers for the OER, thereby enhancing catalytic efficiency [507,508]. GDY is essential for the development of effective, low-cost, and reliable electrocatalysts applicable in sustainable energy technologies, including WS and metal-air batteries [509]. For example, Cui et al. [414] proposed an innovative electrocatalyst, CoCu-ZIF@GDY, which integrates 1D CoCu-derived zeolitic imidazolate framework (CoCu-ZIF) nanosheets with GDY nanowires to enhance the efficiency of the OER and OWS in the alkaline mixture. The CoCu-ZIF nanosheets, produced via a two-step synthesis, demonstrated a 2D structure characterized by a significant presence of $CoCu_2O_4$ spinel. Additionally, GDY contributed to enhanced conductivity, oxygen adsorption, and an abundance of active sites. The combination of CoCu-ZIF and GDY resulted in enhanced OER efficiency, attaining a low overpotential of 250 mV at a current density of 10 mA/cm^2. The catalyst exhibited remarkable durability and a low overpotential of 290 mV in the process of OWS. Their work emphasizes the effectiveness of integrating bimetallic metal-organic frameworks (MOFs) and covalent organic frameworks (COFs) as electrocatalysts in renewable energy applications (Fig. 46a). Similarly, Shi et al. [510] developed an innovative GDY-based NiFe-layered double hydroxide (LDH) composite for catalyzing the OER. The distinct structural characteristics of GDY, such as its conjugated sp^2 and sp-hybridized carbon configurations, contribute to its higher SSA, consistent pore structure, and remarkable chemical durability. The GDY@NiFe composite demonstrated exceptional catalytic efficiency, necessitating a minimal overpotential of 260 mV to reach a current density of 10 mA/cm^2. Their work showed outstanding reliability in alkaline conditions, suggesting superior electrochemical activity for the OER. Their work offers essential perspectives into the development of GDY-supported electrocatalysts for OER applications (Fig. 46b). Furthermore, Shi et al. [413] designed a 2D few-layered GDY/G heterostructure to support NiFe-layered double hydroxides (NiFe-LDH) aimed at improving OER efficiency. The GDY/G heterostructure enhances conductivity for charge transference across the graphene layer and modulates the electronic structure of NiFe-LDH through a robust covalent bond with GDY. The NiFe-LDH/GDY/G catalyst demonstrated a low overpotential of 215 mV at 10 mA/cm^2 and a Tafel slope of 22 mV/dec, attributed to improved

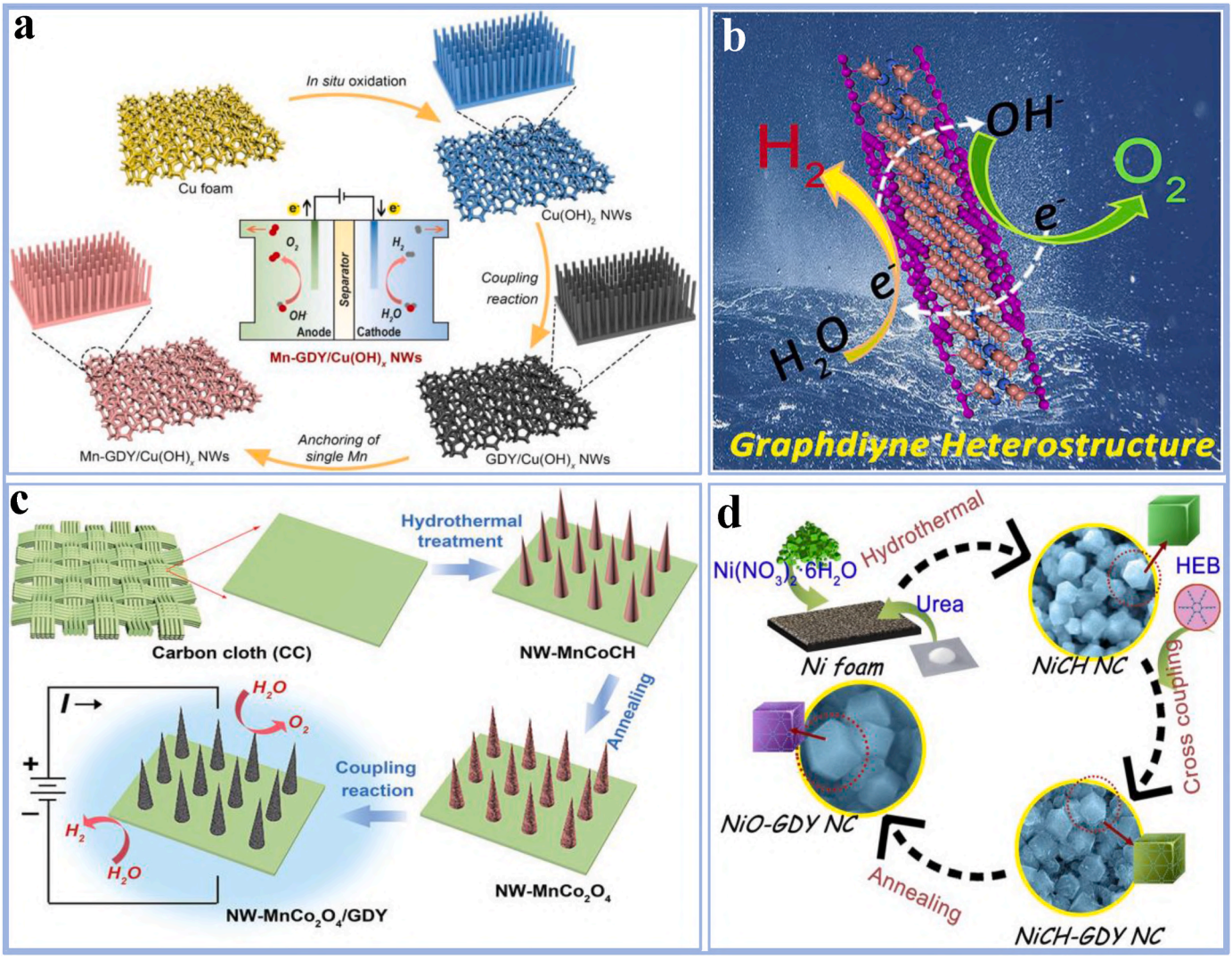

Fig. 47. (a) Proposed electrocatalytic OWS mechanism of Mn–GDY/Cu(OH)$_x$ NWs [517] Copyright © 2024, Elsevier. (b) Proposed electrocatalytic OWS mechanism of GDY-wrapped CN nanosheets [518] Copyright © 2019, Elsevier. (c) Proposed electrocatalytic OWS mechanism of NW-MnCo$_2$O$_4$/GDY [335] Copyright © 2021, John Wiley and Sons. (d) Proposed electrocatalytic OWS mechanism of NiO-GDY NC [409] Copyright © 2019, Elsevier.

electrochemical activity, accelerated charge transference, and an increased active SSA. Their work emphasizes the capability of GDY/G heterostructures to enhance electrochemical performance in OER applications (Fig. 46c). Moreover, Lv et al. [511] fabricated a heterojunction electrocatalyst composed of a 3D GDY nanowall and NiFe layered double hydroxide (LDH) nanodots, referred to as NiFe ND/GDY, aimed at facilitating water oxidation in alkaline solutions. Enhancing the NiFe-LDH loading resulted in a NiFe ND/GDY catalyst characterized by ultrasmall nanodots measuring 2.7 nm, demonstrating strong interfacial coupling to GDY. The distinctive 0D/3D framework facilitated the catalyst in attaining a low overpotential of 252 mV at 10 mA/cm^2, alongside a minimal Tafel slope of 39.70 mV/dec. The catalyst demonstrated a mass activity 70 times greater than that of commercial RuO_2 (631 A/g compared to 9 A/g) and exhibited remarkable long-term stability, with merely 10 % degradation observed over 100 h of continuous electrolysis. Their work illustrates the potential of GDY as an effective substrate for the anchoring of ultrafine catalysts in water oxidation and related applications (Fig. 46d). Their work presents novel findings on the development of nanostructure hybrid electrodes utilizing GDY, highlighting their potential applications in water oxidation and related methods.

6.2.4. *Electrocatalytic OWS*

Electrocatalytic OWS is the procedure of employing electrochemical processes to decompose water into hydrogen and oxygen, primarily via the HER and the OER [512]. This procedure is essential for the feasible production of hydrogen as a clean energy source [513]. GDY significantly enhances electrocatalytic OWS owing to its superior electrical conductivity, extensive SSA, and chemical durability [335]. GDY serves as a supportive structure for anchoring metal-derived catalysts like NiFe-LDH and CoCu-ZIF, enhancing the performance of OWS through improved charge transference, increased active sites, and accelerated electron transport [514,515]. GDY's capacity to sustain stability in extreme conditions and its robust interaction with metal ions render it an optimal substrate for the development of effective electrocatalysts for OWS, thereby promoting advancements in WS technologies for clean hydrogen fabrication [516]. For example, Qi et al. [517] introduced an innovative atomic catalyst (AC) consisting of single Mn atoms distributed on GDY-doped copper hydroxide nanowire arrays (Mn–GDY/Cu(OH)$_x$ NWs). This catalyst markedly improves SSA, active sites, and durability. The elevated catalytic efficiency for the HER and OER is ascribed to the significant insufficient charge transference between the Mn atoms and GDY. The Mn–GDY/Cu(OH)$_x$ NWs demonstrated overpotentials of 188 mV for the OER and 130 mV for the HER at a current

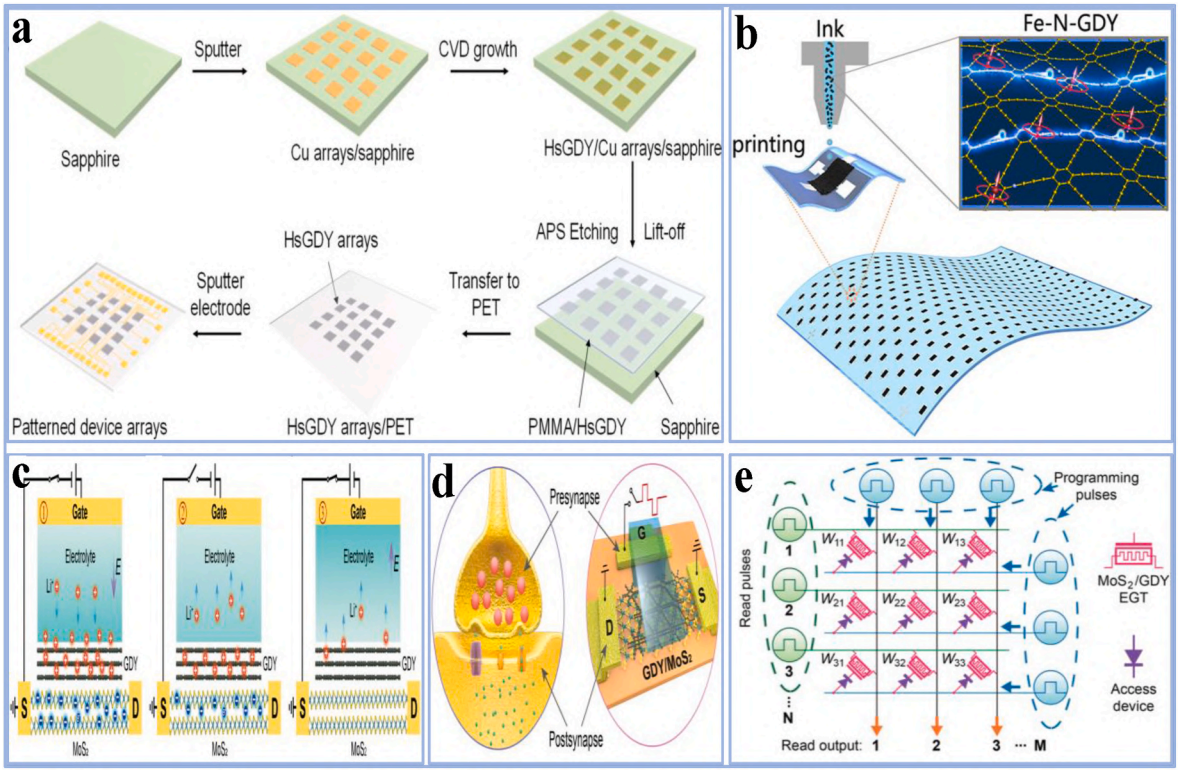

Fig. 48. (a) The synthetic route for flexible sensing arrays encompasses Cu deposition on sapphire, HsGDY film expansion, a PMMA-based transference procedure, and electrode deposition [404] Copyright © 2022, American Chemical Society. (b) Schematic representation of the synthesis process for Fe−N-GDY material [524] Copyright © 2021, American Chemical Society. (c) The intercalation processes of Li ions to GDY layers; (d) Analogy between a biological synapse and the EGT device; (e) The circuits of an EGT-based crossbar array for matrix operations [525] Copyright © 2021, John Wiley and Sons.

density of 10 mA cm^{-2}, exhibiting remarkable long-term stability. In an alkaline electrolyzer, it achieved a current density of 10 mA cm^{-2} at a low cell voltage of 1.50 V, indicating the possibility for effective OWS (Fig. 47a). Similarly, Fang et al. [518] described the controlled production of GDY-wrapped cobalt nitride nanosheets, utilized for the first time as a bifunctional electrocatalyst in WS. The catalyst demonstrated superior catalytic efficiency in 1.0 M KOH, with overpotentials of 70 mV for the HER and 260 mV for the OER at 10 mA cm^{-2}, surpassing commercial Pt/C and RuO_2. In a two-electrode alkaline electrolyzer, a current density of 10 mA cm^{-2} was attained at a low cell voltage of 1.48 V, which is considerably lower than that of the Pt/C–RuO_2 couple, underscoring its outstanding effectiveness for WS (Fig. 47b). Furthermore, Qi et al. [335] developed $MnCo_2O_4$/GDY nanowire arrays on 3D carbon cloth (NW-$MnCo_2O_4$/GDY) to serve as non-precious metallic-derived electrocatalysts for effective OWS. The core/shell nanowire framework, along with the synergistic interaction between $MnCo_2O_4$ and GDY, improved electrical conductance, mass and ion transfer, gas emission, and exposure of active sites, resulting in modified catalytic efficiency and longevity. The alkaline water electrolyzer utilizing NW-$MnCo_2O_4$/GDY demonstrated superior efficiency, necessitating only 1.47 and 1.60 V to reach current densities of 10 and 100 mA cm^{-2}, respectively, surpassing previously documented electrocatalysts (Fig. 47c). Moreover, Yu et al. [409] fabricated a GDY-coated nickel oxide heterojunction to serve as an electrocatalyst for effective OWS. This catalyst improves charge transference, expands the electrocatalytically active surface area, optimizes active sites, and provides protection against corrosion during the durability assessments. It demonstrates superior performance compared to commercial Pt/C and RuO_2 in both HER and OER activities. The catalyst demonstrates enhanced OWS efficiency when utilized as both cathode and anode in a two-electrode alkaline electrolyzer, surpassing the efficiency of the Pt/C||RuO_2 couple. Simulations indicate that the heterostructure enhances charge transference processes and the adsorption of hydrogen and oxygen species, thereby maximizing OWS efficiency (Fig. 47d).

6.3. Electronic devices

Electronic devices encompass a wide array of technologies that manage or alter electrical energy to execute particular functions, including computing, communication, sensing, and signal processing [519]. Components such as transistors, diodes, sensors, and integrated circuits are included [520]. GDY possesses unique sp and sp^2 hybridized carbon frameworks, which confer exceptional electronic characteristics such as high conductivity, a tunable bandgap, and excellent mechanical stability, positioning it as a promising candidate for electronic device applications [521,522]. The material's elevated SSA and electronic adaptability facilitate its use in advanced electronics, such as flexible and transparent devices, advanced transistors, and energy storage systems [523]. GDY effectively transports charge carriers and exhibits chemical stability, making it a potential alternative or complement to conventional materials such as graphene in various electronic applications, thereby improving efficiency, miniaturization, and stability [49]. For example, Cai et al. [404] fabricated a conductive hydrogen-substituted graphdiyne (HsGDY) nanofilm designed for wearable, skin-like sensors intended for noninvasive health surveillance. The sensors possess a coupled porous framework and inherent softness, which reduce discomfort while ensuring high sensitivity and accuracy. The sensors monitor both dynamic and static strains, identifying body movements with a gauge factor of approximately 22.6 under 2 % strain, a rapid response time of around 60 ms, and a durability of approximately 5000 cycles. Furthermore, they are capable of monitoring air inhalation and exhalation, providing valuable insights into health. Their work presents an intriguing strategy for the development of next-generation wearable bioelectronics featuring various functionalities (Fig. 48a).

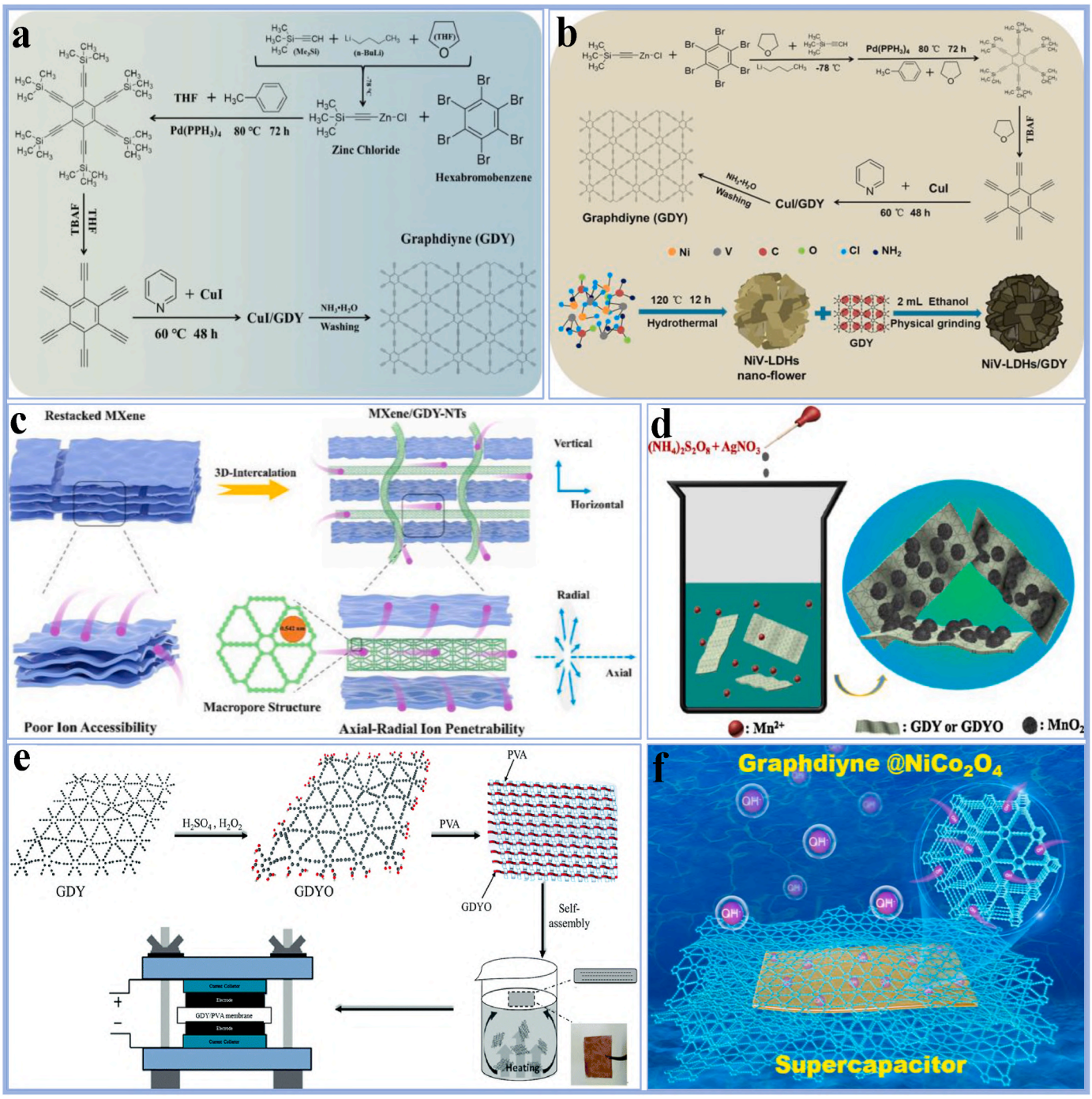

Fig. 49. (a) The proposed working mechanism of GDY SCs [539] Copyright © 2023, Elsevier. (b) The proposed working mechanism of GDY, NiVLDHs and NiV-LDHs/GDY [540] Copyright © 2023, American Chemical Society. (c) Graphical depiction of the cycling stability performance of MXene/GDY MG film [541] Copyright © 2022, Elsevier. (d) The proposed working mechanism of MnO_2@GDY and MnO_2@GDYO [542] Copyright © 2017, Elsevier. (e) The proposed working mechanism of GDYO/PVA membrane [543] Copyright © 2022, Royal Society of Chemistry. (f) The proposed working mechanism of the $NiCo_2O_4$-S@GDY/Ni foam//AC HASD [544] Copyright © 2022, American Chemical Society.

Similarly, Li et al. [524] investigated the influence of Fe/N co-doping on the physical characteristics of GDY materials, successfully achieving dual modulation of magnetic and electrical characteristics. The Fe−N-GDY material exhibits high conductivity and ferromagnetic semiconductor properties, with a Curie temperature approximately at 205 K, rendering it appropriate for spin-related applications. The material functions as conductive ink for printed electronics, including field-effect transistors (FETs), demonstrating high mobility of 215 cm^2 V^{-1} s^{-1}. Additionally, it exhibits superior transference characteristics and durability in flexible FETs utilizing ionic liquid gates, thereby increasing its applicability for large-area, multifaceted electronic and wearable technologies (Fig. 48b). Furthermore, Yao et al. [525] presented an innovative electrolyte-gated transistor (EGT) utilizing a GDY/MoS_2 configuration with an ion-storage layer GDY, positioning it as an intriguing option for neuromorphic computing. The device utilizes a Li-ion storage layer, providing high stability (variation <1 % over 2000 cycles), extremely low energy consumption (50 aJ μm^{-2}), and extended retention (>10^4 s). The system exhibits a quasi-linear

conductivity update characterized by low noise (1.3 %), an exceptionally higher Gmax/Gmin ratio (10^3), and a very low readout conductance (<10 nS). Fig. 48c depicts the functioning of the GDY/MoS_2-derived EGT. Upon the application of a positive gate voltage (<1 V), Li^+ ions from the solid electrolyte accumulate at the GDY junction and infiltrate its interlayers via uniformly distributed pores. The lower conductivity of the GDY layer relative to MoS_2 indicates that charge transfer predominantly occurs via the MoS_2 route, with fluctuations in conductivity mainly ascribed to the MoS_2 layer following the gate pulse. The GDY/-MoS_2-derived EGT simulates synaptic behavior via Li-ion intercalation and deintercalation processes. The side gate serves as the presynapse, receiving signals, whereas the drain functions as the postsynapse, quantifying postsynaptic current. The channel conductivity, G, serves as an indicator of synaptic weight (Fig. 48d). Fig. 48e illustrates a M × N crossbar array designed for matrix operations, utilizing GDY/-MoS_2-derived EGTs as memory elements, wherein their channel conductivity facilitates weight updates during back-propagation. It further illustrates the probability distribution of ΔG, exhibiting high consistency, a narrow dispersion, linearity, symmetry, and low write noise, all of which are critical for the efficacy of neuromorphic algorithms. The characteristics facilitate optimal neuromorphic computing and logic-in-memory functions, underscoring the potential of GDY/-MoS_2-derived EGTs for advanced, low-power electronics that transcend the von Neumann design.

6.4. Supercapacitors (SCs)

The economy's and society's fast expansion has boosted energy consumption, demanding a transition from fossil fuels to renewable energy to minimize pollution [526,527]. SCs have garnered popularity as high-power supplying systems due to their extended lifetime, rapid charging, and stable voltage [528,529]. Transition metallic oxides and sulfides, such as MnO_2, NiO, Co_3O_4, MnS, and MoS_2, are attractive SCs electrode materials because of their excellent pseudo-capacitance, accessibility, and low price [530,531]. Nanostructured $NiCo_2O_4$ is notable for its large reactive SSA for electrochemical energy storage [532]. Despite this promise, real applications encounter issues such as low conductivity and structural deterioration during the charging-discharging phases [533,534]. Scientists have combined $NiCo_2O_4$ with CMs such as carbon nanotubes [535], carbon dots [536], and graphene [537] to improve conductivity and reliability. However, the limited interaction between metallic oxides and carbon compounds continues to hamper efficiency [527]. GDY may grow on various substrates under moderate circumstances, making it perfect for increasing ion and electron conductivity and interfacial shielding in SCs [225,538]. For example, Liu et al. [539] effectively produced lamelliform GDY by a cross-coupling process utilizing cuprous iodide as a mediator. The GDY nano-lamellas performed magnificently as SC electrodes, with a gravimetric capacitance of 137.8 F g^{-1} at 1 A/g and a rate efficiency of 81.28 % at 20 A/g. Over 11,000 cycles, the GDY electrode exhibited low capacitance deterioration. The built symmetrical SC has an energy density of 6.11 Wh/kg and a power density of 5500 W/kg, with an average degradation rate of 0.5 % per cycle after 5000 cycles. This illustrates the promise of GDY-based electrodes for SCs owing to their high electrochemical durability. The GDY//GDY symmetric SC exhibited excellent cyclic endurance, retaining stability with only 0.5 % energy degradation across 5000 charging-discharging cycles. The EIS tests revealed a consistent series resistance (Rs) but a little rise in internal transmission resistance (Rct), suggesting a slight reduction in specific capacity. The GDY electrode material has high internal resistance and excellent conductivity, which greatly enhances its overall performance and facilitates efficient electron transport (Fig. 49a). Similarly, Jin et al. [540] synthesized a nanoflower nickel-vanadium layer double hydroxide/GDY (NiVLDHs/GDY) complex utilizing a two-step technique to improve the conductivity and sustainability of nanoflower NiV-LDHs. This compound had an elevated mass-specific capacitance of 1397 F g^{-1} at 1 A/g, a rate efficiency of 70.01 % at 20 A/g, and was 100 % durable after 5000 cycles. The built asymmetrical SC has an energy density of 35.42 Wh/kg and a power efficiency of 2602.43 W/kg, maintaining 80.52 % of its energy storage capacity after 6000 cycles. These enhancements, due to GDY's abilities to increase porosity morphology and charge transport, indicate that NiV-LDHs/GDY might be used for energy preservation purposes. To assess the electrochemical efficiency of electrodes in SCs, a three-electrode device was employed, using cyclic voltammetry (CV), galvanostatic charging-discharging (GCD) cycles, and electrochemical impedance spectroscopy (EIS) in a 2 M KOH electrolyte. The CV curves for $NiCo_2O_4$ and $NiCo_2O_4$@GDY composites exhibited distinct redox peaks corresponding to Faradaic reactions comprising Co^{3+}/Co^{4+} and Ni^{2+}/Ni^{3+} ions with OH^- anions. The $NiCo_2O_4$@GDY composites had reduced peak shifts and decreased polarization compared to pristine $NiCo_2O_4$, suggesting enhanced electrochemical reversibility and conductivity attributed to GDY. The composites also exhibited greater current responses and integral areas in CV curves, indicating an improved pseudocapacitance. Out of all the samples, $NiCo_2O_4$-S@GDY exhibited the greatest pseudocapacitance, surpassing the performance of the other electrodes. Their results revealed that the $NiCo_2O_4$-S@GDY electrodes exhibit a notable specific capacitance, reaching up to 2245.7 F g^{-1} at 1 A g^{-1}. Additionally, these electrodes show improved capacitance retention, ranging from 81.0 % to 87.6 %, when compared to pure $NiCo_2O_4$-S. Applying GDY coating enhanced long-term cycling stability, as seen by a capacitance retention rate of 98.2 %–98.9 % after 5000 cycles. In contrast, uncoated electrodes only preserved 73.6 %–78.3 % of their capacitance (Fig. 49b). Furthermore, Wang et al. [541] prepared a self-contained, elastic MXene/GDY nanotube (MG) composite film with improved hydronium ion permeation and compositional integrity. This composite has a capacitance of 337.4 F g^{-1} and a rate capability of 73 % at 100 mV/s, beating pristine $Ti_3C_2T_x$ films. An asymmetrical solid-state elastic SC predicated on this material has an energy-yielding of 19.7 Wh/kg at 750 W/kg and 88.2 % capacitance after 10,000 cycles. Their work investigates the possibility of reassembling MXene to improve the effectiveness of flexible SCs. The GCD curves of pure MXene and MG electrodes demonstrate a synergistic use of electrolytic double-layer capacitive (EDLC) and pseudocapacitive charge storage processes. The capacitance of MG electrodes surpasses that of pristine MXene, exhibiting values of 337.4, 287.8, 262, and 216 F g^{-1} at 2, 5, 10, and 20 A g^{-1}, respectively. This performance outshines that of pure MXene and the majority of other MXene-based composites. EIS shows that the ohmic resistance (Rs) of MG electrodes is partially elevated, but their Rct is considerably reduced owing to the 3D intercalation of GDY-NTs. This intercalation improves ion transport and decreases interlayer resistance. Consequently, this increases efficiency and accelerates ion transportation kinetics for MG electrodes. (Fig. 49c). Moreover, Xu et al. [542] indicated that GDY is an efficient substrate for developing MnO_2 nanospheres because of its wide SSA and extensively coupled electrical composition. GDYO is a superior material for MnO_2's capacitor efficiency. The MnO_2@GDYO electrode has an elevated specified capacitance of 301 F g^{-1} at 0.2 A/g and retains 98 % of its original capacitance after 3000 repetitions. This composite has excellent promise as a contender for future electrochemical energy preservation devices. The highest performance is exhibited by MnO_2@GDYO, which retains 98 % of its initial capacitance with 217 F g^{-1} after 3000 cycles, as confirmed by the long-term cycle stability of electrode materials at 1 A g^{-1}. When comparing, it is shown that MnO_2@GO and pure MnO_2 exhibit lesser capacitance retention (91 % and 76 %, respectively) and lower specific capacitances. Furthermore, MnO_2 experiences a considerable decline in efficiency during the first 60 cycles. The MnO_2@GDYO composite exhibits a remarkable coulombic efficiency of around 99 % and retains its capacitance over cycling, demonstrating its exceptional electrochemical stability. GDYO's exceptional electrical conductivity and capacity to inhibit the aggregation of MnO_2 contribute to its outstanding performance, resulting in improved electron transport and capacitance. In

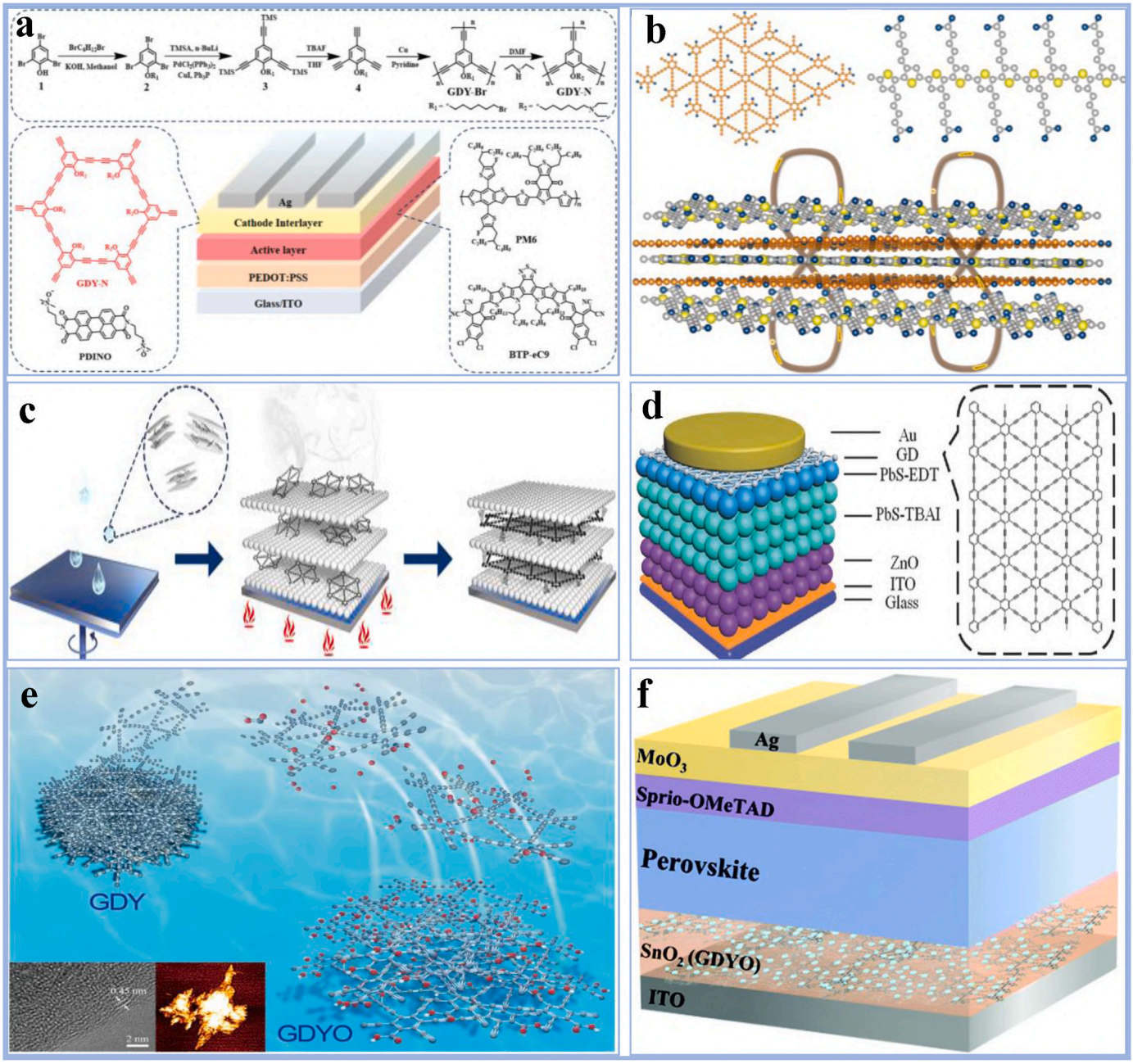

Fig. 50. (a) The proposed working mechanism of GDY-N [550] Copyright © 2024, John Wiley and Sons. (b) The proposed working mechanism of GDYO [551] Copyright © 2022, Springer Nature. (c) The proposed working mechanism of GDYZO films [552] Copyright © 2018, John Wiley and Sons. (d) The proposed working mechanism of the PbS CQD solar cells with GDY anode buffer layer [553] Copyright © 2016, John Wiley and Sons. (e) The proposed working mechanism of GDYO via oxidation of GDY [554] Copyright © 2022, Springer Nature. (f) Schematic of the device structure of SnO_2(GDYO)-containing PSCs [555] Copyright © 2021, Royal Society of Chemistry.

addition, the capacitance values at a scan rate of 5 mV/s are as follows: 77 F g^{-1} for pure MnO_2, 173 F g^{-1} for MnO_2@GO, 192 F g^{-1} for MnO_2@GDY, and 232 F g^{-1} for MnO_2@GDYO. The MnO_2@GDYO composite has the greatest capacitance and consistently maintains better efficiency at varying scan speeds. The decline in specific capacitance as the scan rate increases is attributed to the restricted ion intercalation into the inner active sites of the electrodes at greater scan rates since ions are mostly restricted to the surface. Reducing the scanning speeds improves the diffusion of ions into the active sites, leading to increased capacitance. (Fig. 49d). Likewise, Liang et al. [543] devised a unique method for producing aquatic electrolytic energy storage devices (AEESD) which employ a built-in GDY oxide/polyvinyl alcohol (GDYO/PVA) hybrid film as a separator. This innovative AEESD structure greatly reduces quick self-discharging, resulting in a self-discharging period of 37,160 s (1.0 V–0.3 V), 153 times higher than that of commercialized separators. Furthermore, after 8000 cycles, the cells retained an impressive 95.1 % capacitance. The exceptional electrochemical efficiency of GDYO is assigned to its nano-network framework, good proton conductivity, and great selectivity. The self-discharge characteristics (SDC) of AEESCs were analyzed by charging them to 1 V and measuring the open circuit voltage at different time intervals. The SDC timings were 241 s for PP, 27150 s for GDYO, and 37160 s for GDYO/PVA. The GDYO and GDYO/PVA membranes greatly prolong the self-discharge duration compared to PP, demonstrating their efficacy in

suppressing the self-discharge of SCs. This method offers new opportunities for developing higher-performance AEESDs with longer self-discharge durations (Fig. 49e). In another study, Zhai et al. [544] revealed that transition metallic oxides $NiCo_2O_4$ with varied structures covered with GDY nanofilm may function as efficient pseudo-capacitor electrodes. By increasing conductivity and interface shielding, the GDY film prevents rapid Faradaic processes from degrading the structure and facilitating ions and electrons accessibility to activated spots. The resultant electrode had an elevated specified capacitance of 2245.7 F g^{-1} at 1 A/g and showed remarkable cycling stability over 5000 cycles at 10 A/g. Furthermore, the built asymmetrical SC had an elevated energy content of 62.8 Wh/kg and demonstrated ultra-stable behavior over 10,000 cycles at 20 A/g. This GDY-shielded $NiCo_2O_4$ has considerable potential as a higher-efficiency SC electrode composite. The long-term viability of the HASD device was assessed by subjecting it to 10,000 cycles at a current density of 20 A/g. The device demonstrated a capacitance retention of 97.7 %, surpassing existing devices based on $NiCo_2O_4$. The GCD curves for the early and last cycles exhibited complete overlap, demonstrating exceptional stability. The Nyquist plots demonstrated a low level of charge transfer and Warburg resistance, thereby validating the stability of the electrode interface covered by GDY. The High-Aspect-Ratio Silicon Dioxide (HASD) demonstrated impressive energy densities of 62.8 Wh kg^{-1} at a power density of 747.9 W/kg and 54.3 Wh kg^{-1} with a power density of 15092.7 W/kg, exceeding the energy densities of previously reported devices. The unusual structure of GDY facilitates rapid electron transfer. It enables efficient penetration of OH^- ions, increasing the device's performance (Fig. 49f).

6.5. Solar cells

Organic solar cells (OSCs) have various benefits, including being portable, malleable, and ideal for massive printing, rendering them a viable green innovation for turning sunlight into power [545]. Power converting efficiencies (PCEs) of more than 19 % were reached via innovative planning and enhancement, showing great practical viability [546]. Interface layered composites substantially influence efficiency, but cathode interfacial materials (CIMs) are being developed at a slower rate than functional layered composites [547]. The optimal thickness for CIMs is roughly 10 nm to allow good charge removal, but even minor deviations may significantly impair PCE, limiting massive fabrication. As a result, there is an urgent need to build high-performance CIMs with high thickness tolerance and better understand their functioning principles to get solar cells closer to actual implementations [548,549]. In this regard, Kan et al. [550] synthesized an amino-based GDY variant (GDY-N) with excellent conductivity, acceptable LUMO energy level, and good alcohol stability as OSCs CIMs. The insensitivity of GDY-N-based systems to thickness (95 % efficacy at 25 nm) makes them suitable for massive-scale purposes. An operative coating of D18-Cl:L8-BO yielded an excellent power conversion rate (PCE) of 19.30 % (certified 19.05 %). GDY-N works in both fullerene and non-fullerene networks, providing excellent storage and illumination stability. These properties underline GDY-N's suitability for massive OSC production. OSCs based on GDY-N and PDINO were tested for stability under light and storage conditions. Following 900 h of storage in a glove box filled with nitrogen, PDINO-based devices had a decrease in their PCE to 82 % of the original value. In contrast, GDY-N devices maintained 91 % of their initial PCE. After being exposed to 400 h of LED illumination, GDY-N devices retained 87 % of their original PCE, but PDINO-based devices only retained 65 %. Their findings suggest that devices based on GDY-N have better stability than those based on PDINO. The effectiveness of GDY-N as a CIM was assessed using several photoactive layers, such as PTB7-Th:PC71BM, PM6:Y6, and D18-Cl:L8-BO. OSCs based on GDY-N regularly showed superior power conversion efficiencies (PCEs) compared to those using PDINO. More precisely, OSCs that included the D18-Cl:L8-BO layer demonstrated an outstanding champion PCE of 19.30 % (officially certified as 19.05 %), making it one of the highest PCEs documented. The exceptional performance of GDY-N may be ascribed to its improved capacities in extracting carriers (Fig. 50a). Similarly, Cai et al. [551] proposed an efficient method for improving the efficiency of inverting methylammonium lead triiodide ($MAPbI_3$) perovskite solar cells (PSCs) by employing GDY oxide (GDYO) loaded P3CT-K nanoparticles as the electron transporting channel. The substantial π-π coupling association between GDYO and P3CT-K enhances the properties of the HTL and regulates aggregation, resulting in bigger perovskite particles and improved surface texture. This improves conductivity, charge extraction, and crystallization value, resulting in an ideal power converting effectiveness of 19.06 %, better fill ratio and lower circuit current density. Their work shows that functional GDY can make effective photovoltaics. An investigation was conducted to determine the influence of GDYO on charge-carrier transfer and recombination to comprehend the source of the enhanced device efficiency. Incorporating GDYO resulted in a substantial decrease in leakage current and improved diode properties in devices based on P3CT-K. GDYO enhanced exciton dissociation and charge removal, as shown by a reduced photocurrent density relative to devices without GDYO. The device using P3CT-K with GDYO demonstrated a superior maximum exciton production rate and improved charge collection probability (96 %) compared to the reference device (84 %) at a voltage of 0.2 V. The enhanced charge extraction and lower carrier recombination may be attributable to the decreased aggregation of P3CT-K, which GDYO promotes. The impact of GDYO on conductivity and charge transfer was investigated by evaluating the extraction of holes in hole-only structures (ITO/P3CT-K/MoO_3/Ag and ITO/P3CT-K(GDYO)/MoO_3/Ag). The inclusion of GDYO increased the conductivity of P3CT-K, as shown by the higher hole mobility (4.36×10^{-3} $cm^2/(V{\cdot}s)$) compared to P3CT-K alone (3.10×10^{-3} $cm^2/(V{\cdot}s)$). The steady-state and time-resolved photoluminescence (PL and TRPL) spectra demonstrated a decrease in the intensity of PL peaks and a reduction in carrier recombination in P3CT-K (GDYO). This suggests an enhancement in charge extraction and transfer at the interface with the perovskite layer. The TRPL measurements further confirmed these results by demonstrating extended carrier lifetimes in the device boosted with GDYO (Fig. 50b). Furthermore, Li et al. [552] synthesized a new GDY-ZnO (GDYZO) material using a simple process, revealing that Zn particles form C-Zn and C-O linkages with GDY. This derivative increases composite variation, allowing for the production of superior interlayers. In OSCs, GDZO sheets enhanced PCE to 11.2 % from 10 % with pristine ZnO as electron transporter layers (ETLs). GDYZO also improved device reliability in glove box settings and humid environments (90 % humidity). These results suggest that GDYZO might improve OSC productivity and be used in optoelectronics. Furthermore, ensuring the stability of devices is essential for the industrialization of solar cells. During stability testing, devices using GDZO as an ETL retained 81 % of their original PCE after being stored for 48 days in an argon-filled glove box. In comparison, devices with immaculate ZnO only maintained 75 % of their initial PCE. In addition, when exposed to high humidity levels of 90 % for 18 h, GDZO-based devices maintained 55 % of their PCE, but ZnO-based devices had a significant decrease to just 19 %. The enhanced performance of GDZO may be due to its capacity to uniformly distribute ZnO and minimize charge recombination at the interface, hence improving the stability of the device. (Fig. 50c). Moreover, Jin et al. [553] utilized GDY as an anode buffering layer in PbS colloidal quantum dots (CQD) solar cells, resulting in a considerable PCE boost from 9.49 % to 10.64 %. Impedance spectroscopy (IS) and transient photovoltage (TPV) tests revealed that GDY increases carrier lifetime while decreasing carrier recombination, enhancing the interaction among the PbS-EDT and the Au anode. The device was also stable over time. Impedance spectroscopy (IS) was used to examine carrier recombination in solar systems. The acquired IS data, obtained in both dark and illuminated conditions, indicated that the device exhibited a longer effective carrier lifetime (2.4 μs) compared to the reference device (1.9 μs) under light. The extended lifespan of

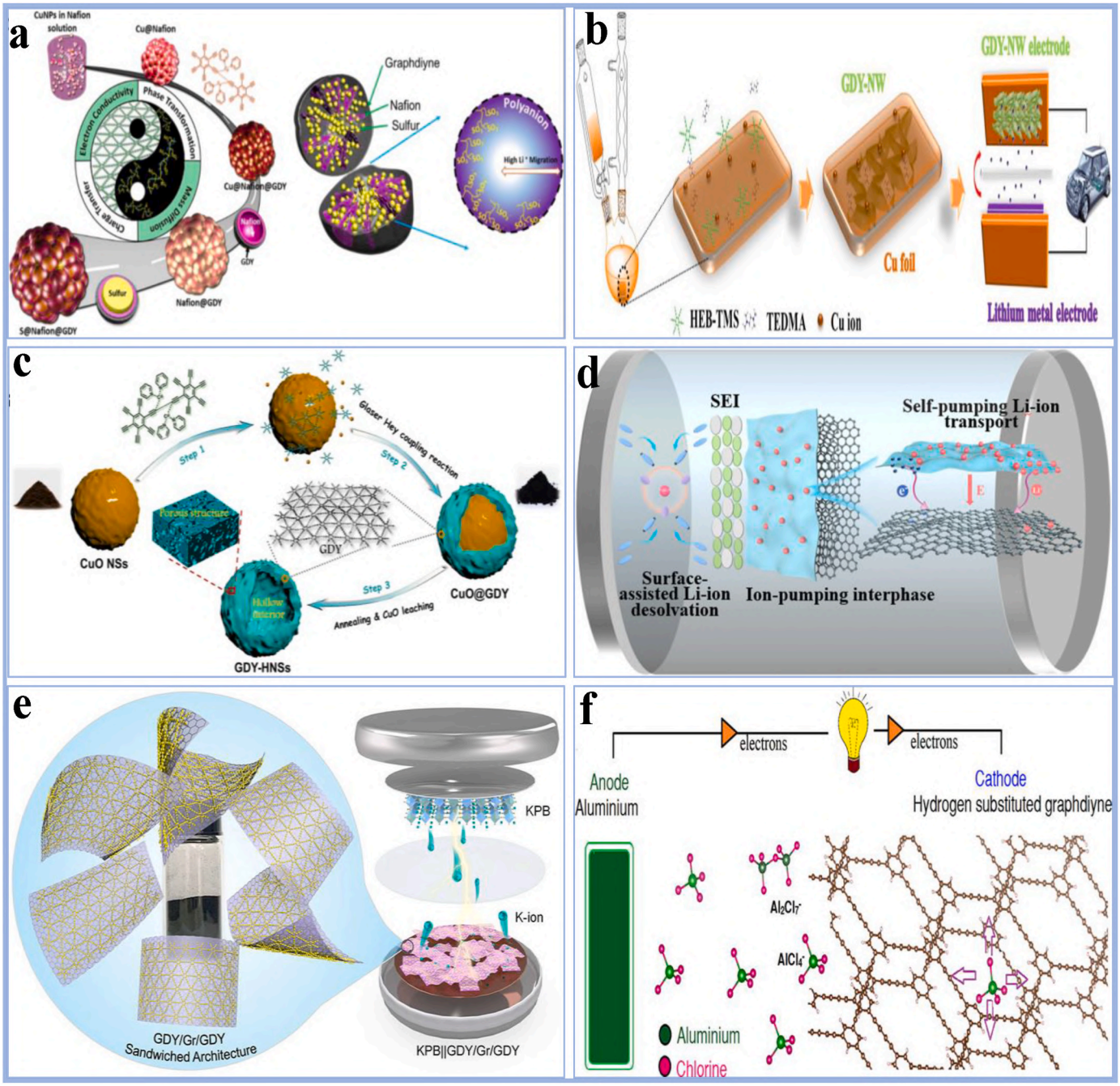

Fig. 51. (a) The proposed working mechanism of S@Nafion@GDY [562] Copyright © 2020, Elsevier. (b) The proposed working mechanism of GDY–NWs preparation method and LIB is based on GDY–NW [563] Copyright © 2017, Elsevier. (c) The proposed working mechanism of GDY-HNSs [564] Copyright © 2021, Elsevier. (d) The proposed working mechanism of PI of GDY regulates the Li-ion solvation [565]. (e) The proposed working mechanism of GDY/Gr/GDY [566] Copyright © 2024, Chinese Chemical Society. (f) The proposed working mechanism of HsGDY [567] Copyright © 2020, American Chemical Society.

these photoexcited carriers implies a lower probability of recombination and allows for a greater opportunity for collection by the anode. Furthermore, the device demonstrated increased recombination resistance, suggesting a decrease in carrier recombination. During a 120-day period of being kept under normal air conditions, both the device and reference device demonstrated exceptional stability. Their work implies that sp^2-and sp-hybridized GDY materials have considerable optoelectronic promise (Fig. 50d). In another stdy, Liu et al. [554] synthesized substantially soluble GDYO with rich carboxyl classes and employed it in a poly(3,4-ethylenedioxythiophene)/poly(styrene sulfonate) (PEDOT: PSS) (GDYO) layer as the electrons transfer layer solar cells. The GDYO boosted J_{sc} and FF by improving charges transference, conductivity, and flexibility. Charge carrier kinetics optimized interfacial and layer-active dissociation and removal. GDYO exhibited tremendous potential for enhancing OSCs efficiency and optoelectronics applications, showing that OSCs have excellent commercial possibilities. Futhermore, an analysis was conducted to examine the influence of GDYO on the recombination and transport of charge carriers. Their work focused on the relationship between the intensity of light and the short-circuit current density (J_{sc}) as well as the open-circuit voltage (V_{oc}). The slope of the J_{sc} against the light intensity curve, which is desired to be near unity to suggest low bimolecular recombination, was determined to be 0.98 for cells based on PEDOT: PSS and 0.99 for cells based on PEDOT: PSS(GDYO). This enhancement indicates that GDYO efficiently

mitigates bimolecular recombination. In addition, the slope of the Voc dependency was 1.10kT/q for cells based on PEDOT: PSS and 1.06kT/q for cells based on PEDOT: PSS(GDYO). The decreased gradient with GDYO suggests a decrease in trap-induced recombination, which is consistent with the reported improvement in fill factor (FF) for GDYO-modified devices (Fig. 50e). Likewise, Yao et al. [555] built a new SnO_2 (GDYO) electron-carrying membrane for outstanding durability planar PSCs. The terminal carboxy and hydroxy units of GDYO thermally link with disordered Sn in SnO_2, minimizing oxygen-vacancy and improving charge transfer. This inclusion increased the purity of both SnO_2 and perovskite films, yielding a PCE of 21.23 %, more than 10 % greater than the regulated system. The SnO_2 (GDYO)-predicated system also demonstrated enhanced stability, retaining 71 % of its original PCE after 160 h of continual irradiation and 84 % after 24 days at 80 °C. TPC and TPV experiments were performed to examine the impact of GDYO on charge extraction. The findings revealed that the SnO_2(GDYO) device exhibited a shorter photocurrent decay time (15.9 ms) in comparison to the SnO_2-only device (29.3 ms), suggesting a more rapid extraction of charges. Furthermore, introducing GDYO doping significantly increased the charge-recombination lifespan from 69.1 ms to 182.5 ms. This indicates enhanced charge extraction and a decrease in recombination. The SCLC measurements showed that the electron mobility in SnO_2(GDYO) films (8.15×10^{-3} $cm^2/V{\cdot}s$) was much greater than in pure SnO_2 films (8.18×10^{-4} $cm^2/V{\cdot}s$). The electron mobility is increased because of the high electronic conductivity of GDYO, which in turn improves electron transport and optimizes device performance. The investigation of EIS indicated that the device based on SnO_2(GDYO) exhibited a bigger diameter of the semicircle than the control device. This implies an increase in charge recombination resistance (Rrec), a decrease in current leakage, and a reduction in electron recombination at the surface. As a result, GDYO doping inhibits the buildup of charge at the interface and improves the efficiency of electron transmission. Their findings highlight the relevance of interface design in PSCs and functionalized GDYO in photovoltaics (Fig. 50f).

6.6. Batteries

The growth of sustainable energy sources such as solar, wind power, hydroelectric power, and geothermal is critical, but better energy preservation options are required to fulfill increasing demands [556]. LIBs have been popular since the 1990s because they offer better energy and power densities than lead-acid and nickel-metallic hydride batteries [43,557]. However, improved LIBs with higher energy densities, power densities, and cycle durability are required for industrial uses such as electric cars. Nanostructured materials electrodes, which provide largely stored energy efficiencies and charging-discharging rates, hold potential for future LIBs [558,559]. Considering theoretic resources, transition metallic oxides and sulfides have low resistivity and consistency. The intriguing properties of carbon nanomaterials, such as graphene and carbon nanotubes, which include conducting and nanoporous frameworks, have not contributed to their practical application [560]. Lithium-ion capacitors (LICs), which combine LIB anodes with electrochemical double-layer capacitor (EDLC) cathodes, provide a combination of high-power density, extended cycle life, and energy productivity. Improving the anode material is critical to increasing LIC efficiency [561]. For example, Wang et al. [562] prepared lithium-S battery Nafion@GDY core-shell nanostructures. GDY has an electronic and conducting structure, while integrated Nafion boosts mass transference and phase change processes, reducing polysulfides shuttle. This framework maintains good capacity retention (CR) after 800 repetitions at elevated current densities (0.5C and 1C), with a volume capacity of 1832 A h L^{-1} (53 % of sulfur's theoretical value). The efficiency of the S@Nafion@GDY electrodes is enhanced by their distinctive heterostructure, which efficiently integrates Nafion into the main GDY particles. The stability and elevated anion content of Nafion improve the retention of polysulfides and the transfer of lithium ions inside the GDY host, leading to enhanced polysulfide conversion and prevention of migration. Raman spectroscopy indicates that the S@Nafion@GDY electrodes undergo faster phase transitions and have lower levels of long-chain polysulfides than S@GDY@Nafion. The presence of Nafion leads to faster response rates and reduces the occurrence of the shuttle effect. The enhanced discharge and charge reactions seen in these electrodes emphasize the essential function of Nafion in augmenting the performance of Li-S batteries. Their invention might benefit catalysis, fuel-cell technology, SCs, and batteries (Fig. 51a). Similarly, Huang et al. [563] investigated GDY-NW with a multilayer porosity framework for LIBs and LICs. This framework, which contains butadiyne connections, provides several functional locations for lithium accumulation and rapid ion transport paths. GDY-NW electrodes demonstrated a reversible potential of about 908 mAh g^{-1} at 0.05 A g^{-1} and maintained 526 mAh g^{-1} at 1 A g^{-1} after 1000 cycles. LICs provided a specified capacitance of ~208 F g^{-1} over 10000 cycles at 1 A g^{-1} and an energy density of 217 Wh kg^{-1} at a specified power of 150 W k g^{-1}. Furthermore, The formation of the Solid Electrolyte Interface (SEI) on GDY-NW anodes during the processes of lithiation and delithiation was investigated using in situ Raman scattering. The Raman spectra revealed that the butadiyne bonds at 2150 cm^{-1} and 1943 cm^{-1} get weaker and vanish when the SEI is formed. Simultaneously, a new peak emerges at 1985 cm^{-1} and shifts with potential changes, showing lithium ions' involvement in the storing process. The D and G bands, with wavenumbers of 1365 cm^{-1} and 1526 cm^{-1} respectively, exhibit a drop in intensity, indicating the occurrence of adsorption and deposition processes. But, their structural stability remains unchanged. The ID/IG ratio exhibits an upward trend as the potential rises, reaching its highest point at the SEI formation potential (about 0.9 V). Subsequently, it declines as lithium ions intercalate and the SEI becomes more stable. The ID/IG ratio varies during charging and reaches its lowest point at 2.5 V, indicating complete removal of lithium ions. This suggests that the ability of GDY-NW to store lithium at various potentials is a result of lithium being inserted into graphene-like layers and hierarchical pores. GDY-NW's hierarchical porosity design makes it a good contender for the outstanding durability of lithium rechargeable batteries (Fig. 51b). Likewise, Zhao et al. [564] prepared GDY-HNSs with hierarchical structures via a simple solvothermal method using CuO NSs as a template and catalyst source. The morphology and thickness of GDY shells were easily adjustable by varying the precursor amount. The unique hollow structure of GDY-HNSs shortens lithium-ion diffusion paths and improves electron conduction efficiency. As a result, GDY-HNSs, used as LIB anodes, exhibited high specific capacity, excellent rate performance, and long-term cycling stability, even at a high mass loading of 2.0 mg cm^{-2}. In addition, the GDY-HNSs-120 anode material demonstrates a remarkable ability to store and release energy repeatedly and efficiently in LIBs, due to its distinctive structure. The hollow nanospheres possess a hierarchical nanowall structure, contributing to a significant increase in SSA and multiple electrochemically active sites. The shells with permeable properties decrease the length of diffusion routes for ions and electrons, hence improving performance. Moreover, the presence of nanopores and structural flaws provides additional sites for storing lithium and allows for accommodating variations in volume during cycling. These structural properties enhance the electrochemical stability and efficiency. Nyquist plots provide further evidence of decreased charge transfer resistance during cycling, improving the material's electrochemical characteristics. The hollow interior also serves as ideal nanocontainers for low-conductivity electrode materials like sulfur, tin, and silicon, offering the potential for further application optimization (Fig. 51c). Furthermore, An et al. [565] present an ion-pumping interphase (IPI) scheme on graphite substrates to improve ion movement dynamics and comprehend the effect on graphite electrode efficiency. GDY is used as the IPI composite because of its outstanding electrochemical characteristics. GDY heterojunctions with graphite hinder electrolyte Li-ion elimination and accelerate disintegration. LiF-rich SEI layers with increased conductivity speed up Li-ion propagation rates. An integrated electrical field in GDY promotes

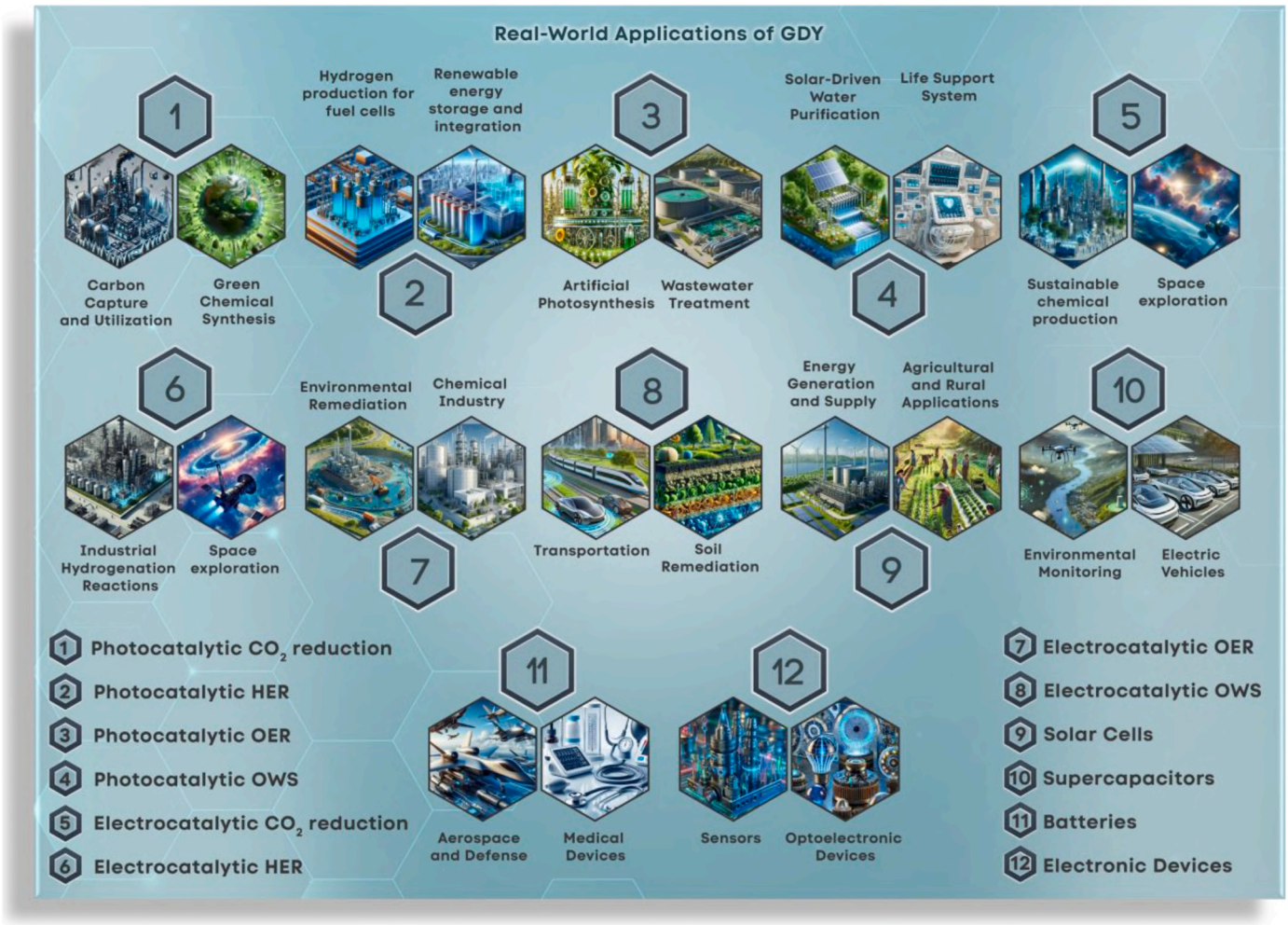

Scheme. 2. Graphical illustration of different potential real-world applications of GDY.

Li-ion transfer to graphite and sustains release during rapid charging. The GDY/graphite anodes have exceptional rapid charging, large capability (217.8 mA h g^{-1} for 6C, 139.2 for 20C), long cycling life (2000 cycles for 6C, 1650 cycles for 20C), and outstanding power accumulation (81.5 % for 6C after 2000 cycles, 86.2 % for 20C after 1650 cycles). Even at −20 °C, GDY/graphite anodes retain good capacity (128.4 mA h g^{-1} for 500 cycles) with 80 % retention at 2 °C. Furthermore, The GDY/graphite composite anode exhibits superior performance compared to graphite-only anodes in terms of its ability to charge rapidly and maintain stability throughout the cycle. GDY improves the diffusion of Li-ion, leading to better performance in terms of rate with a specific capacity of 190 mA h g^{-1} at 8C and outstanding recovery. During cycling testing, GDY/graphite exhibits a significant capacity of 217.8 mA h g^{-1} after 2000 cycles at 6C, with a retention rate of 81.5 %. In comparison, graphite anodes only achieve a capacity of 138.5 mA h g^{-1} and a retention rate of 46.1 %. At a temperature of 20 °C, the GDY/graphite material reaches a discharge capacity of 139.2 mA h g^{-1} and exhibits exceptional stability, retaining 86.2 % of its capacity after 1650 cycles (Fig. 51d). In another study, Li et al. [566] designed a stacked GDY/graphene/GDY (GDY/Gr/GDY) structure via van der Waals epitaxy, resulting in an elevated SSA and purity. In contrast to GDY, the GDY/Gr/GDY electrode had better capacity results, rate potential, and cycle stability. In addition, the GDY/Gr/GDY electrode shows encouraging electrochemical efficiency when used in a half-cell setup with potassium metal foil as the counter electrode. Upon conducting initial cyclic voltammetry, a wide peak is seen at 0.55 V in the first cycle. This peak is due to the formation of a durable SEI layer. The initial Coulombic efficiency (ICE) is low, measuring 23.4 %. This is likely attributed to the significant SSA and imperfections of the GDY/Gr/GDY material. But, the electrode has outstanding rate capabilities, exhibiting reversible capacities of 486 mAh g^{-1} at a current density of 50 mA g^{-1} and 205 mAh g^{-1} at a 2000 mA g^{-1} current density. The long-term cycling stability is excellent, with a capacity of 380 mAh g^{-1} at a current rate of 100 mA g^{-1} after 200 cycles, and a virtually perfect Coulombic efficiency of close to 100 %. At a higher current rate of 1000 mA g^{-1}, the capacity remains at 225 mAh g^{-1}. Conversely, bare graphite and GDY electrodes exhibit reduced capacities and less desirable cycle performance. The GDY/Gr/GDY anode showed remarkable cycle stability in a full-cell system using a potassium Prussian blue cathode, suggesting K-ion battery promise (Fig. 51e). Similarly, Debnath et al. [567] investigated the prospect of GDY and HsGDY as cathode materials for aluminium-ion batteries (AIBs) utilizing DFT simulations. They studied different molecular structures and how $AlCl_4$ ions intercalated. They also analyzed electrical characteristics, such as DOS and charging density variation, voltage distributions, and estimations of stored capacity. The main issue with AIBs is their limited capacity, with current technologies breakthrough batteries only attaining 70 mA h g^{-1}. This constraint arises from the ineffective insertion of $AlCl_4$ into graphite, resulting in just a portion of the cathode area being used. GDY and HsGDY were examined as substitutes because of its lower energy need for interlayer expansion compared to graphite. Their extensive pores can enable the migration of $AlCl_4$ across layers, hence enhancing the use of the cathode material and resolving the capacity problem. Comparative computations of capacity for single-layer and bilayer graphene

Table 2
A comparison assessment of GDY with other functioning carbon materials, focusing on their unique structural, electrical, mechanical, and thermal characteristics.

Property	Graphdiyne (GDY) [6,47,59,344,568]	Graphene (GR) [569–573]	Carbon Nanotubes (CNTs) [431,574–577]	Fullerenes (C60) [578–582]	Graphite [583–587]
Structure	sp-/sp^2 carbon linear structure	sp^2 honeycombs carbon system	carbon sp^2 tubular	sp^2 carbon nanospheres	Layered sp^2 carbon sheeting
Band gap	Variable (0.47–1.12 eV)	Planar (semi-metallic)	Semiconductor with variable chirality	large band gap (~1.5–2.3 eV)	Planar (semi-metallic)
Electrical conductivity	Modifiable by strain or doping	Rapid and very fast	Axial elevation	Average	Average
Dimensionality	2D plane	2D plane	2D plane	2D plane	1D cylindrical
Thermal conductivity	Inferior to GR owing to -C ≡ C- bonding	Remarkably higher (~5000 W/m·K)	Elevated across tube axis (~3000 W/m·K)	Minimal	Average (~500 W/m·K in-plane)
Mechanical strength	Inferior to GR owing to acetylenic bonding	Exceptional tensile force of around 130 GPa	Elevated tensile force (~50–100 GPa)	Minimal	Elevated (anisotropic; diminished interlayer bonding)
Chemical reaction	Strong; -C ≡ C- links increase reaction	Lower as a result of delocalized π-electrons	Average (functionalized by walls and edges)	Elevated owing to torsion stress	Minimal, mostly at borders
Thermal durability	Average, diminished by -C ≡ C- bonding	Elevated and sustained at extreme temperatures	Elevated, but susceptible to oxidation	Modest and fragile at elevated temperatures	Elevated
Applications	Energy storage, catalysis, detectors, electronics	Electronic devices, thermal regulation, nanomaterials	Nanotechnology, pharmaceutical delivery, polymers	Photovoltaic cells, molecular carriers, pharmaceutical delivery	Electrodes, lubricants, composite additives
Stability	Average	Elevated	Elevated	Inadequate	Elevated
Flexibility	Elevated	Rigidly	Elevated	Rigidly	Rigidly

structures reveal that single-layer graphene can bind with four $AlCl_4$ ions and has a stage-1 storage capacity of 124 mA h g^{-1}. In comparison, bilayer graphene can bind with five $AlCl_4$ ions and has a capacity of 155 mA h g^{-1}. The capacity densities of graphene, GDY, and HsGDY are also computed, indicating that HsGDY has a slightly higher storage capacity for $AlCl_4$ per unit area than graphene and GDY. Although GDY and graphite have comparable stage-1 capacities, HsGDY provides much more storage, about three times that of graphene. While stage-1 intercalation is optimal, GDY and HsGDY might probably accomplish stage-2 or stage-3 intercalation because of their lower distortion energies. Large pores in HsGDY allow for easy diffusion of $AlCl_4$ across layers. This indicates that the real storage capacity of HsGDY may be overestimated if it is computed just by dividing the stage-1 capacity. Their research evaluated GDY and HsGDY as cathode materials and compared them to other carbon-predicated materials (Fig. 51f). Furthermore, a graphical illustration of different potential real-world applications of GDY is given in Scheme 2. More importantly, a comprehensive evaluation comparing GDY with other effective carbon materials is provided in Table 2, which analyses their distinct structural, electronic, mechanical, and thermal attributes in details, facilitating an improved comprehension of GDY differences from other carbon-based materials across these significant fields.

7. Conclusion and future prospective

Graphdiyne (GDY) is a two-dimensional carbon material characterized by unique properties, making it suitable for various applications, including catalysis, energy storage, and electronics. This review presents an analysis of GDY, focusing on its molecular structure, electronic properties, synthesis techniques, and applications. The structure of GDY comprises a highly conjugated network of sp- and sp^2-hybridized carbon atoms, imparting distinct electronic, mechanical, and optical properties, which are highlighted. GDY exhibits semiconducting properties that can be tuned through bandgap engineering, doping, and modifications to its surface area and pore size, as thoroughly examined in this review. The combination of these features, along with its remarkable tensile strength and flexibility, renders GDY ideal for optoelectronic devices, which are also explored. Moreover, GDY's thermal and conductive properties are essential for its integration into high-performance energy systems and electronic devices, with these aspects summarized in detail. A significant aspect of GDY is its potential as a metal-free catalyst. Its tunable structure and extensive surface area enhance catalytic activity in reactions, including CO_2 reduction, hydrogen evolution (HER), oxygen evolution (OER), and overall water splitting (OWS), all of which are studied. These characteristics establish GDY as a key material for green and sustainable energy applications, particularly in renewable energy and environmental remediation, as summarized. Various synthesis techniques have been developed to enhance GDY's performance. Methods such as dry and wet chemistry, Cu-surface-mediated synthesis, and template-based techniques facilitate the generation of GDY derivatives with improved properties, which are examined in depth. Reactions like Glaser coupling, Glaser-Hay coupling, and alkynylsilane coupling play crucial roles in regulating GDY's formation and functionality, which are also explored. Modifying the structure of GDY during synthesis is essential for customizing its properties for specific applications, which is emphasized. Improving GDY's performance requires strategies such as bandgap engineering, defect engineering, doping with diverse elements, and surface functionalization, which are discussed in detail. These methods enable precise regulation of GDY's electronic structure and catalytic performance. Functionalization with organic and inorganic molecules like anthraquinone, porphyrin, and triazine enhances its properties for catalysis, energy storage, and electronic devices, highlighted for the first time. The dimensionality of GDY offers enhanced flexibility for various applications. Zero-dimensional quantum dots (QDs) and one-dimensional nanowires exhibit high surface-to-volume ratios, enhancing reactivity and conductivity. Two-dimensional GDY sheets are suitable for energy storage applications, including supercapacitors and batteries, due to their extensive surface areas. Three-dimensional GDY structures improve mechanical strength and structural stability in diverse applications, which have also been studied. A wide range of GDY's potential applications has been explored. GDY shows significant promise in photocatalysis and electrocatalysis, particularly for CO_2 reduction, HER, OER, and OWS, offering solutions for sustainable energy production. Furthermore, GDY's properties position it as a strong candidate for applications in supercapacitors, batteries, and solar cells. In summary, This review serves as a comprehensive guide for scientists interested in exploring the potential of GDY across various scientific and technological domains.

Though, in this review, we have provided the successful fabrication of GDY with diverse structures, morphologies, functionalization, dimensionality, and properties that have been achieved through the utilization of numerous synthesis techniques. But there are still several challenges to obtaining high-yield, high-quality GDY materials.

Table 3
Prospective challenges and solutions GDY in addressing global challenges in energy and catalysis.

Category	Future Challenges	Proposed Solutions
Electrical, mechanical, and thermal characteristics	The link between GDY structure and features is unclear.	Comprehensive investigations are required to establish a correlation between the atomic composition of GDY and its characteristics.
Synthesis methods	The synthesis of scalable GDY is not optimal, inhibiting large-scale production.	Create effective, efficient synthesis methodologies such as Cu-surface-mediated and template-based processes.
Bandgap engineering	Effectively regulating the band gap for individual applications continues to bring challenges.	Enhance band gap control by doping, defect introduction, and surface alterations.
Defect engineering	Incorporate defects without altering the structure or functionality of GDY.	Investigate defect engineering to improve qualities while maintaining stability.
Functionalization	Attaining consistent and effective functionalization for particular applications continues to raise difficulties.	Enhance functionalization methods to modify the features of GDY for certain applications.
Reaction schemes (Catalysis)	Enhance the catalytic efficiency of GDY for CO_2 reduction, HER, OER, and OWS.	Design co-catalysts and optimize interfaces to improve GDY's catalytic efficiency.
Morphologies and dimensionalities	Enhance GDY morphology (0D, 1D, 2D, 3D) for higher efficiency in specified applications.	Improve the performance of quantum dots, nanowires, and sheets via optimization.
Energy storage applications	Enhance the capacity and durability of GDY in energy storage systems.	Enhance the shape and surface area of GDY to improve energy storage efficiency.
Thermal and conductive properties	Enhance the thermal resistance and conductance of GDY in adverse conditions.	Enhance the surface and design of GDY to improve thermal and electric conductivity.
Environmental applications	Emphasize the use of GDY in the degradation of pollutants for environmental remediation.	Investigate the capabilities of GDY in purifying water and CO_2 absorption by altering surfaces.
Application in electronics	Enhance the electronic characteristics of GDY for use in transistors and sensors.	Improve the optoelectronic effectiveness of GDY by doping or functionalization.
Co-catalyst interactions	Interactions between GDY co-catalysts in catalysis need enhanced knowledge.	Investigate GDY-co-catalyst linkages to improve energy catalysis.
Long-term stability	Promote the enduring durability of GDY inside clean energy systems.	Enhance GDY durability via rapid testing and design enhancements.

- Formulating scalable synthesis methodologies for GDY and its derivatives (graphyne) while ensuring excellent quality, cost-efficiency, and stability is essential for both theoretical and practical applications. Achieving this will facilitate the material's integration into practical solutions.
- The synthesis routes for graphyne, graphyne-3, and graphyne-4, which are distinct from GDY, remain hypothetical. Forecasting and optimizing laboratory techniques for the synthesis of these substances is essential since they demonstrate adjustable characteristics and morphologies, facilitating prospective applications in many fields.
- An enhanced method of characterization is essential to connect molecular and atomic-level frameworks with their resultant characteristics and performances. Utilizing sophisticated methodologies will enhance comprehension of these materials and their applications.
- Advancing innovative synthesis processes for GDY is essential for achieving materials with enhanced energy conversion and storage properties. Challenges continue in the regulated synthesis of monocrystalline GDY, SL, FL GDY, and nanostructured variants (e.g., GDY dots) in precise dimensions and configurations at scale.
- The production of GDY films often leads to impurities and uncertain structural characteristics owing to cross-linking side reactions and intricate bonding mechanisms. Furthermore, this has prevented the investigation of GDY's practical applications and intrinsic properties. Utilizing more facile and regulated synthesis techniques may enhance the material's quality and efficiency.
- To expand the practical uses of GDY, large-scale synthesis of high-quality GDY is necessary. Meeting future demand for functioning devices will rely on attaining consistent and repeatable quality in GDY production.
- Attaining control over the morphology, dimensions, and configuration of GDY films and aggregates would markedly enhance its applicability in diverse device designs. This control will allow the material to be customized for certain applications, enhancing performance and adaptability.
- To optimize GDY's electrical, mechanical, and optical characteristics, it is essential to investigate several changes, including surface functionalization and doping. Although energy conversion is a primary emphasis, GDY also has significant potential for many applications, such as sensors, medication delivery, gas separation, batteries, supercapacitors, and saltwater desalination. Nonetheless, many applications remain in the preliminary phases of investigation, necessitating ongoing development and innovation.

More importantly, Table 3 outlining the prospective issues of GDY, considering its many characteristics, synthesis methodologies, reaction pathways, functionalization, morphologies, dimensionalities, and possible applications, accompanied by suggested solutions.

Authors contributions

The manuscript was written with contributions from all authors. All authors have approved the final version of the manuscript work.

Declaration of competing interest

The authors declare that they have no known competing financial interests or personal relationships that could have appeared to influence the work reported in this paper.

Acknowledgement

This work was supported by the King Khalid University, Abha, Saudi Arabia. The authors extend their appreciation to the Deanship of Scientific Research at King Khalid University for funding this work through Large Groups Project under grant number (R.G.P. 2/248/45). The authors also extend their appreciation to the Guangdong Office of Research Projects at the Provincial University (2024KCXTD064).

Appendix A. Supplementary data

Supplementary data to this article can be found online at https://doi.org/10.1016/j.rser.2025.115570.

Data availability

Data will be made available on request.

References

[1] Khan K, et al. Recent progress, challenges, and prospects in two-dimensional photo-catalyst materials and environmental remediation. Nano-Micro Lett 2020;12(1):1–77.
[2] Shi Z, et al. Two-dimensional tellurium: progress, challenges, and prospects. Nano-Micro Lett 2020;12(1):1–34.
[3] Li J, Chen Y, Guo J, Wang F, Liu H, Li Y. Graphdiyne oxide-based high-performance rechargeable aqueous Zn–MnO_2 battery. Adv Funct Mater 2020;30(42):2004115.
[4] Chen Y, Li J, Wang F, Guo J, Jiu T, Liu H, Li Y. Chemical modification: toward solubility and processability of graphdiyne. Nano Energy 2019;64:103932.
[5] Guo J, Guo M, Wang F, Jin W, Chen C, Liu H, Li Y. Graphdiyne: structure of fluorescent quantum dots. Angew Chem Int Ed 2020;59(38):16712–6.
[6] Jia Z, Li Y, Zuo Z, Liu H, Huang C, Li Y. Synthesis and properties of 2D carbon-graphdiyne. Accounts Chem Res 2017;50(10):2470–8.
[7] Khan K, et al. Synthesis, properties and novel electrocatalytic applications of the 2D-borophene Xenes. Prog Solid State Chem 2020;59:100283.
[8] Tong Y, Chen P, Zhou T, Xu K, Chu W, Wu C, Xie Y. A bifunctional hybrid electrocatalyst for oxygen reduction and evolution: cobalt oxide nanoparticles strongly coupled to B, N-decorated graphene. Angew Chem Int Ed 2017;56(25):7121–5.
[9] Khan K, et al. Going green with batteries and supercapacitor: two dimensional materials and their nanocomposites based energy storage applications. Prog Solid State Chem 2020;58:100254.
[10] Fan X, Zhang G, Zhang F. Multiple roles of graphene in heterogeneous catalysis. Chem Soc Rev 2015;44(10):3023–35.
[11] Huang L, Han Y, Dong S. Highly-branched mesoporous Au–Pd–Pt trimetallic nanoflowers blooming on reduced graphene oxide as an oxygen reduction electrocatalyst. Chem Commun 2016;52(56):8659–62.
[12] Georgakilas V, Perman JA, Tucek J, Zboril R. Broad family of carbon nanoallotropes: classification, chemistry, and applications of fullerenes, carbon dots, nanotubes, graphene, nanodiamonds, and combined superstructures. Chem Rev 2015;115(11):4744–822.
[13] Kroto HW, Heath JR, O'Brien SC, Curl RF, Smalley RE. C60: Buckminsterfullerene. Nature 1985;318(6042):162–3.
[14] Iijima S. Helical microtubules of graphitic carbon. Nature 1991;354(6348):56–8.
[15] Novoselov KS, et al. Electric field effect in atomically thin carbon films. Science 2004;306(5696):666–9.
[16] Krätschmer W, Lamb LD, Fostiropoulos K, Huffman DR. Solid C60: a new form of carbon. Nature 1990;347(6291):354–8.
[17] Wang L, et al. Long-range ordered carbon clusters: a crystalline material with amorphous building blocks. Science 2012;337(6096):825–8.
[18] Sun A, Lauher JW, Goroff NS. Preparation of poly (diiododiacetylene), an ordered conjugated polymer of carbon and iodine. Science 2006;312(5776):1030–4.
[19] Tao W, et al. Emerging two-dimensional monoelemental materials (Xenes) for biomedical applications. Chem Soc Rev 2019;48(11):2891–912.
[20] Manzano M, Vallet-Regí M. Revisiting bioceramics: bone regenerative and local drug delivery systems. Prog Solid State Chem 2012;40(3):17–30.
[21] Baughman R, Murthy N, Eckhardt H, Kertesz M. Charge oscillations and structure for alkali-metal-doped polyacetylene. Phys Rev B 1992;46(17):10515.
[22] Service RF. Carbon sheets an atom thick give rise to graphene dreams. American Association for the Advancement of Science; 2009.
[23] Chen R, et al. Use of electronic cigarettes to aid long-term smoking cessation in the United States: prospective evidence from the PATH Cohort Study. Am J Epidemiol 2020;189(12):1529–37.
[24] Huang C, Li Y, Wang N, Xue Y, Zuo Z, Liu H, Li Y. Progress in research into 2D graphdiyne-based materials. Chem Rev 2018;118(16):7744–803.
[25] Baughman R, Eckhardt H, Kertesz M. Structure-property predictions for new planar forms of carbon: layered phases containing sp^2 and sp atoms. J Chem Phys 1987;87(11):6687–99.
[26] Li G, Li Y, Liu H, Guo Y, Li Y, Zhu D. Architecture of graphdiyne nanoscale films. Chem Commun 2010;46(19):3256–8.
[27] Li Y, Xu L, Liu H, Li Y. Graphdiyne and graphyne: from theoretical predictions to practical construction. Chem Soc Rev 2014;43(8):2572–86.
[28] Shukla V. Observation of critical magnetic behavior in 2D carbon based composites. Nanoscale Adv 2020;2(3):962–90.
[29] Diederich F, Rubin Y. Synthetic approaches toward molecular and polymeric carbon allotropes. Angew Chem Int Ed Engl 1992;31(9):1101–23.
[30] Geim A, Novoselov K. In: Rodgers P, editor. Nanoscience and technology: a collection of reviews from nature Journals. Singapore: World Scientific; 2010.
[31] Diederich F, Kivala M. All-carbon scaffolds by rational design. Adv Mater 2010;22(7):803–12.
[32] Haley MM, Brand SC, Pak JJ. Carbon networks based on dehydrobenzoannulenes: synthesis of graphdiyne substructures. Angew Chem Int Ed Engl 1997;36(8):836–8.
[33] Vollhardt KPC. Cobalt-mediated [2+ 2+ 2]-cycloadditions: a maturing synthetic strategy [new synthetic methods (43)]. Angew Chem Int Ed Engl 1984;23(8):539–56.
[34] Novoselov KS, et al. Two-dimensional gas of massless Dirac fermions in graphene. Nature 2005;438(7065):197–200.
[35] Gao X, et al. Robust superhydrophobic foam: a graphdiyne-based hierarchical architecture for oil/water separation. Adv Mater 2016;28(1):168–73.
[36] Zheng Q, et al. Structural and electronic properties of bilayer and trilayer graphdiyne. Nanoscale 2012;4(13):3990–6.
[37] Kharisov BI, Kharissova OV, Kharisov BI, Kharissova OV. General data on carbon allotropes. Carbon allotropes: metal-complex chemistry, properties and applications. 2019. p. 1–8.
[38] Gao X, Liu H, Wang D, Zhang J. Graphdiyne: synthesis, properties, and applications. Chem Soc Rev 2019;48(3):908–36.
[39] Hayat A, et al. State, synthesis, perspective applications, and challenges of Graphdiyne and its analogues: a review of recent research. Adv Colloid Interface Sci 2023;319:102969.
[40] Li Y, Zuo Z, Li Y. 2D carbon graphdiyne: fundamentals and applications. In: Handbook of carbon-based nanomaterials. Elsevier; 2021. p. 461–516.
[41] Assad H, Sharma PK, Kumar A. Two-dimensional carbon graphdiyne. In: Handbook of functionalized carbon nanostructures: from synthesis methods to applications. Springer; 2024. p. 1–33.
[42] Li X, Cui X, Zhang L, Du J. Review of graphdiyne-based nanostructures and their applications. ACS Appl Nano Mater 2023;6(22):20493–522.
[43] Liu J, et al. GeP_3/NbX_2 (X= S, Se) nano-heterostructures: promising isotropic flexible anodes for lithium-ion batteries with high lithium storage capacity. ACS Omega 2021;6(4):2956–65.
[44] Soodchomshom B, Tang I-M, Hoonsawat R. Directional quantum transport in graphyne pn junction. J Appl Phys 2013;113(7):073710.
[45] Chen J, Xi J, Wang D, Shuai Z. Carrier mobility in graphyne should Be even larger than that in graphene: a theoretical prediction. J Phys Chem Lett 2013/05/02 2013;4(9):1443–8. https://doi.org/10.1021/jz4005587.
[46] Serafini P, Milani A, Tommasini M, Bottani CE, Casari CS. Topology-dependent conjugation effects in graphdiyne molecular fragments. Carbon 2021;180:265–73.
[47] Fang Y, Liu Y, Qi L, Xue Y, Li Y. 2D graphdiyne: an emerging carbon material. Chem Soc Rev 2022;51(7):2681–709.
[48] Sakamoto R, Toyoda R, Jingyan G, Nishina Y, Kamiya K, Nishihara H, Ogoshi T. Coordination chemistry for innovative carbon-related materials. Coord Chem Rev 2022;466:214577.
[49] Khan K, Tareen AK, Iqbal M, Shi Z, Zhang H, Guo Z. Novel emerging graphdiyne based two dimensional materials: synthesis, properties and renewable energy applications. Nano Today 2021;39:101207.
[50] Kang B, Lee JY. Electronic properties of α-graphyne nanotubes. Carbon 2015;84:246–53.
[51] Deb J, Bhattacharya B, Sarkar U. Electronic properties of aluminium and silicon doped (2, 2) graphyne nanotube. In: Journal of Physics: Conference series, vol. 759. IOP Publishing; 2016, 012038. 1.
[52] Coluci V, Braga S, Legoas S, Galvao D, Baughman R. Families of carbon nanotubes: graphyne-based nanotubes. Phys Rev B 2003;68(3):035430.
[53] Long M, Tang L, Wang D, Li Y, Shuai Z. Electronic structure and carrier mobility in graphdiyne sheet and nanoribbons: theoretical predictions. ACS Nano 2011;5(4):2593–600.
[54] Matsuoka R, Sakamoto R, Hoshiko K, Sasaki S, Masunaga H, Nagashio K, Nishihara H. Crystalline graphdiyne nanosheets produced at a gas/liquid or liquid/liquid interface. J Am Chem Soc 2017;139(8):3145–52.
[55] Gao X, et al. Ultrathin graphdiyne film on graphene through solution-phase van der Waals epitaxy. Sci Adv 2018;4(7):eaat6378.
[56] Hu G, He J, Chen J, Li Y. Self-assembly of Wheel-shaped nanographdiynes and self-template growth of graphdiyne. J Am Chem Soc 2024.
[57] Xin M, Leong WS, Chen Z, Lan S-Y. An atom interferometer inside a hollow-core photonic crystal fiber. Sci Adv 2018;4(1):e1701723.
[58] Chen X. Graphyne nanotubes as electrocatalysts for oxygen reduction reaction: the effect of doping elements on the catalytic mechanisms. Phys Chem Chem Phys 2015;17(43):29340–3.
[59] Bao H, Wang L, Li C, Luo J. Structural characterization and identification of graphdiyne and graphdiyne-based materials. ACS Appl Mater Interfaces 2018;11(3):2717–29.
[60] Malko D, Neiss C, Vines F, Görling A. Competition for graphene: graphynes with direction-dependent Dirac cones. Phys Rev Lett 2012;108(8):086804.
[61] Li J, et al. Architecture of β-graphdiyne-containing thin film using modified glaser–hay coupling reaction for enhanced photocatalytic property of TiO_2. Adv Mater 2017;29(19):1700421.
[62] Carper J. The CRC handbook of chemistry and physics. In: Bowker magazine group CAHNERS magazine division 249 W 17TH ST, NEW YORK, NY, vol. 124; 1999. p. 192–6.
[63] Peng Q, Ji W, De S. Mechanical properties of graphyne monolayers: a first-principles study. Phys Chem Chem Phys 2012;14(38):13385–91.
[64] Bu H, Zhao M, Zhang H, Wang X, Xi Y, Wang Z. Isoelectronic doping of graphdiyne with boron and nitrogen: stable configurations and band gap modification. J Phys Chem 2012;116(15):3934–9.
[65] Zhang S, et al. Raman spectra and corresponding strain effects in graphyne and graphdiyne. J Phys Chem C 2016;120(19):10605–13.
[66] Li J, et al. Diatomite-templated synthesis of freestanding 3D graphdiyne for energy storage and catalysis application. Adv Mater 2018;30(20):1800548.
[67] Cranford SW, Brommer DB, Buehler MJ. Extended graphynes: simple scaling laws for stiffness, strength and fracture. Nanoscale 2012;4(24):7797–809.
[68] Narita N, Nagai S, Suzuki S, Nakao K. Optimized geometries and electronic structures of graphyne and its family. Phys Rev B 1998;58(16):11009.
[69] Bai H, Zhu Y, Qiao W, Huang Y. Structures, stabilities and electronic properties of graphdiyne nanoribbons. RSC Adv 2011;1(5):768–75.
[70] Gu Z, et al. Membrane insertion and phospholipids extraction by graphyne nanosheets. J Phys Chem C 2017;121(4):2444–50.
[71] Du Y, Zhou W, Gao J, Pan X, Li Y. Fundament and application of graphdiyne in electrochemical energy. Accounts Chem Res 2020;53(2):459–69.

[72] Yu H, Xue Y, Li Y. Graphdiyne and its assembly architectures: synthesis, functionalization, and applications. Adv Mater 2019;31(42):1803101.
[73] Yu W, Song G, Lv F, Huang Y, Bai H, Wang S. Recent advances in graphdiyne materials for biomedical applications. Nano Today 2022;46:101616.
[74] Ali H, et al. The ordering behavior of Co_3Al-based γ' phase with $L1_2$ structure predicted by the thermodynamic model with support of first-principles calculations. Mater Today Commun 2022;33:104447.
[75] Li J, Gao X, Zhu L, Ghazzal MN, Zhang J, Tung C-H, Wu L-Z. Graphdiyne for crucial gas involved catalytic reactions in energy conversion applications. Energy Environ Sci 2020;13(5):1326–46.
[76] Zhao F, Liao G, Liu M, Wang T, Zhao Y, Xu J, Yin X. Precise preparation of triarylboron-based graphdiyne analogues for gas separation. Angew Chem 2024;136(5):e202317294.
[77] Hao W, et al. Synthesis and self-assembly of ultrathin holey graphdiyne nanosheets for oxygen reduction reaction. Small 2023;19(30):2302220.
[78] Chen X, et al. Tunable pore size from sub-nanometer to a few nanometers in large-area graphene nanoporous atomically thin membranes. ACS Appl Mater Interfaces 2021;13(25):29926–35.
[79] Hummel RE. Electronic properties of materials. Springer Science & Business Media; 2011.
[80] Muz İ, Kurban M. The electronic structure, transport and structural properties of nitrogen-decorated graphdiyne nanomaterials. J Alloys Compd 2020;842:155983.
[81] Qin X, Liu Y, Chi B, Zhao X, Li X. Origins of Dirac cones and parity dependent electronic structures of α-graphyne derivatives and silagraphynes. Nanoscale 2016;8(33):15223–32.
[82] Xue Y, Li Y, Zhang J, Liu Z, Zhao Y. 2D graphdiyne materials: challenges and opportunities in energy field. Sci China Chem 2018;61(7):765–86.
[83] Hayat A, et al. Synergetic effect of bismuth vanadate over copolymerized carbon nitride composites for highly efficient photocatalytic H_2 and O_2 generation. J Colloid Interface Sci 2022;627:621–9.
[84] Muz İ, Kurban M. Electronic structures and bonding of graphdiyne and its BN analogs: transition from quasi-planar to planar sheets. J Alloys Compd 2020;846:155987.
[85] Kim BG, Choi HJ. Graphyne: hexagonal network of carbon with versatile Dirac cones. Phys Rev B 2012;86(11):115435.
[86] Luo G, et al. Quasiparticle energies and excitonic effects of the two-dimensional carbon allotrope graphdiyne: theory and experiment. Phys Rev B 2011;84(7):075439.
[87] Jiao Y, Du A, Hankel M, Zhu Z, Rudolph V, Smith SC. Graphdiyne: a versatile nanomaterial for electronics and hydrogen purification. Chem Commun 2011;47(43):11843–5. https://doi.org/10.1039/C1CC15129K. 10.1039/C1CC15129K.
[88] Cui H-J, Sheng X-L, Yan Q-B, Zheng Q-R, Su G. Strain-induced Dirac cone-like electronic structures and semiconductor–semimetal transition in graphdiyne. Phys Chem Chem Phys 2013;15(21):8179–85.
[89] Pan L, Song B, Sun J, Zhang L, Hofer W, Du S, Gao H-j. The origin of half-metallicity in conjugated electron systems—a study on transition-metal-doped graphyne. J Phys Condens Matter 2013;25(50):505502.
[90] Shohany BG, Roknabadi MR, Kompany A. Computational study of edge configuration and the diameter effects on the electrical transport of graphdiyne nanotubes. Phys E Low-dimens Syst Nanostruct 2016;84:146–51.
[91] Hybertsen MS, Louie SG. Electron correlation in semiconductors and insulators: band gaps and quasiparticle energies. Phys Rev B 1986;34(8):5390.
[92] Sani SS, Mousavi H, Asshabi M, Jalilvand S. Electronic properties of graphyne and graphdiyne in tight-binding model. ECS J. Solid State Sci Technol. 2020;9(3):031003.
[93] Achilli S, Milani A, Fratesi G, Tumino F, Manini N, Onida G, Casari CS. Graphdiynes interacting with metal surfaces: first-principles electronic and vibrational properties. 2D Mater 2021;8(4):044014.
[94] Ketabi N, Tolhurst TM, Leedahl B, Liu H, Li Y, Moewes A. How functional groups change the electronic structure of graphdiyne: theory and experiment. Carbon 2017;123:1–6.
[95] Yue Q, Chang S, Kang J, Qin S, Li J. Mechanical and electronic properties of graphyne and its family under elastic strain: theoretical predictions. J Phys Chem C 2013;117(28):14804–11.
[96] Mousavi H, Asshabi M, Jalilvand S, Khodadadi J. Strain effect on the electronic properties of graphdiyne. Thin Solid Films 2022;761:139514.
[97] Pan H, Zhang H, Wang H, Li J, Sun Y, Lu W, Wang X. Unusual mechanical and electronic behaviors of bulk layered hydrogen substituted graphdiyne under biaxial strain. Appl Surf Sci 2020;513:145694.
[98] Li X, Li S. Investigations of electronic and nonlinear optical properties of single alkali metal adsorbed graphene, graphyne and graphdiyne systems by first-principles calculations. J Mater Chem C 2019;7(6):1630–40.
[99] Hou N, Feng R, Fang XH. A theoretical comparison of the electrical and nonlinear optical properties of GDY–π–TPA: the important role of π-conjugated bridge. Int J Quant Chem 2022;122(19):e26965.
[100] Bai Q, et al. Nitrogen-Doped Graphdiyne Quantum-dots as an Optical-Electrochemical sensor for sensitive detection of dopamine. Microchem J 2022;179:107521.
[101] Muz İ, Göktaş F, Kurban M. Size dependence in the electronic and optical properties of a BN analogue of two-dimensional graphdiyne: a theoretical study. Chem Phys 2020;539:110929.
[102] Gao N, et al. Graphdiyne: a new carbon allotrope for electrochemiluminescence. Angew Chem Int Ed 2022;61(28):e202204485.
[103] Liu Q, Feng N, Zou Y, Fan C, Wang J. Exploring the impact of stress on the electronic structure and optical properties of graphdiyne nanoribbons for advanced optoelectronic applications. Sci Rep 2024;14(1):6051.
[104] Zhao Y, Guo P, Li X, Jin Z. Ultrafast photonics application of graphdiyne in the optical communication region. Carbon 2019;149:336–41.
[105] P. A. Klejment, "OF the institute of geophysics polish academy of sciences.".
[106] Zhang J, Ragab T, Basaran C. Comparison of fracture behavior of defective armchair and zigzag graphene nanoribbons. Int J Damage Mech 2019;28(3):325–45.
[107] He F, Li Y. Advances on theory and experiments of the energy applications in graphdiyne. CCS Chem 2023;5(1):72–94.
[108] Ali H, et al. The site preference and doping effect on mechanical properties of Ni_3Al-based γ' phase in superalloys by combing first-principles calculations and thermodynamic model. Arab J Chem 2022;15(11):104278.
[109] Xiao K, Li J, Wu X, Liu H, Huang C, Li Y. Nanoindentation of thin graphdiyne films: experiments and molecular dynamics simulation. Carbon 2019;144:72–80.
[110] Faria B, Guarda C, Silvestre N, Lopes JN. Aluminum composites reinforced by γ-graphynes: the effect of nanofillers porosity and shape on crystal growth and composite strengthening. Comput Mater Sci 2020;176:109538.
[111] Ahangari MG. Effect of defect and temperature on the mechanical and electronic properties of graphdiyne: a theoretical study. Phys E Low-dimens Syst Nanostruct 2015;66:140–7.
[112] S. W. C. A. B and M. J. B. A. B. Mechanical properties of graphyne. Carbon 2011;49(13):4111–21.
[113] Li J, Jing X, Li Q, Li S, Gao X, Feng X, Wang B. Bulk COFs and COF nanosheets for electrochemical energy storage and conversion. Chem Soc Rev 2020;49(11):3565–604.
[114] Xu W, Zhang M, Dong Y, Zhao J. Two-dimensional materials for dendrite-free zinc metal anodes in aqueous zinc batteries. Batteries 2022;8(12):293.
[115] Zhang X, Qiu T, Huang X, Wang L, Luo B. New opportunities and challenges of battery separators. Advan. Mater. Battery Separat. 2024:377–419.
[116] Hayat A, et al. Recent advances and future perspectives of metal-based electrocatalysts for overall electrochemical water splitting. Chem Rec 2023;23(2):e202200149.
[117] Mortazavi B, Makaremi M, Shahrokhi M, Fan Z, Rabczuk T. N-graphdiyne two-dimensional nanomaterials: semiconductors with low thermal conductivity and high stretchability. Carbon 2018;137:57–67.
[118] Xie C, et al. Tuning the properties of graphdiyne by introducing electron-withdrawing/donating groups. Angew Chem 2020;132(32):13644–8.
[119] Liu M, Huang J, Hu S, Ma Z, Yang Y, Chen Y, Liu Y. Mechanism study of trimetallic single-cluster catalysts loaded on graphdiyne for highly efficient oxygen-reduction reactions. Appl Surf Sci 2024;672:160860.
[120] Li H, Lim JH, Lv Y, Li N, Kang B, Lee JY. Graphynes and graphdiynes for energy storage and catalytic utilization: theoretical insights into recent advances. Chem Rev 2023;123(8):4795–854.
[121] Han Y, et al. Hollow N-doped carbon spheres with isolated cobalt single atomic sites: superior electrocatalysts for oxygen reduction. J Am Chem Soc 2017;139(48):17269–72.
[122] Chen R, et al. A general approach to simulate the atom distribution, lattice distortion, and mechanical properties of multi-principal element alloys based on site preference: using FCC_CoNiV and CoCrNi to demonstrate and compare. J Alloys Compd 2023;935:168016.
[123] Zou X, Tang M, Lu Q, Wang Y, Shao Z, An L. Carbon-based electrocatalysts for rechargeable Zn–air batteries: design concepts, recent progress and future perspectives. Energy Environ Sci 2024;17(2):386–424.
[124] Guo J, et al. Rational design of earth-abundant catalysts toward sustainability. Adv Mater 2024;36(42):2407102.
[125] Kong D, et al. Sp^2-carbon dominant carbonaceous materials for energy conversion and storage. Mater Sci Eng R Rep 2019;137:1–37.
[126] Das BK, Sen D, Chattopadhyay K. Nitrogen doping in acetylene bonded two dimensional carbon crystals: ab-initio forecast of electrocatalytic activities vis-à-vis boron doping. Carbon 2016;105:330–9.
[127] Kang B, Shi H, Wu S, Zhao W, Ai H, Lee JY. Revealing the importance of nitrogen doping site in enhancing the oxygen reduction reaction on β-graphyne. Carbon 2017;123:415–20.
[128] Das BK, Sen D, Chattopadhyay K. Implications of boron doping on electrocatalytic activities of graphyne and graphdiyne families: a first principles study. Phys Chem Chem Phys 2016;18(4):2949–58.
[129] Gao X, Shen X. Face-to-face crosslinking of graphdiyne and related carbon sheets toward integrated graphene nanoribbon arrays. Carbon 2017;125:536–43.
[130] Satyapal S, Petrovic J, Read C, Thomas G, Ordaz G. Catal Today 2007;120:246–56.
[131] Berseth PA, et al. Carbon nanomaterials as catalysts for hydrogen uptake and release in $NaAlH_4$. Nano Lett 2009;9(4):1501–5.
[132] Sakintuna B, Lamari-Darkrim F, Hirscher M. Metal hydride materials for solid hydrogen storage: a review. Int J Hydrogen Energy 2007;32(9):1121–40.
[133] Bogdanovic B, felderhoff M, Pommerin A, Schuth F, Spielkamp N. Adv Mater 2006;18:1198.
[134] Shekar SC, Swathi R. Cation− π interactions and rattling motion through two-dimensional carbon networks: graphene vs graphynes. J Phys Chem C 2015;119(16):8912–23.
[135] Ma D, Li T, Wang Q, Yang G, He C, Ma B, Lu Z. Graphyne as a promising substrate for the noble-metal single-atom catalysts. Carbon 2015;95:756–65.
[136] Lin Z-Z. Graphdiyne-supported single-atom Sc and Ti catalysts for high-efficient CO oxidation. Carbon 2016;108:343–50.

[137] Yu H, Du A, Song Y, Searles DJ. Graphyne and graphdiyne: versatile catalysts for dehydrogenation of light metal complex hydrides. J Phys Chem C 2013;117(42):21643–50.
[138] Wu P, Du P, Zhang H, Cai C. Graphdiyne as a metal-free catalyst for low-temperature CO oxidation. Phys Chem Chem Phys 2014;16(12):5640–8.
[139] Song E, Wen Z, Jiang Q. CO catalytic oxidation on copper-embedded graphene. J Phys Chem C 2011;115(9):3678–83.
[140] Li F, Zhao J, Chen Z. Fe-anchored graphene oxide: a low-cost and easily accessible catalyst for low-temperature CO oxidation. J Phys Chem C 2012;116(3):2507–14.
[141] Liu C, et al. CO self-promoting oxidation on nanosized gold clusters: triangular Au_3 active site and CO induced O–O scission. J Am Chem Soc 2013;135(7):2583–95.
[142] Petersen M, Jenkins S, King D. Ridge-bridge adsorption of molecular oxygen on Pt {110}(1× 2) from first principles. J Phys Chem B 2006;110(24):11962–70.
[143] Lu Y-H, Zhou M, Zhang C, Feng Y-P. Metal-embedded graphene: a possible catalyst with high activity. J Phys Chem C 2009;113(47):20156–60.
[144] He J, Ma SY, Zhou P, Zhang C, He C, Sun L. Magnetic properties of single transition-metal atom absorbed graphdiyne and graphyne sheet from DFT+ U calculations. J Phys Chem C 2012;116(50):26313–21.
[145] Kong X, Huang Y, Liu Q. Two-dimensional boron-doped graphyne nanosheet: a new metal-free catalyst for oxygen evolution reaction. Carbon 2017;123:558–64.
[146] Lee JD, et al. Dilute alloys based on Au, Ag, or Cu for efficient catalysis: from synthesis to active sites. Chem Rev 2022;122(9):8758–808.
[147] Wu Z, et al. In situ monitored (N, O)-Doping of flexible vertical graphene films with high-flux plasma enhanced chemical vapor deposition for remarkable metal-free redox catalysis essential to alkaline zinc–air batteries. Adv Sci 2022;9(13):2200614.
[148] Chen W, et al. Heteroatom-doped flash graphene. ACS Nano 2022;16(4):6646–56.
[149] Tang C, Zhang Q. Nanocarbon for oxygen reduction electrocatalysis: dopants, edges, and defects. Adv Mater 2017;29(13):1604103.
[150] Ali H, et al. Efficiency of a novel nitrogen-doped Fe_3O_4 impregnated biochar (N/Fe_3O_4@ BC) for arsenic (III and V) removal from aqueous solution: insight into mechanistic understanding and reusability potential. Arab J Chem 2022;15(11):104209.
[151] Luan Y, et al. Dual-function interface engineering for efficient perovskite solar cells. EcoMat 2021;3(2):e12092.
[152] Zhao Y, et al. Few-layer graphdiyne doped with sp-hybridized nitrogen atoms at acetylenic sites for oxygen reduction electrocatalysis. Nat Chem 2018;10(9):924–31.
[153] Liu B, et al. Revealing the mechanism of sp-N doping in graphdiyne for developing site-defined metal-free catalysts. Adv Mater 2023;35(50):2206450.
[154] Wang L, et al. Conjugated microporous polymer nanosheets for overall water splitting using visible light. Adv Mater 2017;29(38):1702428.
[155] Fan K, et al. In vivo guiding nitrogen-doped carbon nanozyme for tumor catalytic therapy. Nat Commun 2018;9(1):1–11.
[156] Liu R, et al. Nitrogen-doped graphdiyne as a metal-free catalyst for high-performance oxygen reduction reactions. Nanoscale 2014;6(19):11336–43.
[157] Lv Q, et al. Nitrogen-doped porous graphdiyne: a highly efficient metal-free electrocatalyst for oxygen reduction reaction. ACS Appl Mater Interfaces 2017;9(35):29744–52.
[158] Yang S, Bachman RE, Feng X, Müllen K. Use of organic precursors and graphenes in the controlled synthesis of carbon-containing nanomaterials for energy storage and conversion. Accounts Chem Res 2013;46(1):116–28.
[159] Fujii S, Enoki T. Nanographene and graphene edges: electronic structure and nanofabrication. Accounts Chem Res 2013;46(10):2202–10.
[160] Shang H, et al. N-doped graphdiyne for high-performance electrochemical electrodes. Nano Energy 2018;44:144–54.
[161] Das BK, Sen D, Chattopadhyay K. Mechanism of oxygen reduction reaction in alkaline medium on nitrogen-doped graphyne and graphdiyne families: a first principles study. ChemPhysChem 2022;23(9):e202100900.
[162] Shang H, Zuo Z, Li L, Wang F, Liu H, Li Y, Li Y. Ultrathin graphdiyne nanosheets grown in situ on copper nanowires and their performance as lithium-ion battery anodes. Angew Chem Int Ed 2018;57(3):774–8.
[163] Zhou J, et al. Synthesis of graphdiyne nanowalls using acetylenic coupling reaction. J Am Chem Soc 2015/06/24 2015;137(24):7596–9. https://doi.org/10.1021/jacs.5b04057.
[164] Zuo Z, Shang H, Chen Y, Li J, Liu H, Li Y, Li Y. A facile approach for graphdiyne preparation under atmosphere for an advanced battery anode. Chem Commun 2017;53(57):8074–7.
[165] He J, et al. Hydrogen substituted graphdiyne as carbon-rich flexible electrode for lithium and sodium ion batteries. Nat Commun 2017;8(1):1–11.
[166] Jia Z, Zuo Z, Yi Y, Liu H, Li D, Li Y, Li Y. Low temperature, atmospheric pressure for synthesis of a new carbon Ene-yne and application in Li storage. Nano Energy 2017;33:343–9.
[167] Matsuoka R, et al. Expansion of the graphdiyne family: a triphenylene-cored analogue. ACS Appl Mater Interfaces 2018;11(3):2730–3.
[168] Kan X, et al. Interfacial synthesis of conjugated two-dimensional N-graphdiyne. ACS Appl Mater Interfaces 2018;10(1):53–8.
[169] Klappenberger F, Zhang Y-Q, Björk J, Klyatskaya S, Ruben M, Barth JV. On-surface synthesis of carbon-based scaffolds and nanomaterials using terminal alkynes. Accounts Chem Res 2015;48(7):2140–50.
[170] Zhang Y-Q, et al. Homo-coupling of terminal alkynes on a noble metal surface. Nat Commun 2012;3(1):1–8.
[171] Cirera B, et al. Synthesis of extended graphdiyne wires by vicinal surface templating. Nano Lett 2014;14(4):1891–7.
[172] Klappenberger F, et al. Functionalized graphdiyne nanowires: on-surface synthesis and assessment of band structure, flexibility, and information storage potential. Small 2018;14(14):1704321.
[173] Sun Q, Cai L, Ma H, Yuan C, Xu W. Dehalogenative homocoupling of terminal alkynyl bromides on Au (111): incorporation of acetylenic scaffolding into surface nanostructures. ACS Nano 2016;10(7):7023–30.
[174] Gao H-Y, et al. Intermolecular on-surface σ-bond metathesis. J Am Chem Soc 2017;139(20):7012–9.
[175] Shu C-H, et al. On-surface synthesis of poly (p-phenylene ethynylene) molecular wires via in situ formation of carbon-carbon triple bond. Nat Commun 2018;9(1):1–7.
[176] Liu R, et al. Chemical vapor deposition growth of linked carbon monolayers with acetylenic scaffoldings on silver foil. Adv Mater 2017;29(18):1604665.
[177] Niu L, Coleman JN, Zhang H, Shin H, Chhowalla M, Zheng Z. Production of two-dimensional nanomaterials via liquid-based direct exfoliation. Small 2016;12(3):272–93.
[178] Qian X, et al. Self-catalyzed growth of large-area nanofilms of two-dimensional carbon. Sci Rep 2015;5(1):1–7.
[179] Bhuvaneswari R, Nagarajan V, Chandiramouli R. Explosive vapor detection using novel graphdiyne nanoribbons—a first-principles investigation. Struct Chem 2020;31(2):709–17.
[180] Jin Z, Li X. Graphdiyne preparation and application in photocatalytic hydrogen evolution. Langmuir 2024;40(10):5011–25.
[181] Wang F, Zuo Z, Shang H, Zhao Y, Li Y. Ultrafastly interweaving graphdiyne nanochain on arbitrary substrates and its performance as a supercapacitor electrode. ACS Appl Mater Interfaces 2018;11(3):2599–607.
[182] Bie C, Cheng B, Ho W, Li Y, Macyk W, Ghasemi JB, Yu J. Graphdiyne-based photocatalysts for solar fuel production. Green Chem 2022;24(15):5739–54.
[183] Dai D, Fan J. Wet-chemistry synthesis of carbon nanostructures. In: Handbook of functionalized carbon nanostructures: from synthesis methods to applications. Springer; 2023. p. 1–27.
[184] Jin Z, et al. Graphdiyne: ZnO nanocomposites for high-performance UV photodetectors. Adv Mater 2016;28(19):3697–702.
[185] Haley MM. Synthesis and properties of annulenic subunits of graphyne and graphdiyne nanoarchitectures. Pure Appl Chem 2008;80(3):519–32.
[186] Huynh C, Linstrumelle G. A short route to dehydro [12] annulenes. Tetrahedron 1988;44(20):6337–44.
[187] Chen X, Lin Z-Z, Ju M, Guo L-X. Confined electrochemical catalysis under cover: enhanced CO_2 reduction at the interface between graphdiyne and Cu surface. Appl Surf Sci 2019;479:685–92.
[188] Zhang X, Wang N, Li Y. The accurate synthesis of a multiscale metallic interface on graphdiyne. Small Methods 2024:2301571.
[189] Zou H, et al. Electronic perturbation of Cu nanowire surfaces with functionalized graphdiyne for enhanced CO_2 reduction reaction. Natl Sci Rev 2024;11(12):nwae253.
[190] Diercks R, Vollhardt KPC. Cobalt-katalysierte Cyclisierung von Bis (2-ethinylphenyl) ethin-neue Synthese von gewinkeltem [3] Phenylen (Terphenylen), einem Molekül mit einer Cyclohexatrien-Einheit. Angew Chem 1986;98(3):268–70.
[191] Wang SS, et al. Superlyophilicity-facilitated synthesis reaction at the microscale: ordered graphdiyne stripe arrays. Small 2017;13(4):1602265.
[192] Huczko A. Template-based synthesis of nanomaterials. Appl Phys A 2000;70:365–76.
[193] Hulteen JC, Martin CR. A general template-based method for the preparation of nanomaterials. J Mater Chem 1997;7(7):1075–87.
[194] He X, Zhang T, Pan M, Ma Z, Hu C-J. Template-based model generation. Software Syst Model 2019;18:2051–92.
[195] Seebacher UG. Template-based management: a guide for an efficient and impactful professional practice. Springer; 2020.
[196] Luhunu LK. Survey of template-based code generation. 2017.
[197] Liu J, et al. Graphdiyne-templated palladium-nanoparticle assembly as a robust oxygen generator to attenuate tumor hypoxia. Nano Today 2020;34:100907.
[198] Li J, et al. Template synthesis of an ultrathin β-graphdiyne-like film using the eglinton coupling reaction. ACS Appl Mater Interfaces 2018;11(3):2734–9.
[199] Hu G, He J, Chen J, Li Y. Self-assembly of wheel-shaped nanographdiynes and self-template growth of graphdiyne. J Am Chem Soc 2024;146(6):4123–33.
[200] Gao HY, Wagner H, Zhong D, Franke JH, Studer A, Fuchs H. Glaser coupling at metal surfaces. Angew Chem Int Ed 2013;52(14):4024–8.
[201] Cameron M, Bennett G. Use of amines in the glaser coupling reaction. J Org Chem 1957;22(5):557–8.
[202] Sohail M, et al. Nanostructured materials based on g-C_3N_4 for enhanced photocatalytic activity and potentials application: a review. Arab J Chem 2022;15(9):104070.
[203] Zhou J, et al. Synthesis of graphdiyne nanowalls using acetylenic coupling reaction. J Am Chem Soc 2015;137(24):7596–9.
[204] Sindhu K, Anilkumar G. Recent advances and applications of Glaser coupling employing greener protocols. RSC Adv 2014;4(53):27867–87.
[205] Chen X, Jiang X, Yang N. Graphdiyne electrochemistry: progress and perspectives. Small 2022;18(24):2201135.
[206] Jover J, Spuhler P, Zhao L, McArdle C, Maseras F. Toward a mechanistic understanding of oxidative homocoupling: the Glaser–Hay reaction. Catal Sci Technol 2014;4(12):4200–9.
[207] Vilhelmsen MH, Jensen J, Tortzen CG, Nielsen MB. The Glaser–Hay reaction: optimization and scope based on ^{13}C NMR kinetics experiments. Eur J Org Chem 2013;2013(4):701–11.

[208] Wu B, et al. A reasonable approach to describe the atom distributions and configurational entropy in high entropy alloys based on site preference. Intermetallics 2022;144:107489.
[209] Zhou W, Shen H, Zeng Y, Yi Y, Zuo Z, Li Y, Li Y. Controllable synthesis of graphdiyne nanoribbons. Angew Chem Int Ed 2020;59(12):4908–13.
[210] Yu S, Chen J, Chen C, Zhou M, Shen L, Li B, Lin H. What happens when graphdiyne encounters doping for electrochemical energy conversion and storage. Coord Chem Rev 2023;482:215082.
[211] Zhao N, Li J, Chang X, Zheng W, Zhang J, Liu X. Synthesis and application of graphdiyne-based materials for advanced chemical sensors. Coord Chem Rev 2024;521:216171.
[212] Brassell SC, Eglinton Frs TI. Geoffrey Eglinton. 1 November 1927—11 March 2016. The Royal Society; 2024.
[213] Lybrand AM. Studies towards high surface area porous polymers via cross-coupling methodology. Wayne State University; 2024.
[214] Zhou J, Li J, Liu Z, Zhang J. Exploring approaches for the synthesis of few-layered graphdiyne. Adv Mater 2019;31(42):1803758.
[215] Ajmal Z, et al. Embedding aromatic conjugated monomer within carbon nitride for efficient photocatalytic reduction reactions. J Mol Liq 2022;368:120617.
[216] Gao Y, Tykwinski RR. Advances in polyynes to model carbyne. Accounts Chem Res 2022;55(24):3616–30.
[217] Hu G, He J, Li Y. Controllable synthesis of two-dimensional graphdiyne films catalyzed by a copper (II) trichloro complex. ACS Catal 2022;12(11):6712–21.
[218] Nishihara Y, Ikegashira K, Hirabayashi K, Ando J-i, Mori A, Hiyama T. Coupling reactions of alkynylsilanes mediated by a Cu (I) salt: novel syntheses of conjugate diynes and disubstituted ethynes. J Org Chem 2000;65(6):1780–7.
[219] Takahashi T, Xi Z, Obora Y, Suzuki N. Intramolecular coupling of alkynyl groups of bis (alkynyl) silane mediated by zirconocene compounds: formation of silacyclobutene derivatives. J Am Chem Soc 1995;117(9):2665–6.
[220] Kuciński K. Synthesis of alkynylsilanes: a review of the state of the art. Adv Synth Catal 2024.
[221] Xiao Q, Yang X, Guo X, Jin Z. Strong interface coupling of H-substituted graphdiyne-based promotes photocatalytic hydrogen production. Appl Catal, B: Environ Energy 2024;359:124502.
[222] Li J, et al. A deprotection-free method for high-yield synthesis of graphdiyne powder with in situ formed CuO nanoparticles. Angew Chem Int Ed 2022;61(43): e202210242.
[223] Hayat A, et al. Different dimensionalities, morphological advancements and engineering of g-C_3N_4-based nanomaterials for energy conversion and storage. Chem Rec 2023;23(5):e202200171.
[224] He F, Hou L, Wu X, Ding H, Qu J, Chen Y. Enantioselective synthesis of α-alkenylated γ-lactam enabled by Ni-catalyzed 1, 4-arylcarbamoylation of 1, 3-dienes. CCS Chem 2023;5(2):341–9.
[225] Li G, Li Y, Qian X, Liu H, Lin H, Chen N, Li Y. Construction of tubular molecule aggregations of graphdiyne for highly efficient field emission. J Phys Chem C 2011;115(6):2611–5.
[226] Huang C, Wang N. Functionalization of GDYs. Graphdiyne: Fundamentals and applications in renewable energy and electronics. 2022. p. 125–63.
[227] Wang M, Pu J, Hu Y, Zi Y, Wu ZG, Huang W. Functional graphdiyne for emerging applications: recent advances and future challenges. Adv Funct Mater 2024;34(4): 2308601.
[228] Song B, et al. Using graphdiyne (GDY) as a catalyst support for enhanced performance in organic pollutant degradation and hydrogen production: a review. J Hazard Mater 2020;398:122957.
[229] Qian X, Zheng Y, Chen S, Xu J. Atomic-level functionalized graphdiyne for electrocatalysis applications. Catalysts 2020;10(8):929.
[230] Ajmal Z, et al. Current progresses in two-dimensional MXene-based framework: prospects from superficial synthesis to energy conversion and storage applications. Mater Today Chem 2023;27:101238.
[231] Pei J, et al. A surface matrix of Au NPs decorated graphdiyne for multifunctional laser desorption/ionization mass spectrometry. ACS Appl Mater Interfaces 2023; 15(45):52814–26.
[232] Yang X, et al. Ultra-fast preparation of large-area graphdiyne-based membranes via alkynylated surface-modification for nanofiltration. Angew Chem Int Ed 2023; 62(17):e202217378.
[233] Maurer RJ, Liu W, Poltavsky I, Stecher T, Oberhofer H, Reuter K, Tkatchenko A. Thermal and electronic fluctuations of flexible adsorbed molecules: azobenzene on Ag (111). Phys Rev Lett 2016;116(14):146101.
[234] Zhao J, Ma J. Theoretical designs of photoresponsive energy-storage materials based on attachment of π-conjugated molecules onto sulfur-doped graphene. J Phys Chem C 2016;120(43):25131–41.
[235] Kolpak AM, Grossman JC. Azobenzene-functionalized carbon nanotubes as high-energy density solar thermal fuels. Nano Lett 2011;11(8):3156–62.
[236] Zhang X, Feng Y, Huang D, Li Y, Feng W. Investigation of optical modulated conductance effects based on a graphene oxide–azobenzene hybrid. Carbon 2010; 48(11):3236–41.
[237] Peimyoo N, et al. Photocontrolled molecular structural transition and doping in graphene. ACS Nano 2012;6(10):8878–86.
[238] Wang D, Wang X. Self-assembled graphene/azo polyelectrolyte multilayer film and its application in electrochemical energy storage device. Langmuir 2011;27 (5):2007–13.
[239] Shekar SC, Swathi RS. Molecular switching on graphyne and graphdiyne: realizing functional carbon networks in synergy with graphene. Carbon 2018;126: 489–99.
[240] Xiong Z, et al. A supramolecular strategy to precisely fabricate binary-doping metal-free graphdiyne for high-performance zinc-air batteries. Mater Chem Front 2024.
[241] Galvão DS. Fullereneynes: a new family of porous fullerenes Journal Article. Chem Phys Lett 1993;204(1):8–14.
[242] Ivanovskii A. Graphynes and graphdyines. Prog Solid State Chem 2013;41(1–2): 1–19.
[243] Uddin I, et al. Efficient pyrolysis process of lignin over dual catalyst bed for the production of Phenols and Aromatics. South Afr J Bot 2022;149:109–16.
[244] Stankovich S, et al. Graphene-based composite materials. Nature 2006;442 (7100):282–6.
[245] Tang Q, Zhou Z, Chen Z. Graphene-related nanomaterials: tuning properties by functionalization. Nanoscale 2013;5(11):4541–83.
[246] Cranford SW, Buehler MJ. Selective hydrogen purification through graphdiyne under ambient temperature and pressure. Nanoscale 2012;4(15):4587–93.
[247] Autreto P, De Sousa J, Galvao D. Site-dependent hydrogenation on graphdiyne. Carbon 2014;77:829–34.
[248] Li W, et al. Graphdiyne facilitates photocatalytic CO_2 hydrogenation into C^{2+} hydrocarbons. Appl Catal B Environ 2024;340:123267.
[249] Rouhi S, Moradi H, Hakimi Y, Nikpour F. On the mechanical properties of the graphyne and graphdiyne with patterned hydrogenation and hole: a molecular dynamics investigation. Appl Phys A 2020;126(6):465.
[250] Yoo JM, Kang JH, Hong BH. Graphene-based nanomaterials for versatile imaging studies. Chem Soc Rev 2015;44(14):4835–52.
[251] Walter AL, et al. Luminescence, patterned metallic regions, and photon-mediated electronic changes in single-sided fluorinated graphene sheets. ACS Nano 2014;8 (8):7801–8.
[252] Shen J, Zhu Y, Yang X, Zong J, Zhang J, Li C. One-pot hydrothermal synthesis of graphene quantum dots surface-passivated by polyethylene glycol and their photoelectric conversion under near-infrared light. New J Chem 2012;36(1): 97–101.
[253] Noor NFaM, Badri MAS, Salleh MM, Umar AA. Synthesis of white fluorescent pyrrolic nitrogen-doped graphene quantum dots. Opt Mater 2018;83:306–14.
[254] Zheng J-J, Zhao X, Zhao Y, Gao X. Two-dimensional carbon compounds derived from graphyne with chemical properties superior to those of graphene. Sci Rep 2013;3(1):1271.
[255] Bhattacharya B, Singh N, Sarkar U. Tuning of band gap due to fluorination of graphyne and graphdiyne. In: Journal of Physics: Conference series, vol. 566. IOP Publishing; 2014, 012014. 1.
[256] Shen X, et al. Fluorine-enriched graphdiyne as an efficient anode in lithium-ion capacitors. ChemSusChem 2019;12(7):1342–8.
[257] Xiao W, et al. Fluorinated graphdiyne as a significantly enhanced fluorescence material. RSC Adv 2019;9(32):18377–82.
[258] Ramirez-de-Arellano J, Canales M, Magaña L. Carbon nanostructures doped with transition metals for pollutant gas adsorption systems. Molecules 2021;26(17): 5346.
[259] Singsen S, Thasami N, Tangpakonsab P, Bae H, Lee H, Hussain T, Kaewmaraya T. Transition-metal decorated graphdiyne monolayer as an efficient sensor toward phosphide (PH_3) and arsine (AsH_3). Phys Chem Chem Phys 2022;24(43): 26622–30.
[260] Tabandeh Z, Reisi-Vanani A. Manipulation of the CO_2 capture capability of graphdiyne using transition metal decoration and charge injection: a DFT-D2 study. Fuel 2023;333:126295.
[261] Panigrahi P, Dhinakaran A, Naqvi SR, Gollu S, Ahuja R, Hussain T. Light metal decorated graphdiyne nanosheets for reversible hydrogen storage. Nanotechnology 2018;29(35):355401.
[262] Huang C, Wang N. Functionalization of GDYs. In: Graphdiyne; 2022. p. 125–63.
[263] Deng Q, Luo Z, Yang R, Li J. Toward organic carbonyl-contained small molecules in rechargeable batteries: a review of current modified strategies. ACS Sustain Chem Eng 2020;8(41):15445–65.
[264] Xiao L, Wang Z, Guan J. Optimization strategies of covalent organic frameworks and their derivatives for electrocatalytic applications. Adv Funct Mater 2024;34 (11):2310195.
[265] Häupler B, Wild A, Schubert US. Carbonyls: powerful organic materials for secondary batteries. Adv Energy Mater 2015;5(11):1402034.
[266] Hayat A, et al. The photocatalytic H_2O_2 production: design strategies, Photocatalyst advancements, environmental applications and future prospects. Coord Chem Rev 2025;522:216218.
[267] He J, et al. Dual-interface engineering in perovskite solar cells with 2D carbides. Angew Chem Int Ed 2023;62(41):e202311865.
[268] He J, Hu G, Chen J, Li Y. Effect of anthraquinone-substituted graphdiyne analog on the growth of lithium dendrites. Advan Sustain Sys. 2024:2300464.
[269] Ryu SW, Asada H, Hirao A. Synthesis of novel well-defined substituted polystyrenes functionalized with two and four benzyl bromide moieties in each monomer unit and their application to densely branched polymer synthesis. Macromolecules 2002;35(19):7191–9.
[270] Solis DA, Borges DD, Woellner CF, Galvao DS. Structural and thermal stability of graphyne and graphdiyne nanoscroll structures. ACS Appl Mater Interfaces 2018; 11(3):2670–6.
[271] Zhang P, Wu T, Han B. Preparation of catalytic materials using ionic liquids as the media and functional components. Adv Mater 2014;26(40):6810–27.
[272] Yang Z, et al. Chemical modification of the sp-hybridized carbon atoms of graphdiyne by using organic sulfur. Chem–Eur J 2019;25(22):5643–7.
[273] Yuan L, Lin W, Yang Y, Chen H. A unique class of near-infrared functional fluorescent dyes with carboxylic-acid-modulated fluorescence ON/OFF switching: rational design, synthesis, optical properties, theoretical calculations, and

applications for fluorescence imaging in living animals. J Am Chem Soc 2012;134 (2):1200–11.
[274] Pepe G, Cole JM, Waddell PG, McKechnie S. Molecular engineering of cyanine dyes to design a panchromatic response in co-sensitized dye-sensitized solar cells. Mol. Sys. Des. Eng. 2016;1(1):86–98.
[275] Domena JB, et al. Advancing glioblastoma imaging: exploring the potential of organic fluorophore-based red emissive carbon dots. J Colloid Interface Sci 2023; 650:1619–37.
[276] Karaoglu K, Kaya K, Yilmaz I. New Chromenylium– cyanine based dual channel chemosensors for copper and hypochlorite sensing. Dyes Pigments 2020;180: 108445.
[277] Wang R, Hua S, Xing Y, Wang H, Jiang T, Yu F. Organic dye-based photosensitizers for fluorescence imaging-guided cancer phototheranostics. Coord Chem Rev 2024;513:215866.
[278] Xie J, et al. Graphdiyne nanoradioprotector with efficient free radical scavenging ability for mitigating radiation-induced gastrointestinal tract damage. Biomaterials 2020;244:119940.
[279] Kimball DB, Haley MM, Mitchell RH, Ward TR, Bandyopadhyay S, Williams RV, Armantrout JR. Dimethyldihydropyrene– dehydrobenzoannulene hybrids: studies in aromaticity and photoisomerization. J Org Chem 2002;67(25): 8798–811.
[280] Hisaki I, Sonoda M, Tobe Y. Strained dehydrobenzoannulenes. Eur J Org Chem 2006;2006(4):833–47.
[281] Xu T, et al. Topology modulation of tetraphenylethylene graphdiyne at a liquid-liquid interface. Nano Res 2024:1–7.
[282] Zhang L, et al. Carbon based nanomaterials for energy storage. In: Materials for energy storage. CRC Press; 2024. p. 45–73.
[283] Shen H, Zhou W, He F, Gu Y, Li Y, Li Y. A dehydrobenzoannulene-based three dimensional graphdiyne for photocatalytic hydrogen generation using Pt nanoparticles as a co-catalyst and triethanolamine as a sacrificial electron donor. J Mater Chem A 2020;8(9):4850–5.
[284] Ji W, Wang T-X, Ding X, Lei S, Han B-H. Porphyrin-and phthalocyanine-based porous organic polymers: from synthesis to application. Coord Chem Rev 2021; 439:213875.
[285] Zhang Y, Zhao Y, Li R, Liu J. Bioinspired NADH regeneration based on conjugated photocatalytic systems. Sol RRL 2021;5(2):2000339.
[286] Zeng J, et al. Cobalt (III) corrole-tethered semiconducting graphdiyne film for efficient electrocatalysis of oxygen reduction reaction. Mater Today Chem 2022; 25:100932.
[287] Yao B, He Y, Wang S, Sun H, Liu X. Recent advances in porphyrin-based systems for electrochemical oxygen evolution reaction. Int J Mol Sci 2022;23(11):6036.
[288] Hao X, et al. Graphdiyne-porphyrin composite materials GDY/Por and Por@ GDY for lithium ion battery anodes. J Energy Storage 2023;72:108696.
[289] Niu Y, et al. In-situ growth of CuI/Porphyrin-based graphdiyne (PDY) pn heterojunction for high-performance cathodic photoelectrochemical sensing. Mater Today Chem 2023;34:101811.
[290] Lim E-K, Chung BH. Preparation of pyrenyl-based multifunctional nanocomposites for biomedical applications. Nat Protoc 2016;11(2):236–51.
[291] Zhang R, Zhao Y, Li G, Yang D, Ni Z. A new series of pyrenyl-based triarylamines: syntheses, structures, optical properties, electrochemistry and electroluminescence. RSC Adv 2016;6(11):9037–48.
[292] Liu Y, Fan Z, Sun Y, Guo X, Jin Z. Mechanochemical synthesis of pyrenyl graphdiyne coupling CdS/CeO2, constructing a ternary photocatalyst toward efficient hydrogen evolution. ACS Appl Energy Mater 2023;6(18):9743–55.
[293] Bendi A, Bhathiwal AS, Chauhan V, Tiwari A, Raghav N, Praveen PL. Exploration of pyridine-based self-assembled complexes-an overview. J Mol Struct 2024: 138568.
[294] Varshney S, Mishra N. Pyridine-based polymers and derivatives: synthesis and applications. In: Recent developments in the synthesis and applications of pyridines. Elsevier; 2023. p. 43–69.
[295] Reddy KR, Raghu AV, Jeong HM, Siddaramaiah. Synthesis and characterization of pyridine-based polyurethanes. Des Monomers Polym 2009;12(2):109–18.
[296] H. Cheng, X. Zang, S. Wang, and B. Cai, "Pyridine-functionalized organic molecules in perovskite solar cells: toward defects passivation and charge transfer," Sol RRL, p. 2400736.
[297] Hayat A, et al. A novel breakthrough in the invention, properties, synthesis of covalent heptazine framework for its sustainable applications. Mater Today 2025.
[298] Ong WQ, Zeng H. Rapid construction of shape-persistent H-bonded macrocycles via one-pot H-bonding-assisted macrocyclization. J Inclusion Phenom Macrocycl Chem 2013;76:1–11.
[299] Li J, Valenza R, Haussener S. In situ synthesis of Cu_xO/N doped graphdiyne with pyridine N configuration for ammonia production via nitrate reduction. Small 2024:2310467.
[300] Hayat A, et al. Advances/Scope and prospects of g-C_3N_4 derived fascinating photocatalyst as a leading route towards solar energy adaption. J Clean Prod 2024:140568.
[301] Yang J, et al. Engineering 2D photocatalysts for solar hydrogen peroxide production. Adv Energy Mater 2024:2400740.
[302] Lei Z, Chen X, Sun W, Zhang Y, Wang Y. Exfoliated triazine-based covalent organic nanosheets with multielectron redox for high-performance lithium organic batteries. Adv Energy Mater 2019;9(3):1801010.
[303] Kang H, et al. Polyanthraquinone-triazine—a promising anode material for high-energy lithium-ion batteries. ACS Appl Mater Interfaces 2018;10(43):37023–30.
[304] Wang H, et al. Covalent triazine frameworks for carbon dioxide capture. J Mater Chem A 2019;7(40):22848–70.
[305] Sun Q, He J, Gao L, Lu T, Ma X, Huang C. Synthesis methods of graphdiyne and graphdiyne based materials. Chin J Chem 2022;40(7):872–80.
[306] Sun C, Fan C, Kan X, Ma Y, Zhang X, Zhao Y. Enhanced cross-linking performances and carbon black (CB) dispersion in solution styrene butadiene rubber (SSBR) filled with triazine-based graphdiyne (TGDY). Compos Sci Technol 2022;223:109438.
[307] Kulkarni R, et al. Direct growth of crystalline triazine-based graphdiyne using surface-assisted deprotection–polymerisation. Chem Sci 2021;12(38):12661–6.
[308] Zharnikov M, Shoji Y, Fukushima T. Tripodal triptycenes as a versatile building block for highly ordered molecular films and self-assembled monolayers. Accounts Chem Res 2025:1122–6.
[309] Das S, Asyuda A, Shoji Y, Kosaka A, Fukushima T, Zharnikov M. Cyano-substituted triptycene-based monolayers on Au (111): tripodal adsorption, dipole engineering, and charge transfer. J Phys Chem C 2021;125(34):18968–78.
[310] Woźny M, Mames A, Ratajczyk T. Triptycene derivatives: from their synthesis to their unique properties. Molecules 2021;27(1):250.
[311] Ishiwari F, et al. Triptycene tripods for the formation of highly uniform and densely packed self-assembled monolayers with controlled molecular orientation. J Am Chem Soc 2019;141(14):5995–6005.
[312] Jia Z, Pang H, Li H, Wang X. A density functional theory study on complexation processes and intermolecular interactions of triptycene-derived oxacalixarenes. Theor Chem Acc 2019;138:1–11.
[313] Ma H, Yang B-B, Wang Z, Wu K, Zhang C. A three dimensional graphdiyne-like porous triptycene network for gas adsorption and separation. RSC Adv 2022;12 (44):28299–305.
[314] Smith AM, Nie S. Semiconductor nanocrystals: structure, properties, and band gap engineering. Accounts Chem Res 2010;43(2):190–200.
[315] Chaves A, et al. Bandgap engineering of two-dimensional semiconductor materials. npj 2D Mater Appl. 2020;4(1):29.
[316] Koo J, Park M, Hwang S, Huang B, Jang B, Kwon Y, Lee H. Widely tunable band gaps of graphdiyne: an ab initio study. Phys Chem Chem Phys 2014;16(19): 8935–9.
[317] He F. Basic structure and band gap engineering: theoretical study of GDYs. Graph Fundament Appl Renew Energy Electron 2022:13–77.
[318] Hayat A, et al. Recent advances in ground-breaking conjugated microporous polymers-based materials, their synthesis, modification and potential applications. Mater Today 2023.
[319] Zhao Y, et al. Characteristics, properties, synthesis and advanced applications of 2D graphdiyne versus graphene. Mater Chem Front 2022;6(5):528–52.
[320] Zhou Z, Jin Z. Designed of dual direct band gap graphdiyne/Co_2VO_4 S-scheme heterojunction: enhance the bonding stability of Co active sites to promote photocatalytic hydrogen evolution. Chem Eng J 2024;500:157514.
[321] Liu Z, Cui E, Wang X, Jin Z. Energy band engineering over phosphorus-doped CdS/graphdiyne S-scheme heterojunction for enhance photocatalytic hydrogen production. Chem Eng J 2024;486:150060.
[322] Li J, et al. Tuning the electronic bandgap of graphdiyne by H-substitution to promote interfacial charge carrier separation for enhanced photocatalytic hydrogen production. Adv Funct Mater 2021;31(29):2100994.
[323] Zhang J-Q, Hu B, Dong A, Eglitis RI, Yi Z-J, Jia R. Band gap regulation with imino groups in graphdiyne: a promising photocatalyst for water-splitting and CO_2 reduction. ACS Appl Nano Mater 2023;6(23):22506–16.
[324] Zheng Y, et al. Defect engineering in thermoelectric materials: what have we learned? Chem Soc Rev 2021;50(16):9022–54.
[325] Kimerling LC. Defect engineering. MRS Bull 1991;16(12):42–7.
[326] Wang J, Shi H, Wang W, Xu Z, Hong C, Xue Y, Tian F. Defect engineering of graphynes for energy storage and conversion. Chem Eng J 2022;432:133617.
[327] He J, Miao X, Yao H, Wang X, Jin Z. Defect engineering adjusting graphdiyne/$Mn_{0.3}Cd_{0.7}S$ S-scheme heterojunction interface charge arrangement for efficient photocatalytic hydrogen evolution. Sol RRL 2024;8(4):2300916.
[328] Fan W, et al. Grain boundary perfection enabled by pyridinic nitrogen doped graphdiyne in hybrid perovskite. Adv Funct Mater 2021;31(34):2104633.
[329] Gao J, et al. Boosting Fe cationic vacancies with graphdiyne to enhance exceptional pseudocapacitive lithium intercalation. Angew Chem 2023;135(35): e202307874.
[330] Jyothi M, Nayak V, Reddy KR, Naveen S, Raghu A. Non-metal (oxygen, sulphur, nitrogen, boron and phosphorus)-doped metal oxide hybrid nanostructures as highly efficient photocatalysts for water treatment and hydrogen generation. Nanophotocatal Environ Applicat Mater Technol 2019:83–105.
[331] Hayat A, et al. Recent advances, properties, fabrication and opportunities in two-dimensional materials for their potential sustainable applications. Energy Storage Mater 2023;59:102780.
[332] Babu P, Mohanty S, Naik B, Parida K. Synergistic effects of boron and sulfur Co-doping into graphitic carbon nitride framework for enhanced photocatalytic activity in visible light driven hydrogen generation. ACS Appl Energy Mater 2018; 1(11):5936–47.
[333] Yan L, Huang L, Hu T, Ai Y, Wang B, Sun W. Synthesis of sp-hybridized nitrogen doped ultrathin graphdiyne and application to the electrochemical detection for 6, 7-dihydroxycoumarin. Talanta 2022;242:123295.
[334] Li R, et al. Graphdiyne doped with transition metal as ferromagnetic semiconductor. Carbon 2022;188:25–33.
[335] Qi L, et al. 1D nanowire heterojunction electrocatalysts of $MnCo_2O_4$/GDY for efficient overall water splitting. Adv Funct Mater 2022;32(11):2107179.
[336] Yang C, Wang X, Li T, Wu Y, Jin Z. Rational design and construction of graphdiyne (C_nH_{2n-2}) based $NiMoO_4$/GDY/CuO in situ XPS proved double S-scheme heterojunctions for photocatalytic hydrogen production. Langmuir 2023; 39(28):9816–30.

[337] Jin Z, Wang X, Hao X, Wang G, Guo X, Wang K. Graphdiyne based GDY/CuI/NiO parallel double S-scheme heterojunction for efficient photocatalytic hydrogen evolution. 2D Mater 2022;9(2):025014.
[338] Li H, et al. Graphdiyne-based bulk heterojunction for efficient and moisture-stable planar perovskite solar cells. Adv Energy Mater 2018;8(30):1802012.
[339] Jin Z, Wang T, Cui E, Yang X. Constructing a tandem heterojunction: S-scheme heterojunction and Ohmic junction based on graphdiyne, synergistically optimizing photocatalytic hydrogen evolution. Chem Eng J 2023;477:147210.
[340] Deng W, Hao X, Shao Y, Guo S, Jin Z. Construction of 2D-2D S-scheme heterojunction based graphdiyne (g-C_nH_{2n-2}) coupling with highly crystalline nitrogen defect g-C_3N_4 for efficient photocatalytic overall water splitting. Separ Purif Technol 2023;323:124375.
[341] Hao X, Deng W, Fan Y, Jin Z. Engineering of a hierarchical S-scheme 2D/3D heterojunction with graphdiyne (gC_nH_{2n-2}) coated 3D porous $CoAl_2O_4$ nanoflowers for highly efficient photocatalytic H_2 evolution. J Mater Chem A 2024;12(14):8543–60.
[342] Qi L, et al. Controlled growth of metal atom arrays on graphdiyne for seawater oxidation. J Am Chem Soc 2024;146(8):5669–77.
[343] Zheng X, Ban S, Liu B, Chen G. Strain-controlled graphdiyne membrane for CO_2/CH_4 separation: first-principle and molecular dynamic simulation. Chin J Chem Eng 2020;28(7):1898–903.
[344] Li J, Zhu L, Tung CH, Wu LZ. Engineering graphdiyne for solar photocatalysis. Angew Chem Int Ed 2023;62(22):e202301384.
[345] Iqbal O, et al. A review on the synthesis, properties, and characterizations of graphitic carbon nitride (g-C_3N_4) for energy conversion and storage applications. Mater Today Phys 2023;34:101080.
[346] Sang P, et al. Toward high-performance monolayer graphdiyne transistor: strain engineering matters. Appl Surf Sci 2021;536:147836.
[347] Jalili S, Pakzadiyan A. Tensile strain as an efficient way to tune transport properties of Graphdiyne/Borophene hetero-bilayers; a first principle investigation. Comput Mater Sci 2023;224:112161.
[348] Wang Y, et al. An ab initio study of the effect of strain on the permeability of N_2 and CO_2 in N-graphdiyne: implication for gas-selective membranes. ACS Appl Nano Mater 2024.
[349] Li X, Zhang H, Chi L. On-surface synthesis of graphyne-based nanostructures. Adv Mater 2019;31(42):1804087.
[350] Kang F, Zheng W, Sun L, Gao W, Shang L, Chi L, Xu W. On-surface synthesis of hydrogen-substituted γ-graphdiyne with high efficiency. CCS Chem 2024:1–22.
[351] Kang H, Chen Y, Xu L, Lin Y, Feng Q, Yao H, Zheng Y. Top-down strategy synthesis of fluorinated graphdiyne for lithium ion battery. RSC Adv 2019;9(54):31406–12.
[352] Gao L, Yang Z, Li X, Huang C. Post-modified strategies of graphdiyne for electrochemical applications. Chem–Asian J 2021;16(16):2185–94.
[353] Xie C, Wang N, Li X, Xu G, Huang C. Research on the preparation of graphdiyne and its derivatives. Chem–Eur J 2020;26(3):569–83.
[354] Hou J, Sun L, Pan Q, Zhao Y. Recent synthetic methods towards graphdiyne. ChemNanoMat 2023;9(9):e202300273.
[355] Yin C, et al. Catalyst-free synthesis of few-layer graphdiyne using a microwave-induced temperature gradient at a solid/liquid interface. Adv Funct Mater 2020;30(23):2001396.
[356] Kong Y, et al. Rapid synthesis of graphdiyne films on hydrogel at the superspreading interface for antibacteria. ACS Nano 2022;16(7):11338–45.
[357] Jiang G, Du J, Jin F, Yang D, Jin Z. Graphdiyne surface-modified CuS-GDY/$LaCoO_3$ S-scheme heterojunctions for enhanced photocatalytic hydrogen evolution. Separ Purif Technol 2025;356:129831.
[358] Wu X, et al. Current advances in the synthesis, properties, and biomedical applications of two-dimensional graphdiyne: a review. ACS Appl Nano Mater 2024;7(3):2461–93.
[359] Dang Y, Guo W, Zhao L, Zhu H. Porous carbon materials based on graphdiyne basis units by the incorporation of the functional groups and Li atoms for superior CO_2 capture and sequestration. ACS Appl Mater Interfaces 2017;9(35):30002–13.
[360] Xiong Z, et al. A supramolecular strategy to precisely fabricate binary-doped metal-free graphdiyne for high-performance zinc–air batteries. Mater Chem Front 2024;8(6):1665–75.
[361] Shen H, Li Y, Shi Z. A novel graphdiyne-based catalyst for effective hydrogenation reaction. ACS Appl Mater Interfaces 2018;11(3):2563–70.
[362] Psofogiannakis GM, Froudakis GE. Computational prediction of new hydrocarbon materials: the hydrogenated forms of graphdiyne. J Phys Chem C 2012;116(36):19211–4.
[363] Sakamoto R, Fukui N, Maeda H, Matsuoka R, Toyoda R, Nishihara H. The accelerating world of graphdiynes. Adv Mater 2019;31(42):1804211.
[364] Li H-B, Song X-N, Wang C, Hua W, Ma Y. Towards sensitive identification of fluorinated graphdiyne configurations by computational X-ray spectroscopy. Phys Chem Chem Phys 2024.
[365] Fan K, Fu J, Liu X, Liu Y, Lai W, Liu X, Wang X. Dependence of the fluorination intercalation of graphene toward high-quality fluorinated graphene formation. Chem Sci 2019;10(21):5546–55.
[366] Xu S, Kang B, Li H, Yoo PJ, Lee JY. Graphdiyne-supported metals and metal compounds: synthesis, applications, and future prospects. Adv Funct Mater 2024:2403095.
[367] Wang Y, et al. Lithium and sodium decorated graphdiyne as a candidate for hydrogen storage: first-principles and grand canonical Monte Carlo study. Appl Surf Sci 2020;509:144855.
[368] Li S, et al. Template based synthesis of porous graphdiyne nanosheet for reversible and fast NO_2 detection by UV irradiation. ChemPhysChem 2023;24(14):e202300073.
[369] Lin Y, et al. Hybrid nanostructured MnO_2 nanowire/graphdiyne with enhanced lithium-ion performance promoting by interfacial storage. Appl Surf Sci 2020;526:146457.
[370] Ghafary Z, Salimi A, Hallaj R, Akhtari K, Ghasemi F. Light triggering performance of the van der Waals heterojunction of 2D/0D graphdiyne/graphdiyne quantum dot as a novel phototransistor. Carbon 2023;215:118475.
[371] Hayat A, et al. Developing new-generation covalent organic frameworks as sustainable catalysts: synthesis, properties, types and solar energy production. Mater Sci Eng R Rep 2024;157:100771.
[372] Deng W, Wang X, Hao X, Jin Z. Embedding $ZnCo_2O_4$ quantum dots onto graphdiyne (g-C_nH_{2n-2}) nanosheets as a 0D/2D S-scheme heterojunction for highly efficient photocatalytic H_2 evolution. Separ Purif Technol 2024;351:128068.
[373] Ahmed SR, Cardoso AG, Cobas HV, Das P, Chen A, Srinivasan S, Rajabzadeh AR. Graphdiyne quantum dots for H_2O_2 and dopamine detection. ACS Appl Nano Mater 2023;6(10):8434–43.
[374] Bahari D, Babamiri B, Salimi A, Rashidi A. Graphdiyne/graphene quantum dots for development of FRET ratiometric fluorescent assay toward sensitive detection of miRNA in human serum and bioimaging of living cancer cells. J Lumin 2021;239:118371.
[375] Refson K, Parker SF. Assignment of the internal vibrational modes of C70 by inelastic neutron scattering spectroscopy and periodic-DFT. Chemist 2015;4(5):620–5.
[376] Mazzaro R, et al. Uniform functionalization of high-quality graphene with platinum nanoparticles for electrocatalytic water reduction. Chemist 2015;4(3):268–73.
[377] Artyukhov VI, Liu M, Yakobson BI. Mechanically induced metal–insulator transition in carbyne. Nano Lett 2014;14(8):4224–9.
[378] Thilgen C, Wennemers H, Carell T. François Diederich (1952–2020): 40 Years of organic chemistry. 2021.
[379] Li P, Jia Y, Chen P. Design and synthesis of new type of macrocyclic architectures used for optoelectronic materials and supramolecular chemistry. Chem- Eur J 2023;29(54):e202300300.
[380] Zhao W-k, et al. Rectification inversion in oxygen substituted graphyne–graphene-based heterojunctions. Phys Chem Chem Phys 2015;17(5):3115–22.
[381] Vergara E, et al. Supramolecular order of 2, 5-bis (dodecanoxy) phenyleneethynylene–butadiyne Oligomers in the solid state. Langmuir 2015;31(24):6909–16.
[382] Pan L, Zhang L, Song B, Du S, Gao H-J. Graphyne-and graphdiyne-based nanoribbons: density functional theory calculations of electronic structures. Appl Phys Lett 2011;98(17).
[383] Qian X, Ning Z, Li Y, Liu H, Ouyang C, Chen Q, Li Y. Construction of graphdiyne nanowires with high-conductivity and mobility. Dalton Transact 2012;41(3):730–3.
[384] Zhu Y, Bai H, Huang Y. Electronic property modulation of one-dimensional extended graphdiyne nanowires from a first-principle crystal orbital view. ChemistryOpen 2016;5(1):78–87.
[385] Chen Z, Lin T, Li H, Cheng F, Su C, Loh KP. Hydrogen bond guided synthesis of close-packed one-dimensional graphdiyne on the Ag (111) surface. Chem Sci 2019;10(47):10849–52.
[386] Zhu Y, Peng L, Fang Z, Yan C, Zhang X, Yu G. Structural engineering of 2D nanomaterials for energy storage and catalysis. Advan Mater 2018;30(15):1706347.
[387] Mei J, Liao T, Sun Z. 2D/2D heterostructures: rational design for advanced batteries and electrocatalysis. Energy Environ Mater 2022;5(1):115–32.
[388] Wang J, Fang H, Wang X, Chen X, Lu W, Hu W. Recent progress on localized field enhanced two-dimensional material photodetectors from ultraviolet—visible to infrared. Small 2017;13(35):1700894.
[389] Kong Z, Zhang H, Zhou T, Xie L, Wang B, Jiang X. Biomass-derived functional materials: preparation, functionalization, and applications in adsorption and catalytic separation of carbon dioxide and other atmospheric pollutants. Separat Purificat Technol 2024:129099.
[390] Chang F, et al. Microporous and mesoporous materials for gas storage and separation: a review. Asia-Pacific J Chem Eng 2013;8(4):618–26.
[391] Yuan K, de la Asunción-Nadal V, Li Y, Jurado-Sánchez B, Escarpa A. Graphdiyne micromotors in living biomedia. Chemy–A Europ J. 2020;26(38):8471–7.
[392] Ma Y, Chen Y. Three-dimensional graphene networks: synthesis, properties and applications. Nat Sci Rev 2015;2(1):40–53.
[393] Zhang X, Liu D, Yang L, Zhou L, You T. Self-assembled three-dimensional graphene-based materials for dye adsorption and catalysis. J Mater Chem A 2015;3(18):10031–7.
[394] Song H-q, Zhu Q, Zheng X-j, Chen X-g. One-step synthesis of three-dimensional graphene/multiwalled carbon nanotubes/Pd composite hydrogels: an efficient recyclable catalyst for Suzuki coupling reactions. J Mater Chem A 2015;3(19):10368–77.
[395] Yavari F, Chen Z, Thomas AV, Ren W, Cheng H-M, Koratkar N. High sensitivity gas detection using a macroscopic three-dimensional graphene foam network. Sci Rep 2011;1(1):1–5.
[396] Luo B, Zhi L. Design and construction of three dimensional graphene-based composites for lithium ion battery applications. Energy Environ Sci 2015;8(2):456–77.
[397] Xue P, et al. Effects of terminal groups in third components on performance of organic solar cells. Acta Phys Chim Sin 2018;34:1–9.

[398] Gaox ZJ, Du R. RobustsuperhyG drophobic foam: a graphdiyneGbased hierarchical architecturefor oil/water separation. Advan Mater 2016;28(1):168G173.
[399] Lin Z, Liu G, Zheng Y, Lin Y, Huang Z. Three-dimensional hierarchical mesoporous flower-like TiO 2@ graphdiyne with superior electrochemical performances for lithium-ion batteries. J Mater Chem A 2018;6(45):22655–61.
[400] Nomura T, Habe T, Sakamoto R, Koshino M. Three-dimensional graphdiyne as a topological nodal-line semimetal. Phys Rev Mater 2018;2(5):054204.
[401] Kong Y, Li J, Zeng S, Yin C, Tong L, Zhang J. Bridging the gap between reality and ideality of graphdiyne: the advances of synthetic methodology. Chem 2020;6(8):1933–51.
[402] Sakamoto J, van Heijst J, Lukin O, Schlüter AD. Two-dimensional polymers: just a dream of synthetic chemists? Angewandte Chemie Int Edit 2009;48(6):1030–69.
[403] Zhou J, et al. Synthesis of ultrathin graphdiyne film using a surface template. ACS Appl Mater Interfaces 2018;11(3):2632–7.
[404] Cai Y, et al. Graphdiyne-based nanofilms for compliant on-skin sensing. ACS Nano 2022;16(10):16677–89.
[405] Wu B, et al. Nitrogen-rich carbonaceous materials for advanced oxygen electrocatalysis: synthesis, characterization, and activity of nitrogen sites. Advan Function Materi 2022;32(31):2204137.
[406] Ruby Raj M, Lee G, Reddy MV, Zaghib K. Recent advances in development of organic battery materials for monovalent and multivalent metal-ion rechargeable batteries. ACS Appl Energy Mater 2024;7(19):8196–255.
[407] Wang Y, Yang P, Zheng L, Shi X, Zheng H. Carbon nanomaterials with sp^2 or/and sp hybridization in energy conversion and storage applications: a review. Energy Storage Mater 2020;26:349–70.
[408] Xue Y, et al. Anchoring zero valence single atoms of nickel and iron on graphdiyne for hydrogen evolution. Nature Commun 2018;9(1):1460.
[409] Yu H, et al. Graphdiyne-engineered heterostructures for efficient overall water-splitting. Nano Energy 2019;64:103928.
[410] Xie W, et al. CoS_2 nanowires supported graphdiyne for highly efficient hydrogen evolution reaction. J Energy Chem 2021;60:272–8.
[411] He T, Zhang L, Kour G, Du A. Electrochemical reduction of carbon dioxide on precise number of Fe atoms anchored graphdiyne. J CO2 Utiliz 2020;37:272–7.
[412] Yang Z, Zhang D, Wang K, He J, Li J, Huang C. Investigating graphdiyne based materials for rechargeable batteries. Nano Today 2022;46:101588.
[413] Shi M, et al. Graphdiyne/graphene heterostructure supported NiFe layered double hydroxides for oxygen evolution reaction. Colloid Surfaces A: Physicochem Eng Aspect 2022;637:128217.
[414] Cui J, et al. Efficient electrocatalytic water oxidation by using the hierarchical 1D/2D structural nanohybrid of CoCu-based zeolitic imidazolate framework nanosheets and graphdiyne nanowires. Electrochimica Acta 2020;334:135577.
[415] Liu Y, Xue Y, Yu H, Hui L, Huang B, Li Y. Graphdiyne ultrathin nanosheets for efficient water splitting. Advan Function Mater 2021;31(16):2010112.
[416] Parvin N, et al. Few-layer graphdiyne nanosheets applied for multiplexed real-time DNA detection. Advan Mater 2017;29(18):1606755.
[417] Jin J, et al. Graphdiyne nanosheet-based drug delivery platform for photothermal/chemotherapy combination treatment of cancer. ACS Appl Mater Interface 2018;10(10):8436–42.
[418] Sun M-H, Huang S-Z, Chen L-H, Li Y, Yang X-Y, Yuan Z-Y, Su B-L. Applications of hierarchically structured porous materials from energy storage and conversion, catalysis, photocatalysis, adsorption, separation, and sensing to biomedicine. Chem Soc Rev 2016;45(12):3479–563.
[419] Lakkakula J, Satam Y, Alexander S, Bose R, Uddin I. Palladium nanoparticles as a platform for cancer diagnosis and treatment. BioNanoScience 2024;14(4):4342–59.
[420] Liu J, Luo W, Wang L, Zhang J, Fu XZ, Luo JL. Toward excellence of electrocatalyst design by emerging descriptor-oriented machine learning. Advan Functiona Mater 2022;32(17):2110748.
[421] Wan S, Xu J, Cao S, Yu J. Promoting intramolecular charge transfer of graphitic carbon nitride by donor–acceptor modulation for visible-light photocatalytic H_2 evolution. Interdisciplin Mater 2022;1(2):294–308.
[422] Golzani M, Tadjarodi A, Golzani M, Poliki M, Zare-Dorabei R, Dashtian K. γ-Graphyne-based coordination, composite, and hybrid materials: synthesis, characterizations, and advanced applications. Coordinat Chem Rev 2024;510:215838.
[423] Yu J, et al. Graphdiyne nanospheres as a wettability and electron modifier for enhanced hydrogenation catalysis. Angewandte Chemie 2022;134(34):e202207255.
[424] Wu Y, Wang X, Wang T, Zhu P, Jin Z. Phosphating Cu/graphdiyne nanospheres for improved photocatalytic hydrogen production. ACS Appl Nano Mater 2024;7(2):1950–9.
[425] Zhang L, Yi W, Li J, Wei G, Xi G, Mao L. Surfactant-free interfacial growth of graphdiyne hollow microspheres and the mechanistic origin of their SERS activity. Nat Commun 2023;14(1):6318.
[426] Austefjord MW, Gerdes H-H, Wang X. Tunneling nanotubes: diversity in morphology and structure. Commun Integrat Biol 2014;7(1):e27934.
[427] Lehman JH, Terrones M, Mansfield E, Hurst KE, Meunier V. Evaluating the characteristics of multiwall carbon nanotubes. Carbon 2011;49(8):2581–602.
[428] Zhang M, Li J. Carbon nanotube in different shapes. Mater Today 2009;12(6):12–8.
[429] Li Z, et al. Well-defined materials for heterogeneous catalysis: from nanoparticles to isolated single-atom sites. Chem Rev 2019;120(2):623–82.
[430] Zhao Z-G, Ci L-J, Cheng H-M, Bai J-B. The growth of multi-walled carbon nanotubes with different morphologies on carbon fibers. Carbon 2005;43(3):663–5.
[431] Brady-Estevez AS, Kang S, Elimelech M. Carbon nanotubes. Small 2008;4(4):481–4.
[432] Lyons PE, De S, Blighe F, Nicolosi V, Pereira LFC, Ferreira MS, Coleman JN. The relationship between network morphology and conductivity in nanotube films. J Appl Phys 2008;104(4).
[433] Lv Y, et al. A novel carbon support: few-layered graphdiyne-decorated carbon nanotubes capture metal clusters as effective metal-supported catalysts. Small 2021;17(12):2006442.
[434] Zheng Z, et al. Nonlocal response in infrared detector with semiconducting carbon nanotubes and graphdiyne. Advan Sci 2017;4(12):1700472.
[435] Maria JP, Nagarajan V, Chandiramouli R. Boron trifluoride interaction studies on graphdiyne nanotubes–a first-principles insight. Chem Phys Lett 2020;738:136841.
[436] Srimathi U, Nagarajan V, Chandiramouli R. Interaction of Imuran, Pentasa and Hyoscyamine drugs and solvent effects on graphdiyne nanotube as a drug delivery system-A DFT study. J Mol Liq 2018;265:199–207.
[437] Brewster MM, Lu M-Y, Lim SK, Smith MJ, Zhou X, Gradecak S. The growth and optical properties of ZnO nanowalls. J Phys Chem Lett 2011;2(15):1940–5.
[438] Wu Y, Yang B, Zong B, Sun H, Shen Z, Feng Y. Carbon nanowalls and related materials. J Mater Chem 2004;14(4):469–77.
[439] Tang N, Wang W, You H, Zhai Z, Hilario J, Zeng L, Zhang L. Morphology tuning of porous CoO nanowall towards enhanced electrochemical performance as supercapacitors electrodes. Catal Today 2019;330:240–5.
[440] Ali H, et al. A comprehensive Review based on the synthesis, properties, morphology, functionalization, and potential applications of transition metals nitrides. Coordinat Chem Rev 2025;526:216353.
[441] Zhu C, Guo S, Fang Y, Han L, Wang E, Dong S. One-step electrochemical approach to the synthesis of graphene/MnO_2 nanowall hybrids. Nano Res 2011;4:648–57.
[442] Wu Y, et al. Fabrication of a class of nanostructured materials using carbon nanowalls as the templates. Advan Function Mater 2002;12(8):489–94.
[443] Bai Q, et al. Plasmonic nanozyme of graphdiyne nanowalls wrapped hollow copper sulfide nanocubes for rapid bacteria-killing. Advan Function Mater 2022;32(20):2112683.
[444] Gao X, et al. Direct synthesis of graphdiyne nanowalls on arbitrary substrates and its application for photoelectrochemical water splitting cell. Advan Mater (Deerfield Beach, Fla) 2016;29(9).
[445] Zhu Y, et al. Rapid ozone decomposition over water-activated monolithic MoO_3/graphdiyne nanowalls under high humidity. Angewandte Chemie Int Edit 2023;62(39):e202309158.
[446] Wang N, Cai Y, Zhang R. Growth of nanowires. Mater Sci Eng: R: Rep 2008;60(1–6):1–51.
[447] Yu K, et al. Nanowires in energy storage devices: structures, synthesis, and applications. Advan Energy Mater 2018;8(32):1802369.
[448] Dick KA, et al. The morphology of axial and branched nanowire heterostructures. Nano Lett 2007;7(6):1817–22.
[449] Cao Y, Mallouk TE. Morphology of template-grown polyaniline nanowires and its effect on the electrochemical capacitance of nanowire arrays. Chem Mater 2008;20(16):5260–5.
[450] Hayat A, et al. Recent advances in heteroatom-doped/hierarchically porous carbon materials: synthesis, design and potential applications. Prog Mater Sci 2024:101408.
[451] Rao C, Deepak FL, Gundiah G, Govindaraj A. Inorganic nanowires. Prog Solid State Chem 2003;31(1–2):5–147.
[452] Zuo Z, He F, Wang F, Li L, Li Y. Spontaneously splitting copper nanowires into quantum dots on graphdiyne for suppressing lithium dendrites. Advan Mater 2020;32(49):2004379.
[453] Shang H, Zuo Z, Li Y. Highly lithiophilic graphdiyne nanofilm on 3D free-standing Cu nanowires for high-energy-density electrodes. ACS Appl Mater Interfaces 2019;11(19):17678–85.
[454] Yang L, Li J, Yin M, Kong Q, Xi G. Ultrathin graphdiyne nanowires with diameters below 3 nm: synthesis, photoelectric effect, and enhanced Raman sensing. Small 2023;19(28):2300996.
[455] Gao X, Li J, Zuo Z. Advanced electrochemical energy storage and conversion on graphdiyne interface. Nano Res Energy 2022.
[456] Hayat A, et al. Emerging breakthroughs in covalent triazine frameworks: from fundamentals towards photocatalytic water splitting and challenges. Prog Mater Science 2024:101352.
[457] Liu Y, Xue Y, Hui L, Yu H, Fang Y, He F, Li Y. Porous graphdiyne loading CoO_x quantum dots for fixation nitrogen reaction. Nano Energy 2021;89:106333.
[458] Man Z, et al. Hierarchical 3D porous hydrogen-substituted graphdiyne for high-performance electrochemical lithium-ion storage. ACS Appl Mater Interface 2023;15(22):26910–7.
[459] Ju W, et al. Understanding activity and selectivity of metal-nitrogen-doped carbon catalysts for electrochemical reduction of CO_2. Nat Commun 2017;8(1):1–9.
[460] Cometto C, Kuriki R, Chen L, Maeda K, Lau T-C, Ishitani O, Robert M. A carbon nitride/Fe quaterpyridine catalytic system for photostimulated CO_2-to-CO conversion with visible light. J Amer Chem Soc 2018;140(24):7437–40.
[461] Wang Z, et al. Room-temperature synthesis of single iron site by electrofiltration for photoreduction of CO_2 into tunable syngas. ACS Nano 2020;14(5):6164–72.
[462] Ni W, Xue Y, Zang X, Li C, Wang H, Yang Z, Yan Y-M. Fluorine doped cagelike carbon electrocatalyst: an insight into the structure-enhanced CO selectivity for CO_2 reduction at high overpotential. ACS Nano 2020;14(2):2014–23.
[463] Ran J, Jaroniec M, Qiao SZ. Cocatalysts in semiconductor-based photocatalytic CO_2 reduction: achievements, challenges, and opportunities Feb 2018;30(7). https://doi.org/10.1002/adma.201704649.

[464] Hayat A, et al. Molecular engineering optimized carbon nitride photocatalyst for CO_2 reduction to solar fuels. J Sci Advan Mater Dev 2022;7(4):100483.
[465] Sun C, et al. Self-assembled g-C_3N_4 nanotubes/graphdiyne composite with enhanced photocatalytic CO_2 reduction. J Alloys Compound 2021;868:159045.
[466] Wu S, Ji Y, Wang L, Wu X, Xu H. Selective CO_2.to-CH_4 photoconversion in aqueous solutions catalyzed by atomically dispersed copper sites anchored on ultrathin graphdiyne oxide nanosheets. Solar RRL 2021;5(7):2100200.
[467] Su K, Dong G-X, Zhang W, Liu Z-L, Zhang M, Lu T-B. In situ coating $CsPbBr_3$ nanocrystals with graphdiyne to boost the activity and stability of photocatalytic CO2 reduction. ACS Appl Mater Interface 2020;12(45):50464–71.
[468] Wang Y, et al. Constructing van der waals heterogeneous photocatalysts based on atomically thin carbon nitride sheets and graphdiyne for highly efficient photocatalytic conversion of CO_2 into CO. ACS Appl Mater Interface 2021;13(34):40629–37.
[469] Yang C, Wang Y, Yu J, Cao S. Ultrathin 2D/2D graphdiyne/Bi_2WO_6 heterojunction for gas-phase CO_2 photoreduction. ACS Appl Energy Mater 2021;4(9):8734–8.
[470] Zhao J, Xiong Z, Zhao Y, Wang J, Qiu Y, Liu P, Zhang J. 2D/2D heterostructure of metal-free ultrathin graphdiyne/carbon nitride nanosheets for enhanced photocatalytic reduction of carbon dioxide with water. ACS Appl Energy Mater 2021;4(11):12403–10.
[471] Zou H, He B, Kuang P, Yu J, Fan K. NixSy nanowalls/nitrogen-doped graphene foam is an efficient trifunctional catalyst for unassisted artificial photosynthesis. Advan Function Mater 2018;28(13):1706917.
[472] Lukowski MA, Daniel AS, Meng F, Forticaux A, Li L, Jin S. Enhanced hydrogen evolution catalysis from chemically exfoliated metallic MoS_2 nanosheets. J Amer Chem Soc 2013;135(28):10274–7.
[473] Zhang N, Yang M-Q, Liu S, Sun Y, Xu Y-J. Waltzing with the versatile platform of graphene to synthesize composite photocatalysts. Chem Rev 2015;115(18):10307–77.
[474] Ong W-J, Tan L-L, Ng YH, Yong S-T, Chai S-P. Graphitic carbon nitride (g-C_3N_4)-based photocatalysts for artificial photosynthesis and environmental remediation: are we a step closer to achieving sustainability? Chem Rev 2016;116(12):7159–329.
[475] Zhang X, Lai Z, Tan C, Zhang H. Solution-processed two-dimensional MoS_2 nanosheets: preparation, hybridization, and applications. Angewandte Chemie Int Edit 2016;55(31):8816–38.
[476] Xu Q, Zhu B, Cheng B, Yu J, Zhou M, Ho W. Photocatalytic H_2 evolution on graphdiyne/g-C_3N_4 hybrid nanocomposites. Appl Catal B: Environ 2019;255:117770.
[477] Li Y, Yang H, Wang G, Ma B, Jin Z. Distinctive improved synthesis and application extensions graphdiyne for efficient photocatalytic hydrogen evolution. ChemCatChem 2020;12(7):1985–95.
[478] Lv J-X, Zhang Z-M, Wang J, Lu X-L, Zhang W, Lu T-B. In situ synthesis of CdS/graphdiyne heterojunction for enhanced photocatalytic activity of hydrogen production. ACS Appl Mater Interfac 2018;11(3):2655–61.
[479] Borup R, et al. Scientific aspects of polymer electrolyte fuel cell durability and degradation. Chemical Rev 2007;107(10):3904–51.
[480] Seh ZW, Kibsgaard J, Dickens CF, Chorkendorff I, Nørskov JK, Jaramillo TF. Combining theory and experiment in electrocatalysis: insights into materials design. Science 2017;355(6321):eaad4998.
[481] Li L, Wang P, Shao Q, Huang X. Recent progress in advanced electrocatalyst design for acidic oxygen evolution reaction. Advanced Mater 2021;33(50):2004243.
[482] Audichon T, Mayousse E, Morisset S, Morais C, Comminges C, Napporn TW, Kokoh KB. Electroactivity of RuO_2–IrO_2 mixed nanocatalysts toward the oxygen evolution reaction in a water electrolyzer supplied by a solar profile. Int J Hydrog Energy 2014;39(30):16785–96.
[483] Ma Z, et al. Reaction mechanism for oxygen evolution on RuO_2, IrO_2, and RuO_2@IrO_2 core-shell nanocatalysts. J Electroanal Chem 2018;819:296–305.
[484] Si H-Y, et al. Z-scheme Ag_3PO_4/graphdiyne/g-C_3N_4 composites: enhanced photocatalytic O_2 generation benefiting from dual roles of graphdiyne. Carbon 2018;132:598–605.
[485] Wang D, et al. In situ formed Z-scheme graphdiyne heterojunction realizes NIR-photocatalytic oxygen evolution and selective radiosensitization for hypoxic tumors. ACS nano 2022;16(12):21186–98.
[486] Wong MK, Loh JY, Yap FM, Ong WJ. Fueling the future of clean energy with self-supported layered double hydroxides-based electrocatalysts: a step toward sustainability. InfoMat 2024:e12639.
[487] Fan Z, Lu H, Liu Y, Chang C, Guo X, Long G, Jin Z. Distinctive graphdiyne coupled with phosphorylation NiFe-LDH S-scheme heterojunction for photocatalytic overall water splitting. Chem Eng J 2023;477:147008.
[488] Xu J, Wan Q, Anpo M, Lin S. Bandgap opening of graphdiyne monolayer via B, N-codoping for photocatalytic overall water splitting: design strategy from DFT studies. J Phys Chem C 2020;124(12):6624–33.
[489] Zhou S, Guan Z, Chen G, Wu J, Pan Y, Guo Y, Yang Z. Advances and strategies in the electrocatalytic conversion of carbon dioxide to valuable chemicals and fuels. Fuel 2024;377:132539.
[490] Liu A, et al. Current progress in electrocatalytic carbon dioxide reduction to fuels on heterogeneous catalysts. J Mater Chem A 2020;8(7):3541–62.
[491] Ali H, et al. Magnetic splitting induced ferromagnetism in chromium-doped $HfSe_2$. Chinese J Phys 2024.
[492] Chen S, Zheng X, Gao Y, Ping X, Xue Y, Li Y. Controlled synthesis of graphdiyne-based multiscale catalysts for energy conversion. Precis Chem 2024;2(7):355–75.
[493] Shi G, et al. Constructing Cu− C bonds in a graphdiyne-regulated Cu single-atom electrocatalyst for CO_2 reduction to CH_4. Angewandte Chemie 2022;134(23):e202203569.
[494] Gu H, et al. Graphdiyne/graphene heterostructure: a universal 2D scaffold anchoring monodispersed transition-metal phthalocyanines for selective and durable CO_2 electroreduction. J Amer Chem Soc 2021;143(23):8679–88.
[495] Xie W, et al. Graphdiyne-stabilized silver nanoparticles as an efficient electrocatalyst for CO_2 reduction. Advan Energy Sustain Res 2021;2(8):2100037.
[496] Liu F, et al. Rational design of better hydrogen evolution electrocatalysts for water splitting: a review. Advan Sci 2022;9(18):2200307.
[497] Irfan D, Opulencia MJC, Jasim SA, Salimov OR, Mahdi AB, Abed AM, Sarkar A. Systematically theoretical investigation the effect of nitrogen and iron-doped graphdiyne on the oxygen reduction reaction mechanism in proton exchange membrane fuel cells. Int J Hydrogen Energy 2022;47(39):17341–50.
[498] Yang M, Wang Z, Jiao D, Li G, Cai Q, Zhao J. Tuning single metal atoms anchored on graphdiyne for highly efficient and selective nitrate electroreduction to ammonia under aqueous environments: a computational study. Appl Surface Sci 2022;592:153213.
[499] Rana S, Kumar A, Dhiman P, Sharma G, Amirian J, Stadler FJ. Progress in graphdiyne and phosphorene based composites and heterostructures as new age materials for photocatalytic hydrogen evolution. Fuel 2024;356:129630.
[500] Ali H, et al. Recent advances, synthesis, modifications and photogenerated carrier dynamics of g-C_3N_4 for photocatalytic water splitting. Int J Hydrogen Energy 2025;100:79–128.
[501] Wang X, et al. Cobalt-nitrogen-doped graphdiyne as an efficient bifunctional catalyst for oxygen reduction and hydrogen evolution reactions. Carbon 2019;147:9–18.
[502] Xue Y, et al. Extraordinarily durable graphdiyne-supported electrocatalyst with high activity for hydrogen production at all values of pH. ACS Appl Mater Interfaces 2016;8(45):31083–91.
[503] Hu C, Liu H, Liu Y, Chen J-F, Li Y, Dai L. Graphdiyne with tunable activity towards hydrogen evolution reaction. Nano Energy 2019;63:103874.
[504] Yang S, et al. The mechanism of water oxidation using transition metal-based heterogeneous electrocatalysts. Chem Soc Rev 2024.
[505] Li H, Lin Y, Duan J, Wen Q, Liu Y, Zhai T. Stability of electrocatalytic OER: from principle to application. Chem Soc Rev 2024.
[506] He T, Matta SK, Will G, Du A. Transition-metal single atoms anchored on graphdiyne as high-efficiency electrocatalysts for water splitting and oxygen reduction. Small Methods 2019;3(9):1800419.
[507] Zhao Y, Yang N, Yu R, Zhang Y, Zhang J, Li Y, Wang D. Unique structural advances of graphdiyne for energy applications. EnergyChem 2020;2(5):100041.
[508] Weng L, et al. The preferred adsorption sites and catalytic mechanism of FCC_CoFeGaNiZn multi-principal element alloy for oxygen evolution reaction catalysis based on site preference of constituent atom on sublattice. Intermetallics 2024;165:108132.
[509] Sun L, Luo Q, Dai Z, Ma F. Material libraries for electrocatalytic overall water splitting. Coord Chem Rev 2021;444:214049.
[510] Shi G, Yu C, Fan Z, Li J, Yuan M. Graphdiyne-supported NiFe layered double hydroxide nanosheets as functional electrocatalysts for oxygen evolution. ACS Appl Mater Interfaces 2018;11(3):2662–9.
[511] Lv Y, et al. Graphdiyne-anchored ultrafine NiFe hydroxide nanodots electrocatalyst for water oxidation with high mass activity and superior durability. Carbon 2020;169:45–54.
[512] Quan L, Jiang H, Mei G, Sun Y, You B. Bifunctional electrocatalysts for overall and hybrid water splitting. Chemical Reviews 2024;124(7):3694–812.
[513] Hosseini SE, Wahid MA. Hydrogen production from renewable and sustainable energy resources: promising green energy carrier for clean development. Renew Sustain Energy Rev 2016;57:850–66.
[514] Brandon NP, Kurban Z. Clean energy and the hydrogen economy. Philos Trans Royal Soc A: Math Phys Eng Sci 2017;375(2098):20160400.
[515] Ajmal Z, et al. Advancements in MXene-based frameworks towards photocatalytic hydrogen production, carbon dioxide reduction and pollutant degradation: current challenges and future prospects. Coordination Chem Rev 2025;523:216226.
[516] Dincer I. Green methods for hydrogen production. Int J Hydrog Energy 2012;37(2):1954–71.
[517] Qi L, Chen Z, Luan X, Zheng Z, Xue Y, Li Y. Atomically dispersed Mn enhanced catalytic performance for overall water splitting on graphdiyne-coated copper hydroxide nanowire. Chinese J Struct Chem 2024;43(1):100197.
[518] Fang Y, et al. In situ growth of graphdiyne based heterostructure: toward efficient overall water splitting. Nano Energy 2019;59:591–7.
[519] Garimella SV, Persoons T, Weibel JA, Gektin V. Electronics thermal management in information and communications technologies: challenges and future directions. IEEE Trans Compon Packag Manufact Technol 2016;7(8):1191–205.
[520] Mishra P, Singh G. Energy management systems in sustainable smart cities based on the internet of energy: a technical review. Energies 2023;16(19):6903.
[521] Zhang M, Li Y, Li X, Wang N, Huang C. Graphdiyne ink for ionic liquid gated printed transistor. Advan Electron Mater 2020;6(7):2000157.
[522] Ajmal Z, et al. Recent advances in COF-based framework: synthesis, Potential application, Current challenges and Future direction. Mater Today Chem 2024;39:102140.
[523] Niu G, Wang Y, Yang Z, Cao S, Liu H, Wang J. Graphdiyne and its derivatives as efficient charge reservoirs and transporters in semiconductor devices. Advan Mater 2023;35(25):2212159.

[524] Li R, Li X, Zhang M, Li Y, Yang Z, Huang C. A universal Fe/N incorporated graphdiyne for printing flexible ferromagnetic semiconducting electronics. J Phys Chem Lett 2020;12(1):204–10.
[525] Yao BW, et al. Non-volatile electrolyte-gated transistors based on graphdiyne/MoS_2 with robust stability for low-power neuromorphic computing and logic-in-memory. Advan Funct Mater 2021;31(25):2100069.
[526] Li N, Zhu X, Zhang C, Lai L, Jiang R, Zhu J. Controllable synthesis of different microstructured MnO2 by a facile hydrothermal method for supercapacitors. J Alloys Compound 2017;692:26–33.
[527] Ajmal Z, et al. Use of carbon-based advanced materials for energy conversion and storage applications: recent Development and Future Outlook. Fuel 2024;367:131295.
[528] Sun X, Wang H, Lei Z, Liu Z, Wei L. MnO_2 nanoflakes grown on 3D graphite network for enhanced electrocapacitive performance. RSC advances 2014;4(57):30233–40.
[529] Sun M, Huang B. Direct machine learning predictions of C3 pathways. Advan Energy Mater 2024;14(13):2400152.
[530] Fan H, et al. Simple synthesis of bimetal oxide@ graphitized carbon nanocomposites via in-situ thermal decomposition of coordination polymers and their enhanced electrochemical performance for electrochemical energy storage. Electrochimica Acta 2017;224:80–9.
[531] Sun M, Wong HH, Wu T, Dougherty AW, Huang B. Entanglement of spatial and energy segmentation for C_1 pathways in CO_2 reduction on carbon skeleton supported atomic catalysts. Advanced Energy Materials 2022;12(14):2103781.
[532] Song M-S, Lee KM, Lee YR, Kim IY, Kim TW, Gunjakar JL, Hwang S-J. Porously assembled 2D nanosheets of alkali metal manganese oxides with highly reversible pseudocapacitance behaviors. The Journal of Physical Chemistry C 2010;114(50):22134–40.
[533] Liu D, Wang Q, Qiao L, Li F, Wang D, Yang Z, He D. Preparation of nano-networks of MnO_2 shell/Ni current collector core for high-performance supercapacitor electrodes. Journal of Materials Chemistry 2012;22(2):483–7.
[534] Jiang M-J, Zhang Y-N, Meng L-S, Kang J, Li Y-J, Dong A. Recovery and in-situ reduction of precious metals by graphdiyne and graphdiyne oxide for antibacterial use. Rare Metals 2024;43(4):1747–57.
[535] Li L, Hu ZA, An N, Yang YY, Li ZM, Wu HY. Facile synthesis of MnO_2/CNTs composite for supercapacitor electrodes with long cycle stability. J Phys Chemis C 2014;118(40):22865–72.
[536] Lv G, Wu D, Fu R. Preparation and electrochemical characterizations of MnO_2-dispersed carbon aerogel as supercapacitor electrode material. J Non-Crystalline Solids 2009;355(50–51):2461–5.
[537] Cheng Q, Tang J, Ma J, Zhang H, Shinya N, Qin L-C. Graphene and nanostructured MnO_2 composite electrodes for supercapacitors. Carbon 2011;49(9):2917–25.
[538] Wong HH, et al. Neighboring effect in single-atom catalysts for the electrochemical carbon dioxide reduction reaction. eScience 2024;4(1):100140.
[539] Liu G, Wang G, Jin Z. Subtly synthesized graphdiyne nano-lamellas as stable electrode material for supercapacitors. Electrochimica Acta 2023;464:142866.
[540] Liu G, Wang G, Jin Z. Graphdiyne-modified NiV-layered double hydroxide nanostructures for supercapacitor applications. ACS Appl Nano Mater 2023;6(23):21803–17.
[541] Wang Y, et al. MXene/Graphdiyne nanotube composite films for Free-Standing and flexible Solid-State supercapacitor. Chem Eng J 2022;450:138398.
[542] Xu J, Li J, Yang Q, Xiong Y, Chen C. In-situ synthesis of MnO_2@ graphdiyne oxides nanocomposite with enhanced performance of supercapacitors. Electrochimica Acta 2017;251:672–80.
[543] Liang N, et al. A graphdiyne oxide composite membrane for active electrolyte enhanced supercapacitors with super long self-discharge time. J Mater Chem C 2022;10(7):2821–7.
[544] Zhai X, et al. Controlled growth of 3D interpenetrated networks by $NiCo_2O_4$ and graphdiyne for high-performance supercapacitor. ACS Appl Mater Interfaces 2022;14(16):18283–92.
[545] Fu J, et al. 19.31% binary organic solar cell and low non-radiative recombination enabled by non-monotonic intermediate state transition. Nat Commun 2023;14(1):1760.
[546] Zhu L, et al. Single-junction organic solar cells with over 19% efficiency enabled by a refined double-fibril network morphology. Nature Mater 2022;21(6):656–63.
[547] Zhou K, et al. Correlating miscibility, mechanical parameters, and stability of ternary polymer blends for high-performance solar cells. Energy Environ Sci 2023;16(11):5052–64.
[548] Kang Q, et al. A printable organic cathode interlayer enables over 13% efficiency for 1-cm^2 organic solar cells. Joule 2019;3(1):227–39.
[549] Ajmal Z, et al. Recent advances in carbon-nitride based advance materials: synthesis, characterization and photo-electrochemical energy application: key challenges and prospects. Fuel 2024;378:132903.
[550] Kan Y, et al. Amino-functionalized graphdiyne derivative as a cathode interface layer with high thickness tolerance for highly efficient organic solar cells. Advan Mater 2024:2312635.
[551] Cai X, et al. Graphdiyne oxide doping for aggregation control of hole-transport nanolayer in inverted perovskite solar cells. Nano Res 2022;15(11):9734–40.
[552] Li J, et al. Studies of graphdiyne-ZnO nanocomposite material and application in polymer solar cells. Solar Rrl 2018;2(11):1800211.
[553] Jin Z, et al. Graphdiyne: an efficient hole transporter for stable high-performance colloidal quantum dot solar cells. Advan Funct Mater 2016;26(29):5284–9.
[554] Liu L, et al. Graphdiyne oxide-accelerated charge carrier transfer and separation at the interface for efficient binary organic solar cells. Sci China Mater 2022;65(10):2647–56.
[555] Yao L, et al. Graphdiyne oxide doped SnO_2 electron transport layer for high performance perovskite solar cells. Mater Chem Front 2021;5(18):6913–22.
[556] Whittingham MS, Savinell RF, Zawodzinski T. Introduction: batteries and fuel cells. Chemical reviews 2004;104(10):4243–4.
[557] Goodenough JB, Park K-S. The Li-ion rechargeable battery: a perspective. J Amer Chem Soc 2013;135(4):1167–76.
[558] Saulnier M, Trudeau C, Cloutier SG, Schougaard SB. Investigation of CVD multilayered graphene as negative electrode for lithium-ion batteries. Electrochimica Acta 2017;244:54–60.
[559] Ali H, Orooji Y, Alzahrani AYA, Hassan HM, Ajmal Z, Yue D, Hayat A. Advanced porous aromatic frameworks: a comprehensive overview of emerging functional strategies and potential applications. ACS nano 2025.
[560] Liu B, Soares P, Checkles C, Zhao Y, Yu G. Three-dimensional hierarchical ternary nanostructures for high-performance Li-ion battery anodes. Nano letters 2013;13(7):3414–9.
[561] Wu M-S, Wang C, Jow J-J. Self-assembly of one-dimensional nitrogen-doped hollow carbon nanoparticle chains derived from zinc hexacyanoferrate coordination polymer for lithium-ion capacitors. Electrochimica Acta 2016;222:856–61.
[562] Wang F, Zuo Z, Li L, He F, Li Y. Graphdiyne nanostructure for high-performance lithium-sulfur batteries. Nano Energy 2020;68:104307.
[563] Wang K, Wang N, He J, Yang Z, Shen X, Huang C. Graphdiyne nanowalls as anode for lithium—ion batteries and capacitors exhibit superior cyclic stability. Electrochimica Acta 2017;253:506–16.
[564] Zhao F, Li X, He J, Wang K, Huang C. Preparation of hierarchical graphdiyne hollow nanospheres as anode for lithium-ion batteries. Chem Eng J 2021;413:127486.
[565] An J, Wang F, Yang J-Y, Li G, Li Y. An ion-pumping interphase on graphdiyne/graphite heterojunction for fast-charging lithium-ion batteries. CCS Chem 2024;6(1):110–24.
[566] Li J, et al. Graphdiyne/graphene/graphdiyne sandwiched carbonaceous anode for potassium-ion batteries. ACS nano 2022;16(2):3163–72.
[567] Debnath S, Phan C, Searles DJ, Hankel M. Graphdiyne and hydrogen-substituted graphdiyne as potential cathode materials for high-capacity aluminum-ion batteries. ACS Appl Energy Mater 2020;3(8):7404–15.
[568] Zheng Z, Xue Y, Li Y. A new carbon allotrope: graphdiyne. Trend Chem 2022;4(8):754–68.
[569] Geim AK. Graphene: status and prospects. Science 2009;324(5934):1530–4.
[570] Li X, Yu J, Wageh S, Al-Ghamdi AA, Xie J. Graphene in photocatalysis: a review. Small 2016;12(48):6640–96.
[571] Cooper DR, et al. Experimental review of graphene. Int Scholar Res Not 2012;2012(1):501686.
[572] Geim AK, Novoselov KS. The rise of graphene. Nat Mater 2007;6(3):183–91.
[573] Grigorenko AN, Polini M, Novoselov KS. Graphene plasmonics. Nat Photon 2012;6(11):749–58.
[574] Dai H. Carbon nanotubes: opportunities and challenges. Surface Sci 2002;500(1–3):218–41.
[575] Popov VN. Carbon nanotubes: properties and application. Mater Sci Eng: R: Reports 2004;43(3):61–102.
[576] De Volder MF, Tawfick SH, Baughman RH, Hart AJ. Carbon nanotubes: present and future commercial applications. science 2013;339(6119):535–9.
[577] Tasis D, Tagmatarchis N, Bianco A, Prato M. Chemistry of carbon nanotubes. Chemical Rev 2006;106(3):1105–36.
[578] Markovic Z, Trajkovic V. Biomedical potential of the reactive oxygen species generation and quenching by fullerenes (C60). Biomaterials 2008;29(26):3561–73.
[579] Pope CJ, Marr JA, Howard JB. Chemistry of fullerenes C60 and C70 formation in flames. J Phys Chem 1993;97(42):11001–13.
[580] Pan Y, et al. Advances in photocatalysis based on fullerene C_{60} and its derivatives: properties, mechanism, synthesis, and applications. Appl Catalysis B: Environ 2020;265:118579.
[581] Lopez AM, Mateo-Alonso A, Prato M. Materials chemistry of fullerene C_{60} derivatives. J Mater Chem 2011;21(5):1305–18.
[582] Afreen S, Muthoosamy K, Manickam S, Hashim U. Functionalized fullerene (C_{60}) as a potential nanomediator in the fabrication of highly sensitive biosensors. Biosensors Bioelectron 2015;63:354–64.
[583] Chung D. Review graphite. J Mater Sci 2002;37:1475–89.
[584] Chung D. A review of exfoliated graphite. J Mater Sci 2016;51:554–68.
[585] Celzard A, Mareche J, Furdin G. Modelling of exfoliated graphite. Progress in materials science 2005;50(1):93–179.
[586] Sengupta R, Bhattacharya M, Bandyopadhyay S, Bhowmick AK. A review on the mechanical and electrical properties of graphite and modified graphite reinforced polymer composites. Prog poly Sci 2011;36(5):638–70.
[587] Zhang H, Yang Y, Ren D, Wang L, He X. Graphite as anode materials: fundamental mechanism, recent progress and advances. Energy Storage Mater 2021;36:147–70.